

DESIGN, ANALYSIS AND DEVELOPMENT OF HYBRID OFFSHORE FLOATING BREAKWATER

Sanction No: DW-01013(13)/2/2021-Deveopment Wing

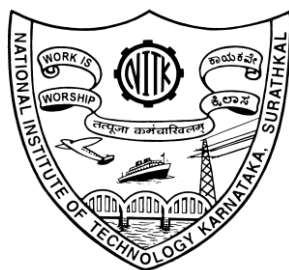
Project Closure Report (1st November 2021 – 31st October 2023)

MINISTRY OF PORTS, SHIPPING & WATERWAYS
GOVERNMENT OF INDIA, NEW DELHI

by

Dr. DEBABRATA KARMAKAR (PI)

Dr. MANU (Co-PI)



DEPARTMENT OF WATER RESOURCES & OCEAN ENGINEERING
NATIONAL INSTITUTE OF TECHNOLOGY KARNATAKA
SURATHKAL, P.O: SRINIVASNAGAR, MANGALORE – 575025
KARNATAKA, INDIA

DECEMBER, 2023

CHAPTER 1

INTRODUCTION

1.1 GENERAL

The coastlines are rich in biodiversity and productive habitats showing an increasing demand in human settlements, agriculture, trade, industry and marine transport activities such as shipping, fishing boats and recreational marinas. This demands in the linear development of the coast line and coast area and hence contributes at large towards the economic development of a country. The present era of innovation and technology has led to rapid industrialization and urbanization with increasing demand for land and energy. These proposed structures include ports, harbours, floating structures, offshore storage base, mega solar plant and wind & tidal energy plants leading to the requirement of protection and safe operation of these structures through the use of breakwaters.

Currently, fossil fuel is a major source of producing energy supplies to huge demands of human beings. However, the type of energy is not generative and would lead to global warming and pollution through the burning process. Electricity generation from fossil fuels is a significant contributor to carbon dioxide (CO₂) emissions. The demand for energy from human beings increases on the other hand. Regardless of the source of energy, demand is growing. With the global population expected to increase by about two billion over the next two decades, and with improving standards of living, it is estimated that by 2040 electricity generation is expected to increase by 52% WEO (2021). In order to secure sustainable development of energy, alternative safe and renewable energy sources are indispensable. The earth has an enormous amount of renewable energy in various forms such as sunlight, heat, wind, ocean waves and tidal currents. Therefore, development of efficiently renewable energy harvesting technologies has attracted great attention.

The rising cost of fossil fuels, allied with considerations about the environmental effects of greenhouse gas emissions, has sparked interest in the development of alternative energy supplies in recent years. Considering that the major component of greenhouse gases is carbon dioxide, there is a global concern about reducing carbon emissions. In this regard, different policies could be applied to reduce carbon emissions, such as enhancing renewable energy deployment and encouraging technological innovations. Two main solutions may be implemented to reduce CO₂ emissions and overcome the problem of climate change: replacing fossil fuels with renewable energy sources as much as possible and enhancing energy efficiency.

1.2 BACKGROUND AND SIGNIFICANCE

With the increasing demand in port commerce, industrialization and human activities in the coastal areas has led to the need for linear infrastructural development along the coastline through land reclamation resulting in overexploitation, pollution and intervention of coastal processes. The effect of global warming with rise in global temperature has set an alarming situation of sea level rise over these places, followed by the natural disasters such as hurricanes, tsunamis which shows a constant threat to these coastal cities and also raises a serious concern over the damage to marine ecosystems. These factors call for the increasing demand in coastal management of the coast and costal structures like ports and harbours. Coastal management is measure for coastal defence against flooding, sea level rise and control erosion for reclaim lands. With the depletion of the traditional energy resources and low carbon requirement, ocean renewable energy is attractive for its large reserves and exploitability in many sea areas. Despite the fact that wave energy utilisation technical solutions have matured to some extent and some devices are in the pre-commercial stage, current research and developments indicate that wave energy devices are still a long way from being used in real engineering applications. The high construction costs of the WECs may result in an uneconomic pricing for electricity generated by the WECs using ocean wave power. Wave power extraction's competitiveness in the energy market can be improved by lowering the building cost. One option for lowering building costs is to use a cost-sharing model. This is accomplished by merging two or more different types of marine constructions into a single installation. It's worth noting that the marine constructions that will be joined will have a synergistic impact and will operate in similar environments. Similarities like these could pave the road for collaboration.

1.3 FLOATING BREAKWATER STRUCTURES

The floating breakwaters are alternative solutions to the fixed structures that are used for protecting the area from the wave action. The first record of using floating breakwater was way back in 19th century was wood floating triangular shaped breakwater, proposed for Plymouth port, in 1811 UK (Cheng et al., 2013). During world war II, floating breakwater composed of wreck and caisson located at 1.6km far from the coast, was used by the British troops named as Bombardon breakwater in Mulberry artificial harbours in the year 1944 (Headland, 1995). When incident wave interacts with the floating breakwater it attenuates surface waves through the mechanism of wave reflection, and transmission. The dynamics of the floating breakwater induced by the wave force is controlled by providing mooring system. These floating structures are found to be effective at larger water depths and in coastal areas with mild wave environment conditions. Floating breakwaters are proven to be advantageous, when the site location is

having poor foundation condition, when the depth of sea exceeds 6m, when toeing and relocating of breakwaters are required, and also in areas under high tide, which requires minimum intrusion on the horizon. These breakwaters are also found to be beneficial to the aqua-life as it shows minimum interference in water circulation and sediment transportation (McCartney, 1985). Commonly, floating breakwater will be effective if the wave height is less than 5 feet or about 1.5 m, as shown in the following Figure 1.1 (Paotonan et al., 2019).

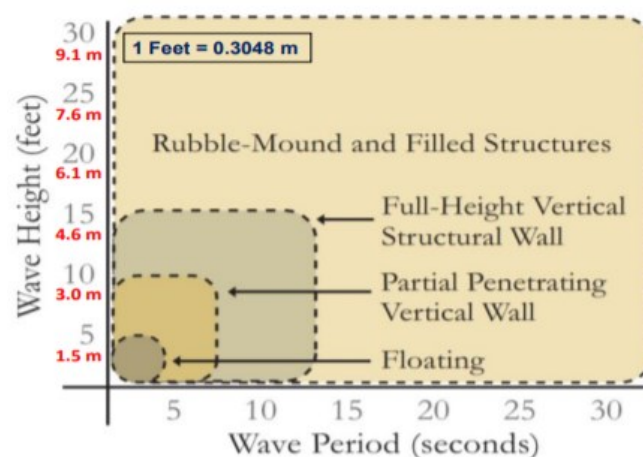


Figure 1.1: Effectivity of breakwaters (Paotonan et al., 2019)

The application prospective of floating breakwaters have been identified in many fields of engineering such as Port Coastal Engineering, offshore engineering, protection of offshore wind farms and aquaculture. (Zhou and Li, 2020).



Figure 1.2: Orchard Harbour Floating Breakwater



Figure 1.3: Floating breakwater Fezzano, SP-Italy

According to their geometrical configuration and functional similarities (McCartney, 1985 and Mani, 1991) classified floating breakwater in to four types namely, (i) box, (ii) Pontoon, (iii) Mat and (iv) Tethered float and are as shown in Figure 1.2.



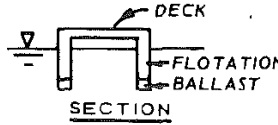
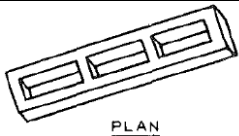
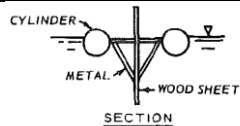
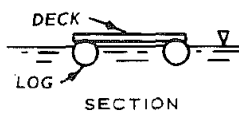


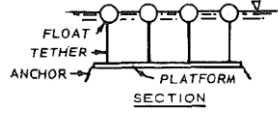
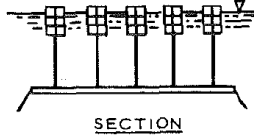
TYPE	VIEW	REMARKS
BOX		
a) Solid Rectangle		Reinforced concrete units are the most common type
b) Barge		
PANTOON		
a) Twin Pontoon		Catamaran shape
b) Open Compartment		Also called Alaska type
c) A Frame		
d) Twin log		Deck in open wood frame
MAT		
a) Tire mat		Scrap tires strung on pole Framework or bound together with chain or belting.
b) Log mat		Log raft chained or Cabled together.
TETHERED		
a) Sphere		Floats placed in rows.
b) Tire		Arrangement similar to spheres. Steel drums with ballasts can be use in lieu of tires.

Fig 1.4: Various types of floating breakwaters (McCartney, 1985).

1.4 LITERATURE REVIEW

In this section a review of the literatures on the hydrodynamics analysis of floating and combination of submerged- floating structures, with different structural and geometrical parameters is discussed. A review of research in areas of hydrodynamics analysis of floating structures, and effect of reef structure to protect these structures is presented.

1.4.1 Wave Interaction with Floating Breakwaters

Bentham in 1811 proposed two stone and one floating breakwater to Admiralty, for the Plymouth Port, UK. The wooden breakwater was to consist of 117 floats of wood, of a triangular or prismatic form; each float thirty feet (9.144m) in breadth and depth, forty feet (12.192m) in length, they were to be moored by iron chains. Although the Admiralty opted for stone breakwater, after years of its construction due to the accumulation of silt and mud within the harbour, water level diminishes to the extent of 5 feet (1.524m) (Stuart, 1842).

With technological and economic development of the countries, application of the floating breakwaters has become popular as a variable alternative to coastal management. One of the earliest floating breakwaters proposed for harbours off the east coast of Ireland, were of cylindrical cross section with 30 feet (9.144m) in diameter and a length of about 10 times the diameter, supporting a submerged platform at a submergence depth of about four fathoms (7.315m). For the lateral stability and to resist transmission of undulatory motion, transverse web stiffeners were used. (Joly, 1905). During the mid of the 19th century, based on the geometrical and functional similarities recognised at least 60 different floating breakwaters configurations by (Jones, 1971) and (Richey and Nece, 1974). Further (Hales, 1981) logically classified these breakwaters in to 11 basic groups, based on their fundamental features. Later, (McCartney, 1985) separated these breakwaters into 4 general categories (box, pontoon, mat, and tethered floats) based on the shape and wave attenuate performance, and evaluated their construction costs.

Nikpour et al. (2019) through his experimental studies concluded that trapezoidal shaped floating breakwater with a side slope of 60^0 performed effectively in wave transformation, reducing mooring forces and structural motion in comparison with rectangular floating breakwater. A series of experiments conducted on box-type floating breakwater to capture the effect of different terrains under regular and irregular wave conditions showed an excellent result in wave attenuating performance. A numerical simulation using Smooth Particle Hydrodynamics (SPH) conducted with respect to wave transmission and mooring force showed good agreement with the experimental results (Cui, et al., 2019).

For investigation of more complex problems, researchers often rely on numerical techniques. One such example of different numerical techniques used for the computation of hydrodynamics performance, for 24 models grouped into the five principal categories as Eigen Function Expansion Method (EFEM), Green Function Method (GFM), Hybrid Green Function Method (HGFM), Finite Element Method (FEM) and other methods was listed by Bando and Sonu (1987). They used variational approach as the basis function for computation of wave scattering properties for bottom and surface obstacles of different proportions, including thin barriers and surface docks. Considering 2D linear potential wave flow, boundary integral was developed by Williams et al. (2000) to analyse hydrodynamic properties for pair of long rectangular floating breakwaters and it was observed that the wave reflection properties of the structure depend on their width, draft, relative spacing and mooring line stiffness. Lee and Cho (2003) presented numerical formulation and implementation of the Element Free Galerkin Method for calculation hydrodynamics coefficients of moored Pontoon-type floating breakwaters. Gesraha (2006) investigated the wave transformations characteristics with EFEM followed by the experimental validation, for long rectangular breakwater with two thin sideboards protruding vertically downward called as Π type configuration. Based on his investigations Π type configuration may result in material saving if design and its mass properties are matched with the incident wave frequency when compared with rectangular breakwaters of same mass. Peng et al. (2013) numerically studied the nonlinear wave interaction between the water waves and moving submerged floating breakwater, based on N-S solver coupled with IB method and VOF method. The numerical method developed showed a good agreement with the experimental results in terms of tension mooring force and floating body dynamics. Karmakar et al. (2013) used EFEM along with the method of least square approximation, the performance of vertical surface-piercing, single and multiple porous membrane breakwaters are analysed for finite water depth for linear water waves conditions. He concluded the effectiveness of the proposed approach in solve water wave hydrodynamics and also observed that multiple porous membrane is more efficient in wave transformation when compared with single surface piercing porous membrane. Ouyang et al. (2015) presented the water wave characteristics of Bragg reflection reflections from a train of fixed floating pontoon breakwaters was studied numerically. Duan et al. (2016) performed numerical investigations on an F-type floating breakwater using Boundary Element Method (BEM) to study the interaction of 2D floating bodies with water waves. The results obtained using the BEM was experimentally validated in terms of reflection and transmission coefficient.

Different cross sections (Rectangular, Circular, Triangle and Trapezoidal) floating breakwaters of same weight are analysed by Masoudi et al. (2017), using Boundary Element Method in ANSYS AQWA software for diffraction problem and concluded that rectangular shaped breakwater perform better in wave transmission among others whereas triangular breakwater demonstrates lowest reflection coefficient. Viscous flow simulation of wave-body interaction is carried out by Zhang et al. (2018) for rectangular and inverted π -type fixed floating breakwater. The proposed model was validated with viscous model, potential flow, and experimental results in terms of wave reflection and transmission coefficients. Further an L-type floating breakwater was derived from the rectangular and inverted π -type, which performed efficiently under the same hydrodynamic conditions. Catipovic et al. (2019) developed a 3D mathematical model considering an additional stiffness matrix to couple the dynamic analysis of array of floating bodies with a hinged connection. Deng et al. (2019) performed hydrodynamic investigation of T-shaped floating breakwater using semi-analytical matched Eigenfunction expansion method. Ding et al. (2019) considered three kind (rectangular, cosinoidal and triangular shaped) surface-piercing fixed floating breakwater in their numerical study using BEM. It was observed that the triangular structure proves to be effective in attenuating the waves by using Bragg reflection. Li et al. (2020) studied the hydrodynamics characteristics of Arc-shaped plate type floating breakwater under long wave considering 2d wave flow through an open-source program (Open Foam) and then validated their results with physical model studies. Tseng et al. (2020) using eigen function matching method (EMM) studied the Bragg reflection by the combined effect of floating structures, bottom variation and oblique water waves incidence.

1.5 RESEARCH OBJECTIVES

Attenuating waves by the use of simple structures built with locally available materials are increasingly in demand in protection of coast line and coastal structures. The energy of water waves can be attenuated by using breakwaters. Breakwaters forms a stumbling block for oceanic water waves; hence wave force is diminished by them naturally. Among several types of breakwaters, floating breakwaters are the most efficient hard solutions in coastlines and coastal structure sheltering, without affecting the aesthetics of coastal view and free seawater exchange in larger depth of sea.

The hydrodynamic characteristics of fixed floating structures of various shapes (namely, rectangular, triangular, and trapezoidal) are coupled individually with submerged breakwaters of various shapes and types (impermeable, permeable, and perforated) that interact with linear water waves of finite water depth under the assumption of small-amplitude water waves will

be examined using multidomain Boundary Element Method. The change in physical parameters such as relative water depth, relative spacing between the floating structure and the submerged breakwater, and their structural properties affect the hydrodynamic scattering coefficients such as wave reflection, transmission coefficients, and exciting force on the fixed floating structure with and without the presence of submerged breakwater. The effect of oblique wave incidence on wave transformation characteristics are also examined under short and long wave conditions. The current MDBEM model is subjected to a convergence analysis to ensure the accuracy of the results in the scenario of a fixed rectangular floating structure coupled with an impermeable trapezoidal submerged breakwater and then, the findings of the numerical computations are compared to those found in the literature. The current analysis identifies a set of incident wave angles and periodic distances between the submerged breakwater and the floating structure where the coupled structures perform well in attenuating wave force acting on the floating structure and optimizing wave transformations. Furthermore, the presence of reef structures in front of the main floating structures helps to maximize wave reflection while reducing wave forces acting on the structures. Due to the considerations of coupling floating structures with submerged breakwaters, significant differences in wave transformation characteristics and wave forces acting on the floating structure are identified when compared to those with solitary floating structures. This research will undoubtedly aid in the selection of various combinations of coupled floating structures with submerged breakwaters of various types and shapes in coastal engineering applications.

1.6 OBJECTIVE OF THE PROPOSED PROJECT

The objective of the present study is to develop numerical tool and perform experimental investigation for wave structure interaction problems and to investigate a class of physical problems associated with the interaction of surface water waves with hybrid floating breakwaters arising in broad area of offshore and coastal engineering.

- ✓ The development of the numerical tool for the wave-induced motions with the hybrid floating breakwaters in shallow water under the influence of waves in the port will be carried out. In addition, the surface gravity wave scattering by floating hybrid breakwater in shallow water due to the changes in bottom topography will also be analyzed.
- ✓ The developed numerical tool will then be utilized to study the behavior and effect of different kinds of floating and immersed breakwaters which were used to improve the

wave conditions at the entrance of ports or in areas where ships may need to anchor in standby positions.

- ✓ The numerical results for the (i) linear diffraction around a semi-infinite breakwater, (ii) linear and non-linear gap diffraction, (iii) non-linear wave run-up on a vertical plate, (iv) scattering of linear waves about a vertical cylinder in open water and (v) regular waves over a semi-circular shoal will also be studied in different cases.
- ✓ The experimental study in the wave flume on various hybrid offshore floating breakwaters will be performed and the results obtained will be compared with the numerical results obtained using the developed numerical approach.

The application of the numerical tool in the present study will reveal interesting physical characteristics of the phenomenon in deep and shallow water for various particular cases. Further, different physical problems in the present study will be useful to engineers for the analysis of wave conditions near the port.

CHAPTER 2

FLOATING STRUCTURE COUPLED WITH SUBMERGED BREAKWATERS

2.1 GENERAL

The application prospective of floating breakwaters has been identified in many fields of engineering such as Port Coastal Engineering, offshore engineering, protection of offshore wind farms, and aquaculture. Zhou and Li, (2020). The dynamics of the floating breakwater induced by the wave force are controlled by providing mooring systems. These floating structures are found to be effective at larger water depths and in coastal areas with mild wave environment conditions. Floating breakwaters are proven to be advantageous when the site location is having poor foundation condition when the depth of sea exceeds 6m, when toeing and relocating breakwaters are required, and also in areas under the high tide, which requires minimum intrusion on the horizon. These breakwaters are also found to be beneficial to the aqua-life as it shows minimum interference in water circulation and sediment transportation by McCartney, (1985). Commonly, the floating breakwater will be effective if the wave height is less than 5 feet or about 1.5 m Paotonan et al., (2019).

In the present study, the wave interaction with floating structures coupled with the submerged breakwater of various configurations depicted in Table 2, Table 3, and Table 4 is examined. The multi-domain boundary element approach is used to investigate the efficiency in decreasing wave exciting pressures on the floating structure due to the presence of submerged breakwaters of various shapes and types and then to determine the fixed body transmission and reflection coefficients under oblique wave conditions. To maximize the effectiveness of the suggested configuration of submerged reef structure constructed combined with the primary fixed floating structure, the reaction to wave reflection and transmission, structural characteristics, geometrical parameters, and morphologies of the breakwater are evaluated.

2.2 THEORETICAL FORMULATION

For the hydrodynamic analysis under the action of regular waves using the Multi-Domain Boundary Element Method (MDBEM), the idealized geometry of a submerged reef structure constructed at some distance in front of the primary fixed floating structure, the coordinate system, the fluid-structure domains, and the boundaries are as shown in Fig. 1. In a constant water depth, the regular waves of small wave amplitude a , time period T and wavelength λ

travelling from left to right at an angle θ with regard to the x -axis direction are considered. The fluid flow is considered to be inviscid, incompressible, and irrotational, and the velocity potential in each zone is of the form $\Phi_j(x, y, z, t) = \text{Re}\{\phi(x, y)e^{i(k_z z - \omega t)}\}$, where Re denotes the real part of the spatial complex potential $\phi(x, y)$ satisfies the Helmholtz's equation given by

$$(\nabla^2 - k_z^2)\phi(x, y) = 0, \text{ in the fluid domain } \Omega. \quad (1)$$

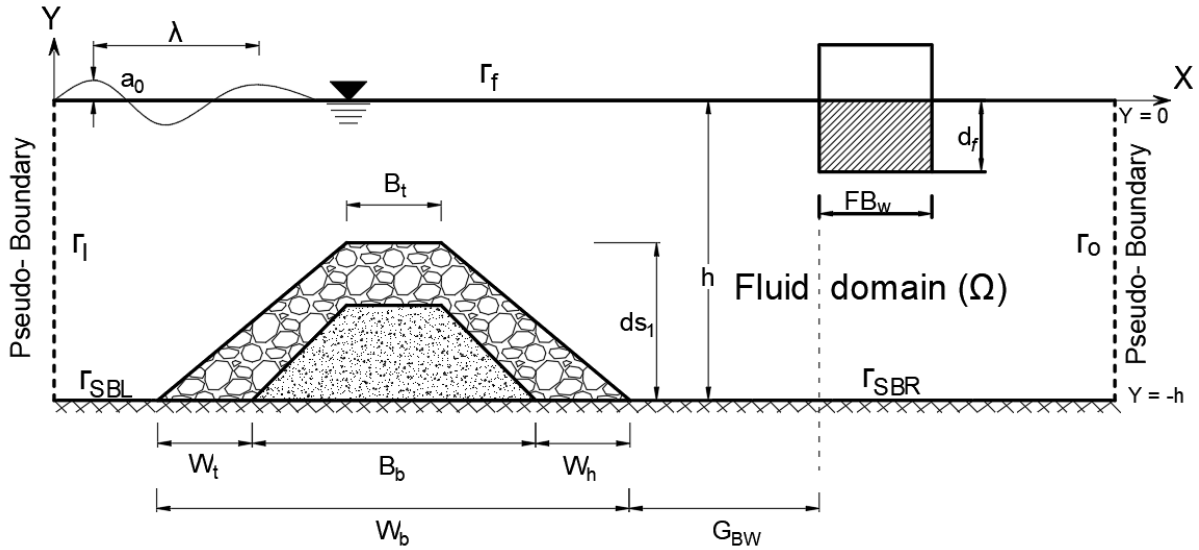


Figure 2.1 shows a submerged perforated trapezoidal breakwater in conjunction with a fixed floating rectangular structure.

In Fig.1, the fluid domain is defined as Ω , the sea-bed boundary is defined as Γ_{SB} , the boundary at the structure interface is defined as Γ_{Str} , the Sommerfeld's radiation boundary is defined as $\Gamma_{I,O}$ and the free surface boundary is defined as Γ_{fs} . The boundary condition at the mean free surface of the fluid is given by

$$\frac{\partial \phi}{\partial y} - \frac{\omega^2}{g} \phi = 0 \text{ on } \Gamma_{fs}, \quad (2)$$

Assuming that the bottom boundary is impervious, the horizontal sea bed boundary condition is stated as

$$\frac{\partial \phi}{\partial y} = 0, \text{ on } \Gamma_{SBL} \text{ and } \Gamma_{SBR} \text{ at } y = -h. \quad (3)$$

Based on the permeability of the structures, the structural region's boundary condition has been defined. The rigid boundary condition is used in the case of impermeable structures, while the permeability boundary condition is used in the case of porous structures. As a result, the no-flow border condition for rigid structures is stated as

$$\frac{\partial \phi}{\partial n} = 0, \quad \text{on } \Gamma_{str}. \quad (4a)$$

Assuming the continuity of pressure and mass flux between the fluid structure interface. The matching boundary conditions for porous structures between the fluid and structural region is written as,

$$\frac{\partial \phi_{str}^f}{\partial n} = -\varepsilon \frac{\partial \phi_{str}^s}{\partial n} \quad \text{and} \quad \phi_{str}^f = (S + if)\phi_{str}^s, \quad (4b)$$

where ϕ^f is the velocity potential in the water region, ϕ^s is the velocity potential in the structural region, ε is the structural porosity, f is the linearized friction coefficient and S is the inertial coefficient of the porous breakwater (Sollitt and Cross, 1972; Dalrymple et al. 1991). The influence of the porous breakwater is reflected in this study by three parameters ε , f and S . The porous structure region becomes an open water region if in case $\varepsilon=1$, $f=0$ and $S=1$. In the present study, arbitrary values of inertial coefficient $S=1$ and the frictional coefficient $f=1$, and structural porosity $\varepsilon=1$ are considered.

At a great distance from the breakwater, the entire velocity potential is decomposed into incident and dispersed potentials, which must meet the radiation requirement expressed as

$$\lim_{r \rightarrow \infty} \sqrt{r} \left(\frac{\partial \phi}{\partial r} - ik\phi \right) = 0, \quad \text{where } r = \sqrt{x^2 + y^2}. \quad (5a)$$

Let ϕ_{inp} and ϕ_{out} be the input and output region wave velocity potential in pseudo-boundary region respectively. To solve the Eq.6(a) applying the method of superposition of waves with the assumption no loss of energy, the velocity potential at input and output region expressed in terms of the incident wave potential (ϕ_I), the reflected wave potential (ϕ_R) and the transmitted wave potentials (ϕ_T) is given by

$$\begin{aligned} \text{Input region } (\Gamma_l) : \quad \phi_{inp} &= \phi_I + \phi_R, \\ \text{Output region } (\Gamma_r) : \quad \phi_{out} &= \phi_T, \end{aligned} \quad (5b)$$

Further, with the assumptions of small amplitude wave theory, the velocity potentials at input and output regions which is a function of incident wave amplitude (I_0), reflected wave amplitude (R_0), transmitted wave amplitude (T_0), and the wave pressure coefficient is be given by

$$\begin{aligned} \phi_{inp} &= (I_0 e^{iq_0 x} + R_0 e^{-iq_0 x}) P_w(k, y), \\ \phi_{out} &= T_0 e^{iq_0 x} P_w(k, y), \end{aligned} \quad (5c)$$

The wave pressure coefficient $P_w(k, y)$ which dependent on pressure response factor (k_p), which varies along the water depth is given by the relation

$$P_w = \frac{ig}{\omega} k_p, \quad (5d)$$

and, k_p is the is of the form

$$k_p = \frac{\cosh k(h+y)}{\cosh kh},$$

Here, h is the water depth, and the reflected and transmitted are wave amplitudes are to be determined at the pseudo-boundaries respectively with $q_0 = \sqrt{k^2 - k_z^2}$.

The angular frequency ω and the progressive wave number k , satisfying the dispersion relation in the mean free surface given by

$$\omega^2 = gk \tanh kh \quad (6)$$

Using the velocity potential (ϕ) in the fluid domain at the input and output region, the reflection (R_0) and transmission (T_0) wave amplitudes are computed as in Chen et al. (2004) based on the property of continuity across the input and output boundaries ($x = 0, L$) is given by

$$R_0 = \left\{ 1 + \frac{k}{n_0 \sinh kh} \int_{-h}^0 \phi(0, y) \cosh k(h+y) dy \right\} \quad (7)$$

$$T_0 = \frac{k}{n_0 \sinh kh} \int_{-h}^0 \phi(L, y) \cosh k(h+y) dy \quad (8)$$

where $n_0 = \frac{1}{2} \left(1 + \frac{2kh}{\sinh(2kh)} \right)$

2.3 NUMERICAL SOLUTION USING MULTI-DOMAIN BEM

To investigate the hydrodynamic performance of a submerged reef structure developed in conjunction with a primary permanent floating structure, the Multi-Domain Boundary Element Method (MDBEM) is used. The boundary element technique is built on the fundamental solution and Green's second identity. The weighted residue and Green-Gauss theorem are used to the Helmholtz equation to determine the solution for the boundary value problem, as shown in Eq (1) over the domain Ω bounded by boundaries Γ . The boundary integral equation in its generalised form is written as

$$c(P) \cdot \phi(P) + \int_{\Gamma} \phi \cdot \frac{\partial G}{\partial n} d\Gamma = \int_{\Gamma} G \cdot \frac{\partial \phi}{\partial n} d\Gamma, \quad (10)$$

The coefficient of free term $c(P)$ is given by

$$c(P) = \begin{cases} 1 & \text{for } P \equiv (\xi, \eta) \in \Omega, \\ \frac{1}{2} & \text{for } P \equiv (\xi, \eta) \in \Gamma \text{ and } \Gamma \text{ is smooth at } P, \\ 0 & \text{for } P \equiv (\xi, \eta) \text{ outside } \Omega. \end{cases} \quad (11)$$

The Green's function G is the fundamental solution of the governing equation which satisfies the relation

$$\nabla^2 G - k_z^2 G = \delta(\xi - x, \eta - y), \quad (10)$$

and G is given by

$$G(x, y; \xi, \eta) = -\frac{K_0(k_z, r)}{2\pi}, \quad (11)$$

The term K_0 is the modified zeroth-order Bessel function of second kind and r is the distance between the field point (x, y) and the source point (ξ, η) given by

$$r = \sqrt{(\xi^2 - x^2) + (\eta^2 - y^2)}. \quad (12)$$

The normal derivative of the Green's function is given by

$$\frac{\partial G}{\partial n} = \frac{k_z}{2\pi} K_1(k_z r) \frac{\partial r}{\partial n}, \quad (13)$$

where K_1 is the modified first-order Bessel function of the second kind. In the case of singularity $r \rightarrow 0$, the asymptotic behaviour of K_0 is given by

$$K_0(k_z r) = -\gamma - \ln\left(\frac{k_z r}{2}\right) \quad (14)$$

where $\gamma = 0.5772$ is the Euler's constant. Further in the case of normal incident angle i.e., when $\theta = 0$, $K_0(k_z r)$ approaches to $-\ln(r)$ as discussed in Kim and Woo (2013).

2.4 DOMAIN DISCRETIZATION

Discretizing the entire boundaries of fluid region and the structure region in to a finite N constant boundary element and assuming the ϕ and G to be constant and equal to a value at mid-element node. The discretized form of integral equation is written as

$$-\frac{1}{2} \cdot \phi(P) + \sum_{j=1}^N (H_{ij} \cdot \phi_j) = \sum_{j=1}^N \left(Q_{ij} \cdot \frac{\partial \phi}{\partial n} \right). \quad (15)$$

where $H_{ij} = \int_{\Gamma_j} \frac{\partial G}{\partial n} d\Gamma$, $Q_{ij} = \int_{\Gamma_j} G_j d\Gamma$, and Γ is the boundaries as defined in section 2.

Using the boundary conditions given in Eq. (2)-(5), the discretized form of boundary integral equation (15) in the fluid region (f_R) and the structure region (St_R) is rewritten as

The integral equation for fluid region (Patil and Karmakar, 2021) is expressed as

$$-\frac{1}{2}\phi^{f_R} + \sum_{j=1}^N (H_{ij}\phi_{SB}^{f_R}) + \sum_{j=1}^N (H_{ij}\phi_{Str}^{f_R}) - \sum_{j=1}^N \left(Q_{ij} \frac{\partial \phi_{Str}^{f_R}}{\partial n} \right) + \sum_{j=1}^N (H_{ij} - ikQ_{ij})\phi_{out}^{f_R} + \sum_{j=1}^N \left(H_{ij} - \frac{\omega^2}{g} Q_{ij} \right) \phi_{fs}^{f_R} + \sum_{j=1}^N (H_{ij} - ikQ_{ij})\phi_{imp}^{f_R} = 0. \quad (16)$$

Similarly, the integral equation for the structure region is expressed as

$$-\frac{1}{2}\phi^{st_R} + \sum_{j=1}^N (H_{ij}\phi_{SB}^{st_R}) + \sum_{j=1}^N (H_{ij}\phi_{Str}^{st_R}) - \sum_{j=1}^N \left(Q_{ij} \frac{\partial \phi_{Str}^{st_R}}{\partial n} \right) = 0. \quad (17)$$

Here, the superscripts f_R and St_R are used to indicate the fluid region and the structures region respectively and the subscripts indicate the boundary regions. Knowing that the common interface boundaries Γ_{Str} , have the same potential ϕ^m and flux $\frac{\partial \phi^m}{\partial n}$, the matching boundary conditions given in Eq. (4b) for porous structure and using Eq. (6b), used to form linear system of algebraic equation. Further, the numerical program is developed in MATLAB to solve for unknown potentials ϕ_R and ϕ_T using Gauss elimination technique.

It may be noted, that as the waves impinge on a structure, some portion of their energy is redirected as a reflected wave. So, relating the reflected wave to the incident wave can demonstrate the extent of protection a structure provides for a desired area. The transmission coefficients and the reflective qualities of a coastal structure are used to quantify the effectiveness of a breakwater to shield an area from approaching waves. The reflection and transmission coefficients are calculated using the formula.

$$K_R = \left| \frac{R_0}{I_0} \right| \text{ and } K_T = \left| \frac{T_0}{I_0} \right|. \quad (18)$$

The incoming wave force equation operating on the breakwater structure as derived in Au and Brebbia (1982) is expressed as

$$F = i\omega\rho \int_{\Gamma_j} \left\{ \begin{matrix} n_x \\ n_y \end{matrix} \right\} \phi d\Gamma, \quad (19)$$

where $F = \begin{Bmatrix} F_x \\ F_y \end{Bmatrix}$, n_x and n_y are unit normal in x and y directions.

According to Seelig and Ahrens (1981), the relationship between wave reflection, dissipation, and transmission coefficient is represented as

$$1 = K_D^2 + K_R^2 + K_T^2. \quad (20)$$

2.5 NUMERICAL RESULTS AND DISCUSSION

The current numerical analysis focuses on wave interactions between floating structures coupled with submerged reef-like structures (i.e., breakwaters of various kinds and shapes) that are designed to work together, as shown in Table 2. The wave reflection coefficient K_R , transmission coefficient K_T , and the wave force F impact on leeward of fixed floating breakwater is analysed to understand the effectiveness of presence of submerged breakwaters. The fluid is assumed to have density $\rho = 1000 \text{ kg/m}^3$, the acceleration due to gravity $g = 9.81 \text{ m/sec}^2$, and for all the porous structures for the sake of comparing the effectiveness of different configuration of tandem breakwater the friction coefficient $f = 1$, structural porosity $\varepsilon = 0.4$, and the virtual mass coefficient $S = 1$ are kept constant throughout the computation.

2.5.1 Verification of Numerical Method

The results evaluated for wave reflection and transmission for water wave interaction with floating structures coupled with submerged breakwaters of various types and shapes are developed using boundary discretization techniques MDBEM, are compared with the established results available in the literature on experimentation and a well as numerical studies developed by the following authors (a) Domain Decomposition Method by Ijima and Okuzono (1982), (b) EFEM and experimental results obtained by Cho et al. (2004) and (c) Meshless method by Ouyang et al. (2016) and Senouci et al. (2019). Further, the results obtained using Eigen Function Expansion Method (EFEM) in Abul-Azam and Gesraha, (2000) are also compared with present MDBEM model for single floating Pontoon. The results achieved in this investigation are very similar to those reported by these authors.

2.5.1.1 Numerical validation of Multi-domain Boundary Element Method (MBEM)

For the case of an impermeable double trapezoidal submerged, the findings obtained by Cho et al. (2004) using EFEM validated with experimental results, Ouyang et al. (2016) using Regularised Meshless Method (RMM), and Fawzi et al. (2019) using Improved Singular

Boundary Element Method (ISBM) are compared to the results produced by applying the current MBDEM model. Fig. 2 shows the fluctuation in reflection coefficient K_R with varying non-dimensionless wave number kh with the structural parameters $X_s/d = 3.0$, $h/d = 0.5$, $w_b/d = 0.5$ and $w_t/w_h = 0.5$. The present MBDEM model, as shown in Fig. 2.2, shows close agreement with the numerical results produced by the above-mentioned authors.

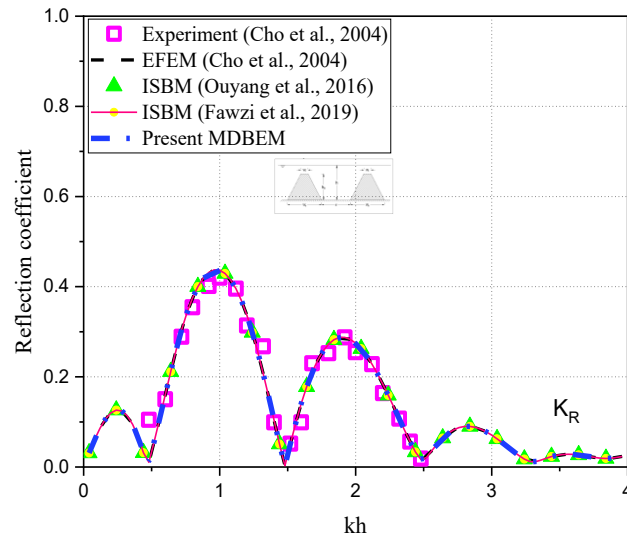


Fig. 2.2: Variation of K_R versus kh for impermeable double trapezoidal submerged breakwater.

To ensure that the current MBDEM model for surface floating structures is valid, the analytical model developed by Abul-Azam and Gesraha (2000) used to determine the wave force on the floating structure as well as the fixed body transmission and reflection coefficients under oblique waves is considered. Fig. 2.3 shows the variation of K_R and K_T versus kh for a fixed rectangular floating Pontoon, having the structural parameters $d_f/h = 0.25$ and $b/h = 0.50$. The results obtained by present MBDEM model fairly matches with the results obtained by Abul-Azam and Gesraha (2000).

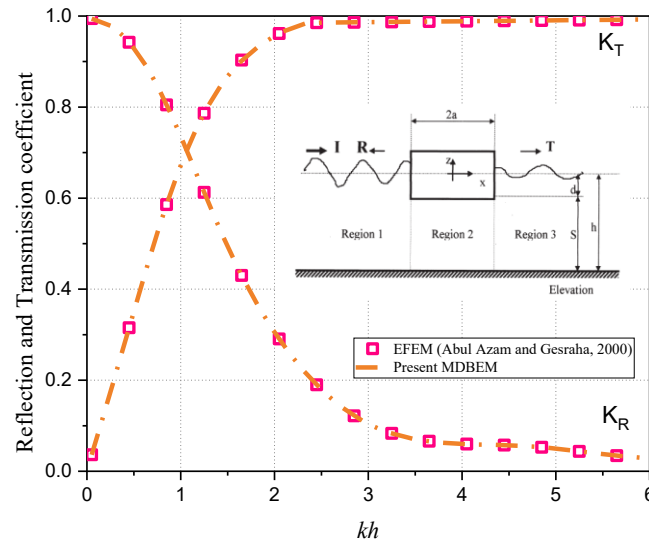


Fig. 2.3: Variation of K_R and K_T versus kh for fixed rectangular floating Pontoon.

2.5.1.2 Convergence of MDBEM model

The boundary surface is split into a finite number of constant panel boundary element units for computer treatment, and the mesh converges to a solution as shown in Table 2.1. The mesh refinement indicates convergence of the numerical findings in the current MDBEM model when a constant panel boundary element with a size of (1/10th) for each 1m of the boundary region is employed to discretize.

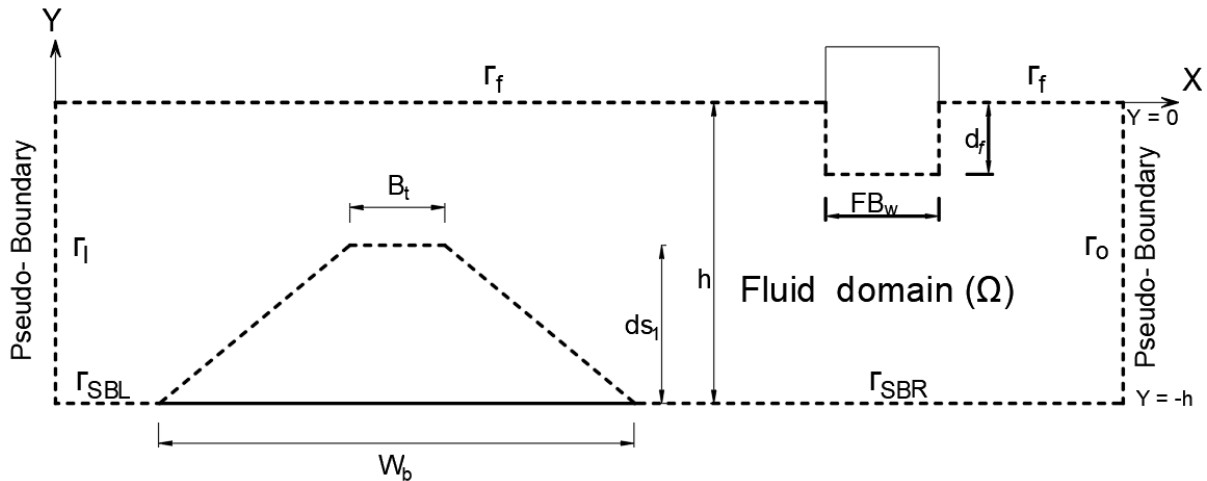


Fig. 2.4: Schematic diagram of boundary element mesh

The wave reflection and transmission coefficients obtained for an impermeable rectangular floating structure coupled with impermeable submerged trapezoidal breakwater is considered as a mesh dependency for convergence of the numerical results with the structural parameters

kept as, draft to depth ratio $d_f/h = 0.40$ and $FB_w/h = 0.50$ for the floating structure and for the trapezoidal submerged breakwater the relative depth of submergence $d_{s1}/h = 0.80$, relative width as $B_i/h = 0.5$ and relative bottom width $B_w/h = 2.5$. The convergence of present MDBEM model is achieved with a constant panel boundary element discretized greater than 344 elements.

Table 2.1: Convergences of K_R and K_T with increasing boundary mesh elements

Γ_{SBL}	Γ_{STR}	Γ_{SBR}	Γ_o	Γ_f	Γ_{fstr}	Γ_l	Constant Element Length(m)	BE	K_R	K_T
4	16	4	2	12	10	2	1.0	50	0.5885	0.7210
8	32	8	4	24	20	4	0.5	100	0.5609	0.7833
40	20	56	50	112	16	50	0.10	344	0.5686	0.8071
80	40	118	100	240	32	100	0.05	710	0.5686	0.8069

2.6 PERFORMANCE OF SUBMERGED BREAKWATERS IN TANDEM

When incident wave interacts with the floating breakwater it attenuates surface waves through the mechanism of wave reflection, and transmission. The dynamics of the floating breakwater induced by the wave force is controlled by providing mooring system. These floating structures are found to be effective at larger water depths and in coastal areas with mild wave environment conditions. Hence in the present study in view of attenuating the wave forces and optimizing the wave transformation characteristic coupling of floating structures with different types and shapes of submerged breakwaters are considered and analysed. These breakwaters serve as a reef to the floating structures that are built a short distance in front of the main floating structure. The details about the different configuration of coupled models are tabulated in Table 2.2, Table 2.3 and Table 2.4. The proposed coupled models were created using MDBEM to assess the hydrodynamic characteristics and to investigate the effectiveness of coupling these floating structures with submerged breakwater of various shapes (rectangular, triangular, and trapezoidal) and structural properties (permeable, impermeable, and perforated) for various height to depth ratios and angles of incidence.

Table 2.2: Models for various types and shapes of submerged breakwaters in conjunction with a rectangular fixed floating structure.

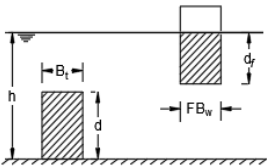

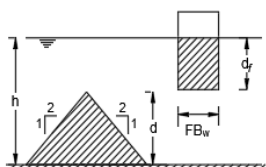
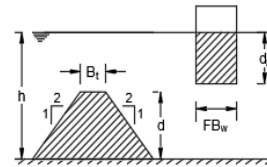
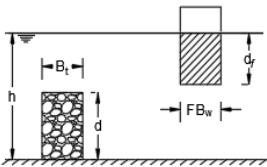

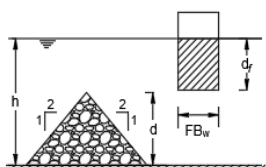
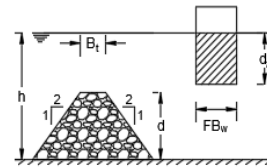


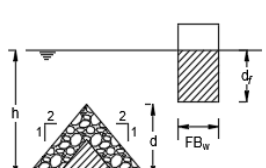
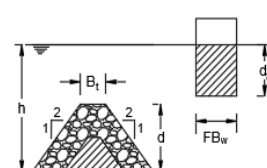
 <p>Rectangular BW Rectangular BW</p>		 IMPERMEABLE BW Top width to depth of water (B_t/h) = 0.5 Height of submerged structure to depth of water (d/h) = 0.80 Draft of floating structure to depth of water (d_f/h) = 0.40	
 <p>Triangular BW Rectangular BW</p>			
 <p>Trapezoidal BW Rectangular BW</p>			
 <p>Rectangular BW Rectangular BW</p>			 PERMEABLE BW Top width to depth of water (B_t/h) = 0.5 Height of submerged structure to depth of water (d/h) = 0.80 Draft of floating structure to depth of water (d_f/h) = 0.40 $\epsilon = 0.4, f = 1.0, S = 1.0$
 <p>Triangular BW Rectangular BW</p>			
 <p>Trapezoidal BW Rectangular BW</p>			
 <p>Rectangular BW Rectangular BW</p>		 PERFORATED BW Top width to depth of water (B_t/h) = 0.5 Height of submerged structure to depth of water (d/h) = 0.80 Draft of floating structure to depth of water (d_f/h) = 0.40 $\epsilon = 0.4, f = 1.0, S = 1.0$	
 <p>Triangular BW Rectangular BW</p>			
 <p>Trapezoidal BW Rectangular BW</p>			

Table 2.3: Models for various types and shapes of submerged breakwaters in conjunction with a triangular fixed floating structure.

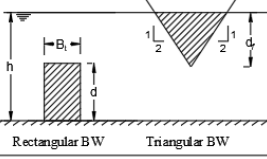
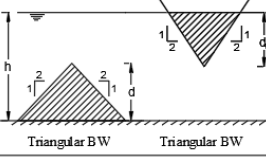

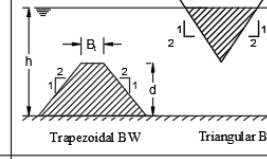
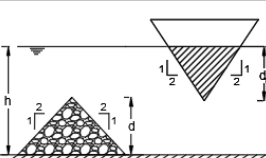

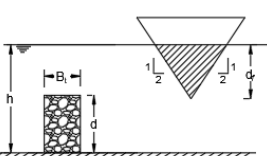
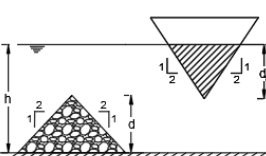
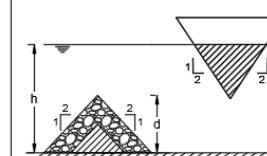
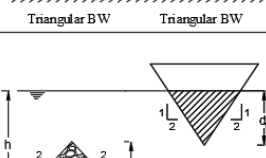
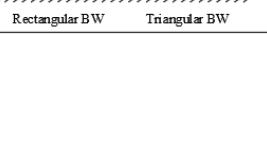
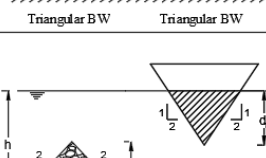
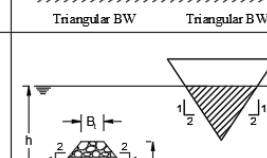
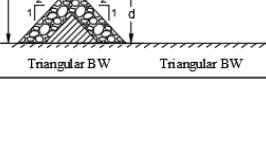
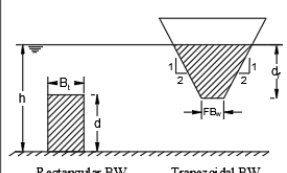
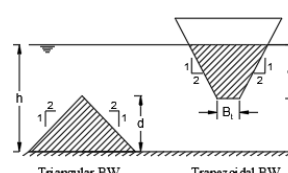
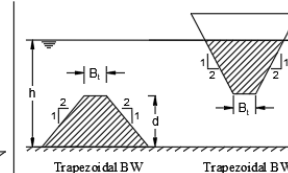

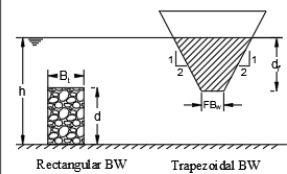
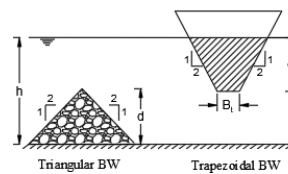
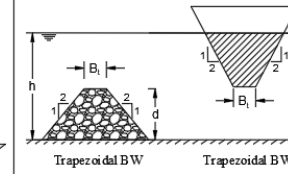


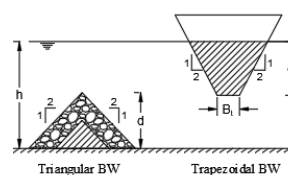
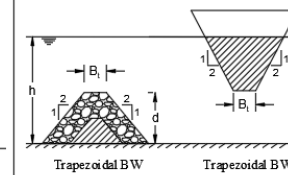

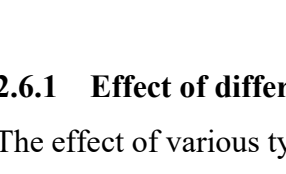
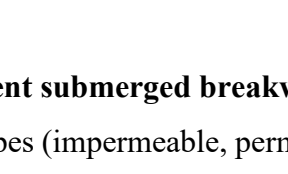
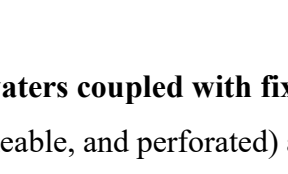

				<div> IMPERMEABLE BW</div> <div>Top width to depth of water (B_t/h) = 0.5</div> <div>Height of submerged structure to depth of water (d/h) = 0.80</div> <div>Draft of floating structure to depth of water (d_f/h) = 0.40</div>	
					<div> PERMEABLE BW</div> <div>Top width to depth of water (B_t/h) = 0.5</div> <div>Height of submerged structure to depth of water (d/h) = 0.80</div> <div>Draft of floating structure to depth of water (d_f/h) = 0.40</div> <div>$\epsilon = 0.4, f = 1.0, S = 1.0$</div>
					
					
					
					

Table 2.4: Models for various types and shapes of underwater breakwaters in conjunction with a trapezoidal fixed floating structure.

						 IMPERMEABLE BW
						 PERMEABLE BW
						 PERFORATED BW
						 PERFORATED BW
						Top width to depth of water (B_1/h) = 0.5 Height of submerged structure to depth of water (d/h) = 0.80 Draft of floating structure to depth of water (d_f/h) = 0.40
						$\epsilon = 0.4$, $f = 1.0$, $S = 1.0$
						Top width to depth of water (B_1/h) = 0.5 Height of submerged structure to depth of water (d/h) = 0.80 Draft of floating structure to depth of water (d_f/h) = 0.40 $\epsilon = 0.4$, $f = 1.0$, $S = 1.0$

2.6.1 Effect of different submerged breakwaters coupled with fixed floating structure

The effect of various types (impermeable, permeable, and perforated) and shapes (rectangular, triangular, and trapezoidal) of submerged breakwaters in combination with rectangular, triangular, and trapezoidal-shaped fixed floating structures on wave reflection and transmission characteristics is studied numerically, and the performance of these floating structures is discussed in depth. The reflection and transmission coefficients for wave scattering due to the coupling of floating structure and bottom undulations were compared by Manisha et al. (2019). Tseng et al. (2020) investigated the influence of a rectangular floating structure behind a parabolic breakwater on reflection and transmission characteristics using the eigenfunction expansion approach.

2.6.1.1 Floating structure coupled with impermeable type submerged breakwaters

The three different shapes of floating structure models (Rectangular, Triangular, and Trapezoidal) are coupled individually with different shapes of impermeable submerged breakwaters namely, (Rectangle, Triangle, and Trapezoidal) are considered and analyzed for wave reflection and transmission characteristics. Fig. 2.6 (a, b), Fig. 2.7(a, b), and Fig. 2.8(a, b) show the reflection coefficient K_R and transmission coefficient K_T obtained for the rectangular floating structure, triangular floating structure, and the trapezoidal floating structure (with $d_f/h = 0.4$) individually coupled with a combination of rectangular, triangular, and trapezoidal-shaped submerged impermeable breakwater with $d/h = 0.8$, analyzed against

non-dimensional wave number kh respectively. All the floating structures coupled with submerged breakwater models show a spike in reflection coefficient and a corresponding decrease in transmission coefficient when compared with a single floating structure with that configuration. The single floating structures show a monotonic increase nature in wave reflection, whereas the rectangular, triangular and trapezoidal floating structures when coupled individually with rectangular submerged breakwater show an increase in reflection coefficient in an oscillatory manner with the increase in wavenumber, a significant multiple increasing periodic peaks occurs. Further, the rectangular, triangular and trapezoidal floating structure when coupled with triangular and trapezoidal-shaped submerged breakwater show a large initial spike in the reflection coefficient in the shallow water region extended up to a part of the intermediate water region and then follows the wavy increasing trend with increase in wavenumber as similar observations made by Manisha et al. (2019). On the other hand, a corresponding initial trough formation is observed in the transmission coefficient for all the proposed models. Higher maxima and minima in wave reflection coefficient along with a phase shift in reflection and transmission coefficient is observed in the case of all types of floating structures coupled individually with rectangular submerged breakwater. This is mainly because the incoming waves are incident normal to the vertical face of rectangular submerged breakwater. At the first resonant peak reflection of respective coupled models, a corresponding sag in transmission coefficient is observed. Except for a slight deviation in the case of rectangular floating structure coupled with submerged breakwater, the coupling of floating structure with submerged breakwater has no substantial effect on transmission coefficient for $kh > 1.25$.

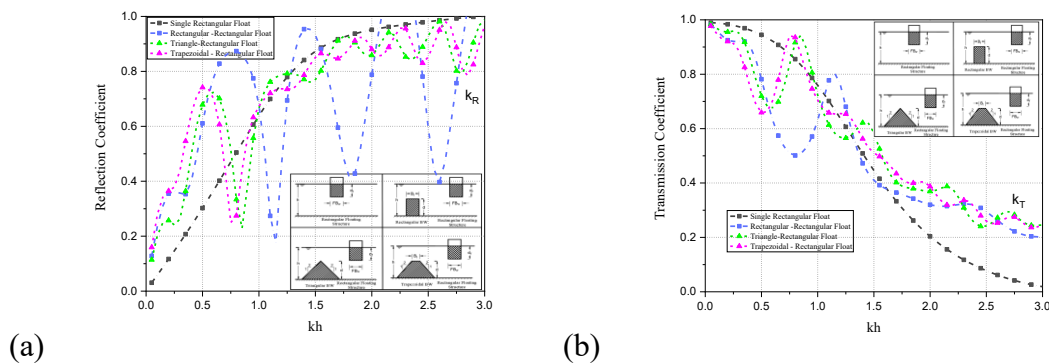


Fig. 2.5: Variation of (a) reflection coefficient (K_R) and (b) transmission coefficient (K_T) versus kh for rectangular floating structures coupled with impermeable submerged

breakwaters of various shapes, with a height of the impermeable structure to water depth ratio of $d/h = 0.8$ and a draught of the floating structure to water depth ratio of $d_f/h = 0.4$.

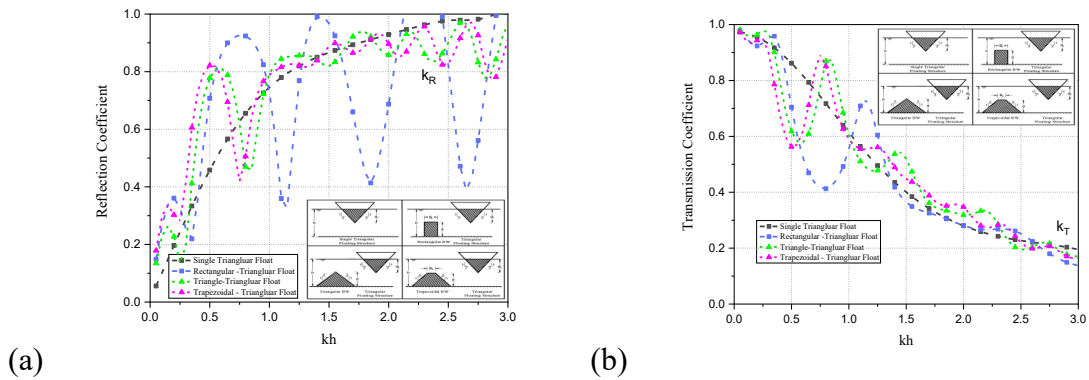


Fig. 2.6: Variation of (a) reflection coefficient (K_R) and (b) transmission coefficient (K_T) versus kh for triangular floating structures coupled with impermeable submerged breakwaters of various shapes, with a height of the impermeable structure to water depth ratio of $d/h = 0.8$ and a draught of the floating structure to water depth ratio of $d_f/h = 0.4$.

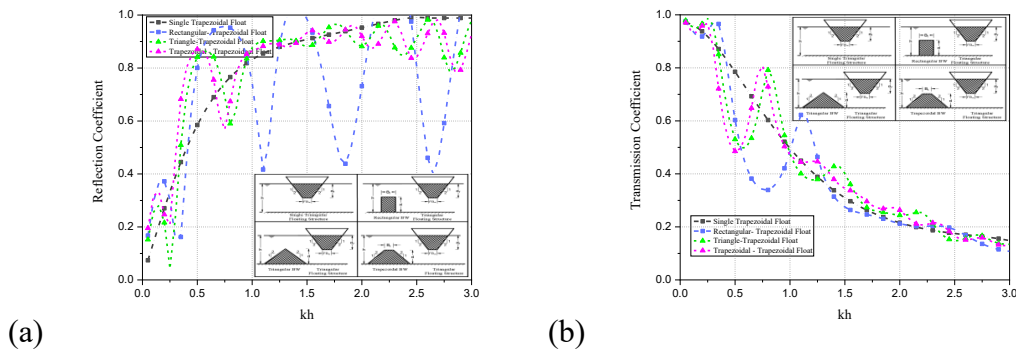


Fig. 2.7: Variation of (a) reflection coefficient (K_R) and (b) transmission coefficient (K_T) versus kh for trapezoidal floating structures coupled with impermeable submerged breakwaters of various shapes, with a height of the impermeable structure to water depth ratio of $d/h = 0.8$ and a draught of the floating structure to water depth ratio of $d_f/h = 0.4$.

2.6.1.2 Floating structures coupled with permeable type submerged breakwaters

The three different shapes of floating structure models (Rectangular, Triangular, and Trapezoidal) are coupled individually with different shapes of permeable submerged breakwaters namely, (Rectangle, Triangle, and Trapezoidal) are considered and analyzed for wave reflection and transmission characteristics. Fig. 9 (a, b), Fig. 10(a, b), and Fig. 11(a, b) show the reflection coefficient and transmission coefficient obtained for the rectangular floating structure, triangular floating structure, and the trapezoidal floating structure (with

$d_f/h = 0.4$) individually coupled with a combination of rectangular, triangular, and trapezoidal-shaped submerged permeable breakwater with $d/h = 0.8$, analyzed against non-dimensional wave number respectively. The coupling of floating structures with permeable submerged breakwaters exhibits the same trend in reflection coefficient as of a single floating structure of that configuration in shallow water region with a marginal difference in its magnitude. Further, in the intermediate water depth region, a significant downfall in the magnitude of reflection coefficient, oscillating periodically about a mean reflection value with increasing kh is observed. On the other side, the transmission coefficient follows the same pattern as of a single floating structure, but interestingly a sagging in transmission coefficient is observed with increasing kh . With the introduction of porosity into the submerged breakwater, reduction in first resonant peak reflection coefficient on an average of 30-45% is observed for all the coupled structures and except, the floating structures being coupled with submerged porous rectangular breakwater show an increase in transmission coefficient, the rest of all the models show an average corresponding reduction in transmission coefficient by 25-35%. The percentage reduction in the first resonant peak reflection coefficient and the corresponding percentage transmission for the coupled structures.

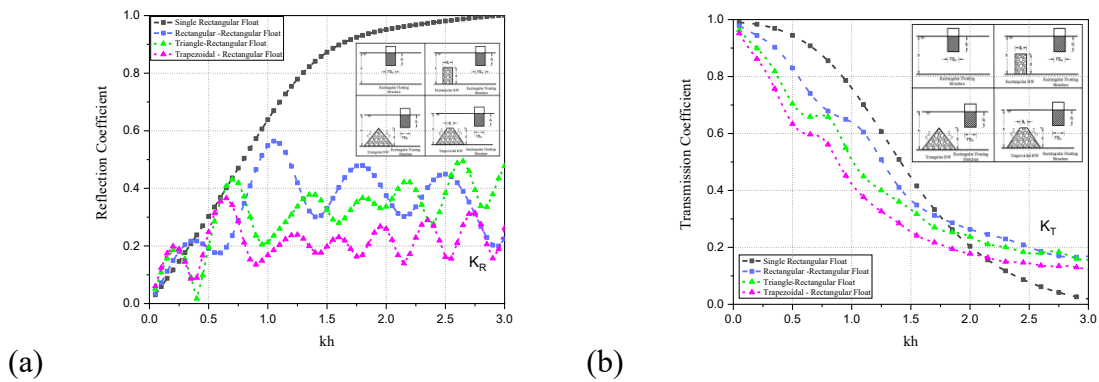


Fig. 2.8: Variation of (a) reflection coefficient (K_R) and (b) transmission coefficient (K_T) versus kh for rectangular floating structures coupled with permeable submerged breakwaters

of various shapes, with a height of the impermeable structure to water depth ratio of $d/h = 0.8$ and a draught of the floating structure to water depth ratio of $d_f/h = 0.4$.

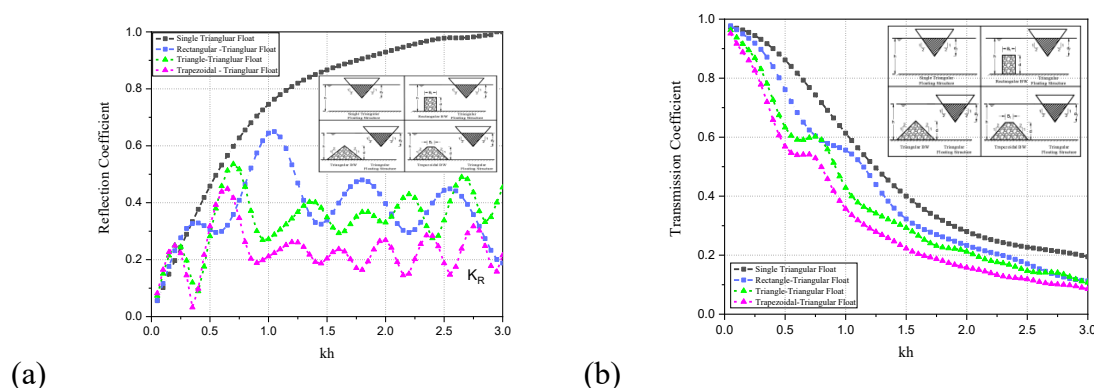


Fig. 2.9: Variation of (a) reflection coefficient (K_R) and (b) transmission coefficient (K_T) versus kh for triangular floating structures coupled with permeable submerged breakwaters of various shapes, with a height of the impermeable structure to water depth ratio of $d/h = 0.8$ and a draught of the floating structure to water depth ratio of $d_f/h = 0.4$.

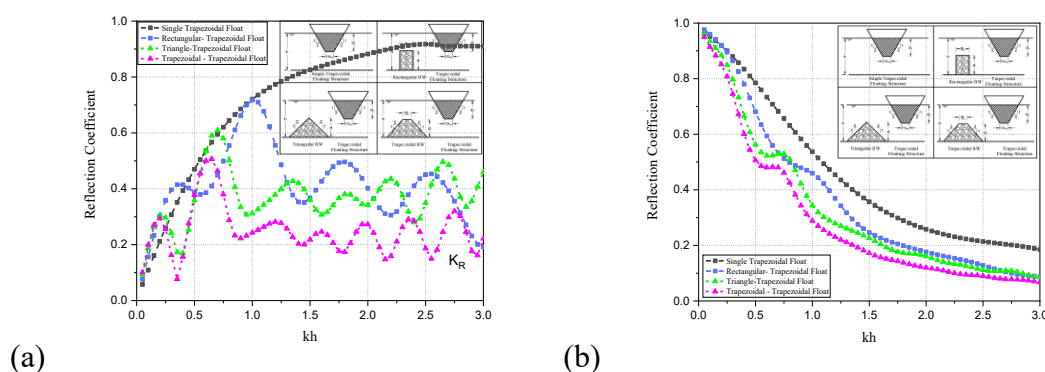


Fig. 2.10: Variation of (a) reflection coefficient (K_R) and (b) transmission coefficient (K_T) versus kh for trapezoidal floating structures coupled with permeable submerged breakwaters of various shapes, with a height of the impermeable structure to water depth ratio of $d/h = 0.8$ and a draught of the floating structure to water depth ratio of $d_f/h = 0.4$.

2.6.1.3 Floating structure coupled with perforated type submerged breakwaters

The wave mitigation affected by the addition of a submerged perforated breakwater in front of various shaped floating structures is investigated. In Fig. 2.12(a, b), Fig 2.13(a, b), and Fig 2.14(a, b), for a water depth ratio of $d/h = 0.8$ and a draught of floating structure to water depth ratio of $d_f/h = 0.4$, the variation in the reflection coefficient K_R and transmission coefficient K_T versus non-dimensional wave number kh for the Rectangular, Triangular, and

Trapezoidal floating structure coupled in combination with triangular, trapezoidal submerged perforated breakwaters is discussed. The submerged structures considered are having a constant top width to depth of water ratio $B_t/h = 0.5$, a 2:1(H: V) side slope, structural porosity parameters $\varepsilon = 0.4$, $f = 1.0$ and $S = 1.0$. The reflection coefficient is reduced by an average of 25-30% with floating structures coupled individually with the perforated submerged breakwater. Further, when compared to permeable breakwaters, the reflection coefficients are enhanced by an average of 10-15%, but the transmission coefficient shows very little variation.

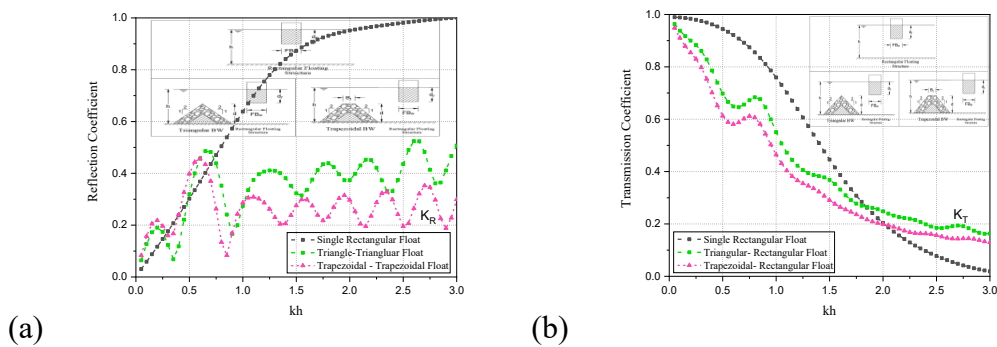


Fig. 2.11: Variation of (a) reflection coefficient (K_R) and (b) transmission coefficient (K_T) versus kh for rectangular floating structures coupled with perforated submerged breakwaters of various shapes, with a height of the impermeable structure to water depth ratio of $d/h = 0.8$ and a draught of the floating structure to water depth ratio of $d_f/h = 0.4$.

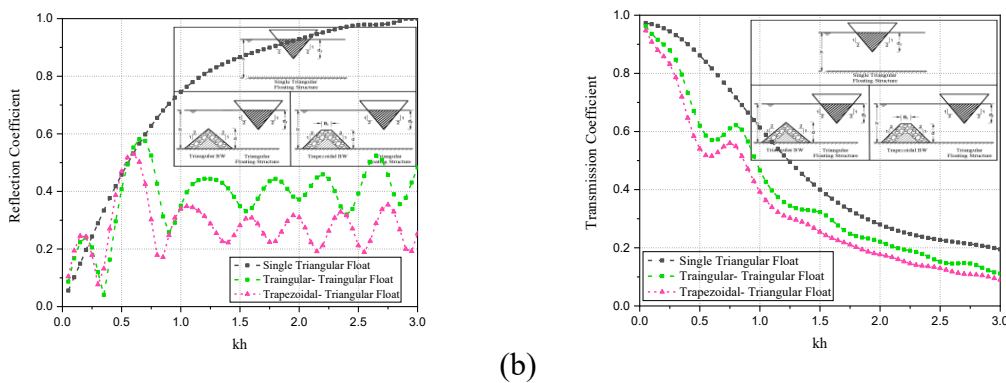


Fig. 2.12: Variation of (a) reflection coefficient (K_R) and (b) transmission coefficient (K_T) versus kh for triangular floating structures coupled with perforated submerged breakwaters of

various shapes, with a height of the impermeable structure to water depth ratio of $d/h = 0.8$ and a draught of the floating structure to water depth ratio of $d_f/h = 0.4$.

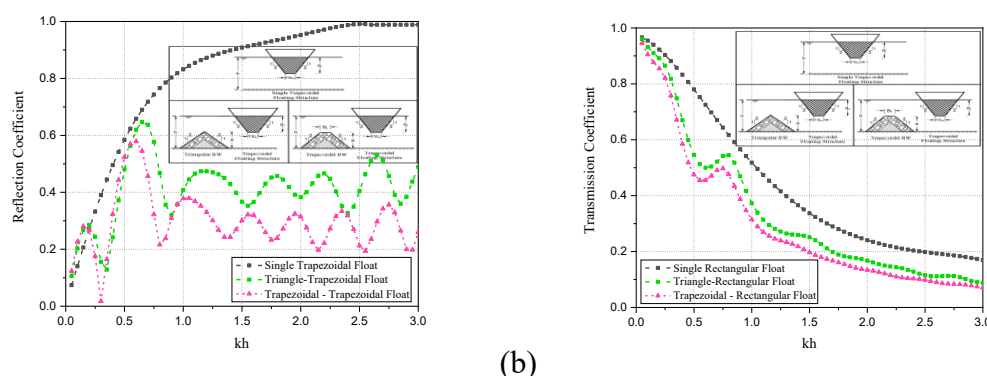


Fig. 2.13: Variation of (a) reflection coefficient (K_R) and (b) transmission coefficient (K_T) versus kh for trapezoidal floating structures coupled with perforated submerged breakwaters of various shapes, with a height of the impermeable structure to water depth ratio of $d/h = 0.8$ and a draught of the floating structure to water depth ratio of $d_f/h = 0.4$.

When perforated submerged breakwaters are combined with rectangular floating structures, the maximum reflection coefficient is 0.48 and the minimum transmission coefficient is 0.46. When perforated submerged breakwaters are combined with triangular and trapezoidal floating structures, the minimum reflection and transmission coefficients are 0.53, 0.58 and 0.39, 0.31, respectively.

2.6.1.4 Effect of incidence angle on floating structures coupled with submerged breakwaters

Table 2.2, Table 2.3, and Table 2.4 show the correlation for reflection and transmission coefficients with varying angle of incidences for floating structures with a draught of floating structure to water depth ratio, coupled individually with submerged breakwaters of various types and shapes with various structural parameters (impermeable, permeable, and perforated) are analysed for relative water depth ratio $d/h = 0.8$ for (a) shallow water wavenumber $kh = 0.2$ and (b) $kh = 0.6$ in intermediate water depth. The choice of wavenumber is relevant to its corresponding peak wave reflection in the shallow and intermediate water depth region.

2.6.1.5 Floating structure coupled with impermeable type submerged breakwaters

In Fig. 2.15, Fig. 2.16, and Fig. 2.17 the reflection coefficient K_R and transmission coefficient K_T are plotted versus varying angle of incidence θ for floating structure having different shapes

namely, rectangular, triangular, and trapezoidal section coupled individually with impermeable submerged breakwaters of different shapes for both shallow water ($kh = 0.2$) and intermediate water depth ($kh = 0.6$) region. The results obtained for single floating rectangular impermeable structure are similar as obtained by Manisha et al. (2019).

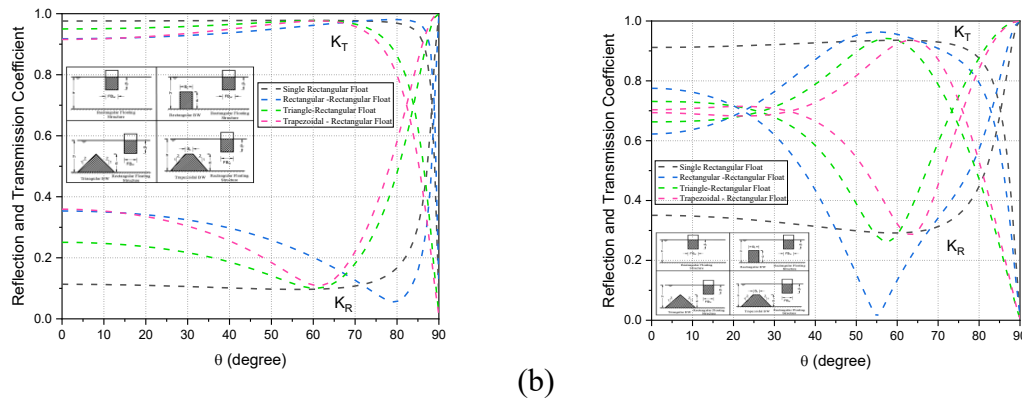


Figure 2.14: Variation of K_R and K_T versus θ for rectangular floating structure coupled with impermeable submerged breakwaters of various forms, when the height of the impermeable structure to water depth ratio of $d/h = 0.8$, and a draft of floating structure to water depth ratio $d_f/h = 0.4$ (a) $kh = 0.2$ and (b) $kh = 0.6$.

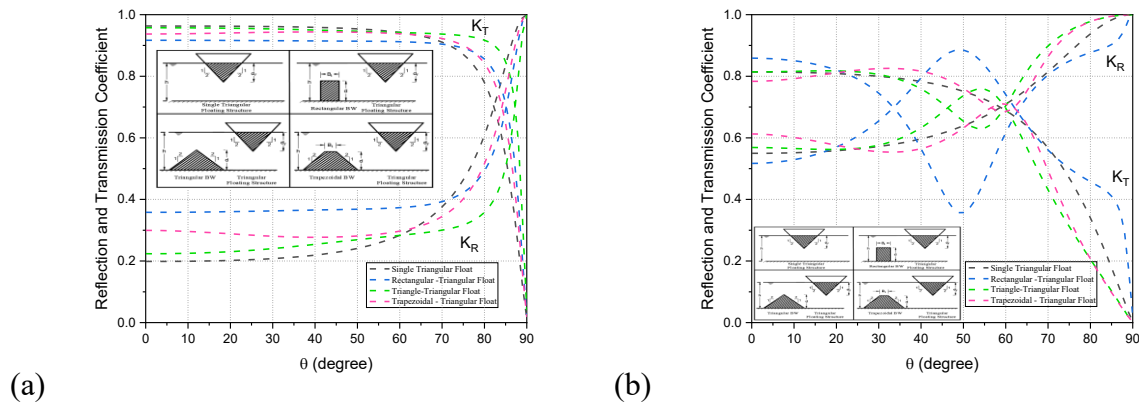


Figure 2.15: Variation of K_R and K_T versus θ for Triangular floating structure coupled with impermeable submerged breakwaters of various forms, when the height of the impermeable

structure to water depth ratio of $d/h = 0.8$, and a draft of floating structure to water depth ratio $d_f/h = 0.4$ (a) $kh = 0.2$ and (b) $kh = 0.6$.

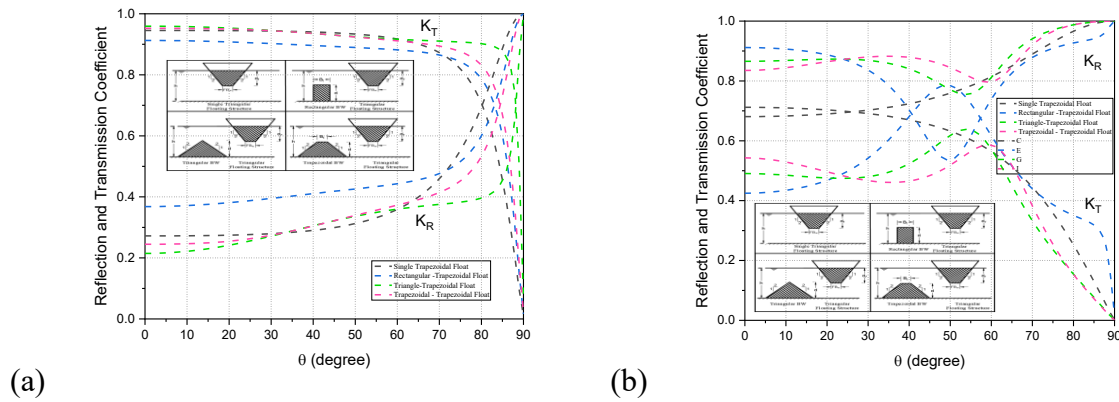


Figure 2.16: Variation of K_R and K_T versus θ for Trapezoidal floating structure coupled with impermeable submerged breakwaters of various forms, when the height of the impermeable structure to water depth ratio of $d/h = 0.8$, and a draft of floating structure to water depth ratio $d_f/h = 0.4$ (a) $kh = 0.2$ and (b) $kh = 0.6$.

When compared to solitary floating structures in the shallow water depth zone ($kh = 0.2$), the coupling of floating structures with submerged breakwaters delivers higher reflection coefficient and lower transmission coefficient with varying angle of incidence for all shapes.. Among these floating structures combined with submerged breakwater models, the rectangular-shaped breakwater was shown to be more efficient in wave transformation, with a larger reflection coefficient and a lower transmission coefficient as the angle of incidence increased up to 70 degrees. This is because the rectangular section's vertical face has a unit normal horizontal vector component of one. The trapezoidal floating structure coupled with impermeable rectangular submerged breakwater demonstrates higher reflection coefficient and corresponding lower transmission among all the combinations for angle of incidence up to 70° . In intermediate water depth region with wavenumber $kh = 0.6$, In a particular case of rectangular floating structure coupled with rectangular submerged breakwater occurrence of critical angle (zero reflection) is observed at angle of incidence equal to 55° and also with the case of triangular and trapezoidal floating structure coupled with impermeable rectangular submerged breakwater an increase in wave transmission leading to crest formation and corresponding decrease in reflection leading to a trough formation is observed for an angle of incidence equal to 50° , further the reflection coefficient shoots up rapidly to reach unity at 90° angle of incidence. Overall, the wave transmission coefficient of the coupled structures, initially starts with 25-30% lower than that of single floating structure. The transmission

coefficient increases parabolically as the angle of incidence increases until it reaches the transmission coefficient of a single floating structure at 50-60° angle of incidence, after which it rapidly decreases.

2.6.1.6 Floating structure coupled with permeable type submerged breakwaters

Figures 2.18, 2.19, and 2.21 show the effect of permeability on reflection and transmission coefficient as the angle of incidence increases for rectangular, triangular, and trapezoidal floating structures individually coupled with various shapes of permeable type submerged breakwater for both shallow ($kh = 0.2$) and intermediate water depth ($kh = 0.6$) regions. In the shallow water depth region ($kh = 0.2$), the presence of a permeable submerged breakwater constructed in front of an impermeable floating structure results in a 60-80% reduction in wave reflection coefficient at initial angle of incidence, and further with varying angle of incidence. a mild slope variation in wave reflection and transmission is observed

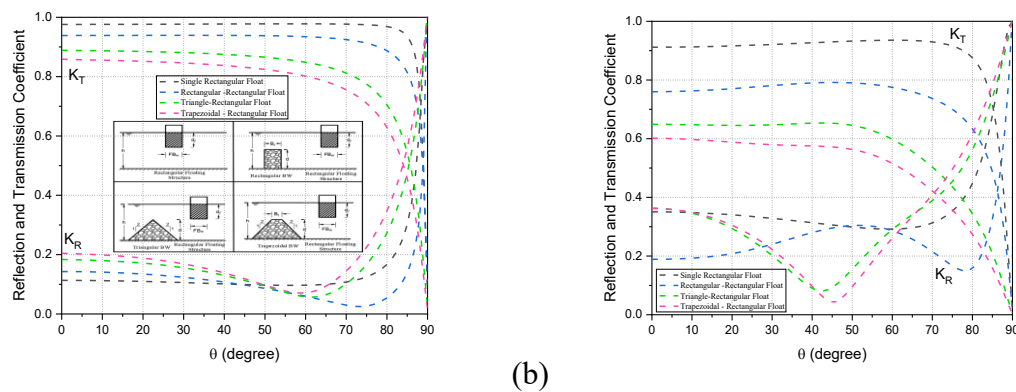


Figure 2.17: Variation of K_R and K_T versus θ for impermeable rectangular floating structure coupled with permeable submerged breakwaters of various forms, when the height of the permeable structure to water depth ratio of $d/h = 0.8$, and a draft of floating structure to water depth ratio $d_f/h = 0.4$ (a) $kh = 0.2$ and (b) $kh = 0.6$.

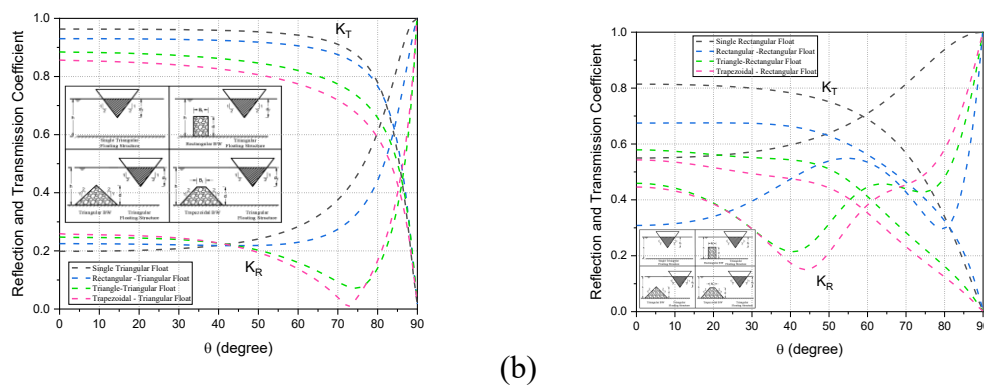


Figure 2.18: Variation of K_R and K_T versus θ for impermeable triangular floating structure coupled with permeable submerged breakwaters of various forms, when the height of the permeable structure to water depth ratio of $d/h = 0.8$, and a draft of floating structure to water depth ratio $d_f/h = 0.4$ (a) $kh = 0.2$ and (b) $kh = 0.6$.

permeable structure to water depth ratio of $d/h = 0.8$, and a draft of floating structure to water depth ratio $d_f/h = 0.4$ (a) $kh = 0.2$ and (b) $kh = 0.6$.

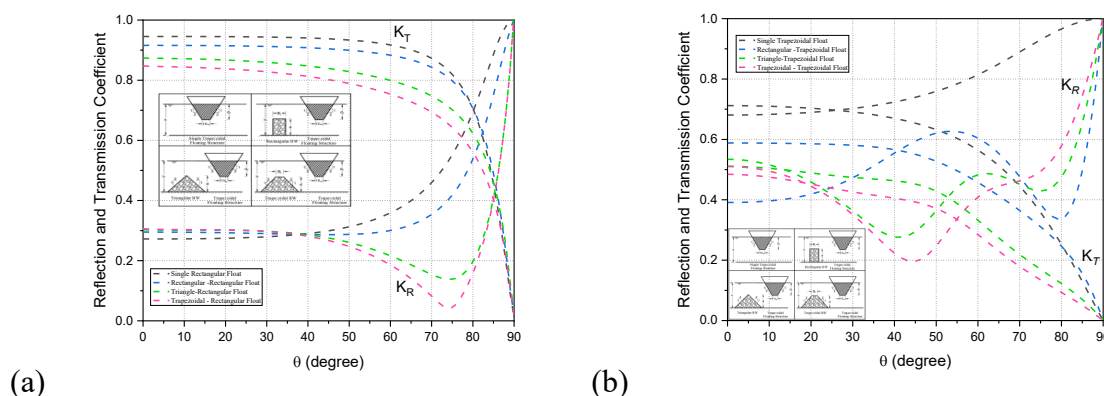


Figure 2.19: Variation of K_R and K_T versus θ for impermeable trapezoidal floating structure coupled with permeable submerged breakwaters of various forms, when the height of the permeable structure to water depth ratio of $d/h = 0.8$, and a draft of floating structure to water depth ratio $d_f/h = 0.4$ (a) $kh = 0.2$ and (b) $kh = 0.6$.

In shallow water depth region ($kh = 0.2$), the reflection coefficient initially starts with 5-10% higher when compared with the single floating structure and then converges to form a node at an angle 50° , 42° , and 37° for rectangular, triangular and trapezoidal floating structure respectively, further the occurrence of critical angle is observed for an angle up to $70-80^\circ$. Whereas the transmission coefficient varies 15-20% lower than that compared with single floating structure of all combinations. Among all the proposed models the trapezoidal floating structure coupled with permeable triangular shaped submerged breakwater exhibits higher reflection and lower transmission coefficient with varying angle of incidence.

In intermediate water depth region, an approximate of 10-15% lower transmission is observed for all coupled structure when compared with single floating structure. The effect of varying angle of incidence is very minimal on transmission coefficient for an angle up to 50° for rectangular floating coupled models and 40° for triangular and trapezoidal floating models, further the transmission coefficient drops down to reach zero value at 90° incident angle. Whereas the reflection coefficient varies like a wave form with increase in angle of incidence and a trough formation is observed at 45° angle of incidence.

2.6.1.7 Floating structure coupled with perforated type submerged breakwaters

The floating structures coupled with perforated submerged breakwater, follows the same trend as that of floating structures coupled with permeable submerged breakwaters. In case of

shallow water depth region, the effect of varying angle of incidence is very minimal on transmission coefficient up to 50° angle of incidence and thereafter it drops down to zero at 90° . There is a gradual decrease in reflection coefficient leading to a trough formation at 62° , 78° and 80° for rectangular, triangular and trapezoidal float structure respectively. In intermediate water depth region, the transmission coefficient remains unaltered for angle of incidence up to 60° , with formation of trough in reflection coefficient, beyond which the reflection increases to reach unity at 90° and corresponding reduction in transmission is observed.

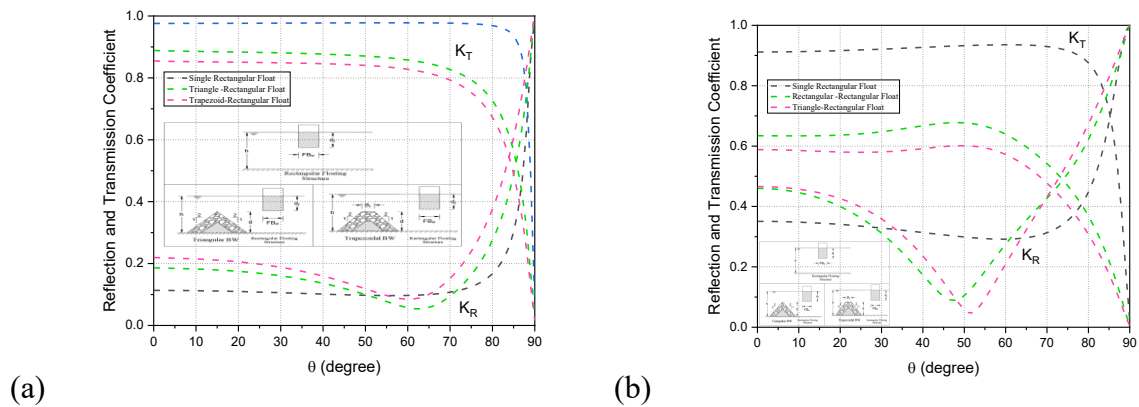


Figure 2.20: Variation of K_R and K_T versus θ for impermeable rectangular floating structure coupled with perforated submerged breakwaters of various forms, when the height of the permeable structure to water depth ratio of $d/h = 0.8$, and a draft of floating structure to water depth ratio $d_f/h = 0.4$ (a) $kh = 0.2$ and (b) $kh = 0.6$.

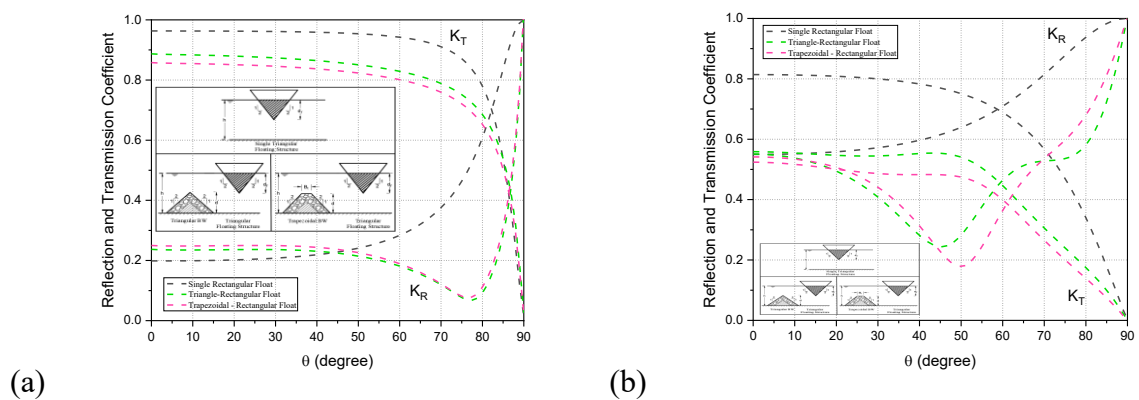


Figure 2.21: Variation of K_R and K_T versus θ for impermeable triangular floating structure coupled with perforated submerged breakwaters of various forms, when the height of the

permeable structure to water depth ratio of $d/h = 0.8$, and a draft of floating structure to water depth ratio $d_f/h = 0.4$ (a) $kh = 0.2$ and (b) $kh = 0.6$.

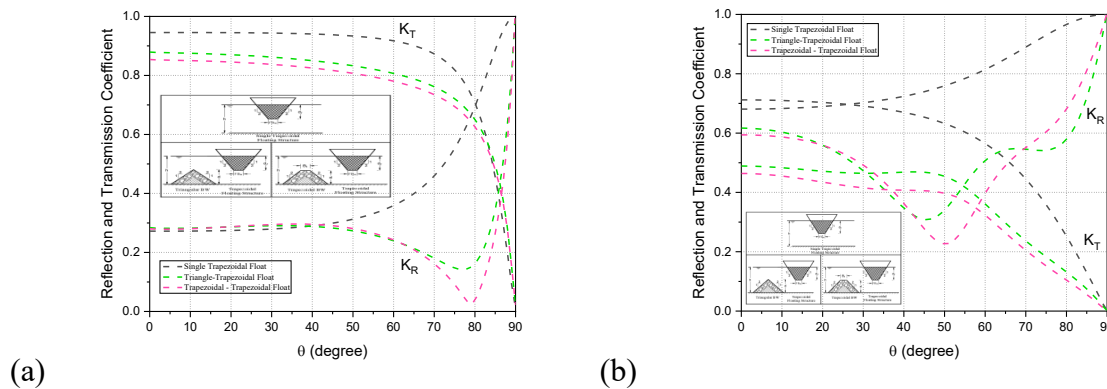


Figure 2.22: Variation of K_R and K_T versus θ for impermeable trapezoidal floating structure coupled with perforated submerged breakwaters of various forms, when the height of the permeable structure to water depth ratio of $d/h = 0.8$, and a draft of floating structure to water depth ratio $d_f/h = 0.4$ (a) $kh = 0.2$ and (b) $kh = 0.6$.

2.6.2 Relative spacing between floating structures and submerged breakwaters

For various shapes and types of floating structures, the effect of varying the distance between the submerged breakwater and the floating structures is investigated. The effect of relative gap $2G_{BW}/\lambda$ on wave reflection coefficient K_R and the transmission coefficients K_T is carried out for impermeable, permeable and perforated submerged breakwaters kept at some distance in front of floating structures for a constant non dimensionless wavenumber $kh = 1.0$. Manisha et al. (2019) studied the effect of varying the length between the bottom undulations (breakwater and a trench) in the sea bed and the floating bridge on wave reflection. The increasing length shows increase in the wave reflection followed by occurrence of node phenomena in intermediate water depth. The Bragg resonance occurs when the incoming wavelength $\lambda = 2\pi$ is twice the spacing between breakwaters, as shown in Figs (2.24-2.26), resulting in amplification of the reflection coefficient and subsequent lowering of the transmission coefficient. It is evident from the Figs (24-26) that, as the incident wavelength is twice as the spacing between breakwaters, the Bragg resonance occurs, leading to amplification in reflection coefficient and subsequent reduction in transmission coefficient. Li et al. (2015) and Ouyang et al. (2016) made similar observations in their numerical studied in the case of double impermeable rectangular and trapezoidal breakwaters.

2.6.2.1 Effect of spacing between the floating structures and the impermeable submerged breakwaters

The change in reflection coefficient K_R and transmission coefficient K_T vs $2G_{BW}/\lambda$ for rectangular, triangular, and trapezoidal floating structures with impermeable submerged breakwaters of various forms is shown in Fig. 2.24. In all type of breakwaters, the variation in K_R and K_T is observed to be periodic with regular intervals.

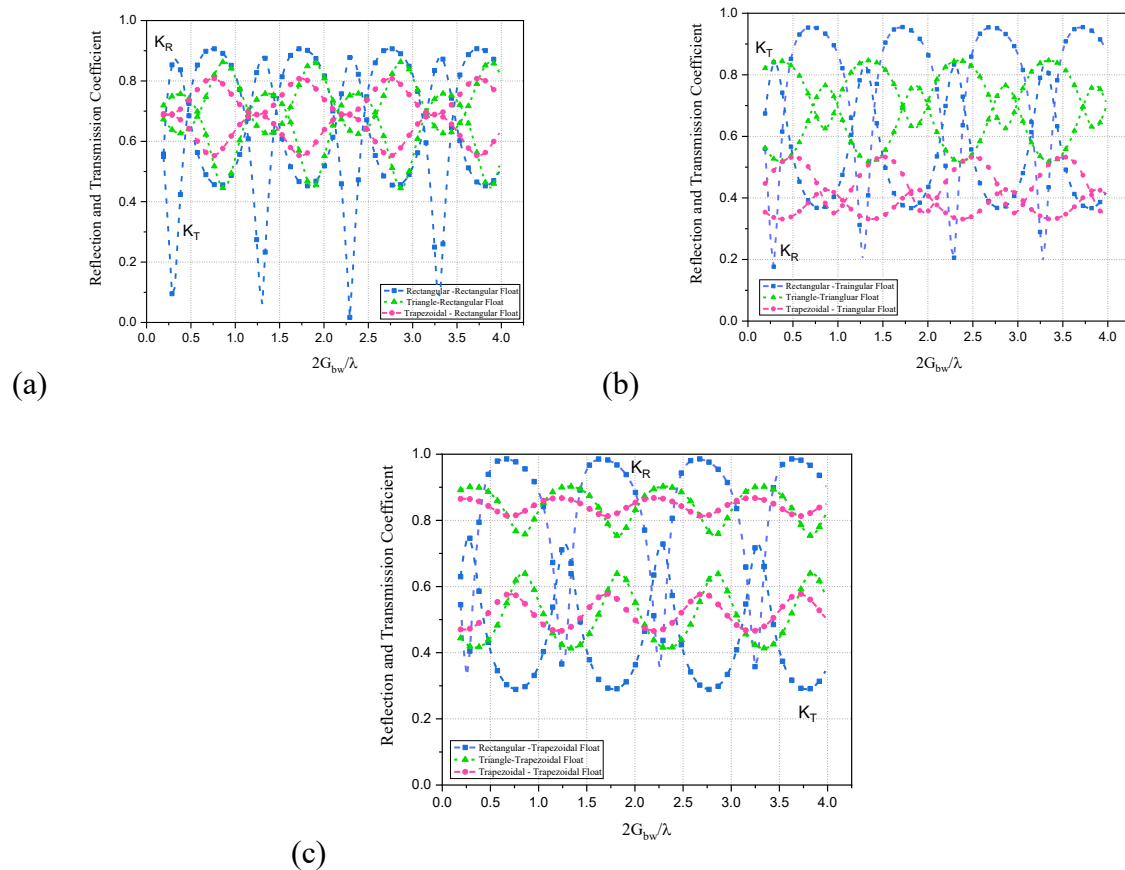


Fig. 2.23: Variation of K_R and K_T versus $2G_{BW}/\lambda$ for $d/h = 0.80$ in the case of (a) Rectangular floating structure, (b) Triangular floating structure and (c) Trapezoidal floating structure, coupled with impermeable submerged breakwater of different shapes.

The rectangular floating structure coupled with impermeable rectangular submerged breakwater has the lowest transmission coefficient of 0.017 at a relative spacing of 2.292 and the highest reflection coefficient of 0.833 at a relative spacing of 3.310. It is also observed that there is no significant difference in transmission coefficient is observed when a rectangular floating structure coupled with triangular or a trapezoidal shaped submerged impermeable breakwater, but the rectangular floating structure coupled with trapezoidal shaped submerged

breakwater has a 10% higher reflection coefficient than the rectangular floating structure coupled with triangular submerged breakwater.

In case of triangular floating structure coupled with trapezoidal submerged breakwater offers lowest transmission coefficient of 0.331 at a relative spacing of 0.832 and a maximum reflection coefficient of 0.533 at a relative spacing of 0.509, but coupling with rectangular submerged breakwater lie the same range of transmission coefficient of 0.366 at a relative spacing of 0.796 and a maximum reflection coefficient is higher among all the configuration, with a coefficient value of 0.955 at relative spacing of 0.700. The mean of periodic oscillation in wave reflection and the transmission coefficient is 15-20% lower in case of triangular floating structure coupled with impermeable trapezoidal submerged breakwater than that of coupling with rectangular and or trapezoidal shaped impermeable submerged breakwater and also the minimum and maximum in wave transmission and reflection coefficient lies in the range of 0.30 to 0.35 and 0.43 to 0.53 respectively. This means that the coupling of triangular floating structure with trapezoidal shaped impermeable submerged breakwater is optimum among the three models.

A substantial gap between the maximum and minima of wave reflection and transmission coefficient is reported in the case of trapezoidal floating structures linked with impermeable submerged breakwater models. At a relative spacing of 0.764 and 0.367, the coupling of a trapezoidal floating structure with a rectangular submerged breakwater shows a minimum transmission coefficient of 0.289 and a higher reflection coefficient of 0.986. The same wave transformation characteristics are demonstrated by a trapezoidal floating structure coupled with a triangular and trapezoidal shaped impermeable submerged breakwater.

2.6.2.2 Effect of spacing between floating structure and the permeable submerged breakwater

Fig. 2.24 shows the variation in reflection coefficient K_R and transmission coefficient K_T versus $2G_{BW}/\lambda$ for rectangular, triangular, trapezoidal floating structure coupled with permeable submerged breakwaters of different shapes. The occurrence of reflection coefficient K_R and transmission coefficient K_T at regular interval demonstrates the Bragg resonance.

On comparing the coupling of floating structures with submerged permeable breakwater, the rectangular floating structures coupled individually with submerged permeable breakwaters shows higher reflection and transmission coefficients, except in floating structure coupled with rectangular shaped submerged permeable breakwater, there is a reduction in wave reflection

coefficients. In the case of a coupled triangular floating structure, the reflection coefficient is reduced by 55.3 percent on average, while the transmission coefficient is reduced by 21.9 percent. Similarly, coupled trapezoidal floating structures show a 62.1 percent reduction in reflection coefficient and a 24.5 percent drop in transmission coefficient. When the relative spacing between the floating structure and the submerged breakwater is in the range of 0.5 to 2.0, the overall coupling of floating structures with trapezoidal shaped submerged permeable breakwater shows lower reflection coefficients in the range of 0.15 to 0.23 and transmission coefficients in the range of 0.28 to 0.41.

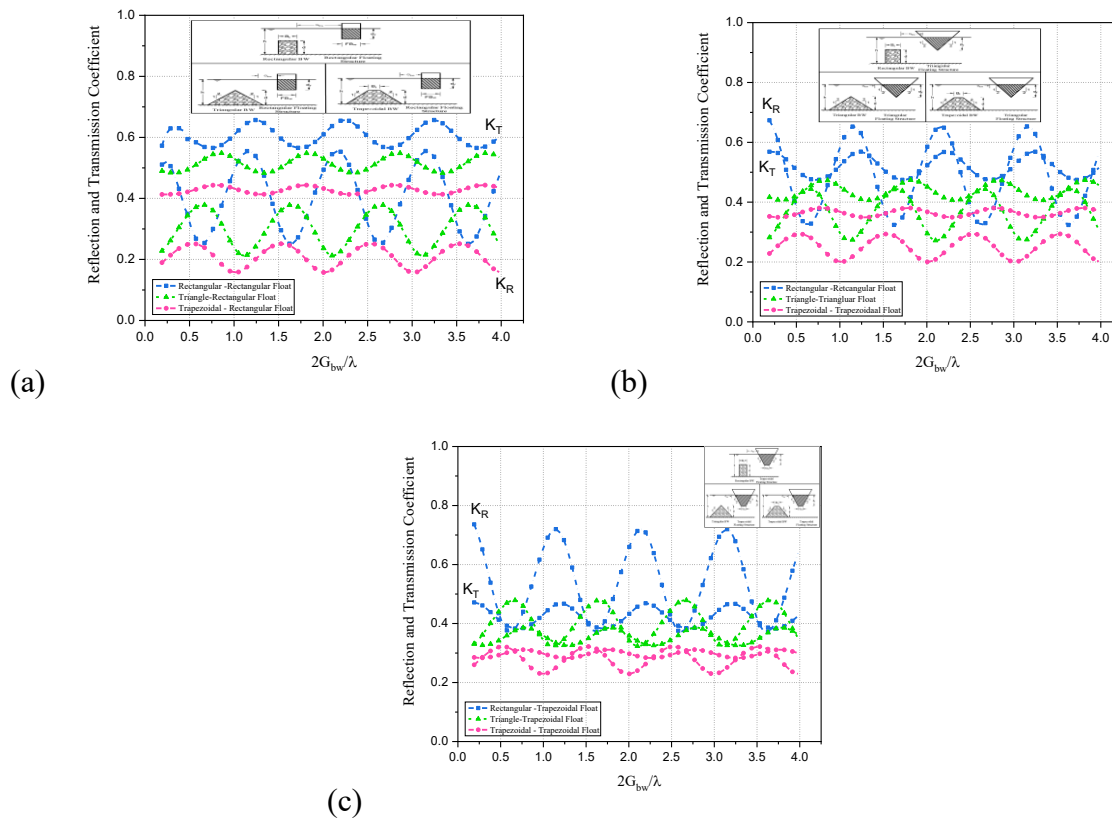


Fig. 2.24: Variation of K_R and K_T versus $2G_{BW}/\lambda$ for $d/h = 0.80$ in the case of (a) Rectangular floating structure, (b) Triangular floating structure and (c) Trapezoidal floating structure, coupled with permeable submerged breakwater of different shapes.

2.6.2.3 Effect of spacing between the floating structure and the perforated submerged breakwaters

The fluctuation in reflection coefficient K_R and transmission coefficient K_T vs $2G_{BW}/\lambda$ relative gap between the submerged perforated breakwaters and the floating structures is depicted in Fig. 2.25. When comparing floating structures with perforated submerged breakwaters to floating structures with permeable submerged breakwaters, the average

reflection coefficients are 12 percent higher, with no significant variation in transmission coefficient.

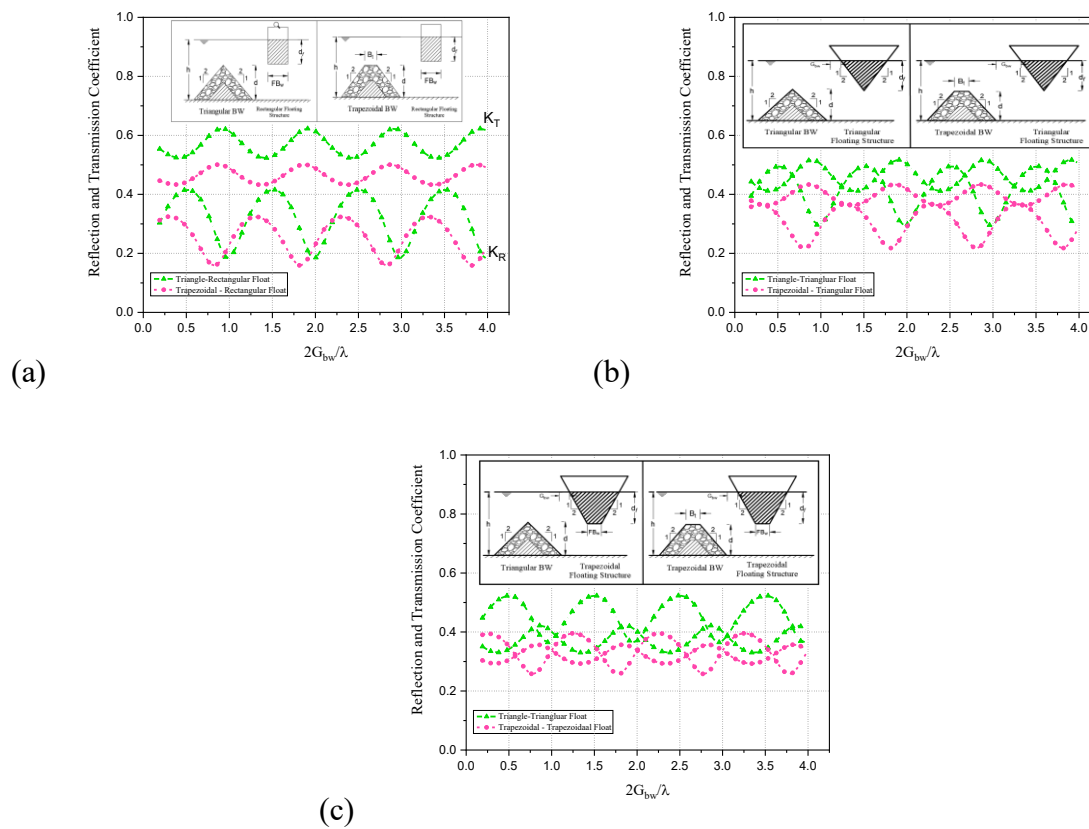


Fig. 2.25: Variation of K_R and K_T versus $2G_{BW}/\lambda$ for $d/h = 0.80$ in the case of (a) Rectangular floating structure, (b) Triangular floating structure and (c) Trapezoidal floating structure, coupled with perforated submerged breakwater of various forms.

The rectangular and trapezoidal shaped floating structure coupled with perforated trapezoidal submerged breakwaters seems to be efficient in wave transformation in comparison with coupling with perforated triangular submerged breakwater. Whereas in case of triangular floating structure coupled with perforated triangular submerged breakwater is optimum in wave transformation. When a trapezoidal-shaped submerged perforated breakwater is compared to a triangle-shaped submerged perforated breakwater, the presence of a crest width indicates a lower reflection and transmission coefficient.

2.7 Conclusions

The hydrodynamic performance of floating structures of various shapes coupled individually with submerged breakwaters of various types and shapes as depicted in table 2.3, 2.4 and 2.5, which are designed to work together, was investigated using the multi-domain boundary

element method in terms of wave transformation, angle of incidence, and body forces acting on the fixed floating structure. The accuracy of the results for the present numerical model (MDBEM) is determined through a convergency study for the specific case of a fixed rectangular floating structure coupled with an impermeable submerged trapezoidal breakwater, as shown in table 1, and several results are compared to available results in the literature to test the validity of numerical computation. The following are the findings of the current study:

- The increase in relative depth of submergence for submerged breakwater coupled with fixed floating structure shows an increase in reflection coefficient and corresponding reduction in transmission coefficient. The coupling of floating structures with impermeable submerged breakwaters has no significant effect on transmission coefficient for in comparison with single floating structure, except in the case of rectangular floating structure coupled with submerged breakwater a small deviation is observed. The coupling of floating structures with either permeable or perforated submerged breakwaters exhibits the same trend in reflection coefficient as of a single floating structure of that configuration in shallow water region with a marginal difference in its magnitude. Further, in the intermediate water depth region, a significant reduction of about 40-50% in the magnitude of reflection coefficient, oscillating periodically about a mean reflection value with increasing kh is observed. On the other hand, a 10-15% drop in transmission coefficient is observed in both shallow and intermediate sea depth region, except in case of rectangular floating structures couple with either permeable or perforated submerged breakwaters higher transmission coefficient is observed for kh beyond 2.0.
- The effect of varying angle of incidence on transmission coefficient is very minimal in the case of rectangular floating structures coupled with the impermeable submerged breakwaters in shallow water depth region. Whereas in intermediate water depth region with wavenumber kh , a considerable reduction in transmission coefficient of around 20-25% and a notable increase in reflection coefficient of 40-50% is observed for angle of incidence up to 35° . Further the transmission coefficient increases linearly to reach maximum of 0.90 at 60° incident angle, thereafter the transmission coefficient decreases to reaches zero at 90° and a multiple crossing of wave reflection and the transmission coefficient is observed for coupled models in comparison with single floating structure. This means at that particular angle of incidence where these node point occurs, indicate the optimum wave transformation. In both shallow and intermediate water depths, similar

wave transformation patterns are found in the case of triangular and trapezoidal floating structures coupled with impermeable submerged breakwaters.

- In case of floating structures coupled individually with permeable and perforated submerged breakwaters with varying angle of incidence a reduction of around 50% in transmission coefficient is observed in shallow and intermediate water depth region for initial varying angle of incidence up to 45^0 , further a gradual decreasing trend is observed to reach zero at 90^0 incident angle. Overall coupling of floating structures with trapezoidal shaped submerged permeable or perforated breakwaters are more efficient in wave transformations with varying angle of incidence in comparison with single floating structure.
- For a constant non-dimensionless wavenumber, the effect of relative gap on wave reflection coefficient K_R and transmission coefficients K_T for impermeable, permeable, and perforated submerged breakwaters kept at a certain distance in front of fixed floating structures shows that increasing the length between the floating structure and submerged breakwater leads to amplification in reflection coefficient and subsequent reduction in transmission coefficient at regular intervals when wave length is twice the spacing between the floating structure and the submerged breakwater. Floating structures of different shapes coupled with impermeable submerged breakwater models, the one which is coupled with rectangular shaped impermeable submerged breakwaters demonstrates higher reflection and lower transmission coefficient with varying gap between the structures. Whereas the optimum transmission is obtained with those floating models coupled with trapezoidal shaped permeable or perforated submerged breakwaters.
- On comparing the impending horizontal wave force on single rectangular floating structure with rectangular floating structure coupled with impermeable submerged breakwater the presence of reef structure brings out an approximate of 50% reduction in wave force imparted on the floating structure in both shallow and intermediate water depth region. A comparison of wave force imparted on triangular and trapezoidal floating structures coupled with impermeable submerged breakwater shows that the presence of reef structures has no effect in reducing wave force on the floating structures in shallow water depths, but significant multiple peaks in horizontal and vertical wave force are observed in intermediate water depths.
- In comparing to floating structures coupled with impermeable submerged breakwaters, the horizontal and vertical component coefficients of wave force of floating structures coupled

with perforated and or permeable submerged breakwaters are reduced by 50% to 60%. In shallow and intermediate water depths, the horizontal wave force is much lower than the vertical wave force in both the case of triangular floating and trapezoidal floating structures coupled with permeable or perforated submerged breakwaters, and the wave forces remain almost flat for non-dimensionless wave number.

Finally, the floating structures coupled with submerged trapezoidal shaped perforated breakwater perform exceedingly well in terms of wave transformations for both short and long wave circumstances, as shown in Table 2. As a result, in terms of design considerations and floating structure stability, a reef-like structure in front of the main floating structure aids in lowering the wave stresses inflicted on the fixed floating structure and also aids in optimum wave transformation.

CHAPTER 3

HYDRODYNAMICS OF A WAVE ENERGY CONVERTER INTEGRATED TO A PILE RESTRAINED FLOATING STRUCTURE NEAR A PARTIALLY SEAWALL

3.1 THEORETICAL FORMULATION

The idealised two-dimensional (2D) geometry of the physical problem is depicted in Fig. 3.1 using Cartesian coordinates. The PRFB, which has a drafts d_f and a breadth B , is symmetrically positioned about $x=0$, with the y -axis pointed vertically upwards from the origin on the still water level, and is located at a definite distance S from a vertical partially reflecting seawall. The PRFB is assumed to respond linearly in heave, when subjected to train of regular waves of small wave amplitude A_0 and angular frequency ω travelling in positive x -direction. If the fluid is assumed to be inviscid and incompressible, and the associated motion is irrotational, a velocity potential of the form $\Phi_j(x, y, t) = \text{Re}\{\phi(x, y)e^{-i\omega t}\}$ exists, which satisfies Laplace's equation given by

$$\nabla^2 \phi = 0 \text{ in the entire fluid domain } \Omega, \quad (3.1)$$

where $\omega = 2\pi/T$ is the circular frequency, t is the time in seconds, i is a unit imaginary number $i = \sqrt{-1}$, and Re denotes the real part of the spatial complex potential.

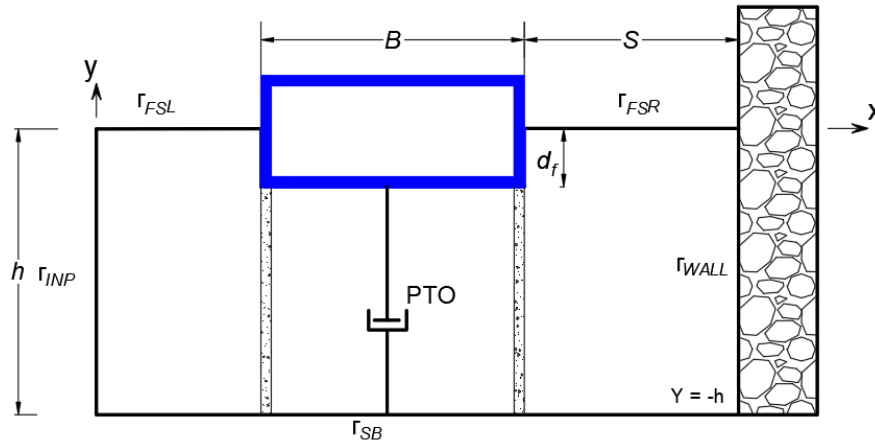


Fig. 3.1: Schematic diagram of WEC integrated with PRFB

On combining complex amplitudes of incident ϕ_I , scattering ϕ_S and heave radiation potential ϕ_R and the heave displacement γ of the PRFB, defined as $\gamma(t) = \text{Re}\{\xi e^{-i\omega t}\}$, the total velocity potential is

$$\phi(x, y) = \phi_I + \phi_S + \xi \phi_R \quad (3.2)$$

The mean free surface of the fluid boundary condition is given by

$$\frac{\partial \phi}{\partial y} - \frac{\omega^2}{g} \phi = 0 \quad \text{on } \Gamma_{fs} \text{ at } y = 0 \quad (3.3)$$

Assuming a finite water depth, the impervious sea bed boundary condition is given as

$$\frac{\partial \phi}{\partial y} = 0, \quad \text{on } \Gamma_{SBL} \text{ and } \Gamma_{SBR} \quad \text{at } y = -h \quad (3.4)$$

On the surface of the PRFB the following boundary conditions are considered

$$\frac{\partial \phi}{\partial n} = \begin{cases} -\frac{\partial \phi_I}{\partial n}, & \text{for scattering problem} \\ V_y, & \text{for heave radiation problem} \end{cases} \quad \text{on } \Gamma_{Str} \quad (3.5)$$

where ϕ_I is the incident wave potential given by

$$\phi_I = -\frac{igA_0}{\omega} \frac{\cos h[k(y+h)]}{\cosh(kh)} e^{-ikx} \quad (3.6)$$

and V_y is the unit normal velocity of the radiating PRFB in the heave mode

the boundary condition on the partially reflecting seawall as considered in Vijay et al (2022) is given by

$$\frac{\partial \phi}{\partial n} = ik \left(\frac{1-C_R}{1+C_R} \right) \phi, \quad \text{on } \Gamma_{Wall} \quad (3.7)$$

where C_R is the reflecting coefficient of the partially reflecting seawall; k is the wave number, which is determined by the dispersion relationship; h is the water depth

Lastly, the far field radiation condition is given as follows:

$$\lim_{r \rightarrow \infty} \sqrt{r} \left(\frac{\partial \phi}{\partial r} - ik\phi \right) = 0, \quad \text{where } r = \sqrt{x^2 + y^2} \quad (3.8)$$

3.2 NUMERICAL SOLUTION BY USING BOUNDARY ELEMENT METHOD

The boundary element technique is based on the fundamental solution and Green's second identity. The weighted residue and Green-Gauss theorem are used in the Laplace's equation Eq. (2.1) to determine the solution for the boundary value problem, over the fluid domain Ω bounded by the boundaries Γ as shown in Fig. (3.2).

The boundary integral equation corresponding to Eq. (3.1) expressed in the generalized form is written as

$$c(P)\phi(P) + \int_{\Gamma} \phi \frac{\partial G}{\partial n} d\Gamma = \int_{\Gamma} G \frac{\partial \phi}{\partial n} d\Gamma \quad (3.9)$$

where G is the free-space Green's function given as $G = \frac{1}{2\pi} \log(r)$ and r is the radial distance between the source point $P(\alpha, \beta)$ and the source point $q(x, y)$ calculated as $r = \sqrt{(\alpha^2 - x^2) + (\beta^2 - y^2)}$. The free term coefficient $c(P)$ is given by

Applying the integral Eq. (3.9) over the fluid domain Ω bounded by the boundaries Γ , the boundary integral equation is obtained as

The boundary integral Eq. (2.11) is solved by discretizing the domain in N constant elements that are numbered in an anticlockwise sequence and stated for the element j by integrating and on the nodal point i on the boundary Γ . The value of N is selected to be large enough such that the results obtained in terms of unknown potentials converge. Now, considering the influence factors $-\frac{1}{2}\phi + \int_{\Gamma_i} \frac{\partial G}{\partial n} d\Gamma = H_{ij}$ and $\int_{\Gamma_i} G_j d\Gamma = Q_{ij}$, and after imposing the boundary

44
68

scattered and radiation are solved independently for the unknowns implementing Gauss elimination technique as discussed below.

3.2.2 Scattering of gravity waves by Fixed Floating Structure

In scattering problem, the PRFB is assumed to have zero heave displacement $\gamma = 0$, so that the boundary condition Eq. 2.5(a) at the surface of PRFB is applicable which leads to zero radiation potential $\phi_R = 0$. Thus, the velocity potential $\phi(x, y) = \phi_I + \phi_S$, where ϕ_I is the known incident potential as mentioned in Eq. (2.6) and ϕ_S is the unknown scattering potential to be determined. The discretized equation for scattering problem upon imposing the boundary conditions as in Eq. 3.3-3.8 is expressed as follows:

$$\begin{aligned} & \sum_{j=1}^N (H_{ij} \phi_S^{SB}) + \sum_{j=1}^N \left(H_{ij} - ikG_{ij} \left(\frac{1-C_R}{1+C_R} \right) \right) \phi_S^{WALL} + \sum_{j=1}^N \left(H_{ij} - \frac{\omega^2}{g} G_{ij} \right) \phi_S^{fsR} \\ & + \sum_{j=1}^N (H_{ij} \phi_S^{STR}) + \sum_{j=1}^N \left(H_{ij} - \frac{\omega^2}{g} G_{ij} \right) \phi_S^{fsL} \\ & + \sum_{j=1}^N (H_{ij} - ikG_{ij}) \phi_S^{INP} = - \sum_{j=1}^N \left(G_{ij} \frac{\partial \phi_I^{Str}}{\partial n} \right) \end{aligned} \quad (3.12)$$

After solving Eq. (2.12), the unknown velocity potentials at the discretized boundary element's mid-nodes are obtained and utilized to compute other quantities of engineering importance such as wave reflection coefficient, wave-induced forces on the fixed PRFB, and partially reflecting wall. The frequency-dependent expression for scattering potential vertical force F_Y acting the PRFB is expressed in the non-dimensional form as follows:

$$F_Y = \frac{\left| i\rho\omega \int_a^{-a} n_y \phi_s dx \right|}{\rho g A_0 h} \quad (3.13)$$

The horizontal wave-induced force acting on the partial reflection seawall F_{Wall} is obtained as

$$F_{Wall} = \frac{\left| i\rho\omega \int_{-h}^0 n_x \phi_s^{WALL} dy \right|}{\rho g A_0 h} \quad (3.14)$$

The non-dimensional free-surface wave elevation in the open water region is given by

$$\zeta_{fs(L,R)} = \frac{-i\omega \phi_s^{fs(L,R)}}{g A_0} \quad (3.15)$$

3.2.3 Radiation of gravity waves due to heaving of PRFB

In the radiation problems, the body is subjected to a unit normal velocity in the vertical y-direction as stated in Eq. 3.5(b) and is assumed to exhibit small heave motion in the still water in the absence of incoming wave and accompanying scattering. Thus, the total velocity potential for the radiation problem is reduced to $\phi(x, y) = \xi \phi_R$. After applying the boundary

conditions as stated in Eq. 2.3-2.8 to the integral Eq. (2.11), the discretized equation for the radiation problem is given as follows.

$$\begin{aligned}
& \sum_{j=1}^N (H_{ij} \phi_R^{SB}) + \sum_{j=1}^N \left(H_{ij} - ikG_{ij} \left(\frac{1-C_R}{1+C_R} \right) \right) \phi_R^{WALL} + \sum_{j=1}^N \left(H_{ij} - \frac{\omega^2}{g} G_{ij} \right) \phi_R^{fsR} \\
& + \sum_{j=1}^N (H_{ij} \phi_R^{STR}) + \sum_{j=1}^N \left(H_{ij} - \frac{\omega^2}{g} G_{ij} \right) \phi_R^{fsL} \\
& + \sum_{j=1}^N (H_{ij} - ikG_{ij}) \phi_R^{INP} = \sum_{j=1}^N (G_{ij} V_y)
\end{aligned} \tag{3.16}$$

The unknown radiation potential ϕ_R is obtained by solving Eq. (2.16). The hydrodynamic radiation vertical force F_H , added mass A_{22} and radiation damping coefficient B_{22} in heave mode of PRFB are computed using the following equations respectively:

$$F_H = i\rho\omega \int_a^{-a} n_y \phi_R^{Str} dx \tag{3.17}$$

$$A_{22} = \text{Re} \left[\rho \int_a^{-a} \phi_R n_y dy \right] \tag{3.18}$$

$$B_{22} = \text{Im} \left[\rho\omega \int_a^{-a} \phi_R n_y dy \right] \tag{3.19}$$

where Re and Im represent the complex number's real and imaginary components, and n_y is the unit normal vector along the positive y -axis.

3.3 EQUATION OF MOTION

The separated scattering and radiation problems are now coupled in the equation of motion to determine the dynamic heave response of PRFB.

$$(M + A_{22}) \ddot{\gamma}(t) + (B_{22}) \dot{\gamma}(t) + C\gamma(t) = F_e \tag{3.20}$$

where $F_e = F_y e^{-i\omega t}$ is the wave excitation force, M is the mass per unit length of the structure ($= \rho B d_f$), ρ is density of sea water ($= 1025 \text{ kg/m}^3$), C is the hydrodynamic restoring force ($= \rho g B$). Further, substituting assumed heave displacement function $\gamma(t) = \xi e^{-i\omega t}$, its velocity $\dot{\gamma}(t) = -i\omega \xi e^{-i\omega t}$, and acceleration $\ddot{\gamma}(t) = -\omega^2 \xi e^{-i\omega t}$ in to Eq. (3.20) we get

$$\{-\omega^2 (M + A_{22}) - i\omega (B_{22}) + C\} \xi e^{-i\omega t} = F_y e^{-i\omega t} \tag{3.21}$$

With the objective of integration of PRFB with WEC, a liner power take-off (PTO) damping is used to calculate the absorbed power. The heave response amplitude ξ for a coupled PRFB with WEC is expressed as

$$\xi = \frac{F_y}{\{-\omega^2 (M + A_{22}) - i\omega (B_{22} + \lambda_{PTO}) + C\}} \tag{3.22}$$

where λ_{PTO} denoted the PTO damping. For a freely heaving structure $\lambda_{PTO} = 0$ and for scattering problem λ_{PTO} considered to be very large so that the resulting heave response amplitude $\xi = 0$. The optimal PTO damping $\lambda_{optimal} = \sqrt{\left[C / \omega - \omega^2 (M + A_{22}) \right]^2 + (B_{22})^2}$ as defined by Zhao et al. (2017) is considered in the analysis. The heave response amplitude operator RAO is defined as the ratio of heave response amplitude to the incident wave amplitude and is written as

$$H_{RAO} = |\xi / A_0| \quad (3.23)$$

The undamped heave natural frequency is ω_n is defined as

$$\omega_n = \sqrt{\frac{\rho g B}{(M + A_{22})}} \quad (3.24)$$

3.4 POWER CAPTURE AND EFFICIENCY

The capture width ratio η_e which significantly affects the hydrodynamic efficiency of WEC device is defined as the ratio of the power extracted by the device to the power in the incident wave Zhang et al. (2019) and is expressed as follows.

$$\eta_e = \frac{P_{capture}}{P_{incident}} \quad (3.25)$$

where, incident wave power per unit transverse length is theoretically calculated as

$$P_{incident} = \frac{1}{16} \frac{\rho g H_i^2 \omega}{k} \left(1 + \frac{2hk}{\sinh(2hk)} \right) \quad (3.26)$$

and the mean power captured by the PRFB with PTO damping (λ_{PTO}) as stated in Jeong et al. (2022) is given by

$$P_{capture} = \frac{1}{2} \lambda_{PTO} \dot{\xi}^2 \quad (3.27)$$

3.5 HYDRODYNAMICS OF PRFB

The efficiency of PRFB as a shore or coastal protection structure is measured in terms of wave reflection K_R , energy dissipation K_D and resulting wave transmission K_T are expressed as follows respectively:

$$K_R = \left| \frac{\phi_S - i\omega\xi\phi_R}{\phi_I} \right| \quad (3.28)$$

$$K_D = \sqrt{1 - (K_R^2 + K_T^2)} \quad (3.29)$$

$$K_T = \left| \frac{\phi_I + \phi_S - i\omega\xi\phi_R}{\phi_I} \right| \quad (3.30)$$

3.6 NUMERICAL RESULTS AND DISCUSSIONS

To investigate the PRFB's hydrodynamic performance, breakwater efficiency, and wave energy conversion efficiency of the WEC system, a numerical code for a 2D constant BEM is developed in MATLAB and the results are validated with the available literature to analyse the

scattering and radiation problem using small amplitude linear wave theory. The hydrodynamic coefficients such as heave added mass (A_{22}), radiation damping coefficient (B_{22}), response amplitude operator (H_{RAO}), heave motion response (ξ), efficiency as a breakwater measured in terms of wave reflection (K_R), energy dissipation coefficient (K_D), and resulting wave-induced force on the seawall and its capture width ratio (η_e) which is a measure of PRFB's wave energy conversion capability, are investigated for various structural parameters with and without the presence of a seawall in the frequency domain. The influence of varying structural parameters, namely relative drafts (d_f/h), relative structural width (B/h), vertical seawall with varied reflection coefficients (C_R), and its relative distance to the PRFB (S/B), on the suitability of the PRFB as a Hybrid system, are investigated in the following sections. It is to note that the wave parameters such as the density of seawater $\rho = 1025 \text{ kg/m}^3$, acceleration to gravity $g = 9.81 \text{ m/sec}^2$, incident wave amplitude $A_0 = 1.0 \text{ m}$, angle of incidence $\theta = 0^\circ$ and WEC PTO damping coefficient $\lambda_{PTO} = \lambda_{optimal}$ are kept constant throughout the analysis unless otherwise mentioned.

3.7 VALIDATION OF THE NUMERICAL RESULTS

Two specific examples from the available literature are considered to verify the correctness of the present numerical BEM model developed to solve radiation and scattering problems (a) analytical solution obtained by Zheng et al. (2004) for radiation and diffraction potentials and validated against BEM for a freely floating rectangular structure in a finite water depth with a leeward rigid vertical wall and $B/h = 1/3$, $d_f/h = 0.4$ and $S/h = 0.2$ are the geometrical parameters. The Fig. 3.3(a,b) shows the results of the added mass and radiation damping coefficient for heave motion response in presence of a rigid vertical wall ($C_R = 1.0$) obtained using the current BEM model closely match those of Zheng et al. (2004).

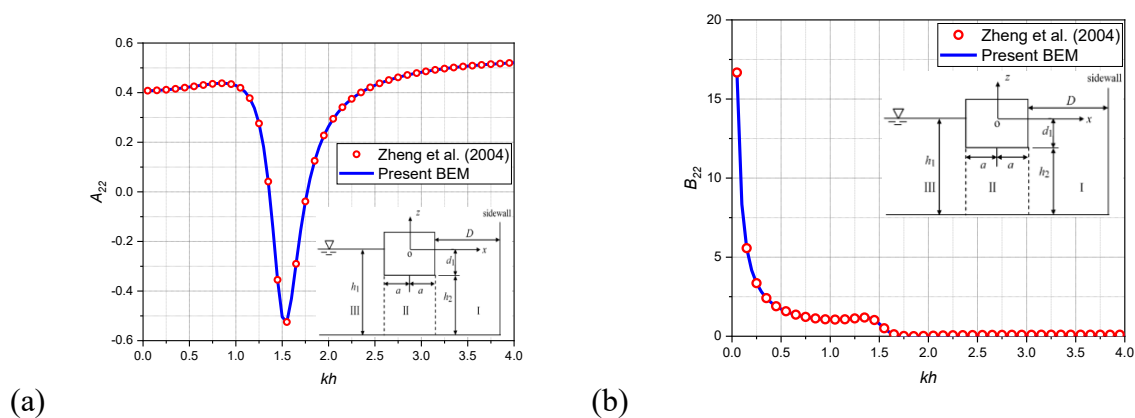


Fig. 3.3: Variation of (a) added mass A_{22} and (b) radiation damping coefficient B_{22} versus kh for a freely floating breakwater in presence of a leeward rigid vertical wall.

Second example verifies the results obtained using the present BEM model for the heave RAO (H_{RAO}), and wave reflection (K_R) by comparing against the results of Zhao et al. (2017) using matched Eigen function expansion technique for a WEC integrated with floating breakwater

for $B/h = 0.8$, $d_f/h = 0.25$ and incident wave amplitude $A_0 = 1.0m$. Since the effect of WEC is represented by coupling a PTO damping as a velocity component in equation of motion, the value chosen for PTO damping $\lambda_{PTO} = \lambda_{optimal}$ for heave motion with WEC, $\lambda_{PTO} = 0$ for a freely heaving PRFB and $\lambda_{PTO} = 100000\lambda_{optimal}$ for a fixed floating PRFB. The heave response RAO (H_{RAO}) with and without WEC plotted against the non-dimensional wave number using the current technique is shown in Fig. 3.4(a), which is consistent with the results reported by Zhao et al. (2017). Finally, the current BEM approach for wave reflection coefficients presented in Fig. 3.4(b) for a fixed, free, and WEC integrated with PRFB utilizing the aforementioned parameters agrees satisfactorily with the results of Zhao et al (2017).

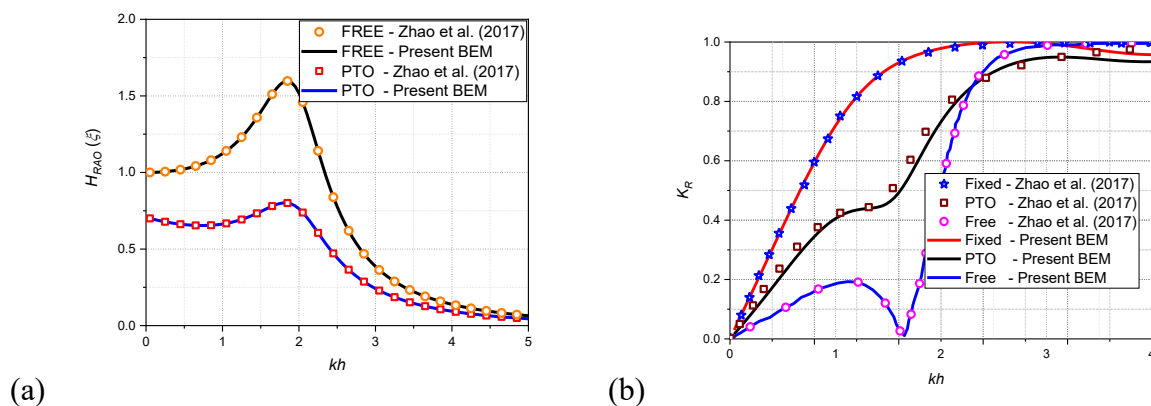
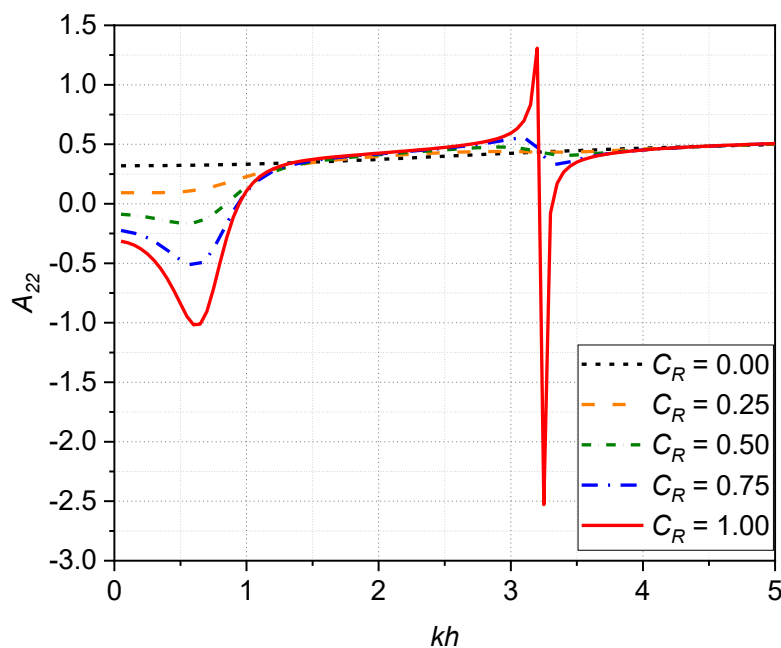


Fig 3.4: (a) Variation of the heave response operator (H_{RAO}) and (b) Variation of the K_R and K_T versus kh for a fixed, freely as well as a PRFB coupled with WEC

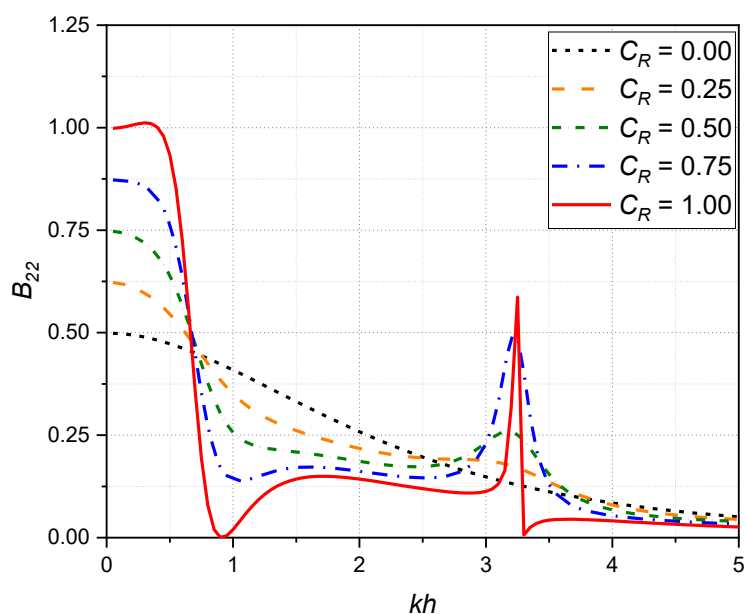
3.8 EFFECT OF SEAWALL OF DIFFERENT POROSITY ON WEC INTEGRATED WITH PFRB

In this section, the influence of varying the reflection coefficient parameter C_R of vertical seawall positioned at a set distance $S/h = 1.0$ on the leeward side of PFRB on its hydrodynamic performance and the efficiency of the WEC system are examined. The geometrical parameters of PRFB that are considered are $B/h = 1.0$ and $d_f/h = 0.25$, with the PTO damping coefficient of WEC system equal to its ideal value (i.e., $\lambda_{PTO} = \lambda_{optimal}$). While the seawall's reflection coefficient parameter C_R is changed from 0 to 1 with 0.25 increments. It is worth noting that when $C_R = 0$, the existence of a vertical seawall diminishes, indicating that the transmitted propagating waves are completely dissipated by the partially reflecting seawall. On the other hand for $C_R = 1$, the transmitted propagating waves are entirely reflected by the vertical seawall, implying that the seawall is an impervious barrier. Similar analysis was carried out to estimate the hydrodynamic coefficients of a rectangular floater by Isaacson and Qu (1990), Zhao et. al. (2017) and Vijay et al. (2022). Wang et al. (2022) considered a floater as WEC device with perforated wall and Zhao et al. (2021) considered interconnected dual pontoon system in presence of partially reflection seawall to study their hydrodynamic

performance of the system. Fig 3.5(a and b) shows the heave added mass A_{22} and radiation damping coefficient B_{22} plotted against the non-dimensional wavenumber kh . The spike in A_{22} and B_{22} is evident at $kh = 3.25$ for $C_R = 1$, displaying its resonance behaviour, which is mostly due to wave energy entrapment in the region between the PRFB and the totally reflecting impermeable vertical seawall may provoke in frequency shift phenomena, Dodge (2000).



(a)



(b)

Fig 3.5: Variation of (a) added mass A_{22} and (b) radiation damping coefficient B_{22} versus kh for a WEC integrated with PRFB in presence of a leeward vertical seawall of varying porosity. Moreover, for values of $C_R \geq 0.5$ in shallow water ($kh < (\pi/10)$) and $C_R = 1$ at $kh = 3.25$, negative heave added mass A_{22} and zero heave radiation damping are observed. The reason for the same is due to the presence of seawall of higher porosity $C_R \geq 0.5$ positioned on the leeward of the floating structure which has a relatively smaller draft d_f/h compared to its structural width B/h . This develops a local flow field in which no waves of a specific frequency radiate to the distant field, causing the system to function as a motion-trapping structure, Evans and Porter (2007). It is worth to note that for presence of vertical seawall, even though the radiation damping coefficient initially starts with 1.25 times higher for every increase of $C_R = 0.25$ as compared to a no wall condition, but then for $0.5 \leq kh \leq 0.75$ a sudden drop in its value lower than that of with $C_R = 0$ and even it touches zero value ($B_{22} = 0$) for a particular case of $C_R = 1$. Thereafter B_{22} continues to remain lower for higher kh values except at its resonance region for $3.0 \leq kh \leq 3.5$. It is worth noting that in the presence of a vertical seawall, the radiation damping coefficient B_{22} initially starts with 1.25 times higher for every increase of $C_R = 0.25$ as compared to a no wall condition $C_R = 0$, but then the radiation damping coefficient B_{22} values with $C_R > 0$ are lower than that of B_{22} value with $C_R = 0$ for range of $0.5 \leq kh \leq 2.6$ and for $kh > 3.5$. When $C_R = 1$, the radiation damping coefficient B_{22} is close to zero for $kh = 0.9$ and 3.25 . This implies that at these two kh values, the PFRB heave response amplitude will be close to zero, as seen in Fig (3.6) verifying that at these frequencies the system operates as motion trapping structure.

Fig. 3.6 shows the variation in heave response operator H_{RAO} as a function of non-dimensional wavenumber kh for change in reflection coefficient C_R of the vertical partially reflecting seawall. For shallow water and a portion of the intermediate water depth zone $kh = 2.25$, significant spikes and dips in the heave response operator H_{RAO} of identical magnitude are seen for every 0.25 increase in reflection coefficient C_R compared to a no seawall conditions $C_R = 0$. Thereafter the heave response operator H_{RAO} follows the similar trend as of a no seawall condition except a local spike at $kh = 3.25$, indicating that the presence of seawall on the leeward side of the PRFB structure has negligible influence on its dynamics heave response in short wave regime, which is substantiated in Fig. (3.8) which shows no variation in wave reflection coefficient K_R for $kh > 2.25$. Furthermore, for each value of C_R examined in the study, the occurrence of global maxima in heave response operator H_{RAO} corresponds to its heave fundamental natural frequency $\omega_n = 4.017 \text{ rad/sec}$ computed from Eq. (2.24), which is located at $kh = 1.645$.

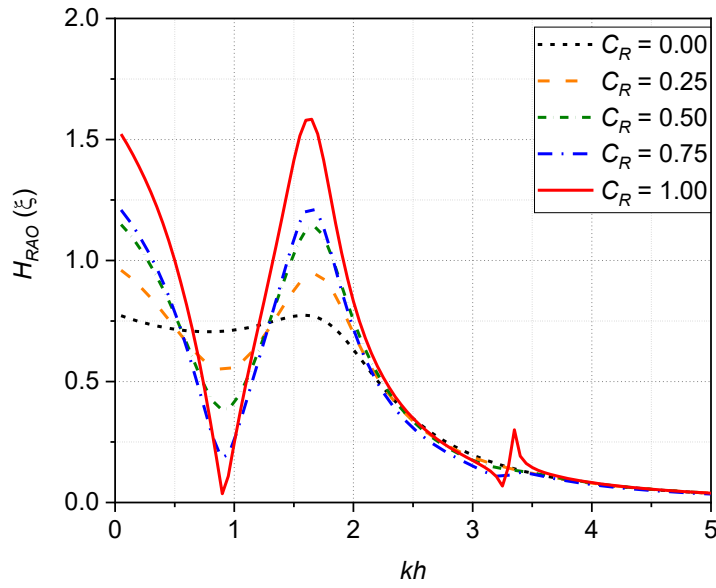


Fig 3.6: Variation in the heave response operator (H_{RAO}) versus kh for a WEC integrated with PRFB in presence of a leeward vertical seawall of varying porosity.

From the Fig. (3.7), it is found that the capture width ratio η_e which has a unimodal trend for the case of no seawall $C_R = 0$ condition exhibits a multiple peak trend for increasing C_R . Although, the first individual peaks in the capture width ratio η_e curve occurs at $kh = 0.5$ for all C_R values, even when $C_R = 1$, its maximum capture width ratio η_e does not exceed 55%. In fact, when the value of excitation frequency is nearly equal to the heave fundamental natural frequency $\omega_n = 4.017 \text{ rad/sec}$ the second peaks attains their global maximum. When $C_R = 1$ the $\eta_e = 99.95\%$ at $kh = 1.65$ and for $C_R = 0.75$ occurrence of resonant capture width ratio $\eta_e = 86.11\%$ is shifted at $kh = 1.70$, whereas for remaining $C_R = 0$ to 0.50 , the resonant capture width ratio's $\eta_e = 50.00\%$, 61.28% and 73.12% respectively are shifted towards $kh = 1.75$. This small shift may be due to anti symmetric sloshing mode at different excitation wave frequency caused by varying C_R between the trap zone (distance between the PRFB and the vertical sea wall). Interestingly the area under the efficiency curve of capture width ratio η_e , for an impermeable seawall $C_R = 1$ is approximately 35.68%, 17.00%, 6.86% and 1.44% more than compared to the area under the efficiency curve of capture width ratio η_e having no seawall $C_R = 0$. It is also learnt that, when $C_R = 0$, the frequency bandwidth for which the capture width ratio η_e is at least 20% and can go up to a maximum of 50% in the range of $0.5 \leq kh \leq 3$. Further, when $C_R = 0.25$, the criteria of $\eta_e \geq 20\%$ is satisfied in the range of $0.4 \leq kh \leq 2.9$ and can reach to a maximum of 61.28% capture width ratio η_e . For higher values of C_R , although multiple higher efficiency peaks are obtained, but the criteria of at least $\eta_e \geq 20\%$ is not satisfied for wavenumber $0.7 \leq kh \leq 1.1$.

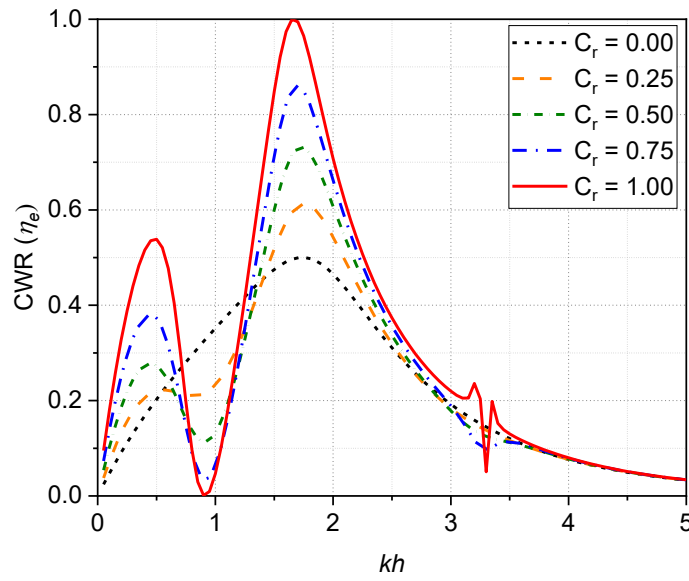


Fig 3.7: Variation in the capture width ratio (η_e) versus kh for a WEC integrated with PRFB in presence of a leeward vertical seawall of varying porosity.

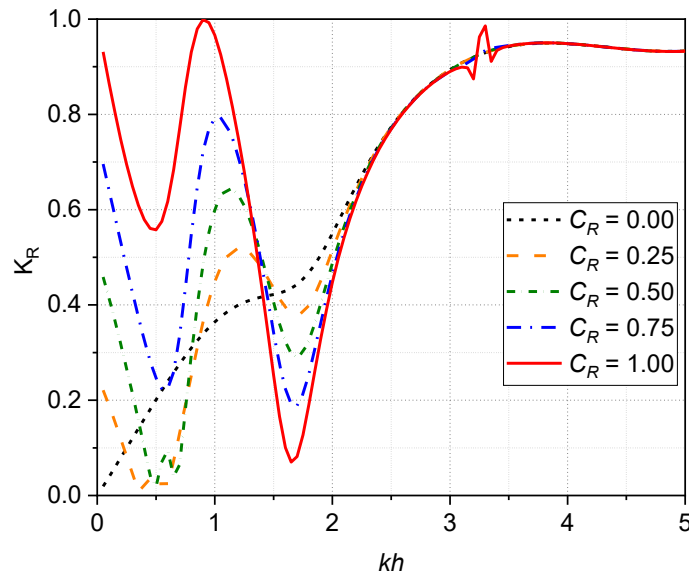


Fig 3.8: Variation in K_R versus kh for a WEC integrated with PRFB in presence of a leeward vertical seawall of varying porosity.

The influence of reflection coefficient C_R of the vertical seawall on wave reflection coefficient K_R plotted as a function of kh shown in Fig. (3.8), indicates that significant variation in wave reflection coefficient K_R appears in the presence of vertical seawall. However, this variation is limited up to the non-dimensional wave number $kh = 2.25$, thereafter the influence of

seawall and its porosity diminishes thereby following the same trend as of a no seawall $C_R = 0$ condition. The reason for this is that the wave excitation frequency ω_e in the short-wave regime is substantially greater than the fundamental natural frequency ω_n , causing the heave response amplitude to be suppressed. The salient features of this variation in wave reflection coefficient K_R due to presence of seawall indicates that, even though the K_R starts initially with higher amplitudes as compared to a no seawall $C_R = 0$ condition, the K_R reduces in shallow water and part of the intermediate water depth region for $kh = 0.5$, thereafter it increases to reach their first peak maxima in the range of kh 1 to 1.25, then it falls down abruptly to reach their minima at that value of kh which corresponds to the heave fundamental natural frequency ω_n . Furthermore, it increases to merge with the curve of a K_R which is of a no seawall condition $C_R = 0$ at $kh = 2.25$. It also worth to note that, for the amplitude of oscillation in K_R for $C_R < 0.5$, reduces with increasing kh , and for those with $C_R > 0.5$ the amplitude of oscillation increases with increasing kh , until they coincide with each other at $kh = 2.25$.

Fig. (3.9) shows that the peaks in horizontal wave-induced force F_{WALL} acting on seawall of varying porosity occurs at two instances of wavenumber kh closely nearer to 0.6 (moderate peak) and at $kh = 3.25$ (sharp peak). However, this peak in the wave-induced horizontal force F_{WALL} diminishes with increasing porosity by lowering C_R of the seawall. This happens because, larger the porosity greater the wave energy dissipation, which suppresses the development of frequency shift phenomena of fluid sloshing between the trap zone. This wave-induced force is similar in pattern but opposite in nature (positive sign) as that of heave added mass A_{22} .

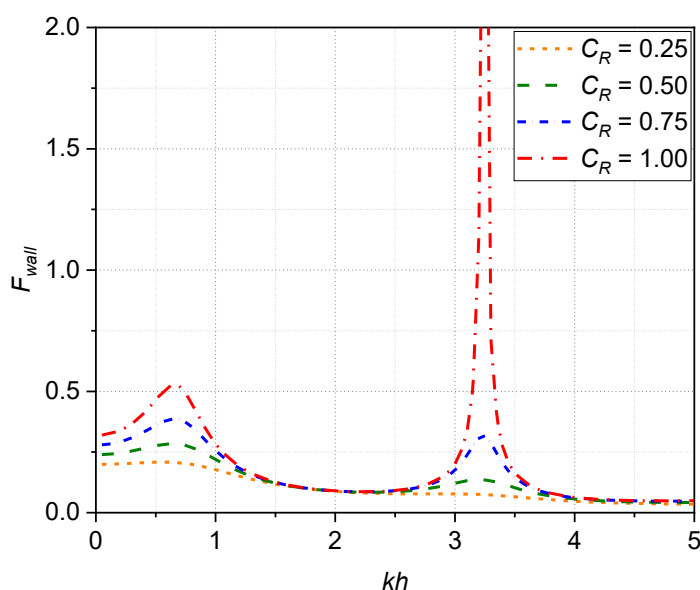
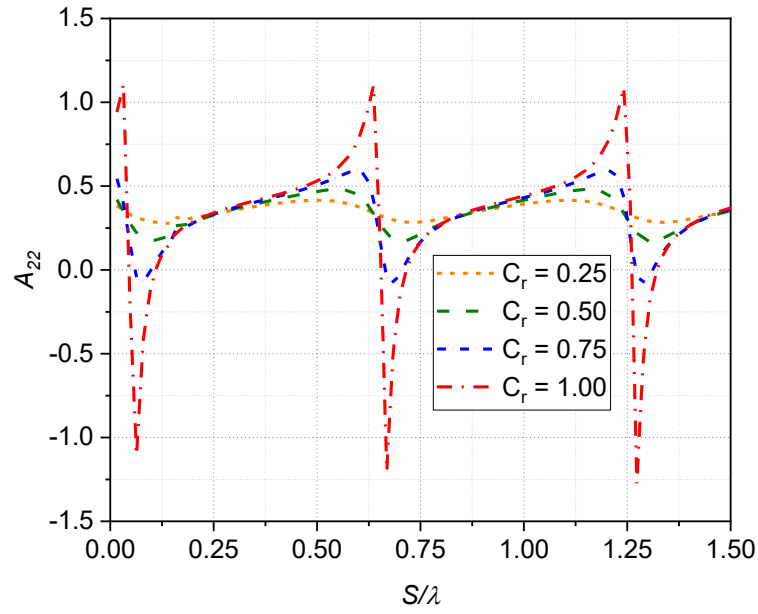


Fig 3.9: Variation in horizontal wave-induced force F_{WALL} on seawall of varying porosity versus kh for a WEC integrated with PRFB.

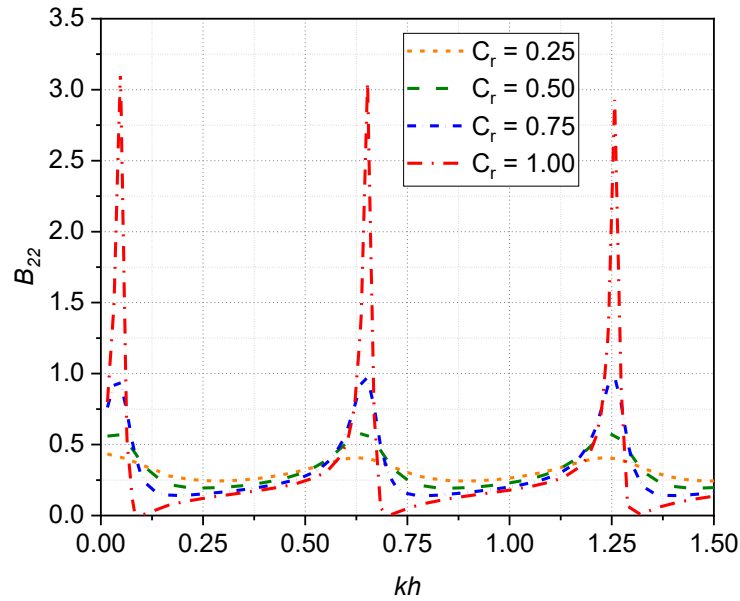
3.9 EFFECT OF RELATIVE SPACING BETWEEN THE PFRB AND THE VERTICAL SEAWALL.

When the wavelength λ of the radiated waves is twice the clearance distance S , a phenomenon known as harbour seiching occurs due to free-surface oscillation of the water column between the floating body and the partially reflecting barrier Vijay et al. (2022). Under such conditions, the associated hydrodynamic coefficients of the floating body will exhibit resonant behaviour. Effect of varying relative spacing S/λ is explored on the performance of the WEC integrated with PRFB in presence of a vertical seawall for $kh=1.65$ which corresponds to the heave fundamental natural frequency ω_n . The geometrical parameters are $B/h=1$ and $d_f/h=0.25$. Fig. (3.10-3.12) shows the variation of the heave added mass A_{22} , radiation damping coefficient B_{22} , heave amplitude operator H_{RAO} , Capture width ratio η_e , wave reflection coefficient K_R and horizontal wave-induced force F_{WALL} on seawall with the varying the relative spacing S/λ in the presence of a partially reflecting vertical seawall.

Fig. 3.10(a and b) shows that the occurrence of resonant peaks in heave added mass A_{22} and the radiation damping coefficient B_{22} are regular with increasing relative spacing S/λ for various values of reflection coefficient of partially reflection seawall, demonstrating the Bragg's phenomena as reported by Zhao et al. (2017) in the case of a fixed breakwater and a wave energy device moving in heave. The resonant peaks in heave added mass A_{22} and the radiation damping coefficient B_{22} are exceptionally larger when the seawall is fully impermeable $C_R=1$ and for lower values of $C_R \leq 0.75$, the resonant peaks are suppressed by 2 to 3 times as compared to the peaks with $C_R=1$. Furthermore, for $C_R=1$, the resonant peaks of heave added mass A_{22} oscillate periodically at a relative spacing $S/\lambda=0.605$ with equal magnitude of negative and positive amplitudes, with the impulsive character persisting for a very narrow band width of $S/\lambda=0.032$. While, the radiation damping coefficient B_{22} have positive impulses at the same regular intervals. On the other hand, for $C_R \leq 0.5$ the occurrence of resonance in the hydrodynamics coefficients A_{22} and B_{22} almost diminishes and varies almost uniformly with increasing relative spacing S/λ .



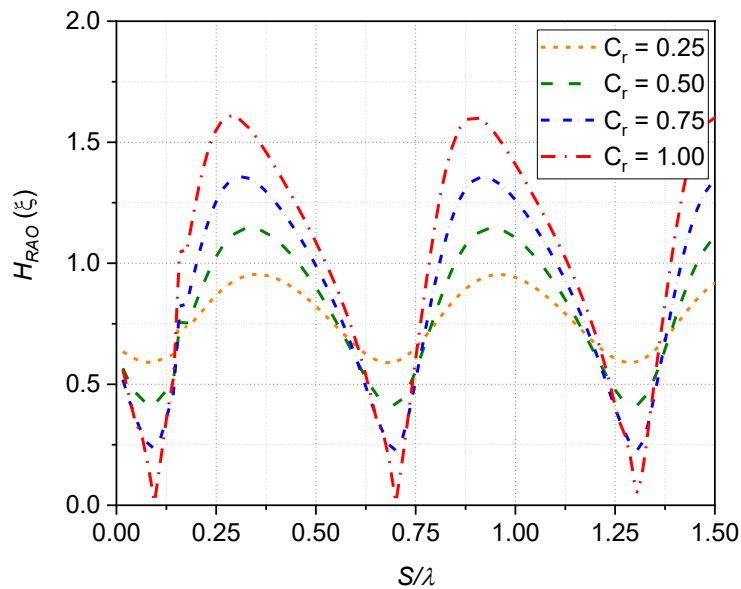
(a)



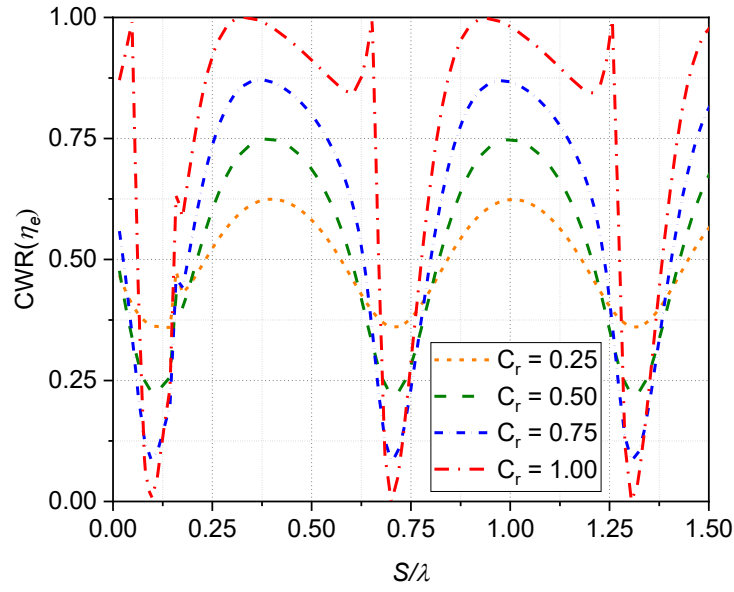
(b)

Fig. 3.10: Variation of the (a) heave added mass A_{22} and (b) radiation damping coefficient B_{22} with varying the relative spacing S/λ in the presence of a partially reflecting vertical seawall. The heave response operator H_{RAO} plotted against the varying relative spacing S/λ for various values of C_r shown in Fig. 3.11 (a) oscillates at regular intervals of relative spacing S/λ with equal amplitudes around a mean value of $H_{RAO} = 0.75$. Global minima occur at the S/λ for which the resonance in the hydrodynamics coefficients A_{22} and B_{22} was observed, as seen in Fig. 3.10 (a and b). Further, with increase in C_r , heave response operator H_{RAO} peaks

of maxima and minima increases, with their valley values becomes sharper as they come closer to their global minima and a small shift in the peaks of maxima to a lower S/λ . In fact, the resonant spike in hydrodynamics coefficients A_{22} and B_{22} is driving the corresponding H_{RAO} to reach their global minima. From the Fig. 3.11(b), it is observed that, larger band width of S/λ can be chosen for which the desired efficiency at least a more than 50% can be achieved. With increase in C_R , the capture width ratio η_e attains a maximum of about 62.5% for $C_R = 0.25$ and reached about 99.98% for $C_R = 1$. Moreover, C_R with higher values offers wider range of S/λ for the same value of capture width ratio η_e . However, when $C_R > 0.5$ the value of S/λ for which the value of capture width ratio η_e drops abruptly below 20% are extremely narrow of about $S/\lambda = 0.032$ and that are the locations that corresponds to the resonance of heave added mass A_{22} and the radiation damping coefficient B_{22} .



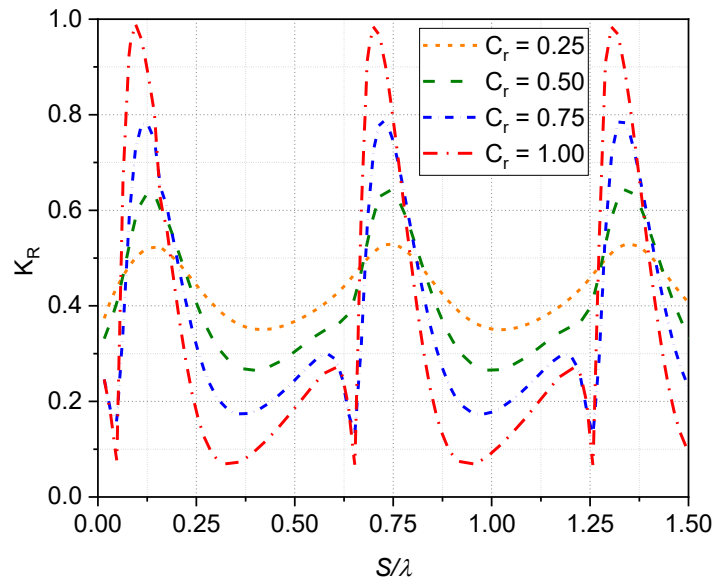
a)



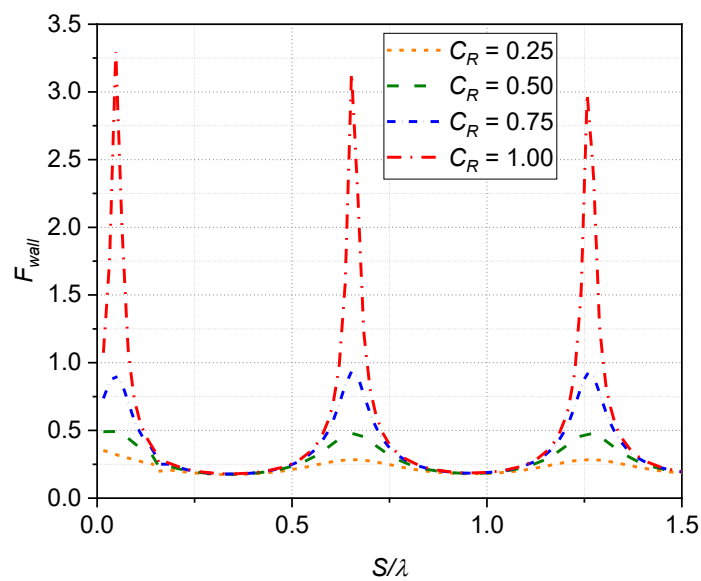
(b)

Fig. 3.11: Variation of the (a) heave amplitude operator H_{RAO} and (b) Capture width ratio η_e with varying the relative spacing S/λ in the presence of a partially reflecting vertical seawall. While designing the position of the hybrid system composed of a WEC integrated with floating structure in presence of a seawall/barrier, the key parameters that should be satisfied are (i) energy capture efficiency and (ii) hydrodynamic performance as a costal/structure protecting structure. Considering the influence of relative spacing S/λ on the capture width ratio η_e , which is a measure of WEC efficiency discussed as above, the wave reflection coefficient K_R and the wave force F_{WALL} imparted on to the partially reflecting sea wall is illustrated in Fig. 3.12 (a and b). A similar trend with exactly opposite nature in wave reflection coefficient K_R is observed with increasing S/λ for various range of C_R considered in the study. Interestingly, the range of S/λ for which the capture width ratio η_e exhibits their maximum efficiency, the corresponding wave reflection coefficient K_R values are much lower than the set threshold value of $K_R \leq 0.5$, for ranges of C_R presented in Fig. 2.12 (a). Consequently, a subsidence in wave-induced force on the partially reflection seawall is recorded as shown in Fig. 2.12 (b). However, as expected, increasing the porosity of the partially reflecting vertical seawall leads in a slackening of the resonant peaks of the non-dimensional horizontal wave-induced force F_{WALL} . Furthermore, the strong peaks of wave reflection coefficient K_R and non-dimensional horizontal wave-induced force F_{WALL} corresponds to the valleys of capture width ratio η_e .

These findings show that there is enough scalability for selecting S/λ depending on site conditions without forfeiting hydrodynamic performance or WEC efficiency as a hybrid system.



(a)



(b)

Fig. 3.12: Variation of the (a) wave reflection coefficient K_R and (b) horizontal wave-induced force F_{WALL} with varying the relative spacing S/λ in the presence of a partially reflecting vertical seawall.

3.10 EFFECT OF PTO DAMPING.

The presence of partially reflecting seawall, exaggerate the heave response amplitude, thereby resulting an undesirable hydrodynamic performance especially the wave reflection coefficient

K_R in shallow water and part of the intermediate water depth region. It is obvious from Eq. (3.22) that the heave response amplitude ξ can be tuned either by changing mass (M), and the hydrodynamic coefficients (A_{22} and B_{22}) by altering the geometrical properties (B and d_f) or by adding an external damping via coupling WEC PTO damping coefficient λ_{PTO} to the system. Since the overall performance of a hybrid system is a measure of both the wave energy extraction efficiency and wave attenuation performance, they are taken into account simultaneously, the effect of PTO damping considering $C_R = 1$ on the heave response operator H_{RAO} , capture width ratio η_e , and the reflection coefficient K_R are examined and are illustrated in Fig (3.13-3.14) respectively. The results of hydrodynamic coefficients (A_{22} and B_{22}) are not presented as they are independent of WEC PTO damping. Utilizing the Optimum PTO damping $\lambda_{optimal}$ as a reference, a spectrum of WEC PTO damping λ_{PTO} values ranging from $0.25\lambda_{optimal}$ to $5\lambda_{optimal}$ are examined to determine the ideal value for the proposed model. Fig. 2.13 shows that the heave amplitude operator H_{RAO} decreases with increase in λ_{PTO} , consequently, leading to increasing in wave reflection coefficient K_R as seen in Fig. (3.15). On the other hand, the increase in λ_{PTO} up to a value of $\lambda_{PTO} = \lambda_{optimal}$, the capture width ratio η_e increases, thereafter any increase in λ_{PTO} beyond its $\lambda_{optimal}$ value, the capture width ratio η_e reduces for all values of non-dimensional wavenumber kh . Interestingly, the influence of varying PTO damping values does not alter its trend pattern, but increasing λ_{PTO} from $0.25\lambda_{optimal}$ to $\lambda_{optimal}$, the percentage increase in second resonant peak is about 56.35%, increasing further from $\lambda_{optimal}$ to $1.5\lambda_{optimal}$, $1.5\lambda_{optimal}$ to $2.0\lambda_{optimal}$ and $2.0\lambda_{optimal}$ to $5.0\lambda_{optimal}$ an reduction of 4%, 7.42% and 37.54% is recorded at their second resonant peaks respectively. This is a clear indication that the value of PTO damping $\lambda_{PTO} = \lambda_{optimal}$ is an ideal value for a WEC integrated with PRFB in presence of a seawall of any porosity. However, the peaks of capture width ratio η_e occurs at $kh = 1.65$ and are not altered for different λ_{PTO} . This is due to the that fact that heave natural frequency ω_n as stated in Eq. (3.24) is a function of hydrodynamic restoring force C , mass of the system M and added mass coefficient A_{22} . Therefore, in the subsequent sections, geometrical parameters are examined to study the influence of width and draft of the PRFB.

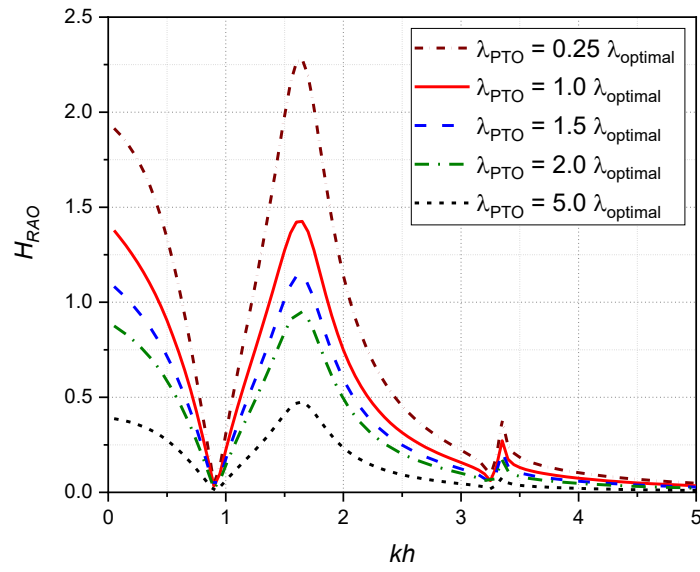


Fig. 3.13: Variation of the heave amplitude operator H_{RAO} versus kh for various values of PTO damping.

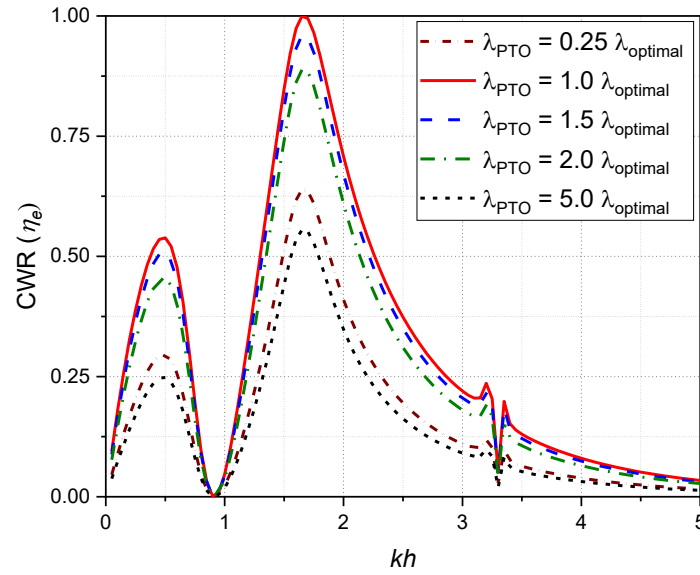


Fig. 3.14: Variation of the Capture width ratio η_e versus kh for various values of PTO damping

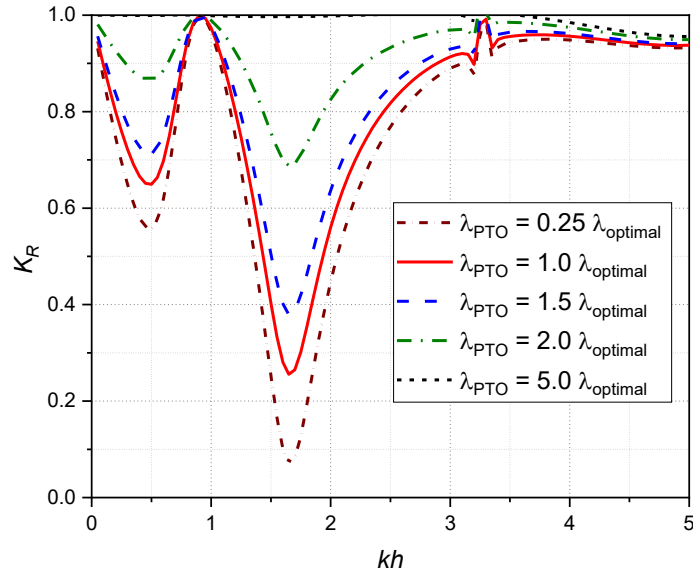


Fig. 3.15: Variation of the wave reflection coefficient K_R versus kh for various values of PTO damping.

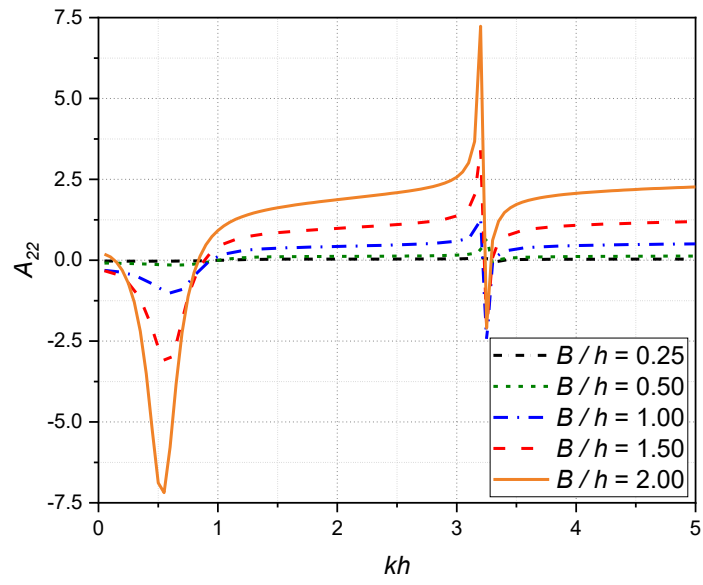
3.11 PARAMETRIC STUDY

This section addresses the effect of relative structural width B/h and the relative structural draft d_f/h of PRFB, which are key parameters that largely influence both the hydrodynamic coefficients and its characteristics. Considering the reflection coefficient $C_R=1.0$ of the partially reflecting seawall, it enables the WEC device to harness wave energy efficiently but limited to a certain range of wavenumbers kh , relative spacing $S/\lambda=0.32$, which corresponds to the peak of capture width ratio η_e for $C_R=1.0$ referring Fig. 3.11(b) and opting an ideal WEC damping PTO $\lambda_{PTO} = \lambda_{optimal}$ obtained from section 4.4, the effect of relative structural width B/h and relative structural draft d_f/h on the hydrodynamic coefficients (A_{22} and B_{22}), capture width ratio η_e , wave reflection coefficient K_R are discussed in section 3.5.1 and section 3.5.2 respectively. Zhao et al. (2017) conducted a similar investigation on a WEC integrated with a pile restrained breakwater on an isolated floating structure.

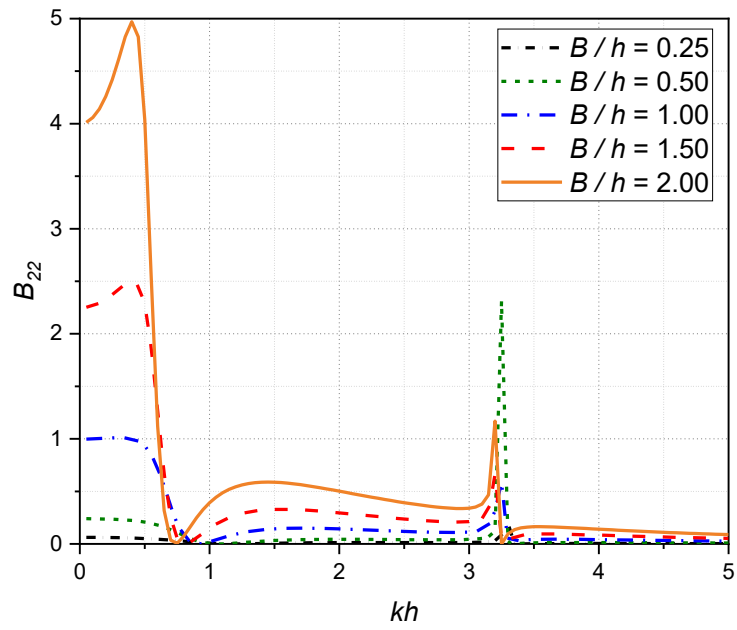
3.18.1 Effect of Relative Structural Width

Effect of varying the structural width B/h of PRFB on the hydrodynamic properties of the system are investigated considering the following four cases of $B/h = 0.25, 0.5, 1, 1.5$ and 2.0 , while maintaining a constant structural draft $d_f/h = 0.25$. Fig. (3.16 – 3.18) illustrates the variations of the hydrodynamic coefficients (A_{22} and B_{22}), heave amplitude operator H_{RAO} , capture width ratio η_e , and wave reflection coefficient K_R against the non-dimensional wavenumber kh in the presence of seawall having $C_R = 1.0$.

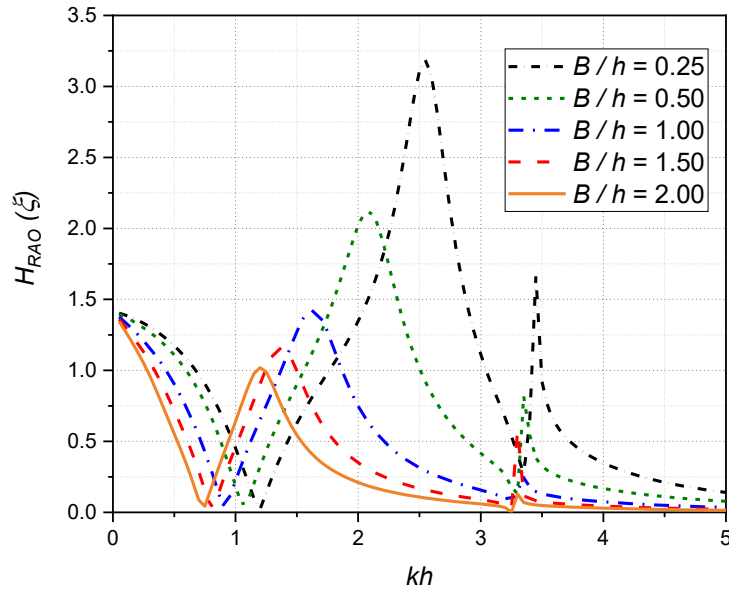
The effect of varying relative structural width B/h of the WEC integrated with PRFB between 0.25 and 2.0 for a fixed structural draft $d_f/h = 0.25$ on heave added mass A_{22} , radiation damping coefficient B_{22} and heave amplitude operator H_{RAO} is shown in Fig. 3.16 (a, b and c) respectively. The results of which indicate that, for each increase in the value of B/h , the influence of width to draft ratio B/d_f increases, causing the system to operate as a motion trapping structure at excitation frequencies corresponding to $kh = 0.9$ and 3.25 , by acquiring a higher negative amplitude of heave added mass and a zero radiation damping coefficient B_{22} . Further, the salient features of heave added mass A_{22} and radiation damping coefficients B_{22} not only indicates the amplification in their magnitude, but also exhibit a phase shift towards lower wavenumber kh , which is mainly due the fact that, the fundamental natural frequency ω_n decreases increase in relative structural width B/h . As a result of this, amplification in hydrodynamic coefficients (A_{22} and B_{22}) leads to reduction in heave response operator H_{RAO} is seen in Fig.3.16 (c) with increasing structural width B/h . However, this amplification is limited to both the peaks of heave added mass A_{22} and first resonant peak of B_{22} , whereas the second resonant peak of B_{22} decrease for initial change in B/h from 0.5 to 1.0 and further any increase in B/h it increases. On the other hand, in Fig. 3.16(c) the heave amplitude operator H_{RAO} reduces in magnitude followed by a phase shift for the reason as explained above, indicating that higher ratio of B/d_f leads closer to lower heave response motion. However, the effect of this aspect ratio of B/d_f significantly affect the first and second resonant peak amplitudes of heave response operator H_{RAO} to decay exponential for initial increase in values of B/h from 0.25 to 1.0, thereafter the reduction is uniform. More importantly, the system will be acting as a motion-trapping structure under these conditions, denoting a full wave reflection $K_R = 1.0$, for the wavenumber kh in Fig. 3.16(c) for which the heave response operator $H_{RAO} = 0$ and also corresponding to wavenumber kh in Fig. 3.16(a and b) for which the heave added mass A_{22} has achieved its maximum negative value and the radiation damping coefficient $B_{22} = 0$.



(a)



(b)



(c)

Fig. 3.16: Variation of the (a) heave added mass A_{22} , (b) radiation damping coefficient B_{22} and (c) heave amplitude operator H_{RAO} versus kh for various values of relative structural width B/h .

Although changing the relative structural width B/h from 0.25 to 2.0 leads to reduction heave response operator H_{RAO} as shown in Fig. 3.16 (c), but this change has no effect on the magnitude of the global maxima of capture width ratio η_e as seen in Fig. 3.17. However, it has a significant impact on gaining higher efficiency by increasing the magnitude of the capture width ratio η_e of second global maxima that occurs at lower wave number kh . Moreover, the increase in relative structure width B/h resulted in shift in peaks of capture width ratio η_e to lower wave number kh , for the same reason that, the fundamental natural frequency ω_n decreases as depicted in Table 1 and $\lambda_{optimal}$ increases with increasing structural width B/h . Furthermore, at lower relative structural depth $B/h < 1.0$, third resonant peak in capture width ratio η_e becomes impulsive at $kh = 3.25$ exhibiting a significant sloshing caused by the frequency shift phenomenon as noted earlier. Increasing structural width B/h while retaining the same draft $d_f/h = 0.25$ should inevitably increase the heave response operator H_{RAO} since wetted surface area contributing to heave force increases (consequently heave added mass increases as stated in Table 2.1), however this is not the case as shown in Fig. 3.16. Also, the percentage area under the curve shown in Table 1, initially increases when the B/d_f was doubled from 1 to 2, further increasing B/d_f from 2 to 4, 6 and 8, the area under the curve remains almost the same. The reason for this is because as structural width B/h increases, so does the system's mass M and hydrodynamic restoring force C , resulting in a decrease in the fundamental natural frequency ω_n .

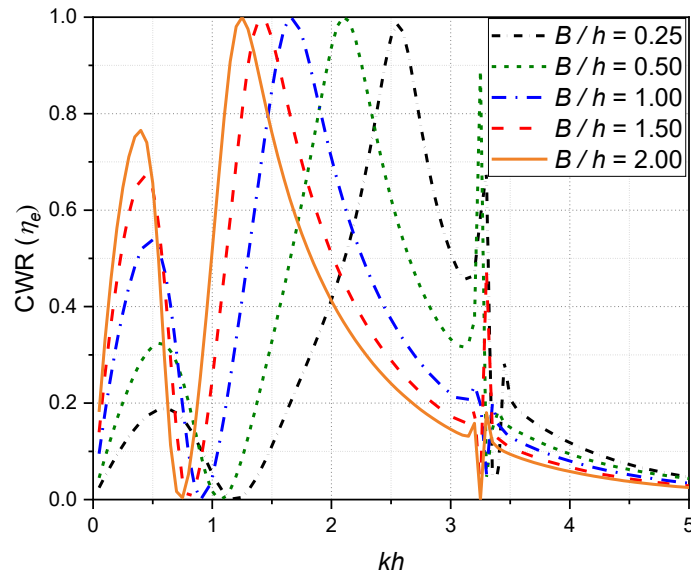


Fig. 3.17: Variation of the Capture width ratio η_e versus kh for various values of relative structural width B/h .

Table 3.1: Percentage area under the curve of CWR (η_e), natural frequency (ω_n) and wavenumber (kh) corresponding to excitation frequency.

Structural width (B/h)	Width to depth ratio (B/d_f)	Mass of the system (M) kg	Heave added mass coefficient (A_{22})	Natural frequency (ω_n)	Wavenumber corresponding to excitation frequency (kh)	Percentage Area under the CWR (η_e) curve
0.25	1	64.062	37.306	4.980	2.55	26.37%
0.5	2	128.125	122.011	4.483	2.10	30.13%
1.0	4	256.250	402.051	3.908	1.65	30.95%
1.5	6	384.375	854.766	3.489	1.40	30.82%
2.0	8	512.500	1441.282	3.208	1.25	29.69%

More wave energy is dissipated as the structural width B of the floating structure increases, indicating that the breakwater is more effective, as reported by Pena et al. (2011) during their experimental studies on floating breakwaters and Patil and Karmakar (2022) by numerical investigation on hydrodynamics of floating tunnel with submerged rubble mound breakwater. Similarly in Fig. 3.18, the wave reflection coefficient K_R decreases with increasing structural width B/h , with no change in their trends along varying wavenumber kh . It is also true that, the trend of wave reflection coefficient K_R is mirrored vertically as the trend lines of capture width ratio η_e shown in Fig. 3.17, indicating any reduction in wave reflection coefficient K_R

aids to capture more wave energy, which substantiate the law of conservation of energy. It is worth to witness the evidence to corroborate that the system is functioning as a motion trapping structure at the excitation frequencies which corresponds to wavenumber $kh = 1.2, 1, 0.9, 0.8$ and 0.75 by observing that complete wave reflection $K_R = 1.0$ is recorded at those excitation frequencies. However, the range of wavenumbers kh (frequency band width) for which the set threshold value of $K_R \leq 0.5$ is achieved and the corresponding minimum and maximum capture width ratio η_e for different values of B/h considered in the study is depicted in Table 3.2. Results from Table 3.2 indicates that the frequency band width increases with increase in relative structural width up to a value of $B/h = 1$, thereafter it decreases.

Table 3.2: Range of wavenumbers kh for which $K_R \leq 0.5$ and the corresponding minimum and maximum capture width ratio η_e for different values of B/h

Relative structural width B/h	Range of wavenumbers kh for which $K_R \leq 0.5$	Percentage of capture width ratio η_e	
		Maxima	Minima
0.25	$2.30 \leq kh \leq 2.75$	69.50%	97.00%
0.50	$1.80 \leq kh \leq 2.40$	68.00%	99.99%
1.00	$1.40 \leq kh \leq 2.05$	66.10%	99.95%
1.50	$1.20 \leq kh \leq 1.80$	65.60%	99.91%
	$0.35 \leq kh \leq 0.50$	63.91%	67.20%
2.00	$1.05 \leq kh \leq 1.60$	65.80%	99.99%
	$0.25 \leq kh \leq 0.50$	64.68%	75.12%

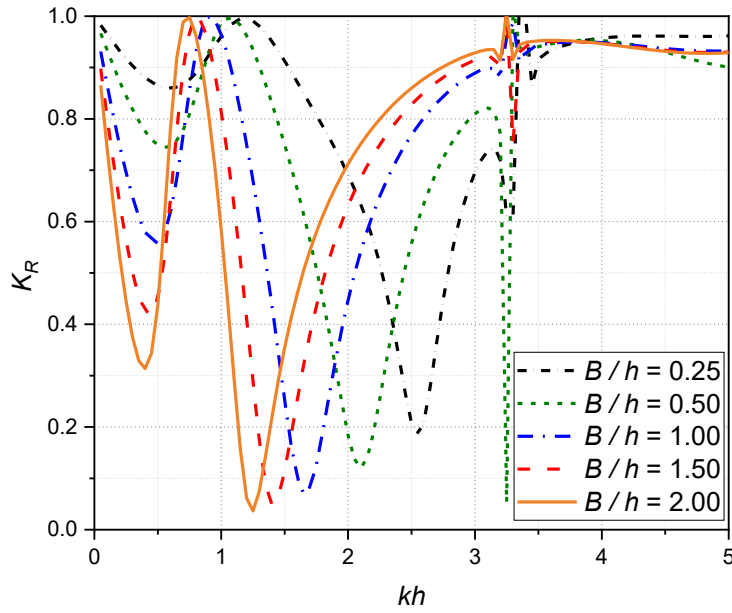


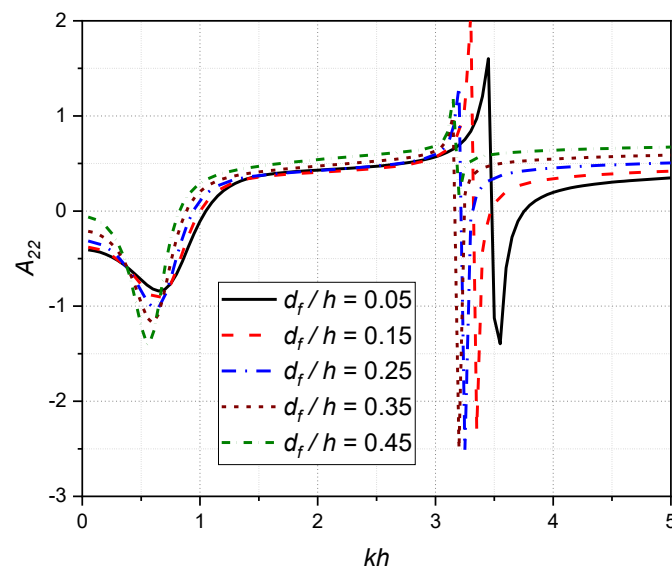
Fig. 3.18: Variation of the wave reflection coefficient K_R versus kh for various values of relative structural width B/h .

3.18.2 Effect of Relative Structural Draft

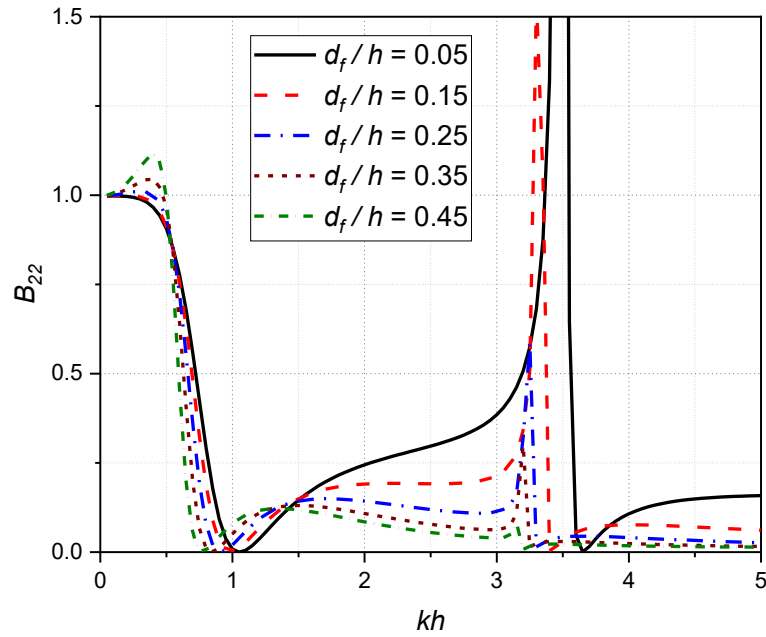
The parameters that influence the hydrodynamic coefficients, performance and its WEC capturing efficiency of the system are examined by varying the relative structural draft d_f/h between 0.05 to 0.45 while maintaining a constant relative structural width $B/h = 1.0$ and opting PTO damping $\lambda_{PTO} = \lambda_{optimal}$. The resulting hydrodynamic coefficients (A_{22} and B_{22}), heave amplitude operator H_{RAO} , capture width ratio η_e , and wave reflection coefficient K_R against the non-dimensional wavenumber kh in the presence of seawall having $C_R = 1.0$ are presented in Fig. (3.19-3.21) respectively for various values of relative structural draft d_f/h varying between 0.05 to 0.45.

The effect of varying relative structural depth d_f/h of the WEC integrated with PRFB between 0.05 and 0.45 while retaining the structural width $B/h = 1.0$ on heave added mass A_{22} , radiation damping coefficient B_{22} and heave amplitude operator H_{RAO} are shown in Fig. 3.19 (a, b and c) respectively. Although the trends in Fig. 3.19(a and b) and Fig. 3.16(a and b) are identical in nature, the hydrodynamic coefficients (A_{22} and B_{22}) in Fig. 3.19(a and b) are much lower in magnitude as compared to those in Fig. 3.16(a and b). The reason for this is that increasing the relative structural width B/h widens the wetted surface, which captures more heave radiation force, resulting in a stronger influence on amplifying the magnitudes of heave added mass A_{22} and radiation damping coefficient B_{22} . However, when the relative structural depth d_f/h increases, the wetted surface remains unchanged, and the water wave pressure that changes along the water depth lends little contribution to amplify the heave radiation

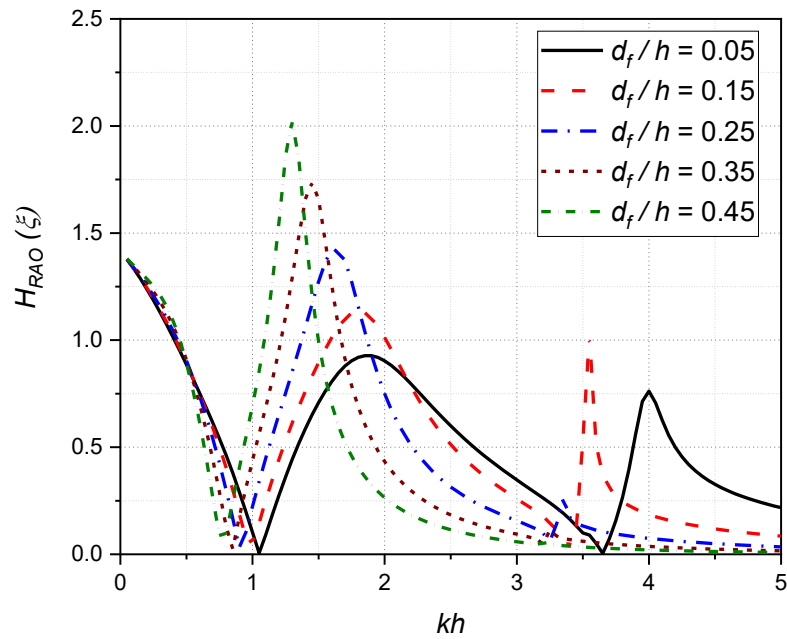
forces. As a result of the fact that wave energy is largely concentrated at the free surface as we move to the deep sea. The amplification in the magnitude of heave added mass A_{22} and the radiation damping coefficient B_{22} are relative more intense in the deep sea region than in the shallow water region, as shown in Fig. 3.19 (a and b). Moreover, varying the relative structural draft d_f / h from 0.05 to 0.45 while maintaining a constant relative structural width $B / h = 1.0$, the hydrodynamic restoring force C remains constant, however the mass changes naturally, resulting in a change in the fundamental natural frequency ω_n of the system and influence to shift the hydrodynamic coefficients A_{22} and B_{22} towards lower wavenumber kh . This may be one of the reasons as to why in Fig. 3.19(c) the resonant peaks of heave amplitude operator H_{RAO} is increasing with increasing relative structural depth d_f / h and a non-zero values are obtained for $d_f / h > 0.25$. The effect of increase in structural draft d_f / h from 0.05 to 0.45 on heave amplitude operator H_{RAO} is almost negligible in shallow water depth region, whereas multiple cross-overs indicating increasing and decreasing trend at different wavenumbers kh are observed in intermediate and deep-sea state region, for the same reason as applicable to heave radiation coefficients.



(a)



(b)



(c)

Fig. 3.19: Variation of the (a) heave added mass A_{22} , (b) radiation damping coefficient B_{22} and (c) heave amplitude operator H_{RAO} versus kh for various values of relative structural depth d_f/h .

Table 3.3 shows the percentage variation of area under the capture width ratio η_e for the curves corresponding to Fig. 3.20 for various values of relative structural depth d_f/h ranging from

0.05 to 0.45 and the heave added mass A_{22} are obtained from Fig. 2.19 (a) for wavenumber kh corresponding to maximum heave response operator H_{RAO} from Fig. 3.19(c). Although increasing the relative structural draft d_f/h from 0.05 to 0.45 while maintaining a constant relative structural width $B/h = 1.0$ results in no reduction in global maxima of capture width ratio η_e , except for the case where $d_f/h = 0.45$ decreases by 45%, the area under the capture width ratio η_e curve decreases significantly with increasing relative structural draft d_f/h as illustrated in Table 3.1. The reason that $d_f/h = 0.45$ could not achieve its global maximum of capture with ratio $\eta_e = 99.99\%$ as it did with lower relative structural draft's d_f/h is that of low excitation frequency caused by change in fundamental natural frequency ω_n , wherein for a given displacement ξ refer Eq. (2.22) if both the heave added mass A_{22} , as well as the system's mass M are increasing, and the radiation damping coefficient B_{22} is reducing, then λ_{PTO} has to decrease resulting to reduction in capture width ratio η_e . Furthermore, as the amplitudes of the heave response operator H_{RAO} increase for increasing the relative structural draft's d_f/h , as seen in Fig. 3.19 (c), not only does the capture width ratio η_e decrease, but it also narrows the response range (frequency bandwidth kh), resulting in a decrease in the percentage area under the capture width ratio η_e curve, as shown in Table 3.3.

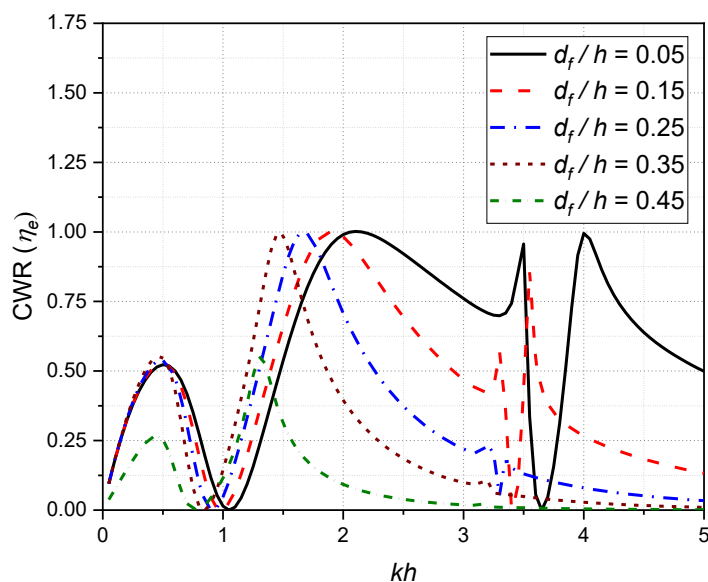


Fig. 3.20: Variation of the Capture width ratio η_e versus kh for various values of relative structural depth d_f/h .

Table 3.3: Percentage area under the curve of CWR (η_e), natural frequency (ω_n) and wavenumber (kh) corresponding to excitation frequency.

Structural draft (d_f / h)	Width to depth ratio (B / d_f)	Mass of the system (M) kg	Heave added mass coefficient (A_{22})	Natural frequency (ω_n)	Wavenumber corresponding to excitation frequency (kh)	Percentage area under the CWR (η_e) curve
0.05	20.00	51.250	428.797	4.577	2.14	59.99%
0.15	6.67	153.750	424.160	4.171	1.80	43.75%
0.25	4.00	256.250	402.051	3.908	1.65	30.95%
0.35	2.86	358.750	413.351	3.609	1.45	23.71%
0.45	2.22	461.250	440.169	3.340	1.30	8.89%

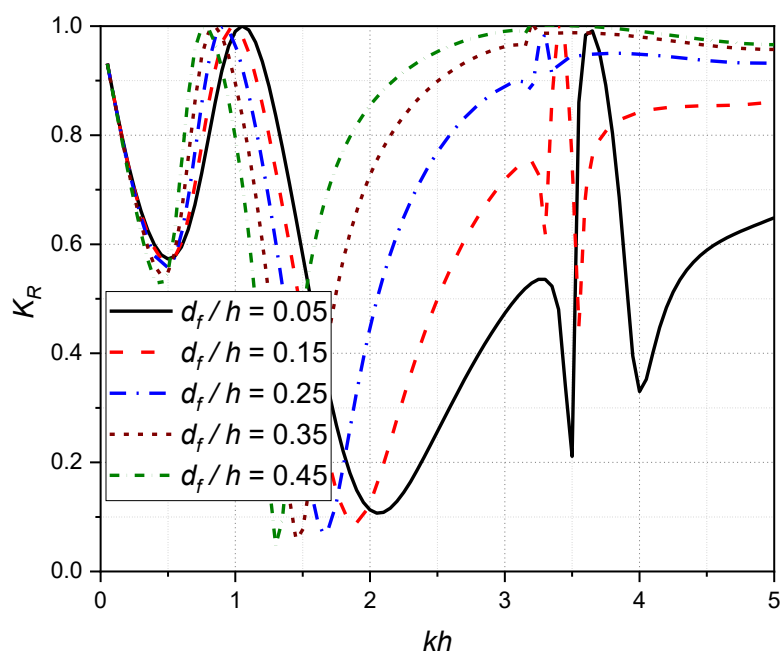


Fig. 3.21: Variation of the wave reflection coefficient K_R versus kh for various values of relative structural depth d_f / h .

From the Fig. 3.21, as deeper the draft d_f / h of the PRFB, the float stability of the system increases, resulting an increase in wave reflection coefficient K_R as well reduction in the motion responses as is evident in Fig. 3.19(c), except at those wavenumbers kh which corresponds to excitation frequency ($1.0 \leq kh \leq 2.0$). However, at wavenumbers $kh = 0.75$, 0.85 , 1.0 and 1.05 the wave reflection coefficient $K_R \approx 1.0$ as well as the heave added mass A_{22} attains negative maximum values and the corresponding heave radiation damping coefficient attains zero value which indicates that the WEC integrated with PRFB will be operating as motion trapping structure. As the wave reflection coefficient K_R is mirrored

vertically as the trend lines of capture width ratio η_e , the frequency band width kh for which the wave reflection coefficient $K_R \leq 0.5$ is obtained shown in Table 3.4, not only reduces with increasing relative structural draft d_f/h but also shift's towards lower wavenumber kh indicating the motion response and hydrodynamic coefficients are controlled by the damping of the system.

Table 3.4: Range of wavenumbers kh for which $K_R \leq 0.5$ and the corresponding minimum and maximum capture width ratio η_e for different values of d_f/h

Relative structural draft d_f/h	Range of wavenumbers kh for which $K_R \leq 0.5$	Percentage of capture width ratio η_e	
		Maxima	Minima
0.05	$1.60 \leq kh \leq 3.05$	67.97%	99.99%
0.15	$1.50 \leq kh \leq 2.50$	65.95%	99.99%
0.25	$1.40 \leq kh \leq 2.05$	66.10%	99.95%
0.35	$1.30 \leq kh \leq 1.70$	69.02%	99.55%
0.45	$1.15 \leq kh \leq 1.50$	29.14%	55.30%

3.19 CONCLUSIONS

Hydrodynamic performance as a costal/structure protecting structure as well as energy capture efficiency capabilities of a hybrid system composed of a WEC integrated with PRFB in presence of a vertical seawall of varying porosity, is analysed using boundary element method using linear small amplitude wave theory. To analyse the efficiency of a hybrid system with and without a seawall, the effect of different physical factors such as relative structural width B/h , relative structural draft d_f/h , separation between PRFB and the seawall S/λ , and change in WEC PTO damping coefficient λ_{PTO} are analyzed. The following outcomes are drawn about the WEC integrated to a PRFB's appropriateness as a hybrid system:

- In comparison to a WEC integrated with PRFB with no seawall condition $C_R = 0$, where the frequency bandwidth is in the range of shallow water to deep sea region ($0.5 \leq kh \leq 3$) for which the capture width ratio η_e is at least 20% and can go up to a maximum of 50%, the presence of seawall on the lee side of WEC integrated with PRFB certainly aids in amplifying the capture width ratio η_e much above the threshold

value of $\eta_e \geq 20\%$, but at the cost of narrowing in frequency bandwidth with increasing C_R . Moreover, for the reflection coefficient $C_R \geq 0.5$, the criteria of at least $\eta_e \geq 20\%$ is not satisfied for wavenumber $0.7 \leq kh \leq 1.1$ where the heave response amplitude (ξ) are suppressed due to the phenomena that system is operating as no motion structure, indicating full wave reflection coefficient $K_R = 1.0$. However, impact of the wave-induced horizontal force F_{WALL} on the partially reflecting seawall diminishes with increasing porosity by lowering C_R of the seawall.

- The presence of seawall on the leeward side of WEC integrated with PRFB has negligible influence on its dynamic heave responses in short wave regime $kh \geq 2.25$, as a result the WEC efficiency η_e is much lower than the set threshold value of 20%, corresponding the wave reflection coefficient $K_R > 0.5$.
- By customising the distance S/λ between the WEC integrated with PRFB and the seawall, it is feasible to achieve the target wave conversion efficiency η_e of at least more than 50% without going over the set threshold value wave reflection coefficient $K_R \leq 0.5$. As a result, there is sufficient scalability for a hybrid system to be chosen based on the site requirements without sacrificing hydrodynamic performance or WEC efficiency.
- When the WEC damping coefficient λ_{PTO} is increased up to a value of $\lambda_{PTO} = \lambda_{optimal}$, the capture width ratio η_e increases, thereafter any increase in λ_{PTO} beyond its $\lambda_{optimal}$ value, the capture width ratio η_e reduces for all values of nondimensional wavenumber kh . As a result, it is stated that the value of WEC PTO damping $\lambda_{PTO} = \lambda_{optimal}$ is an ideal value for an WEC integrated with PRFB in presence of a seawall of any porosity.
- Increasing relative structural width B/h while maintaining a constant structural draft d_f/h agitates the system to behave as a motion trapping structure at particular wave excitation frequencies, signifying a full wave reflection coefficient $K_R = 1.0$, when the heave response operator $H_{RAO} = 0$, negative amplitude of heave added mass A_{22} , and a heave radiation damping $B_{22} = 0$ are all achieved simultaneously.
- Any increase in relative structural width B/h over the minimum required triggers a significant increase in heave added mass A_{22} and radiation damping B_{22} , indicating that inherent system properties such as system's mass M and heave added mass A_{22} dominate motion responses H_{RAO} and result in a reduction in area under the efficiency curve (lowering capture width ratio η_e). However, increasing relative structural width B/h leads to lowering in fundamental natural frequency ω_n thereby shifting the range

of wavenumbers kh from deep sea region to shallow water depth region as well as reducing the frequency bandwidth, for which $K_R \leq 0.5$.

- Increasing the relative structural draft d_f / h for a constant structural width $B / h = 1.0$ results in an increase in heave response operator H_{RAO} amplitudes, resulting in a drop in capture width ratio η_e and a narrowing of the energy efficiency frequency bandwidth followed by a corresponding increase in wave reflection coefficient K_R .
- As the hydrodynamic restoring force C is independent of structural draft d_f / h of the system, the motion responses H_{RAO} and hydrodynamic coefficients (A_{22} and B_{22}) are controlled by the damping of the system indicating higher efficiency with broader frequency bandwidth as compare to increase in relative width B / h . However, a small shift in the range of wavenumbers kh is observed due to change in fundamental natural frequency ω_n .

CHAPTER 4

HYDRODYNAMIC PERFORMANCE OF OSCILLATING WATER COLUMN WEC INTEGRATED INTO H-TYPE BREAKWATER

4.1 THEORETICAL FORMULATION

The theoretical analysis of OWC integrated into H-type breakwater is performed using the Boundary Element Method (BEM) as in Fig.1. A 2D coordinate system is considered with x-axis considered as horizontal, and y-axis, vertically downward negative. The front wall of the H-type breakwater is located with the OWC device. The OWC is carved into the H-type breakwater such that its opening on the front wall of width D_2 is at a depth of $1.25 D_1$, where D_1 is the draft of the H-breakwater. The width of the breakwater B_1 and the width of the “bridge” of the H-type breakwater is B_2 considered as. The breakwater is held in place with piles supporting at the bottom. The device extends infinitely in the z-axis, which means that its dimension in that direction is very large in comparison to the wavelength of waves. The chamber of the OWC is not a vertical column, but instead a mirrored “J” shape, with the width D_1 being maintained all throughout till the top opening of the OWC chamber. The Wells turbine is fitted at top of the chamber, directly over the internal free surface. The external free surface extends both ways from outside the chamber, i.e., one from the back wall and one from the top wall. The Boundary Element Method (BEM) is employed and the external free surfaces is assumed to be finite. Hence, two auxiliary vertical boundaries are considered, Γ_{in} at $x = 0$ and Γ_{out} at “ h ” distance behind the H-type breakwater.

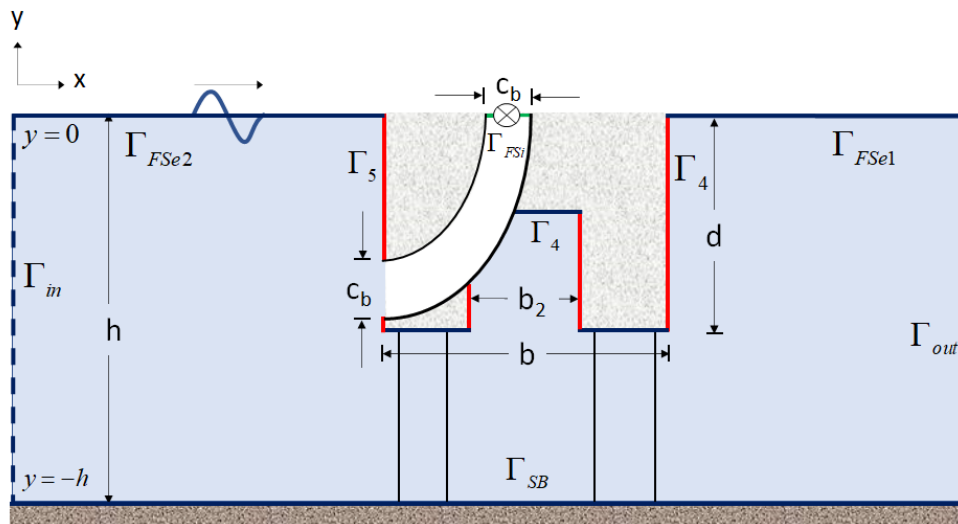


Fig. 1: Schematic representation of pile restrained OWC device integrated with H-type breakwater.

Based on the assumptions of linear wave theory, the fluid being inviscid, incompressible, irrotational and time-harmonic with angular frequency ω , the velocity potential exists, and is of the form $\Phi(x, y, t) = \text{Re}\{\phi(x, y)e^{-i\omega t}\}$. Therefore, $\phi(x, z)$ satisfies the Laplace equation

$$\frac{\partial^2 \phi}{\partial x^2} + \frac{\partial^2 \phi}{\partial y^2} = 0. \quad (1)$$

The boundary conditions at the mean free surfaces $y = 0$ is given by

$$\frac{\partial \phi}{\partial n} = \frac{\omega^2}{g} \phi \text{ on } \Gamma_{FSe1} \text{ and } \Gamma_{FSe2}, \quad (2)$$

$$\frac{\partial \phi}{\partial n} = \frac{\omega^2}{g} \phi + \frac{i\omega p}{\rho g} \text{ on } \Gamma_{FSi}, \quad (3)$$

where, g is the gravitational acceleration and $\partial/\partial n$ represents normal derivative. The boundary condition on the rigid sea bed is given by

$$\frac{\partial \phi}{\partial n} = 0 \text{ on } \Gamma_{SB}. \quad (4)$$

The boundary conditions on the impermeable body of the OWC is given by

$$\frac{\partial \phi}{\partial n} = 0 \text{ on } \Gamma_4. \quad (5)$$

The total velocity potential $\phi(x, y)$ is decomposed into two parts (Evans, 1982), given by

$$\phi = \phi^S + \left(\frac{i\omega p}{\rho g} \right) \phi^R, \quad (6)$$

where, ϕ^S denotes the scattered velocity potential associated with the scattering of a plane incident wave in the absence of an imposed pressure on the internal free surface and ϕ^R denotes the radiated velocity potential, which is the solution to the radiation problem due to imposed pressure on the internal free surface. The scattered potential ϕ^S can be further decomposed into incident potential ϕ^I and diffracted potential ϕ^D . The incident potential can be obtained analytically as

$$\phi^I = \frac{i\omega}{k} \frac{\cosh k(h+y)}{\sinh kh} e^{-ikx}, \quad (7a)$$

where k_0 represents the wave number, and is the positive real root of the dispersion relation given by

$$\omega^2 = gk \tanh kh. \quad (7b)$$

The scattered velocity potential ϕ^S and radiated velocity potential ϕ^R satisfy the boundary condition Eq. (1)-(5), but the Eq. (2) is modified as

$$\frac{\delta \phi^S}{\delta n} = \frac{\omega^2}{g} \phi^S \text{ on } \Gamma_{FSe1}, \Gamma_{FSe2}, \Gamma_{FSi} \quad (8a)$$

$$\frac{\delta\phi^R}{\delta n} = \begin{cases} \frac{\omega^2}{g} \phi^R & \text{on } \Gamma_{FSe1}, \Gamma_{FSe2} \\ \frac{\omega^2}{g} \phi^R + 1 & \text{on } \Gamma_{FSi} \end{cases} \quad (8b)$$

The far-field boundary condition is given by

$$\begin{aligned} \phi^S(x, y) &= e^{ikx} f_0(k, y) + A_0^S e^{-ikx} f_0(k, y), \quad \text{as } x \rightarrow \infty, \\ \phi^R(x, y) &= A_0^R e^{-ikx} f_0(k, y), \quad \text{as } x \rightarrow -\infty, \end{aligned} \quad (9)$$

where, $f_0(k, y) = \frac{\cosh k(h+y)}{\cosh kh}$ and A_0^S and A_0^R are the coefficients associated with the

amplitude of the reflected and radiated waves at $x = -\infty$ respectively. As mentioned earlier, two auxiliary boundaries, Γ_{in} and Γ_{out} are considered at $x = 0$ and behind the back wall of OWC respectively. The boundaries are sufficiently far away from the OWC device and hence, the far-field boundary conditions as in Eq. (9) hold true. The entire structure along with the fictitious boundaries is considered to be located far from the shore so as not to be affected by wave reflection coming from the shore. A modified version of the far-field conditions is used in BEM, given by

$$\begin{aligned} \frac{\partial(\phi^S - \phi^I)}{\partial n} &= ik(\phi^S - \phi^I) \quad \text{on } \Gamma_{in} \text{ and } \Gamma_{out} \\ \frac{\partial\phi^R}{\partial n} &= ik\phi^R \quad \text{on } \Gamma_{in} \text{ and } \Gamma_{out} \end{aligned} \quad (10)$$

4.2 HYDRODYNAMIC PARAMETERS ASSOCIATED WITH OWC DEVICE

In this section, the relations and explicit expressions for various hydrodynamic parameters associated with the performance of OWC device are discussed. The time harmonic induced volume flux $Q(t) = \text{Re}\{qe^{-i\omega t}\}$ across the internal free surface (Evans and Porter, 1995), is given by

$$q = \int_{FSi} \frac{\partial\phi}{\partial y} dx = q^S - \frac{i\omega p}{\rho g} q^R \quad (11)$$

where q^S and q^R are the volume fluxes across the internal free surface F_{Si} for the scattering and radiation problems, respectively. The volume flux for the radiation problem can be further decomposed into real and imaginary parts as

$$\frac{i\omega p}{\rho g} q^R = -(\bar{B} - i\bar{A})p \quad (12)$$

where \bar{A} and \bar{B} , are the radiation susceptance and radiation conductance parameters (Evans and Porter, 1995), and are analogous to the added mass and the radiation damping coefficients in a rigid body system respectively. The expressions for these two parameters are given by

$$\bar{A} = \frac{\omega}{\rho g} \text{Re}\{q^R\}, \quad \bar{B} = \frac{\omega}{\rho g} \text{Im}\{q^R\} \quad (13)$$

The volume flux through the turbine is assumed to be linearly proportional to the pressure drop across the internal free surface given by

$$q = \Lambda p \quad (14)$$

where, Λ is a real control parameter associated with the turbine characteristics. The mean rate of work done by the pressure force over one wave period is given by

$$W = \frac{1}{8} \frac{|q^s|^2}{\bar{B}} \left\{ \frac{4\Lambda\bar{B}}{(\Lambda + \bar{B})^2 + \bar{A}^2} \right\} \quad (15)$$

In the case of known values of \bar{A} and \bar{B} , the optimum value for Λ can be obtained as

$$\Lambda_{opt} = \sqrt{\bar{A}^2 + \bar{B}^2} \quad (16)$$

Hence, the maximum work done by the pressure force over one wave period is of the form

$$W_{max} = \frac{1}{8} \frac{|q^s|^2}{\bar{B}} \left\{ \frac{2\bar{B}}{\Lambda_{opt} + \bar{B}} \right\} \quad (17)$$

The available power over one wave period of a plane progressive of unit amplitude (Dean and Dalrymple, 1991), is given by

$$P_w = EC_g = \frac{\rho\omega k_0 A_0}{2}, \quad A_0 = \frac{2k_0 h + \sinh(2k_0 h)}{4k_0 \cosh^2(k_0 h)} \quad (18)$$

In order to obtain an explicit expression for the parameter \bar{B} , Green's second identity is applied on ϕ^R and its complex conjugate $\bar{\phi}^R$ over the whole domain bounded by $\Gamma = \Gamma_{in} \cup \Gamma_{SB} \cup \Gamma_{out} \cup \Gamma_{FSe1} \cup \Gamma_4 \cup \Gamma_{FSi} \cup \Gamma_{FSe2}$. Thus, summing up the contributions from all boundaries, we get

$$\bar{B} = \frac{\omega}{\rho g} k_0 \left(\frac{\omega^2}{g} \right) |A_0^R|^2 A_0 \quad (19)$$

The expression for scattered volume flux q^s can be written as

$$q^s = -2ik_0 \left(\frac{\omega^2}{g} \right) A_0^R A_0 \quad (20)$$

Using Eq. (18), (19) and (20), the relation between P_w and \bar{B} is obtained as

$$\bar{B} = \frac{|q^s|^2}{8P_w} \quad (21)$$

Thus, the efficiency η of the OWC device using Eq. (15) and (21) is given by

$$\eta = \frac{W}{P_w} = \frac{4\Lambda\bar{B}}{(\Lambda + \bar{B})^2 + \bar{A}^2} \quad (22)$$

The maximum efficiency η_{max} using Eq. (17) and (21), is given by

$$\eta_{max} = \frac{2\bar{B}}{\Lambda_{opt} + \bar{B}} \quad (23)$$

The dimensionless form of the parameters \bar{A} and \bar{B} (Evans and Porter, 1995), is given by

$$\mu = \frac{\rho g}{\omega b} \bar{A} \text{ and } \nu = \frac{\rho g}{\omega b} \bar{B} \quad (24)$$

Consequently, using Eq. (23) and (24), the dimensionless form of η_{max} is given by

$$\eta_{\max} = \frac{2\nu}{\nu + \sqrt{\nu^2 + \mu^2}} = \frac{2}{1 + \sqrt{1 + \left(\frac{\mu}{\nu}\right)^2}} \quad (25)$$

Finally, the reflection and transmission coefficients are given by

$$K_r = \left| \frac{R_0}{I_0} \right| \text{ and } K_t = \left| \frac{T_0}{I_0} \right| \quad (26)$$

where, I_0 is the incident wave amplitude, R_0 is the reflected wave amplitude and T_0 is the transmitted wave amplitude at the input and output boundaries. The dissipation coefficient is given by

$$K_d = \sqrt{1 - K_r^2 - K_t^2} \quad (27)$$

4.3 NUMERICAL SOLUTION BY USING BOUNDARY ELEMENT METHOD

In this section, the solution approach for the wave interaction with integrated OWC with breakwater is analysed using Boundary Element Method (BEM). The fundamental solution and Green's second identity are the pre-requisites for BEM. To obtain the solution for the boundary value problem, the weighted residue and Green-Gauss theorem is applied to the Laplace equation as in Eq. (1). The generalised form of boundary integral equation is expressed as

$$c(P) \cdot \phi(P) + \int_{\Gamma} \phi \cdot \frac{\partial G}{\partial n} d\Gamma = \int_{\Gamma} G \cdot \frac{\partial \phi}{\partial n} d\Gamma \quad (28)$$

where ϕ is the unknown flow potential, $\partial\phi/\partial n$ is the derivative of the potential relative to normal unit vector on the boundary, G is the fundamental solution to Laplace equation and Γ denotes the computational domain boundary. The free term coefficient $c(P)$ depends on the shape of the boundary and is given by

$$c(P) = \begin{cases} 1 & \text{for } P \equiv (\xi, \tau) \in \Omega, \\ \frac{1}{2} & \text{for } P \equiv (\xi, \tau) \in \Gamma \text{ and } \Gamma \text{ is smooth at } P, \\ 0 & \text{for } P \equiv (\xi, \tau) \text{ outside } \Omega \end{cases} \quad (29)$$

The fundamental solution G , known as free-space Green's function, and its normal derivative $\partial G/\partial n$ corresponding to Laplace equation in two dimensions are given by

$$G = \frac{1}{2\pi} \ln r \quad \text{and} \quad \frac{\partial G}{\partial n} = \frac{1}{2\pi r} \frac{\partial r}{\partial n} \quad (30)$$

where r is the distance between the field point $X(x, y)$ and the source point $P(\xi, \tau)$ given by

$$r = \sqrt{(\xi^2 - x^2) + (\tau^2 - y^2)}. \quad (31)$$

The boundary is assumed to be divided into ' N ' constant elements. The value of ϕ and G are assumed to be constant over each element and assumed to be equal to the value at the mid-element node. Further, Eq. (28) is discretised into ' N ' constant boundary elements before applying the boundary conditions, and is expressed as

$$\frac{1}{2}\phi(P) + \sum_{j=1}^N \left(\int_{\Gamma_j} \phi_j \frac{\partial G}{\partial n} d\Gamma \right) = \sum_{j=1}^N \left(\int_{\Gamma_j} G_j \frac{\partial \phi}{\partial n} d\Gamma \right), \quad (32)$$

where, Γ_j is the boundary in the j^{th} element. Now, considering $\int_{\Gamma_j} \frac{\partial G}{\partial n} d\Gamma - \frac{1}{2}\delta_{ij} = H_{ij}$, where δ_{ij} is the Kronecker delta defined as $\delta_{ij} = 0$ for $i \neq j$ and $\delta_{ij} = 1$ for $i = j$, and $\int_{\Gamma_j} G_j d\Gamma = Q_{ij}$,

the discretized equation can be rewritten as

$$-\frac{1}{2}\phi(P) + \sum_{j=1}^N (H_{ij}\phi_j) = \sum_{j=1}^N \left(Q_{ij} \frac{\partial \phi}{\partial n} \right). \quad (33)$$

The line integrals H_{ij} and Q_{ij} represent the influence functions between element i at which the fundamental solution is applied and any other element j under consideration. On applying the boundary conditions given in Eq. (2), (4), (5), (8) and (10) in the discretized equation, the integral equation for radiated potential is derived as

$$\begin{aligned} -\frac{1}{2}\phi^R + \int_{\Gamma_{SB}} \phi_{SB}^R \frac{\partial G}{\partial n} d\Gamma + \int_{\Gamma_{out}} \phi_{out}^R \left(\frac{\partial G}{\partial n} - ik_0 G \right) d\Gamma + \int_{\Gamma_{FS1}} \phi_{FS1}^R \left(\frac{\partial G}{\partial n} - \frac{\omega^2}{g} G \right) d\Gamma \\ + \int_{\Gamma_4} \phi_4^R \frac{\partial G}{\partial n} d\Gamma + \int_{\Gamma_{FSi}} \phi_{FSi}^R \left(\frac{\partial G}{\partial n} - \frac{\omega^2}{g} G \right) d\Gamma + \int_{\Gamma_6} \phi_6^R \frac{\partial G}{\partial n} d\Gamma \\ + \int_{\Gamma_{FS2}} \phi_{FS2}^R \left(\frac{\partial G}{\partial n} - \frac{\omega^2}{g} G \right) d\Gamma + \int_{\Gamma_{in}} \phi_{in}^R \left(\frac{\partial G}{\partial n} - ik_0 G \right) d\Gamma = \int_{\Gamma_{FSi}} G d\Gamma. \end{aligned} \quad (34)$$

Similarly, using boundary conditions on Eq. (32), the integral equation for scattered potential is derived as

$$\begin{aligned} -\frac{1}{2}\phi^S + \int_{\Gamma_{SB}} \phi_{SB}^S \frac{\partial G}{\partial n} d\Gamma + \int_{\Gamma_{out}} \phi_{out}^S \left(\frac{\partial G}{\partial n} + ik_0 G \right) d\Gamma + \int_{\Gamma_{FS1}} \phi_{FS1}^S \left(\frac{\partial G}{\partial n} - \frac{\omega^2}{g} G \right) d\Gamma \\ + \int_{\Gamma_4} \phi_4^S \frac{\partial G}{\partial n} d\Gamma + \int_{\Gamma_{FSi}} \phi_{FSi}^S \left(\frac{\partial G}{\partial n} - \frac{\omega^2}{g} G \right) d\Gamma + \int_{\Gamma_6} \phi_6^S \frac{\partial G}{\partial n} d\Gamma + \int_{\Gamma_{FS2}} \phi_{FS2}^S \left(\frac{\partial G}{\partial n} - \frac{\omega^2}{g} G \right) d\Gamma \\ + \int_{\Gamma_{in}} \phi_{in}^S \left(\frac{\partial G}{\partial n} + ik_0 G \right) d\Gamma = \int_{\Gamma_{in}} G \left(\frac{\partial \phi^I}{\partial n} - ik_0 \phi^I \right) d\Gamma + \int_{\Gamma_{out}} G \left(\frac{\partial \phi^I}{\partial n} - ik_0 \phi^I \right) d\Gamma. \end{aligned} \quad (35)$$

Now, the integral equation for the radiated and scattered potential can be discretised into the following form given by

$$\begin{aligned} \sum_{j=1}^{N_{SB}} (H_{ij}) \phi_j^R \Big|_{\Gamma_{SB}} + \sum_{j=1}^{N_{out}} (H_{ij} - ik_0 Q_{ij}) \phi_j^R \Big|_{\Gamma_{out}} + \sum_{j=1}^{N_{FS1}} \left(H_{ij} - \frac{\omega^2}{g} Q_{ij} \right) \phi_j^R \Big|_{\Gamma_{FS1}} \\ + \sum_{j=1}^{N_4} (H_{ij}) \phi_j^R \Big|_{\Gamma_4} + \sum_{j=1}^{N_{FSi}} \left(H_{ij} - \frac{\omega^2}{g} Q_{ij} \right) \phi_j^R \Big|_{\Gamma_{FSi}} + \sum_{j=1}^{N_6} (H_{ij}) \phi_j^R \Big|_{\Gamma_6} \\ + \sum_{j=1}^{N_{FS2}} \left(H_{ij} - \frac{\omega^2}{g} Q_{ij} \right) \phi_j^R \Big|_{\Gamma_{FS2}} + \sum_{j=1}^{N_{in}} (H_{ij} - ik_0 Q_{ij}) \phi_j^R \Big|_{\Gamma_{in}} = \sum_{j=1}^{N_{FSi}} Q_{ij} \Big|_{\Gamma_{FSi}}. \end{aligned} \quad (36)$$

$$\begin{aligned}
& \sum_{j=1}^{N_{SB}} (H_{ij}) \phi_j^S \Big|_{\Gamma_{SB}} + \sum_{j=1}^{N_{out}} (H_{ij} + ik_0 Q_{ij}) \phi_j^S \Big|_{\Gamma_{out}} + \sum_{j=1}^{N_{FS1}} \left(H_{ij} - \frac{\omega^2}{g} Q_{ij} \right) \phi_j^S \Big|_{\Gamma_{FS1}} \\
& + \sum_{j=1}^{N_4} (H_{ij}) \phi_j^S \Big|_{\Gamma_4} + \sum_{j=1}^{N_{FSi}} \left(H_{ij} - \frac{\omega^2}{g} Q_{ij} \right) \phi_j^S \Big|_{\Gamma_{FSi}} + \sum_{j=1}^{N_6} (H_{ij}) \phi_j^S \Big|_{\Gamma_6} + \sum_{j=1}^{N_{FS2}} \left(H_{ij} - \frac{\omega^2}{g} Q_{ij} \right) \phi_j^S \Big|_{\Gamma_{FS2}} \\
& + \sum_{j=1}^{N_{in}} (H_{ij} + ik_0 Q_{ij}) \phi_j^S \Big|_{\Gamma_{in}} = \sum_{j=1}^{N_{in}} \left(\frac{\partial \phi^I}{\partial n} - ik_0 \phi^I \right) Q_{ij} \Big|_{\Gamma_{in}} + \sum_{j=1}^{N_{out}} \left(\frac{\partial \phi^I}{\partial n} - ik_0 \phi^I \right) Q_{ij} \Big|_{\Gamma_{out}} .
\end{aligned} \quad (37)$$

The values of H_{ij} and Q_{ij} are calculated using a standard Gaussian quadrature (Katsikadelis, 2016). Finally, using the method of point collocation, in which the source point $P(\xi, \tau)$ runs over each boundary element, the discretized radiated and scattered potential as in Eq. (36) and (37) can be written as

$$\begin{aligned}
& [H][\phi^R] \Big|_{\Gamma_{SB}} + ([H] - ik_0 [Q])[\phi^R] \Big|_{\Gamma_{out}} + \left([H] - \frac{\omega^2}{g} [Q] \right) [\phi^R] \Big|_{\Gamma_{FS1}} \\
& + [H][\phi^R] \Big|_{\Gamma_4} + \left([H] - \frac{\omega^2}{g} [Q] \right) [\phi^R] \Big|_{\Gamma_{FSi}} + [H][\phi^R] \Big|_{\Gamma_6} \\
& + \left([H] - \frac{\omega^2}{g} [Q] \right) [\phi^R] \Big|_{\Gamma_{FS2}} + ([H] - ik_0 [Q])[\phi^R] \Big|_{\Gamma_{in}} = [Q] \Big|_{\Gamma_{FSi}} .
\end{aligned} \quad (38)$$

$$\begin{aligned}
& [H][\phi^S] \Big|_{\Gamma_{SB}} + ([H] + ik_0 [Q])[\phi^S] \Big|_{\Gamma_{out}} + \left([H] - \frac{\omega^2}{g} [Q] \right) [\phi^S] \Big|_{\Gamma_{FS1}} \\
& + [H][\phi^S] \Big|_{\Gamma_4} + \left([H] - \frac{\omega^2}{g} [Q] \right) [\phi^S] \Big|_{\Gamma_{FSi}} + [H][\phi^S] \Big|_{\Gamma_6} + \left([H] - \frac{\omega^2}{g} [Q] \right) [\phi^S] \Big|_{\Gamma_{FS2}} \\
& + ([H] + ik_0 [Q])[\phi^S] \Big|_{\Gamma_{in}} = \left(\frac{\partial \phi^I}{\partial n} - ik_0 \phi^I \right) [Q] \Big|_{\Gamma_{in}} + \left(\frac{\partial \phi^I}{\partial n} - ik_0 \phi^I \right) [Q] \Big|_{\Gamma_{out}} .
\end{aligned} \quad (39)$$

The velocity potentials ϕ^S and ϕ^R are the unknown scattered and radiated velocity potentials to be determined. In Eq. (38-39), Γ_{in} , Γ_{SB} , Γ_{out} , Γ_{FS1} , Γ_4 , Γ_{FSi} , Γ_{FS2} corresponds to the boundaries of the far-field, free surface, seabed, floating structure and the interface. Once the unknown potentials are obtained at the nodes of the discretized boundary elements, the hydrodynamic quantities of engineering interest are obtained.

2.3 NUMERICAL ANALYSIS USING ANSYS-AQWA

The numerical investigation of wave interaction with integrated OWC with breakwater is performed using Ansys-AQWA and the hydrodynamic parameters are analysed using the potential flow theory. The linear superposition can be used to get the velocity potential within fluid domain using first order potential theory of diffraction and radiation of waves. The fluid flow surrounding a floating body can be written as

$$\Phi(\vec{X}, t) = a\varphi(\vec{X})e^{-i\omega t}. \quad (40)$$

The dispersion relation connects the wave number and frequency is given by

$$\omega^2 = gk \tanh kh. \quad (41)$$

Considering the potential due to incident, diffraction and radiation waves, the total first order hydrodynamic force can be expressed as

$$F_j = \left[(F_{lj} + F_{dj}) + \sum_{i=1}^6 F_{rji} x_i \right], \quad (42)$$

where $j=1,2,\dots,6$ are the respective global direction such as $j=1$ is for x -direction, $j=2$ is for y -direction, $j=3$ is for z -direction, $j=4$ is for rotation in r_x -direction, $j=5$ is for rotation in r_y -direction and $j=6$ is for rotation in r_z -direction, F_{lj} is j -th Froude-Krylov force due to incoming wave, F_{dj} is j -th diffracting force due to diffraction wave and F_{rji} is the j -th radiation force generated as a radiative result of i -th body motion. In the present study the floating integrated OWC breakwater is pile restrained, so the floating body is fixed in position and there is no motion in body. Thus, F_{rji} will be zero, so the total hydrodynamic force will be consisting of the wave excitation force. Wave exciting force is consisting of the Froude-Krylov force and the diffraction force and are given by

$$F_{lj} = -i\omega\rho \int_{S_0} \varphi_l n_j dS, \quad (43)$$

and

$$F_{dj} = -i\omega\rho \int_{S_0} \varphi_d n_j dS, \quad (44)$$

where S_0 is surface below water level and n_j is unit normal vector of structure surface. The non-dimensional excitation force coefficient EFC_j is obtained as

$$EFC_j = \begin{cases} \frac{|F_j/A_{in}|}{\rho g A_{CWP}} & \text{for } j=1,2,3, \\ \frac{|F_j/A_{in}|}{0.5\rho g A_{CWP} b} & \text{for } j=4,5,6, \end{cases} \quad (45)$$

where A_{in} is incident wave amplitude, A_{CWP} is cross-sectional area of cutting water plane and b is width of breakwater. The hydrodynamic performance of breakwater integrated with oscillating water column in terms of its power capture efficiency is studied using Ansys-Fluent. The Reynolds-Averaged Navier-Stokes (RANS) equations are used and the power capture efficiency is calculated. The power capture efficiency is solved using two-dimensional numerical modelling using the volume of fluid methods (VOF) for two-phase fluid flow. The governing equations are the continuity equations and RANS equations. In the case of 2D axisymmetric geometries, the continuity equation is given by

$$\frac{\partial \rho}{\partial t} + \frac{\partial}{\partial x}(\rho v_x) + \frac{\partial}{\partial r}(\rho v_r) + \frac{\rho v_r}{r} = S_m, \quad (46)$$

where x is the axial coordinate, r is the radial coordinate, v_x is the axial velocity, v_r is the radial velocity, and S_m is the mass added to the continuous phase from the dispersed second phase and any user-defined source.

In the case of 2D axisymmetric geometries, the axial and radial momentum conservation equations are given by

$$\begin{aligned} \frac{\partial}{\partial t}(\rho v_x) + \frac{1}{r} \frac{\partial}{\partial x}(r \rho v_x v_x) + \frac{1}{r} \frac{\partial}{\partial r}(r \rho v_r v_x) = -\frac{\partial \rho}{\partial x} + \frac{1}{r} \frac{\partial}{\partial x} \left[r \mu \left(2 \frac{\partial v_x}{\partial x} - \frac{2}{3} (\nabla \cdot \vec{v}) \right) \right] \\ + \frac{1}{r} \frac{\partial}{\partial r} \left[r \mu \left(\frac{\partial v_x}{\partial r} + \frac{\partial v_r}{\partial x} \right) \right] + F_x, \end{aligned} \quad (47a)$$

$$\begin{aligned} \frac{\partial}{\partial t}(\rho v_r) + \frac{1}{r} \frac{\partial}{\partial x}(r \rho v_x v_r) + \frac{1}{r} \frac{\partial}{\partial r}(r \rho v_r v_r) = -\frac{\partial \rho}{\partial r} + \frac{1}{r} \frac{\partial}{\partial x} \left[r \mu \left(\frac{\partial v_r}{\partial x} + \frac{\partial v_x}{\partial r} \right) \right] \\ + \frac{1}{r} \frac{\partial}{\partial r} \left[r \mu \left(2 \frac{\partial v_r}{\partial r} - \frac{2}{3} (\nabla \cdot \vec{v}) \right) \right] - 2 \mu \frac{v_r}{r^2} + \frac{2}{3} \frac{\mu}{r} (\nabla \cdot \vec{v}) + \rho \frac{v_z^2}{r} + F_r, \end{aligned} \quad (47b)$$

where, $\nabla \cdot \vec{v} = \frac{\partial v_x}{\partial x} + \frac{\partial v_r}{\partial r} + \frac{v_r}{r}$ and v_z is the swirl velocity, F_x and F_r are external body forces.

On resolving just one set of momentum equations and keeping track of each fluid's volume fraction across the domain, the Volume of Fluid (VOF) model simulate two or more immiscible fluids. Under the VOF model, the open channel wave boundary conditions allow the simulation of the propagation of both regular and irregular waves, which is helpful for assessing wave kinematics and wave impact loads on moving objects and offshore structures. The open channel wave boundary conditions perform well with both small amplitude and finite amplitude wave theories. Considering the wave breaking or wave impacts on a structure, turbulence is a crucial physical process, and the Reynolds-averaged Navier-Stokes (RANS) equation is the governing equation for turbulence in Ansys-Fluent and is given by

$$\frac{\partial \rho}{\partial t} + \frac{\partial}{\partial x_i}(\rho u_i) = 0, \quad (48)$$

$$\frac{\partial}{\partial t}(\rho u_i) + \frac{\partial}{\partial x_j}(\rho u_i u_j) = -\frac{\partial \rho}{\partial x_i} + \frac{\partial}{\partial x_j} \left[\mu \left(\frac{\partial u_i}{\partial x_j} + \frac{\partial u_j}{\partial x_i} - \frac{2}{3} \delta_{ij} \frac{\partial u_l}{\partial x_l} \right) \right] + \frac{\partial}{\partial x_j}(-\rho \overline{u_i' u_j'}), \quad (49)$$

where, $\overline{u_i}$ and u_i' are the velocity components (mean and fluctuating), ρ is fluid density and μ is fluid viscosity. The turbulent flow model is used in this study of Shear-Stress Transport (SST) $k - \omega$ model. It is an improved model over the standard $k - \omega$ model, which is based on model transport equations for the specific dissipation rate ω and the kinetic energy of the turbulence k . SST $k - \omega$ model is suitable for free surface flows. The solver has pre-defined theories, which helps in the discretization of continuity and momentum equations. Among them, PREssure STaggering Option (PRESTO) scheme uses the discrete continuity balance for a staggered control volume about the face for pressure interpolation, and the SIMPLE algorithm enforces mass conservation and derives the pressure field through a link between velocity and pressure adjustments.

The variation in air velocity at a vertex point on the OWC outlet point and pressure inside the OWC chamber were recorded using Fluent modelling, and the efficiency of the power capture η of the OWC due to incident wave is obtained as

$$\eta = \frac{P_o}{P_i}, \quad (50)$$

where, P_o is power output due to airflow inside the OWC chamber and P_i is incident wave power. The expected absorbed power by OWC P_o (Singh et al., 2020) during test duration of t_d can be determined as

$$P_o = \frac{1}{t_d} \int_0^{t_d} p(t) A_o v(t) dt, \quad (51)$$

where, $p(t)$ is pressure variation over time of incident wave and $A_o v(t)$ is air flow rate due to oscillation of free water surface inside the chamber. $v(t)$ is airflow velocity and A_o is the cross-sectional area of the OWC chamber outlet. In order to mitigate the error in input power calculation due to loss of energy before it reaches the OWC chamber, the instantaneous energy flux is averaged over time to get the mean incident power P_i (Dean and Dalrymple, 1991) given by

$$P_i = \frac{1}{T} \int_t^{t+T} \int_{-h}^0 (p + \rho g z) u \, dz \, dt, \quad (52)$$

where, T is incident wave period, $(p + \rho g z)$ is dynamic pressure, u is water particle velocity in x -direction for zero wave incidence angle and it is given by

$$u = \frac{H}{2} \omega \frac{\cosh k(h+z)}{\sinh kh} \cos(kx - \omega t). \quad (53)$$

Further, simplification of the above equation of incident wave power leads to the expression of P_i for regular waves as

$$P_i = \frac{1}{8} \rho g H^2 C_g, \quad (54)$$

where, H is wave height, C_g is the group celerity given by

$$C_g = nC, \quad (55)$$

where, the factor n for shallow waters is $n=1$, for deep waters $n=0.5$, and for intermediate water depth

$$n = \frac{1}{2} \left[1 + \frac{4\pi h / \lambda}{\sinh(4\pi h / \lambda)} \right] \quad (56)$$

The results obtained from fluent modelling is further used to obtain the efficiency of OWC integrated into H-shape breakwater.

The shear force and bending moment along a neutral axis parallel to x -direction is calculated using AQWA, which is the summation of the following components, namely, external hydrodynamic force \vec{F}_f and moment \vec{M}_f , and gravitational force \vec{F}_g and moment \vec{M}_g with reference to the intersection point \vec{X}_0 given by

$$\vec{F}_f(\omega, x_0) = \iint_{S_x} (-p_T \vec{n}) dS \quad \text{and} \quad \vec{M}_f(\omega, x_0) = \iint_{S_x} [(\vec{X} - \vec{X}_0) \times (-p_T \vec{n})] dS. \quad (57)$$

$$\vec{F}_g(\omega, x) = \sum_{X=X_s}^x (0, 0, -m_j g) \quad \text{and} \quad \vec{M}_g(\omega, x) = \sum_{X=X_s}^x (\vec{X}_j - \vec{X}_0) \times (0, 0, -m_j g). \quad (58)$$

where, S_x is the wetted surface of the part from wave incidence point on structure X_s to the cross-section point where shear force and bending moment is being determined X_0 , p_T is total pressure including hydrostatic and hydrodynamic component, n is surface normal pointing toward fluid domain, m_j is the mass and \vec{X}_j is the geometric centre of the j -th section between X_s and X_0 .

2.4 NUMERICAL RESULTS AND DISCUSSIONS

In this section, the numerical results associated with the hydrodynamic performance of pile restrained OWC integrated H-type breakwater are plotted and discussed in detailed. Firstly, the validation of both numerical methods, BEM and Ansys-AQWA is performed by comparing results obtained using previously published results in the literature. Thereafter, the results associated with change in various geometrical properties of the hybrid setup are analysed.

2.5 VALIDATION OF THE NUMERICAL RESULTS

The present BEM model is validated by comparing the results obtained by Evans and Porter (1995). The bottom standing OWC is considered same as Evans and Porter (1995) with parameters $b/h=1$ and $a/h=1/4$. The maximum efficiency is plotted against the non-dimensional wave number kh and compared in Fig. 3.

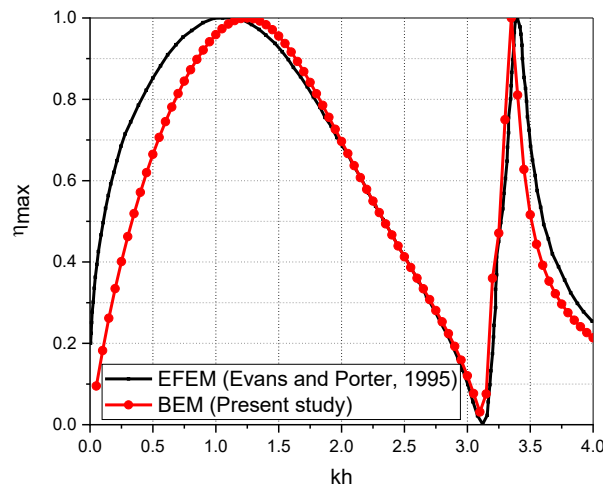


Fig. 3: Comparative study of maximum efficiency η_{\max} versus kh for bottom standing OWC.

It is observed that for the non-dimensional wave number within $0 \leq kh \leq 1$, the efficiency obtained using both methods show similar trend, but there is a slight right shift in the values obtained from the present study. For $1 \leq kh \leq 3$, the numerical values using both methods are same having slight variation at the extremes. Further, for $3 \leq kh \leq 4$, a slight shift in the

efficiency values can be observed. The present study using BEM approach gives reasonable and acceptable results for calculation of hydrodynamic properties of OWC device.

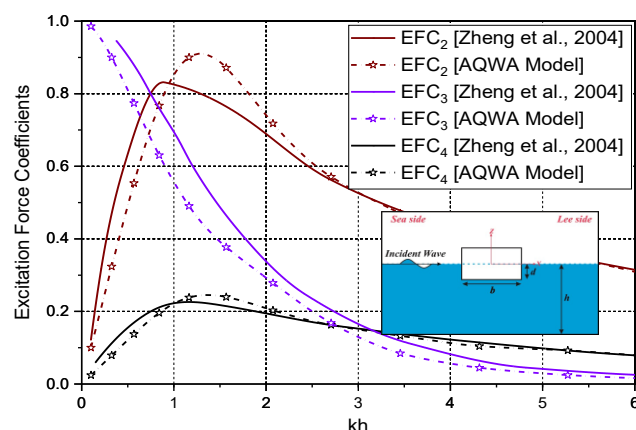


Fig. 4: Variation of wave excitation force coefficients EFC_j versus kh in sway, heave and roll motions.

The study performed for the floating rectangular buoy as in Zheng et al. (2004) is validated with Ansys model in Fig. 4 for the floating breakwater having $h = 2d$ and $b = 2d$. The wave is considered to be regular wave with zero incident angle. The values of EFC_j obtained for sway, heave and roll motions are plotted against kh . Minor variations in EFC_2 is observed within $1.2 < kh < 1.9$ but apart from this, for all values of kh including shallow, intermediate and deep-water region, the result is almost similar as compared to Zheng et al. (2004). Thus, the results obtained using the present AQWA model are in good agreement with Zheng et al. (2004).

2.6 HYDRODYNAMIC PERFORMANCE OF OWC INTEGRATED WITH BW USING ANSYS

The hydrodynamic performance of OWC integrated with H-type breakwater is evaluated using Ansys-AQWA and Fluent. The hydrodynamic parameters for the analysis of performance of pile restrained breakwater considered is the Wave Excitation Force Coefficient (EFC), Shear Force (SF), Bending Moment (BM), Response Amplitude Operators (RAOs), and Transmission Coefficient K_T . The performance of OWC integrated inside H-type breakwater is evaluated in terms of its power capture efficiency. The numerical results are presented for Wave Excitation Forces, Shear Forces, Bending Moments, Transmission Coefficient and Power Capture Efficiency.

2.6.1 Integrated H-type breakwater and OWC model description

The H-type floating breakwater integrated with OWC in fixed position using piles is described in Fig. 5. The OWC inlet is kept at a distance x below water level and the chamber width c_b and OWC inlet height is kept equal. The air flow opening ratio (orifice diameter) to chamber

width c_0 is fixed to 0.5. The curve part of OWC geometry is having radius R_1 and R_2 with R_1 is considered to be equal to c_b and R_2 is equals to two times c_b .

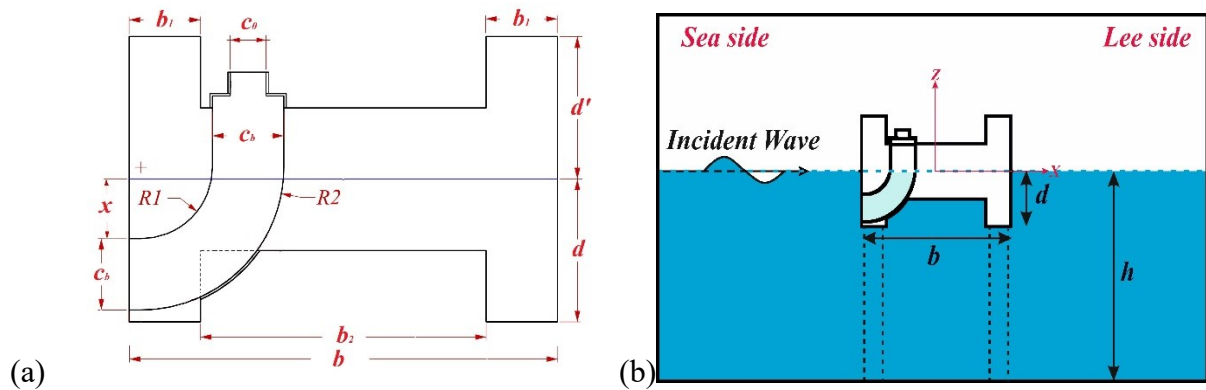


Fig. 5: Schematic representation of the H-type pile-restrained hybrid breakwater.

The integrated H-type breakwater with OWC model is considered to be of unit length for two-dimensional analysis and length of three times width is considered for three-dimensional analysis. The incident wave angle θ is considered 0° in x -direction. The non-dimensional relative draft d/h , width, and chamber width are varied to understand the effect of wave transformation of efficiency of the integrated system. The OWC inlet depth x is considered equals to $d - (c_b - 0.25)$ for the present integrated H-type breakwater with OWC model.

2.6.2 Numerical Domain in Ansys-Fluent

Ansys-Fluent model analysis is performed to validate the numerical result with Boundary Element Method (BEM). The numerical wave tank is developed for the study model (Fig. 5) for relative draft $d/h = 0.1$. The volume of fraction for water is considered as unity in numerical domain. The two phases of fluids are considered namely air and water to use the volume of fluids method to simulate ocean waves. On using open channel wave boundary conditions, the wave generation on inlet side is enabled and numerical beach is created to eliminate the reflection of waves within considered domain by dampening the waves over a particular length. The present numerical domain contains inlet, outlet and seabed boundaries and the initial boundary conditions are set by using flat-type hybrid initialization method starting from inlet boundary. A constant value of surface tension coefficient of 0.072 N/m between air and water phase interaction is used along with k- ω viscosity model for proper sea wave simulation. The mesh size considered for the numerical domain is 0.5m near boundaries and 0.05m near the breakwater with OWC structure. The parameters in numerical domain are considered same as in BEM modelling. The wave excitation force coefficients EFC_j , shear forces, bending moments and K_T are obtained using Ansys-AQWA and the efficiency of the hybrid model is obtained using Ansys-Fluent modelling. The hydrodynamic parameters are assessed over a range of kh for different relative draft and incident wave angles. The maximum element size is kept at the value corresponding to the maximum frequency for the

hydrodynamic analysis. In the present study the numerical study is performed for the hybrid breakwater model with $b/h = 1.0$, $c_b/h = 0.15$ and $b_1/h = 0.15$.

2.6.2.1 Wave Excitation Forces

The wave excitation force coefficient EFC_j in Fig. 6(a-c) is analysed on varying the relative draft d/h for incident wave angle $\theta = 0^\circ$. The study shows that for $d/h = 0.5$, the EFC_1 (Fig. 6a) and EFC_3 (Fig. 6b) rise to maximum value of 0.99 and 0.93 respectively in intermediate water region $kh \leq 3.14$. For EFC_5 (Fig. 6c), the maximum value of wave excitation force is noted to be 0.62 for $d/h = 0.2$ in deep water region $kh > 3.14$.

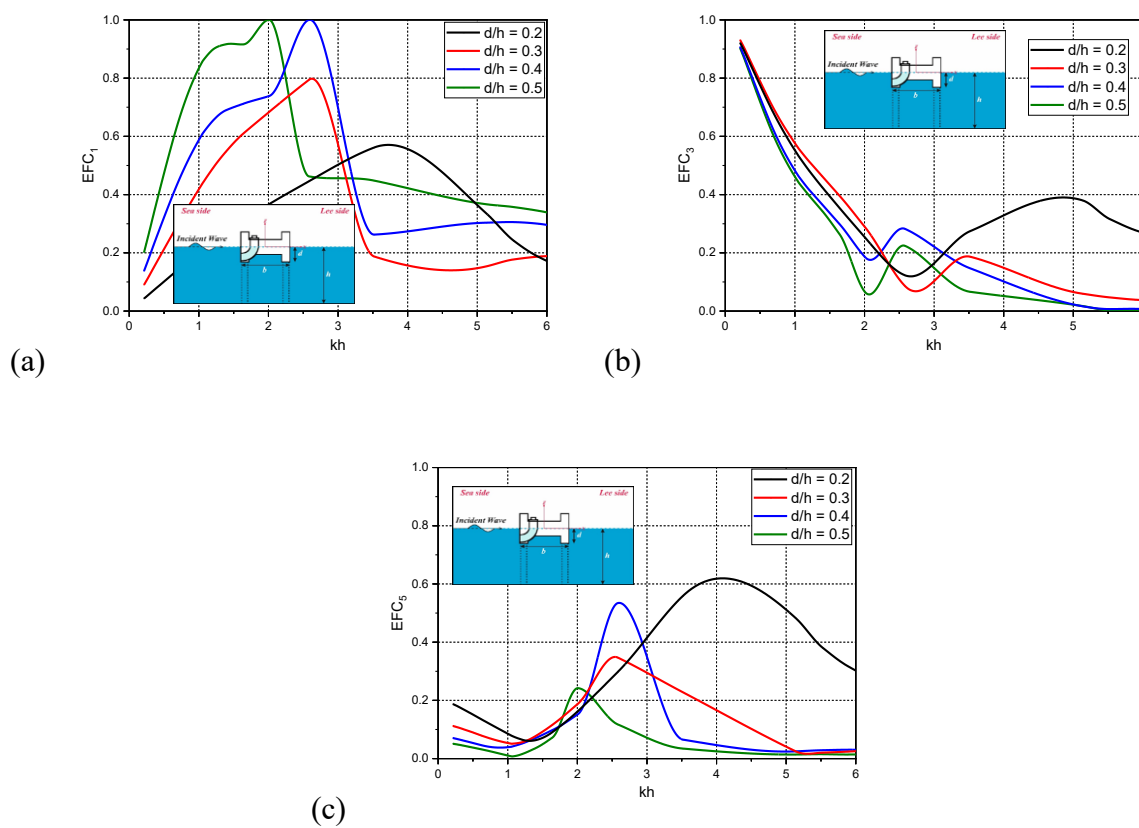


Fig. 6: Variation in wave excitation force coefficients (a) EFC_1 , (b) EFC_3 and (c) EFC_5 versus kh for various values of d/h considering $\theta = 0^\circ$.

As the relative draft increases, the slope of peak value rises to become steeper for EFC_1 which results in shift of peak toward intermediate-water region. The peak amplitude of wave excitation force coefficient shows decrease of about 30% in EFC_1 and increase of about 60% in EFC_5 while transitioning from intermediate water region to deep water region due to change in d/h . In the case of $kh = 2.01$, as d/h increases, the increase in EFC_1 of about 86%, 8% and 35% respectively, increase in EFC_3 of about 14%, 36%, and 65% respectively and EFC_5 shows of about 16% increase, 19% decrease, and 58% increase respectively. The variation

observed may be due to change in number of diffracting panels of the hybrid breakwater with the increment in draft. The variation happens because large surface area interacting with waves results changes in diffracted wave potential which affects the diffraction force and hence excitation force changes. The maximum wave excitation force is observed for $d/h = 0.5$ in $EFC_1 = 0.99$ at $kh = 2.01$. The wave excitation force coefficient in deep water region in all direction is noted below 0.6. The high wave excitation force results in high value of structural stresses.

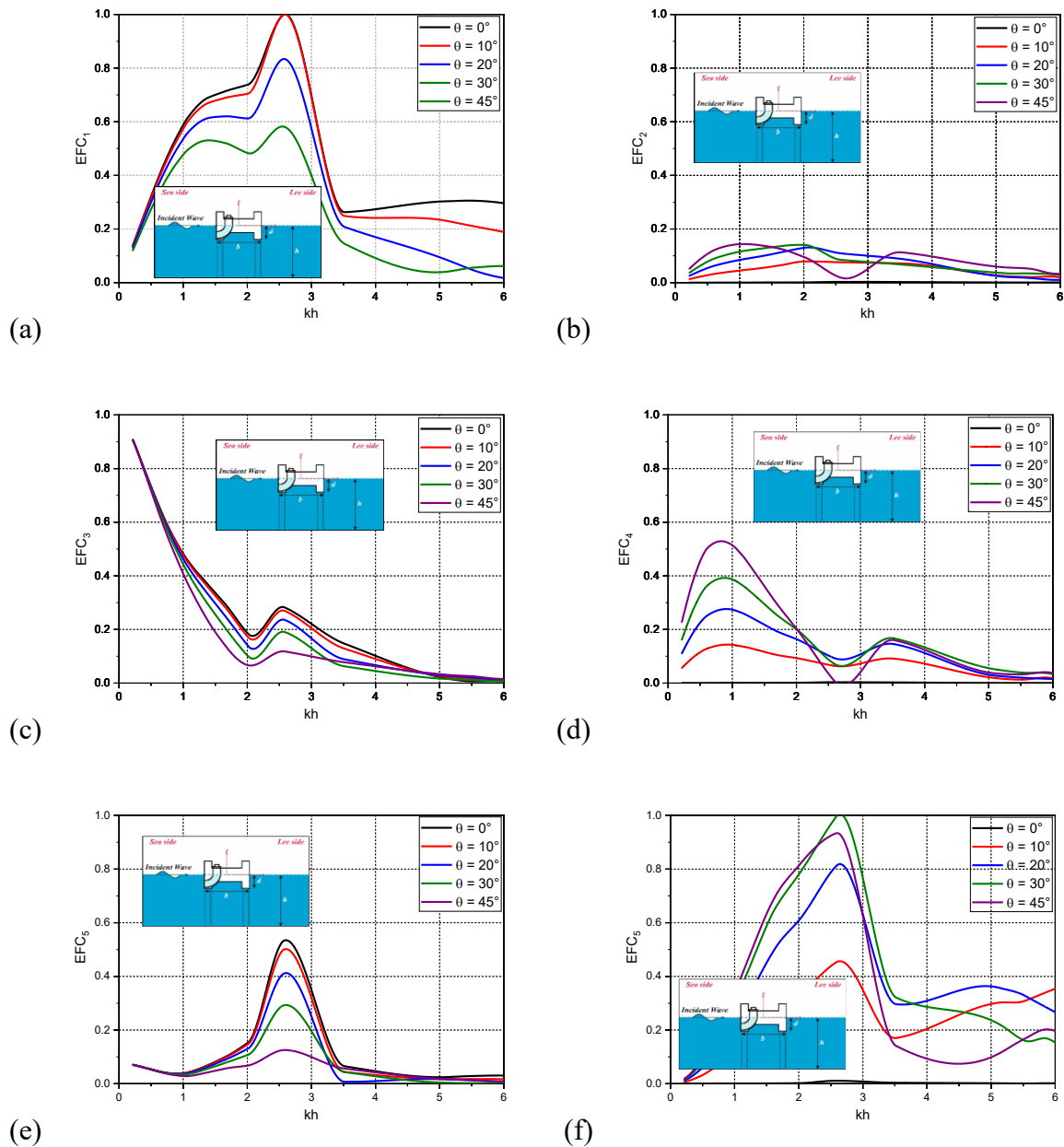


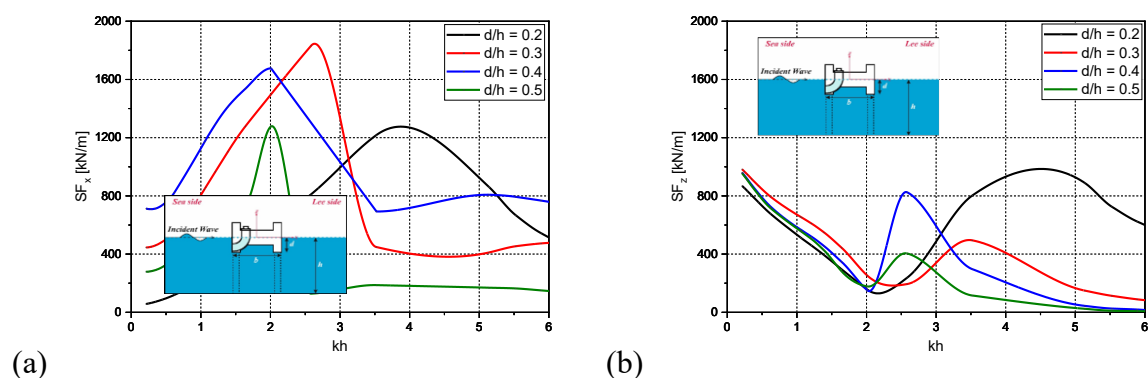
Fig. 7: Variation in wave excitation force coefficients (a) EFC_1 , (b) EFC_2 , (c) EFC_3 , (d) EFC_4 , (e) EFC_5 and (f) EFC_6 versus kh for various values of θ considering $d/h = 0.4$.

In Fig. 7(a-f), the wave excitation force coefficients EFC_j are analysed due to change in the incident wave angle considering $d/h=0.4$. Fig. 7(a-f) clearly demonstrates that there is almost minimal change in the wave excitation force coefficient values in z -direction and r_y -directions due to change in θ for $0 \leq kh \leq 2$ and except for the range of $2 \leq kh \leq 3.14$ around 3 - 8% variation is observed. In deep water region $kh > 3.14$, it can be observed that when θ is increasing the wave excitation force coefficient decreases and ultimately drops to zero for further increase in θ in x -direction and r_y -direction. The variation in wave excitation force may be due to dependence of wave energy on the velocity which is influenced by the angle of incidence θ . The cosine component of velocity decreases with increase in θ , resulting in decrease in velocity and ultimately leading to decrease in the wave excitation force. The increase of incidence angle is with respect to x -direction, z -direction and r_y -direction. The EFC_1 shows no change for $0^\circ < \theta < 10^\circ$ and $kh \leq 3.14$, and thereafter each increment of $\theta > 10^\circ$ shows decrease in value of about 20 - 25%. The wave excitation force coefficient EFC_2 , EFC_3 , EFC_4 and EFC_5 values remain below 0.2 for deep water region. The EFC_3 also shows no significant changes due to change in θ except for $2 \leq kh \leq 3.14$, which shows decrease in wave excitation force coefficient of about 5 - 12% with increase in θ . The EFC_2 and EFC_4 shows an increase of two-fold for each 10° increment of θ . The increment of 1.5 to 3-fold can be seen for EFC_6 at the intermediate water region, but for deep water region as θ changes from 0° to 10° the wave excitation force coefficient increases from 0 to 0.4 and for increment of θ beyond 10° the wave excitation force coefficient decreases again toward 0. The increase in wave excitation force is due to increase of velocity component with increase in θ . For $d/h=0.4$ and $\theta=0^\circ$ wave excitation force is dominant in x -direction and r_y -direction for $0 < kh < 4$. The wave excitation force coefficient which are insignificant in case of zero incidence angle are showing significant changes as θ increases, especially in region of shallow and intermediate waters. In case of x -direction, y -direction and r_y -direction, the formation of critical angle at which the wave excitation force is nearly equal to zero is within $4 < kh < 6$ with increase in angle of incidence.

2.6.2.2 Shear Forces and Bending Moments

The shear force and bending moment corresponds to force/moment per unit wave amplitude. The variation in shear force and bending moment with respect to relative draft variation and angle of wave incidence are investigated. The components of shear force is for x - and z -directions and bending moment is considered for y -direction because these forces/moments are dominant in the specified directions for the considered model. In Fig. 8(a-c), the numerical investigation is performed at middle of the structural cross-section (i.e. at $b/2$ distance from sea side) for change in relative draft considering wave incidence angle of 0° . Fig. 8(a) shows that the highest SF_x for the considered frequency range and increases as d/h increases within $0.2 < d/h < 0.3$ which results in shift of peak value from deep water region to intermediate

water region. With further increase in relative draft, the shear force in x -direction SF_x decreases in shallow and intermediate water region but the same is not true for deep water region. For $kh > 3.14$, as d/h changes varies within $0.3 < d/h < 0.4$ the increase in SF_x is noted of about 50-70% and as d/h varies within $0.4 < d/h < 0.5$ the SF_x results in decrease of about 70-75%. The bending moment in y -direction BM_y (Fig. 8c) follows the same trend as obtained for the wave excitation force in respective direction. The sudden drop in the peak value of force z -direction and moment in y -direction can be observed while transitioning from deep water region to intermediate water region. As d/h increases within $0.2 < d/h < 0.3$, the decrease in peak value for SF_z and BM_y is about 44-45% for both shear force and bending moment. Shear force per unit wave amplitude in x -direction initially increase to a peak value and then suddenly drops and remains below 800 kN/m for deep water region, for all relative drafts. The shear force in SF_z in z -direction (Fig. 8b) first decreases within the range of 150 - 250 kN/m and then start increasing with non-dimensional wave number, and attains a peak value and then drops nearly to zero for all relative drafts. Similar pattern is observed in BM_y (Fig. 8c). The shear force and bending moment experienced by the structure is directly proportional to pressure variation on structure due to wave incidence. Thus, rise and fall in shear force and bending moment with respect to a given draft can be due to changes in the structure's surface area in the water and the resultant variations in pressure. Fig. 8(a-c) also shows that as the relative draft changes, the rate of increase to peak value of SF_x in x -direction and BM_y in y -direction is almost similar, but the rate of decrease after peak is different for all forces/moments. Further, the wave frequency bandwidth for large value of SF_x , SF_z and BM_y is observed to be decreasing with increase in relative draft. The maximum value of shear force observed in x -direction is 1832 kN/m for $kh = 2.58$ and $d/h = 0.3$, in z -direction is 888 kN/m for $kh = 2.58$ and $d/h = 0.2$, and bending moment in y -direction is 5855 kN.m/m for $kh = 2.58$ and $d/h = 0.4$.



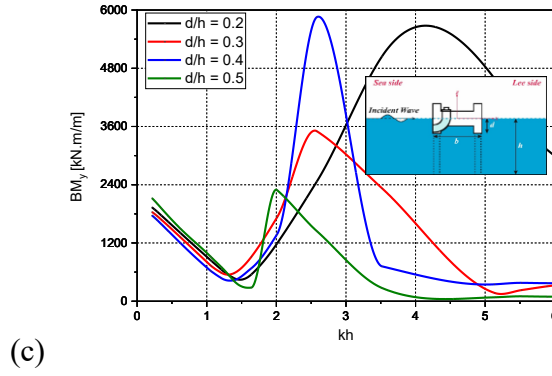


Fig. 8: Variation of (a) SF_x , (b) SF_z and (c) BM_y versus kh for various values of d/h considering $\theta = 0^\circ$.

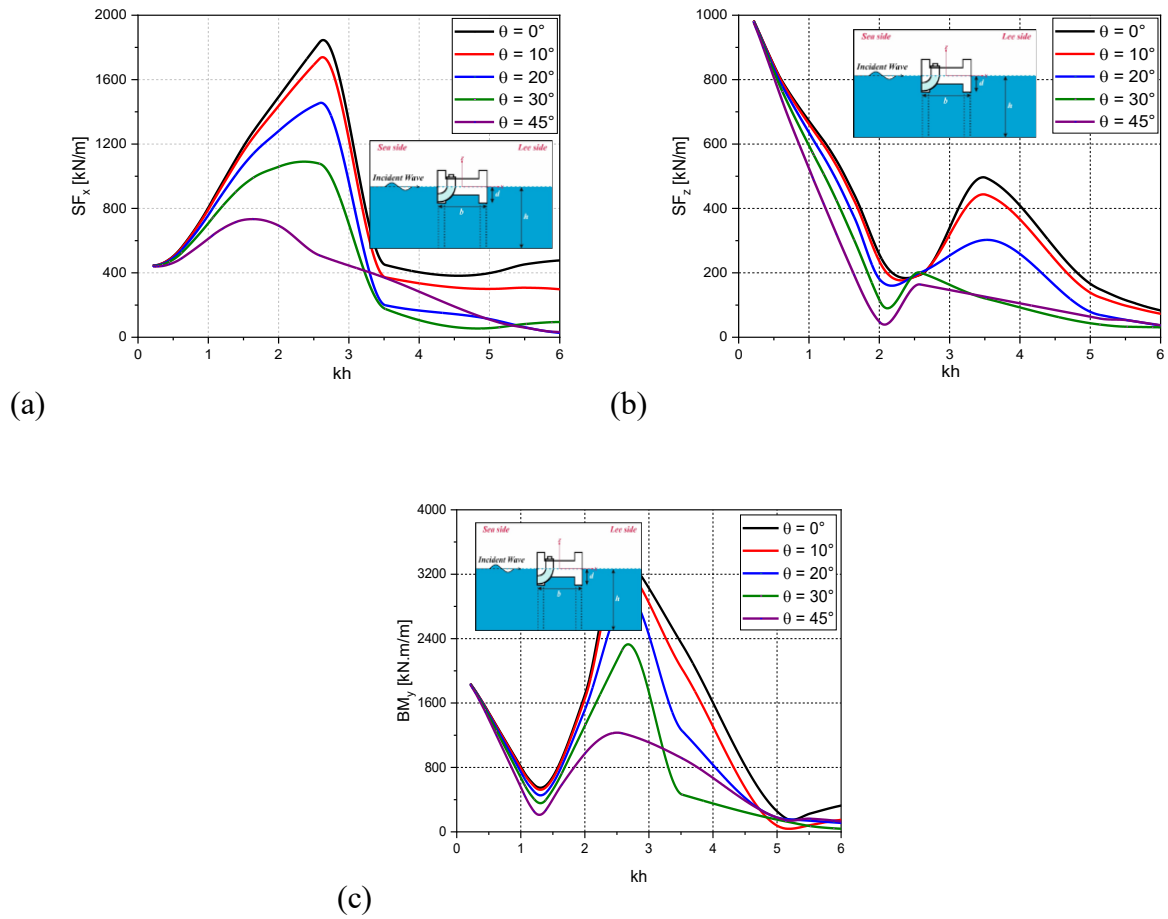


Fig. 9: Variation of (a) SF_x , (b) SF_z and (c) BM_y versus kh for various values of θ considering $d/h = 0.3$.

Fig. 9(a-c) shows that, with the change in wave incidence angle, there is no significant change in the values of the SF_z and BM_y for $kh \leq 2$ and $kh > 5$. The variation in the SF_z and BM_y is observed for $2 < kh < 5$. The SF_x decrease by about 6% to 50% for $kh < 3.5$ as θ increases, the SF_z is observed to be decreasing (about 10% to 60%) with increase of θ for $kh > 2.5$, and

BM_y decreases (about 5% to 50%) as θ increases for $2 < kh < 3.5$ but for $\theta = 45^\circ$ there is increase in the value of BM_y for deep water region $kh > 3.14$. The shear force and bending moment with change in θ is due to the dependence of wave energy on the velocity which is influenced by the angle of incidence θ . For most of the deep water region $kh > 5$, the SF_x and SF_z is having value below 600 kN/m and 100 kN/m respectively and the BM_y is confined below 500 kN.m/m for $kh > 5$.

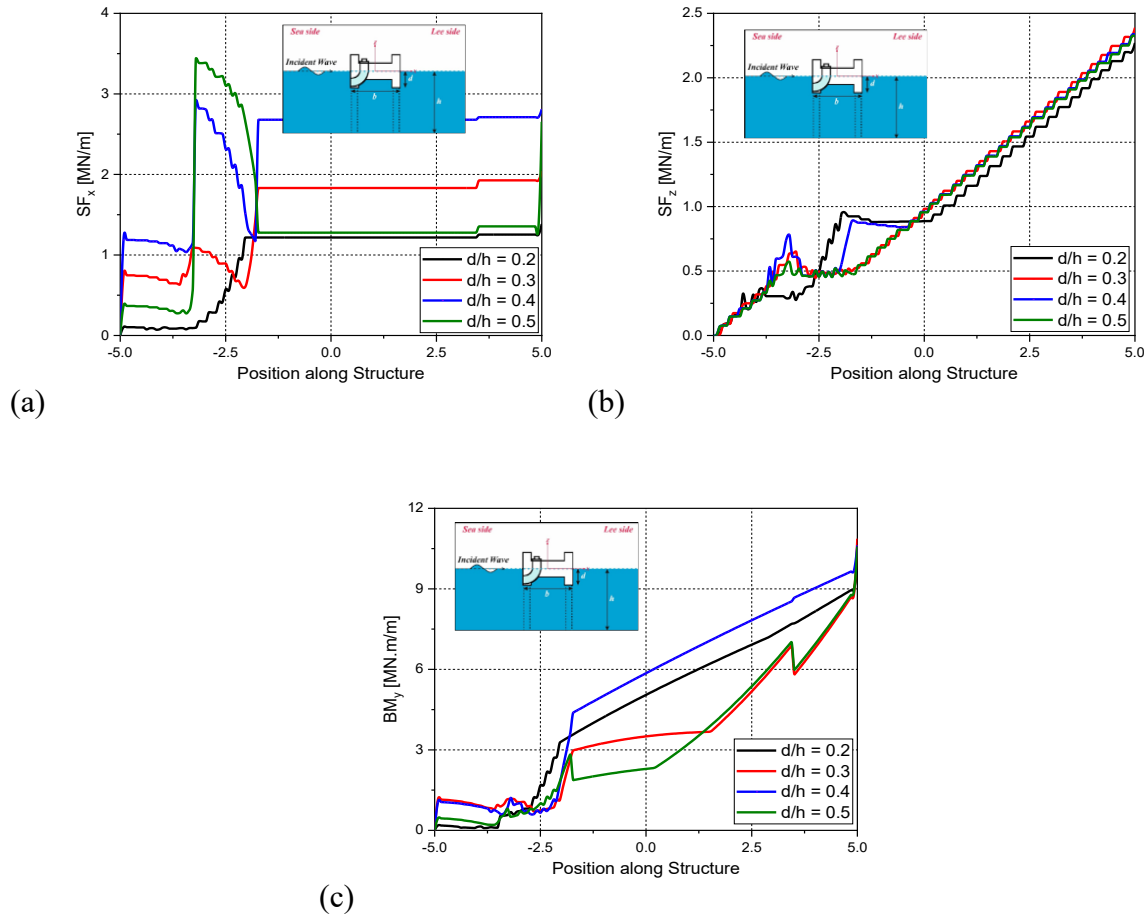


Fig. 10: Variation of (a) SF_x , (b) SF_z and (c) BM_y versus distance along the structure for various values of d/h considering $\theta = 0^\circ$.

Fig. 10(a-c) shows the maximum value of shear force and bending moment among all of the calculated wave frequency values. The shear force and bending moment near sea side of the structure (near position -5.0m) are observed to be insignificant when compared to the values near lee side (near position 5.0m). The variation is observed due to the intersection point X_0 (Eq. 57 and Eq. 58) initializes from sea side. The SF_x remains same between -5.0 to -3.125m and due to the presence of OWC chamber it shows sharp increase. As the OWC structure ends, again sharp increase (of about 1.5 times) in SF_x can be observed and then it remains almost constant for the rest part of the structure. SF_z shows linear increase from one end to another,

with small deviation between -3.75m to 0.0m with change in relative draft. BM_y is below 1.5 MN.m/m till -2.5m then increase in higher slope (of about 3 times) is observed which is followed by linear increase. In Fig. 10(a-c), it is worth noting that as relative draft increases the SF_x increases within OWC region by 1.5 to 2 times but for the rest of the structure it show 45-50% increase up to $d/h \leq 0.4$ and when d/h varies within $0.4 < d/h < 0.5$, it shows decrease in value by about 50%. Approximately same decrease is observed in value of BM_y for the same change in relative draft.

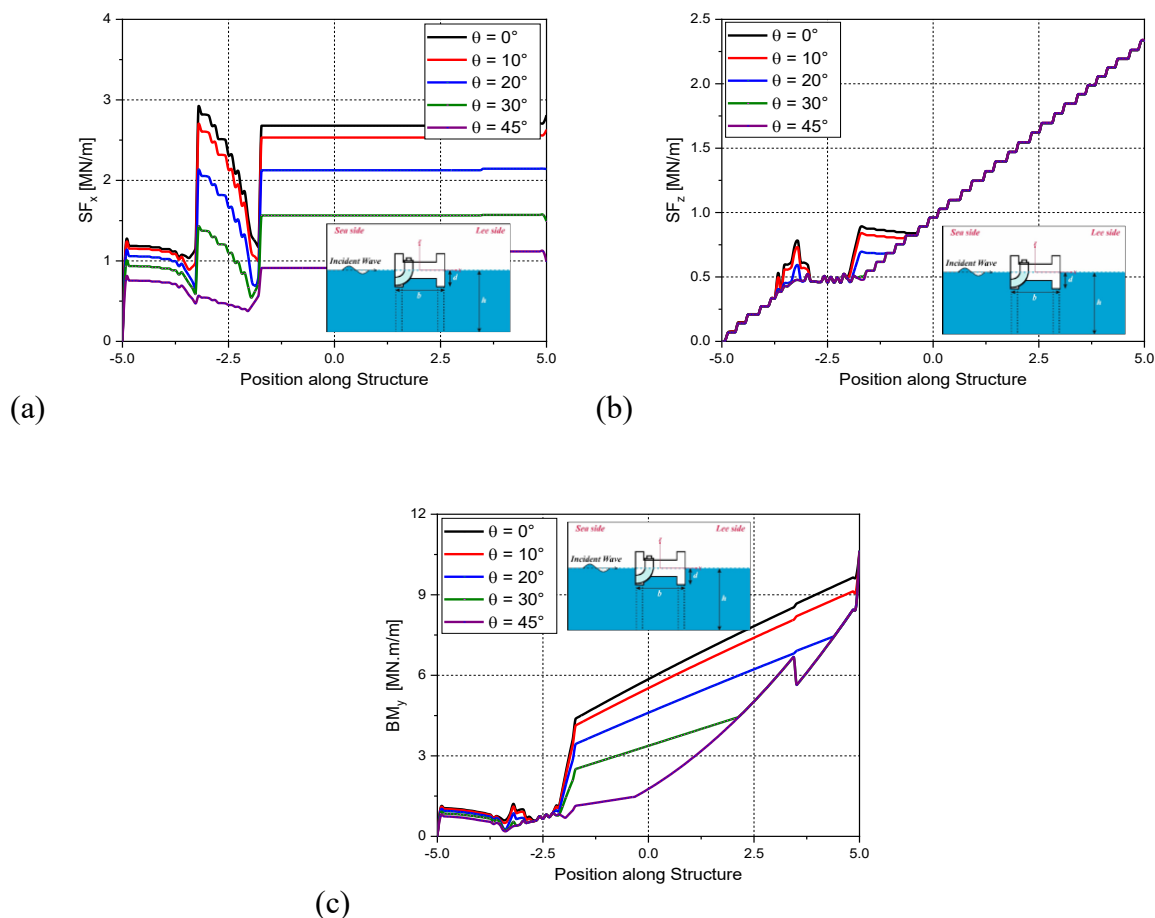


Fig. 11: Variation of (a) SF_x , (b) SF_z and (c) BM_y versus distance along the structure for various values of θ considering $d/h = 0.4$.

In Fig. 11(a-c), the effect of change in wave incidence angle on the shear force and bending moment along the width of structure is analysed and the maximum value is represented at a point among whole range of wave frequency. The SF_x (Fig.11a) shows decrease in the value in the range of 7% - 60% with increase in θ within $0^\circ < \theta < 45^\circ$ in OWC and 5% - 40% for rest of the structure. Further, the study shows that SF_z (Fig. 11b) has minimal effect on varying angle of incidence θ near OWC chamber and for $\theta > 30^\circ$ there is no effect on SF_z for whole structure width. The BM_y (Fig. 11c) shows very small changes up to -2.5m position as θ

increases from 0° - 45° and beyond that position with increase in θ the value of BM_y decreases by 5% - 50%. Along the width of the structure, the shear force and bending moment variation is due to changes in point of cross-section and change in the magnitude of the bending normal stresses and transverse shear stresses placed on the structure by the waves.

2.6.2.3 Transmission Coefficient

The wave transmission coefficient on the lee side of breakwater is analysed using Ansys-AQWA in Fig. 12(a,b). The transmission coefficient K_T is plotted versus kh for different relative draft d/h (Fig. 12a) considering relative width of the breakwater same and also with different relative width of breakwater b/h (Fig. 12b) considering same relative draft.

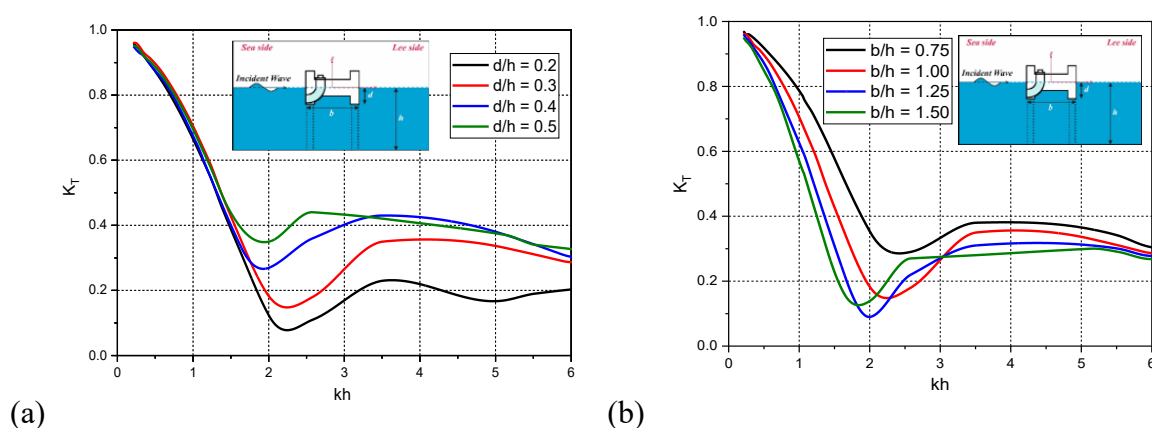


Fig. 12: Variation in transmission coefficients versus kh for various values of (a) d/h considering $b/h=1.0$ and (b) b/h considering $d/h=0.3$.

The study shows that with the increase in relative draft d/h (Fig. 12a), the transmission coefficient K_T is observed to be increasing but is noted to be almost same for $kh < 2$. In the case of shallow and intermediate water depth region the value of transmission coefficient decreases up to a certain value rapidly and then with small increase it remains almost same for the rest of the intermediate and deep-water region. The K_T value remains below 0.43 for $kh > 2$ for all relative draft. However, the transmission coefficient K_T is greater than 0.1 for $d/h \geq 0.2$ for all range of kh . The reduction in transmission coefficient K_T for smaller draft $d/h = 0.2$ is due to the presence of OWC inlet near water surface which results in more wave absorption (or dissipation) by hybrid structure. As the relative draft increases, the wave absorption by hybrid structure starts decreasing and results in more transmission. For $d/h \geq 0.2$, low wave transmission is observed for the part of intermediate water region and deep water region. For a breakwater structure, low wave transmission is an important phenomenon and for an OWC and wave dissipation at structure is required to capture wave energy. So, low reflection and low transmission along with high wave energy dissipation is favourable condition for hybrid breakwater structure. In addition, Fig.12(b) shows the effect of change in relative breakwater width b/h on K_T considering $d/h=0.3$. It is noted that as

breakwater relative width increases the K_T decreases by about 7 - 12 % for each increment of b/h for $kh > 3.14$. As b/h increases from 0.75 - 1.00, the K_T decreases by 38% for $2 < kh < 3$, and as b/h increases from 1.00 - 1.25, and 1.25 - 1.50 the K_T increases by 23% for each increment. Further, transmission coefficient is within $0.2 < K_T < 0.4$ for the deep-sea region $kh > 3.14$.

2.6.2.4 Power Capture Efficiency

The power capture efficiency is calculated on analysing the variation of air chamber pressure and velocity of air flow over the simulation period using Ansys-Fluent. It is noteworthy that the power capture efficiency is greater than 35% for the intermediate water depth and deep-sea condition $kh \geq 2.5$ as observed in Fig. 13. This is mainly due the fact that the air pressure in the OWC chamber induced by wave excitation force is considerably high due to more frequent oscillations of the air column caused by shorter wavelength waves. Further, the power capture efficiency using Ansys-Fluent is validated with BEM for $d/h = 0.1$, $c_b/h = 0.05$ and $b/h = 0.3$, and it is observed that the numerical model using Ansys-Fluent has good agreement with the BEM.

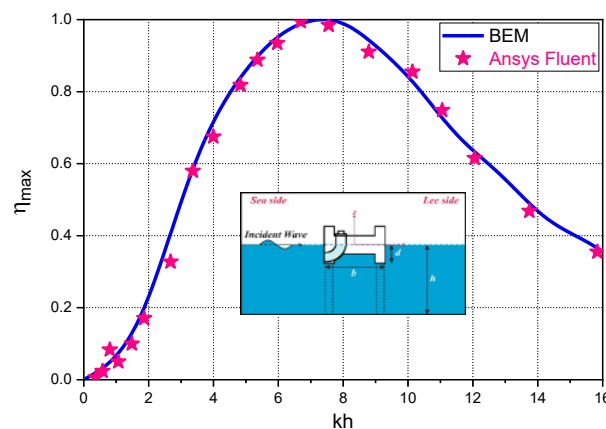
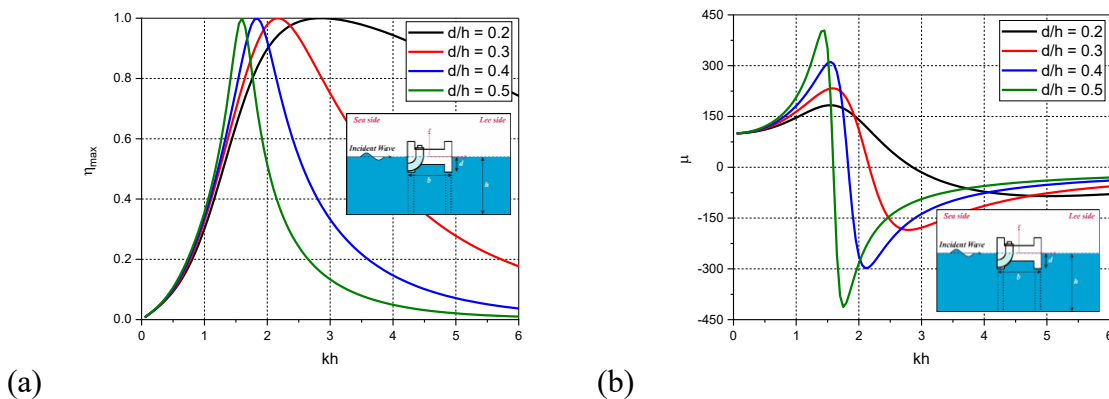
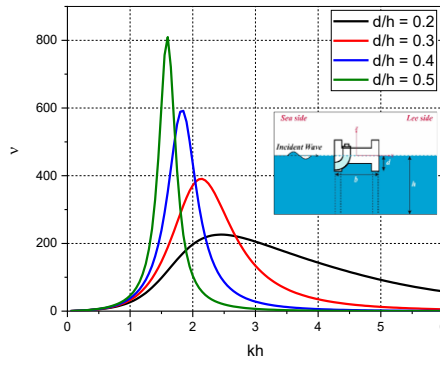


Fig. 13: Comparative study of η_{\max} versus kh using BEM and Ansys-Fluent.

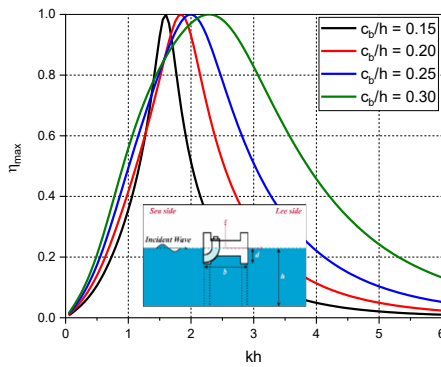




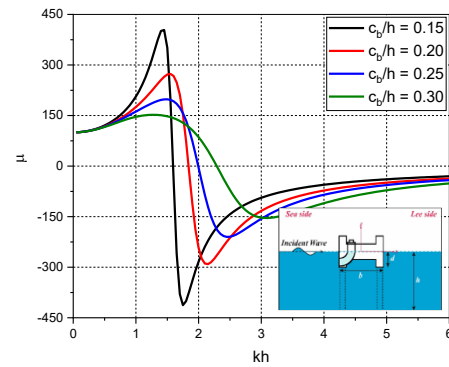
(c)

Fig. 14: Variation of (a) η_{\max} , (b) μ and (c) ν versus kh for different relative drafts d/h considering $b/h=1$ and $c_b/h=0.3$.

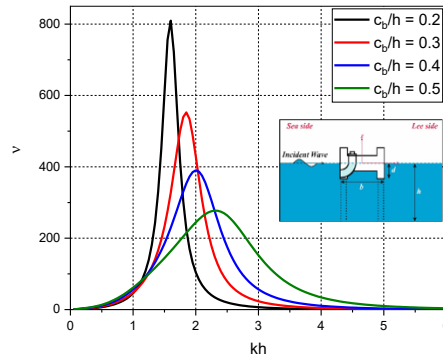
In Fig. 14(a-c), the investigations are carried out to analyse the effect of increasing relative draft on the power capture efficiency of the device using BEM approach. It is observed that upon increasing the relative draft, $0.2 < d/h < 0.5$, the peak of the efficiency η_{\max} (Fig. 14a) shifts towards lesser wavenumber range. Also, the decline in efficiency gets steeper after peak value is attained with increase in relative draft, implying the ability of the device to maintain high efficiency for greater range of wavenumber decreases with increase in relative draft. The device shows lesser efficiency for higher relative draft in the deep-water region $kh > 3.14$. The dimensionless radiation susceptance parameter μ (Fig. 14b) crosses the zero mark at the wavenumber where η_{\max} reaches maximum value. The difference in magnitude of the highest and lowest value of μ increases with increase in relative draft, and the highest and lowest peaks shift towards decreasing wavenumber with increase in d/h . The dimensionless radiation conductance parameter ν (Fig. 14c) reaches its peak value at the kh where η_{\max} is maximum and the peak increases with the increase in d/h . The device performs better with lower relative draft as the opening of the OWC is nearer to the surface where the wave energy is predominantly present.



(a)



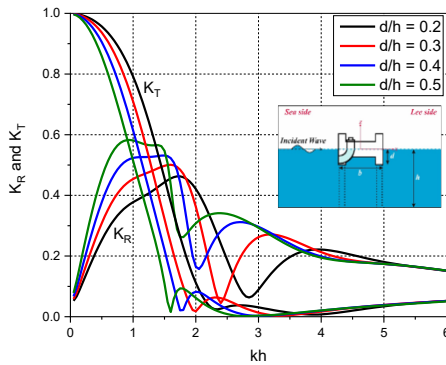
(b)



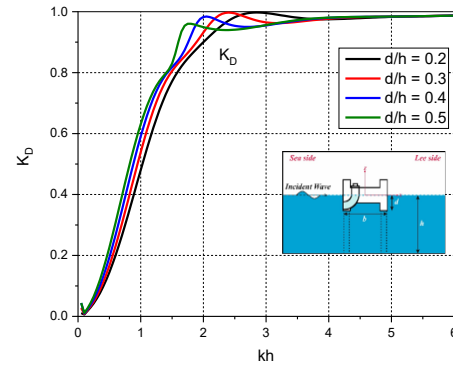
(c)

Fig. 15: Variation of (a) η_{\max} , (b) μ and (c) ν versus kh for different relative chamber width c_b/h considering $b/h=1$, and $d/h=0.5$.

In Fig. 15(a-c), the investigation is carried out to analyse the effect of increasing relative chamber width on the performance of the OWC. In Fig. 15(a), it is observed that on keeping the relative draft and width of the structure same and increasing the relative chamber width, the peak of the efficiency curve shifts towards higher value of kh , as well as the peak value shows wider plateaus, suggesting that the device maintains high efficiency for wider wavenumber range. The overall trend of the efficiency curve for all configurations remains same, constituting a steep incline to the peak value at $kh \approx 2$ followed by a steep decline and then approaching to zero at all higher wavenumber range. Further, it is observed that, here too, the radiation susceptance parameter μ (Fig. 15b) crosses the zero mark at the wavenumber where efficiency is highest. The difference in magnitude of the highest and lowest value of μ decreases with increase in relative chamber width, and the highest and lowest peaks shift towards higher wavenumber with increase in c_b/h . The radiation conductance parameter ν (Fig. 15c) also shows similar behaviour as observed in Fig. 14(c), reaching the peak value at kh where η_{\max} is highest, with the value of the peak decreasing and shifting towards higher kh as c_b/h increases. The device performs better with higher relative chamber width as more volume of water enters the chamber, consequently compressing more volume of air and producing more energy.



(a)



(b)

Fig. 16: Variation of (a) K_R and K_T and (b) K_D versus kh for different d/h considering $b/h=1$ and $c_b/h=0.15$.

In Fig. 16(a-b), the reflection, transmission, and dissipation coefficients of the OWC integrated in H-type breakwater under the action of normal regular incident waves is analysed for different relative draft d/h . The reflection coefficient K_R (Fig. 16a) increases steeply for all configurations and attains highest value within $0.5 \leq kh \leq 2.0$, thereafter it drops steeply and recovers again for a brief range of wavenumbers and then gradually continues towards zero value. With increase in d/h , the peak of K_R increases and shifts towards lower value of kh . Further, it is observed that the transmission coefficient K_T (Fig. 16a) for all configurations follows a trend of decreasing steeply to almost zero at $kh \approx 1.5$ and then is maintained at that level of value less than 0.1 in deep water region. In addition, with increase in relative draft d/h , the steepness of K_T increases very slightly and the local minima at $kh \approx 1.5$ shifts towards the lower value of kh . The dissipation coefficient K_D (Fig. 16b) increases steeply for all configurations and attains peak value of nearly 1.0 with increase in kh . On varying the relative draft d/h , the K_D shows similar effect of reaching the first peak value within $1.5 \leq kh \leq 3.0$, with the peak decreasing and shifting towards lower value of kh as d/h increases. The K_D remains close to one within $3.0 \leq kh \leq 6.0$ suggesting most of the wave energy is dissipated instead of being reflected or transmitted. As the draft of the device increases, the inlet portion of the OWC goes deeper below the mean water surface forcing the incoming waves to reflect off the flat surface above the inlet.

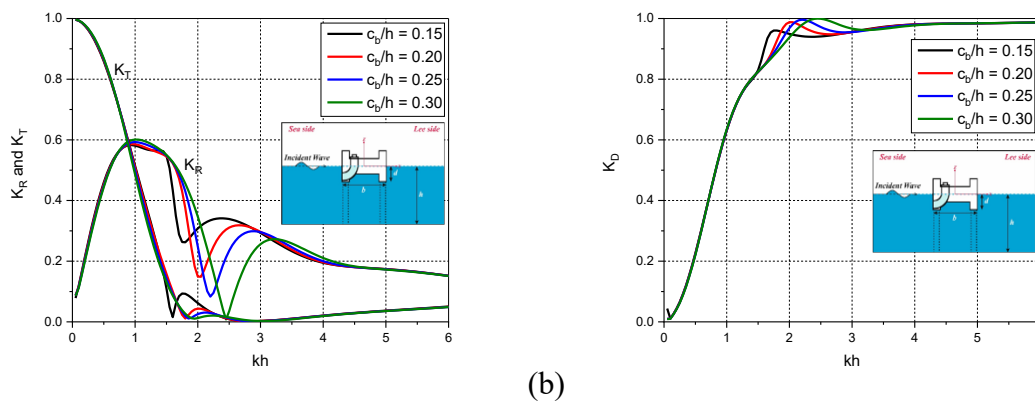


Fig. 17: Variation of (a) K_R and K_T and (b) K_D versus kh for different c_b/h considering $b/h=1$ and $d/h=0.5$.

In Fig. 17(a), it is observed that, in the case of changing relative chamber width c_b/h , the K_T remains almost same for all configurations with minor changes occurring at $kh \approx 2.0$, however, the K_R shows distinct patterns for various relative chamber width within $1.5 \leq kh \leq 3.5$, wherein the local minima in the value of K_R reaches lower values with increase in c_b/h and shifts towards higher value of kh . The dissipation coefficient K_D (Fig. 17b) exhibits the same trend with very minor variation in the first peak within $1.5 \leq kh \leq 3.5$ but the value of the peak increases and shift for higher value of kh with increase in c_b/h . The decrease in K_R with increase in c_b/h can be attributed to the fact that higher amount of the incoming wave particles enters the chamber of the OWC causing less water to be reflected back.

2.7 CONCLUSIONS

In the present study, the hydrodynamic performance of pile restrained OWC integrated in H-type breakwater is investigated in terms of wave excitation force, wave reflection coefficient, transmission coefficient and power capture efficiency of OWC. The numerical investigation is performed using Ansys-AQWA and Ansys-Fluent for the determination of the hydrodynamic parameters in regular waves. The effect of variation in relative draft and incident wave angle on hydrodynamic parameter is assessed. The validation for the numerical model is performed and the variation in wave excitation force and transmission coefficient with the relative draft variation is analysed. Further, effect of incident wave angle is assessed and the conclusions drawn from the present study is as follows:

- In the case of normal incident angle, as relative draft $d/h \leq 0.3$ the OWC integrated in H-type breakwater results in 30% decrease in wave excitation force EFC_1 . The wave excitation force EFC_5 shows increase of 2-fold for transition from intermediate to deep water region as d/h varies within $0.2 < d/h < 0.3$.
- The shear force SF_x increases with increase in relative draft up to 0.4 then decrease when relative draft increases beyond 0.4 for $kh < 2$ and $kh > 7$. The SF_z and BM_y decreases with increasing relative draft for a part of intermediate water region and deep-water region $kh > 3$.
- The critical angle for the wave excitation force EFC_1 at $kh=6$, EFC_3 at $kh=5$, and EFC_5 at $kh=4$ is almost equal to zero with increasing angle of incidence. The shear force SF_x and SF_z , and bending moment BM_y shows decreasing trend for intermediate and shallow water region with increase in wave incidence angle for $kh \leq 4$.
- At certain range of the intermediate water depth and deep-water depth, $kh \geq 2.5$, the power capture efficiency η_{\max} is 35% higher which is mostly caused by the air pressure in the OWC chamber being significantly higher for $kh \geq 2.5$ due to frequent oscillations of short wavelength waves.
- Numerical analysis using BEM revealed that on keeping the relative chamber width and relative device width constant, the best performing configuration in terms η_{\max} is the one with the lowest relative draft, $d/h=0.2$. A lower draft corresponds to the inlet of OWC chamber being nearer to the surface, where all the wave energy is concentrated.
- On keeping the relative draft and relative device width constant, the configuration with largest relative chamber width opening, $c_b/h=0.3$ performs the best in terms of η_{\max} . A larger opening corresponds to more wave energy entering the OWC chamber resulting in better efficiency.
- On increasing the relative draft d/h , the reflection coefficient K_R increases at the first peak and also shifts towards lower value of kh , whereas the transmission coefficient K_T does not show much variation at the first local minima, but only shifts towards lower value of kh .

- On increasing the relative chamber width c_b/h , the K_T remains almost same, however, variations occur in K_R within $1.5 \leq kh \leq 3.5$, wherein the local minima in K_R decreases with increase in c_b/h and shifts towards higher value of kh .
- In both the cases of increasing relative draft and relative chamber width, the dissipation coefficient K_D does not vary much and follows same trend with minor variations at $kh \approx 2$. Most of the wave energy is observed to get dissipated in the intermediate as well as deep water region as the waves of shorter wavelength interacts more with the structure's geometry instead of getting reflected or transmitted.

The proposed study performed helps to understand the hydrodynamic behaviour of fixed surface piercing structures, which can perform as a breakwater and as a wave energy conversion device. The present study will assist in the development of analogous hybrid structures for effective and feasible implementation. Further, Ansys-AQWA model and Ansys-Fluent model can be used to investigate similar hybrid structure in freely floating environment with different seabed and ocean conditions.

CHAPTER 5

HYDRODYNAMIC PERFORMANCE OF EDINBURGH DUCK WAVE ENERGY CONVERTER INTEGRATED WITH FLOATING BREAKWATERS

5.1 THEORETICAL FORMULATION

In the present study, the Edinburgh Duck is considered as point absorbing Wave Energy Converter (WEC) integrated to different shapes of floating breakwater. The configuration of the setup is represented in Fig. 1. The global right hand Cartesian co-ordinates of the system $O-XYZ$ is introduced at the origin with OZ pointing upwards and passing through center of rotation of the ED-WEC at $(0,0,Z_c)$ and OXY plane lies on the still water surface level. The ED-WEC is symmetrical about the line l_d and the radius R of ED-WEC at the stern. The angle between OX and l_d is defined by β .

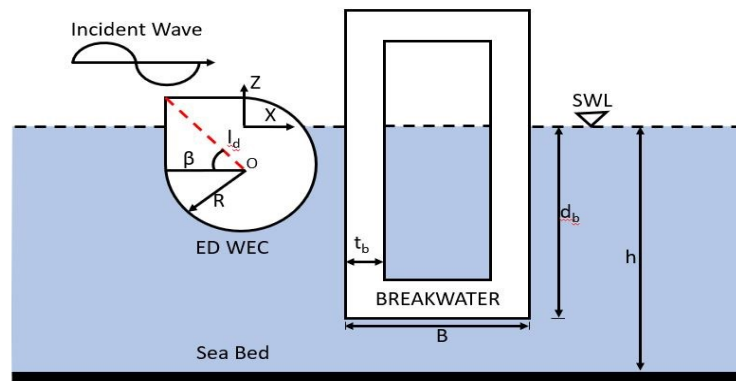


Fig. 1. Schematic representation of ED-WEC with breakwater.

The breakwater considered is a box-type breakwater having breadth B along X -axis, height H_b along Z -axis, length L_b along Y -axis and having thickness t_b and draught d_b . The breakwater is considered to be floating and is impermeable. The distance between the face of the breakwater to the center of rotation Z_c of ED-WEC is taken as B_1 and water is considered to be of finite depth h . The hybrid system of ED-WEC breakwater is considered to have only in heave motion with ED-WEC on the seaside of the system and the incident waves is considered to be regular.

2.1.1 Governing Equations

The potential flow theory for radiation and diffraction problem is considered in the present study and in the case of fluid flow field around the floating structure, the velocity potential is described as

$$\phi(\vec{X}, t) = \eta \phi(\vec{X}) e^{-i\omega t} \quad (1)$$

where η is the incident wave amplitude, t is the time, ω is the wave frequency and $\vec{X} = (x, y, z)$ is the location with respect to fixed reference axes. The rotational and translational motions of the floating body excited by the incident wave of unit amplitude is given by

$$x_j = u_j, \text{ for } j = 1, 2, 3 \quad \text{and} \quad x_j = \theta_{j-3}, \text{ for } j = 4, 5, 6 \quad (2)$$

where, the total potential $\varphi(\vec{X})$ can be considered as a sum of three component, such as incident wave potential φ_I , diffracted wave potential φ_D and radiated wave potential φ_R . The incident, diffracted and radiated velocity potentials satisfy the Laplace equation and is represented as

$$\varphi(\vec{X})e^{-i\omega t} = \left[\varphi_I + \varphi_D + \sum_{j=1}^6 \varphi_{Rj} x_j \right] e^{-i\omega t} \quad (3)$$

where φ_I is the first order incident wave potential with unit wave amplitude, φ_D is the diffraction wave potential and φ_{Rj} is the radiation wave potential due to the j^{th} motion with unit wave motion amplitude. The velocity potential satisfies the Laplace equation in the fluid domain is expressed as

$$\nabla^2 \varphi(x, y, z) = 0 \quad (4)$$

The linearized free surface boundary condition at the free surface is written as

$$-\omega^2 \varphi + g \frac{\partial \varphi}{\partial z} = 0 \quad (5)$$

The body surface condition s_b for the boundary value problems for wave interaction with the ocean structure on the wetted body surface x_0 is given by

$$\frac{\partial \varphi}{\partial n} = -i\omega n_j, \text{ for radiation potential,} \quad (6)$$

$$\frac{\partial \varphi}{\partial n} = -\frac{\partial \varphi}{\partial n}, \text{ for diffraction potential,} \quad (7)$$

where φ is the velocity potential function indicating initial incoming waves. The seabed boundary condition s_z at $z = -h$ is expressed as

$$\frac{\partial \varphi}{\partial z} = 0 \quad (8)$$

2.1.2 Equations of Motion and RAOs

The governing equation for the heaving type point absorber wave energy converter can be expressed as

$$m\ddot{z} = f_e + f_r + f_h + f_{PTO} + f_v \quad (9)$$

where m is the mass of the of the point absorber buoy, f_e is the excitation force on body due to incident wave, f_r is the radiation force, f_h is the hydrostatic force derived from buoyancy and gravity force, f_{PTO} is the forced applied by the power take off system, f_v is the damping force occurring due to viscosity of the fluid interacting the body, z , \dot{z} and \ddot{z} represents vertical

displacement, velocity, and acceleration of the floating body respectively. The force f_e represents the force introduced due to the dynamic pressure of undisturbed waves, while f_r is caused by disturbed waves due to the existence and oscillation of the point absorber. The radiation force f_e can be obtained by integrating the dynamic pressure p of incident waves over mean wet surface of the OB WEC, and dynamic pressure can be represented as

$$p = -\rho \frac{\partial \phi}{\partial t} \quad (10)$$

$$\phi = \frac{g\eta}{\omega} \frac{\cosh k(z+h)}{\cosh kh} \cos(\omega t - kx) \quad (11)$$

where g is the gravitational acceleration constant, h is the water depth, ρ is the fluid density, η is the wave amplitude, ω is the angular frequency and κ is the wave number of the incident wave. In the fluid regions the expansion of the velocity potential can be performed, and the solutions of Laplace equations satisfies the boundary condition on the free surface for heaving device given by

$$-K\phi_j^{l,m} + \frac{\partial \phi_j^{l,m}}{\partial z} = 0, \quad j = 0, A \quad \text{and} \quad z = -h \quad (12)$$

2.1.3 Mooring System

In order to analyse the dynamics of the cable motion, different factors such as cable mass, cable drag and tension should be considered. The forces applied to the cable vary with time and it behaves as nonlinearly. The simulation of cable dynamics is required to be discretized along its length and assembled mass and applied forces. The general equation for the force and moment acting on the cable can be expressed as

$$\frac{\partial \vec{T}}{\partial l_e} + \frac{\partial \vec{Q}}{\partial l_e} + \vec{W} + \vec{F}_{Eh} = m \frac{\partial^2 \vec{R}}{\partial t^2} \quad (13)$$

$$\frac{\partial \vec{M}}{\partial l_e} + \frac{\partial \vec{R}}{\partial l_e} * \vec{V} = -\vec{q} \quad (14)$$

where, \vec{R} is the position vector at the first node of cable, \vec{T} is the tension force vector at the first node of cable, \vec{V} is the shear force vector at the first node of cable, \vec{W} is the element weight per unit length, \vec{F}_{Eh} is the hydrodynamics loading vector per unit length, m is the mass per unit length, \vec{M} is the bending moment vector at the first node of cable, q is the distribution moment loading per unit length, ∂l_e is the length of the element and D is the diameter of the element.

2.1.3.1 Length and strain

The length of the mooring line can be stretched in response to tensile force arising from the motion of the WEC. The length of the mooring line can be expressed as

$$L = \int_{\text{anchor}}^{\text{WEC}} dx \quad (15)$$

and the strain of the mooring force of length L and for change in length due to stretch ΔL is given by

$$\varepsilon = \frac{\Delta L}{L} \quad (16)$$

2.1.3.2 Tension in the cable

The tension defines the force that the mooring line impose on the WEC. Moreover, the tension indicates the maximum and cyclic loads that the mooring lines are subjected to and are more vital in mooring design for extreme loads and fatigue analysis. The tension is related to the mooring line strain and strain-stress relation given by

$$T = f(\varepsilon, \dot{\varepsilon}, s) \quad (17)$$

In the case of linear stress-strain relationship, the tension can be stated as

$$T = EA\varepsilon \quad (18)$$

where, A is the cross-section area, E is the modulus of elasticity (Young's modulus).

2.1.3.3 Position of Mooring

The position of the mooring line is generally determined by the two positions in the global reference frame. First the anchor point and second the connection point with the breakwater. The position of the top of the mooring line $x(L)$ can be determined by the position of breakwater x_{BW} center of mass and the mooring line connection point on the breakwater x_o given by

$$x(L) = x_{BW} + x_o \cos \varphi \quad (19)$$

5.2 NUMERICAL SOLUTION

The forces acting on the structure can be determined by integrating the pressure over the wetted surface of the hybrid system body. The equations of motion are used for translation and rotational motion corresponding to the rigid body motions to get the general forms of forces and moments acting on the structure. The generalized form of first order hydrodynamic force and moment component can be expressed as

$$F_j e^{-i\omega t} = \left[-i\omega\rho \int_{x_0} \varphi(\vec{X}) n_j dS \right] e^{-i\omega t} \quad (20)$$

where x_0 is the mean wetted surface of ED-WEC. The forces due to fluid are categorized into active and reactive components. The active component or wave excitation force component consists of Froude-Krylov and diffraction force. The reactive force consists of radiation force due to the radiated waves induced by body. The solution for Eq. (20) is obtained as total first order hydrodynamic force and then divided into active and reactive component. The active component, first order hydrodynamic force for j^{th} Froude-Krylov due to incident wave after solving the total first order hydrodynamic force can be written as

$$F_{lj} = -i\omega\rho \int_{x_0} \varphi_l(\vec{X}) n_j dS \quad (21)$$

while for j^{th} diffracting force due to diffraction wave equation is given as

$$F_{Dj} = -i\omega\rho \int_{x_0} \varphi_D(\vec{X}) n_j dS \quad (22)$$

and for reactive force, j^{th} radiation force due to radiated wave induced on the rigid body motion for unit amplitude is given by

$$F_{Rjk} = -i\omega\rho \int_{x_0} \varphi_{Rk}(\vec{X}) n_j dS \quad (23)$$

The reactive force can also be expressed for real and imaginary parts. The radiated wave potential φ_{Rk} can be expressed as

$$F_{Rjk} = -i\omega\rho \int_{x_0} \left\{ \text{Re} \left[\varphi_{Rk}(\vec{X}) \right] + i \text{Im} \left[\varphi_{Rk}(\vec{X}) \right] \right\} n_j dS \quad (24)$$

and is substituted into Eq. (23) to determine the added mass and wave damping coefficients given by

$$F_{Rjk} = \omega\rho \int_{x_0} \text{Im} \left[\varphi_{Rk}(\vec{X}) \right] n_j dS - i\omega\rho \int_{x_0} \text{Re} \left[\varphi_{Rk}(\vec{X}) \right] n_j dS \quad (25)$$

$$F_{Rjk} = \omega^2 A_{jk} + i\omega B_{jk} \quad (26)$$

where A_{jk} is added mass and B_{jk} is radiation damping and is given by

$$A_{jk} = \frac{\rho}{\omega} \int_{x_0} \text{Im} \left[\varphi_{Rk}(\vec{X}) \right] n_j dS \quad (27)$$

$$B_{jk} = -\rho \int_{x_0} \text{Re} \left[\varphi_{Rk}(\vec{X}) \right] n_j dS \quad (28)$$

The solution obtained from the Laplace equations for the diffraction and radiation problems can be combined with the equation of motion of the floating breakwater to analyze the dynamic response of the structural system in time domain. The equation of motion in the time domain is expressed as

$$m_a \ddot{z}(t) + C\dot{z}(t) + Kz(t) = F(t) \quad (29)$$

m_a is the added mass in the mass matrix, C is the hydrodynamic damping in the damping matrix, K is the total stiffness matrix, $F(t)$ is the external force which has constant amplitude. On employing the convolution integral form, the equation of motion can also be defined as

$$(m + m_a) \ddot{z}(t) + c\dot{z}(t) + Kz(t) + \int_0^t V(t-\tau) \dot{z}(\tau) d\tau = F(t) \quad (30)$$

where m_a is the added mass matrix, c is the damping matrix including radiation damping results, V is the velocity impulse function and K is the total stiffness matrix. The response amplitude operator (RAO) is the motion of a floating structure in six degrees of freedom (Surge, Sway, Heave, Roll, Pitch and Yaw) due to hydrodynamic wave force. The RAOs are generally utilized as an input data for the calculation of displacement, acceleration and velocities at a given location. Basically, RAO is calculated by the ratio of response amplitude x_j of

breakwater to the wave amplitude η_i for linear motion. In the case of rotational motion, it is defined as the ratio of response amplitude x_j of breakwater to the wave slope α_i .

$$RAO = \frac{x_j}{\eta_i}, \text{ where } x_j = u_j, j = 1, 2, 3 \quad (31)$$

$$RAO = \frac{x_j}{\alpha_i}, \text{ where } x_j = \theta_{j-3}, j = 4, 5, 6 \quad (32)$$

where α_i is the wave slope, η_i is the wave amplitude, and x_j is the response amplitude of floating breakwater in rotational θ_{j-3} and displacement u_j mode. All the wave forces considered interacting with the structure are a function the wetted body surface only and is independent of the structural mass characteristics of the body.

5.3 NUMERICAL MODEL SETUP

The numerical modelling for the hybrid breakwater system consisting of ED point absorber WEC integrated with different shapes of floating breakwater such as box-type FBW, trapezoidal-type FBW, π -type FBW, parabolic-type FBW and semi-circular-type FBW on the sea side of the hybrid system to investigate wave structure interaction response and behavior in regular waves. Similar study is performed for Rectangular-type FBW by Zhou et al. (2021, 2022) on 2D numerical wave tank using CCM+CFD software. The ED-WEC has only one degree of freedom and is allowed to oscillate only in heave direction. A similar 2D numerical model is used to study the heave motion of floating breakwater as an oscillating buoy WEC (Zhang et al., 2020a) and a hybrid system of floating breakwater and oscillating buoy WEC (Zhang et al., 2020b, 2021a). The design of the Edinburgh duck body is of circular arc from stern of radius R and is divided symmetrically about the red dash line l_d of length 11.8 m (Fig. 2f). The curvature of the duck can be expressed as

$$X^2 + (5 - Z^2) = R^2 \quad (33)$$

where R is the distance from center of rotation to the curvature of the shape and it can be expressed as

$$R = \begin{cases} 5e^{\frac{2\pi}{100}Z}, & \text{for } X < 0, 11.8 \geq R \geq 5 \\ 5, & \text{for } X \geq 0 \end{cases} \quad (34)$$

The ED is inclined at $\beta = 45^\circ$ to the still water level. The weight of ED-WEC is kept as 20730 kg and is scaled down to 1/5. The shapes of FBWs were chosen from different literatures and is adjusted on the box-type FBW. So, without increasing the submergence volume by changing the drafts, all the shapes are compared and the main dimensions for all shapes are kept same. The general common parameters of different shapes of breakwaters are B/d_b ratio is 3.0 (B is width of FBW and d_b is draft of FBW), weight of FBW is 369000 kg, weight of ED WEC is 20730 kg, convergence mesh size is 0.3m and length of FBW is 20m. The detail parametric design of the floating breakwater is mentioned in Table 1. The different shapes of FBW considered in the offshore region is having its own importance and advantages in the wave attenuation. The box-type FBW is simple structure with high durability, easy in maintenance

and flexible in draft variation with ballasting.

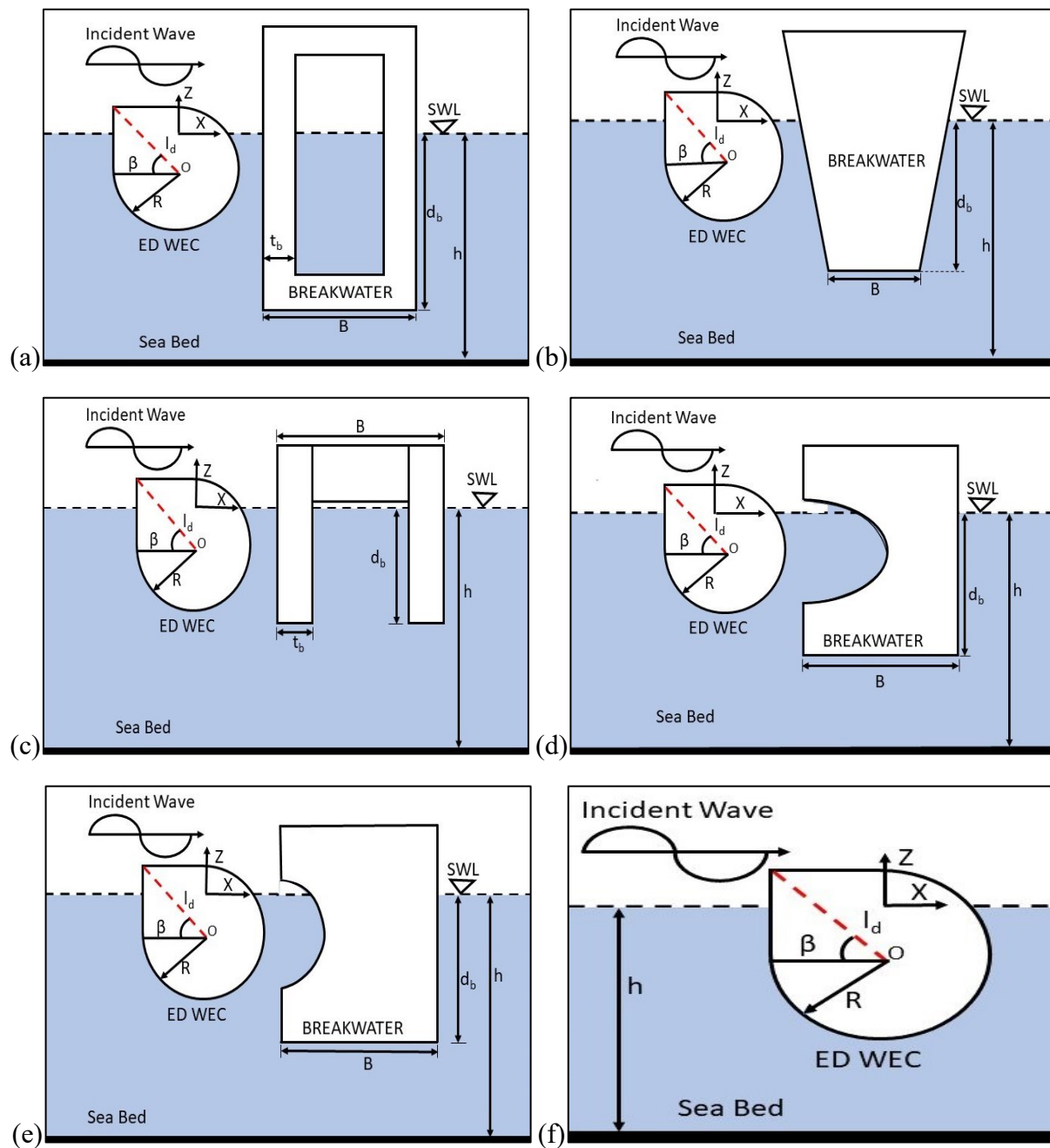


Figure. 2. Schematic diagram of ED-WEC integrated to (a) box-type, (b) trapezoidal-type, (c) π -type, (d) parabolic-type, (e) Semi-circular-type shapes of breakwaters and (f) ED-WEC.

The π -type FBW are a low-cost solution to increase draft and enhance wave reflection. But the buoyancy force decreases with increase in draft, so to achieve high wave reflection, the required draft thickness of the legs has to be increased. The trapezoidal type FBW generates smooth wave attenuation as it splits incident wave into components on its slope and regulates reflected waves effectively and requires to be moored to prevent overturning under high waves. Further, as the parabolic reflector reflect sound towards focal point, the parabolic-type FBW is used to converge propagating waves towards focus position. The wave energy harvesting can be increased when WEC is placed at focus but adjusting focus at the appropriate position for

WEC can sometimes results in increase in width of parabolic opening which results in increase in overall height of FBW. The semi-circular-type FBW considered in the present study is the modified dimensions of parabolic-type FBW with same opening and depth of parabola as radius.

Table1. Parametric details of floating breakwaters

Shape of floating breakwater	Parameters	Values
Box-type FBW	Draft of FBW (d_b)	3.0m
	Thickness of box	1.5m
	Height of center open of box	2.0m
	Submerged open area height	1.5m
Trapezoidal-type FBW	Draft of FBW (d_b)	2.24m
	Base at water surface level	9.31m
	Base at bottom of FBW	6.72m
	Slope of FBW	$\sqrt{3} : 1$
π - type FBW	Draft of FBW (d_b)	4.0m
	Top width of FBW	12.0m
	Depth of top deck	2.0m
	Height of leg of FBW	4.5m
	Thickness of leg of FBW	2.25m
Parabolic-type FBW	Draft of FBW (d_b)	2.5m
	Mouth of parabolic FBW (b)	3.0m
	Depth of parabolic FBW (a)	0.75m
	Focus of parabolic FBW $\left(\frac{b^2}{16a}\right)$	0.75m
	Thickness of FBW at top & bottom	1.0m
Semi-circular-type FBW	Draft of FBW (d_b)	2.7m
	Radius of Semi-Circle	2.2m
	Thickness of FBW at top & bottom	0.5m

The box-type and π -type FBW as in Rajabi and Ghassemi, 2021 considered in the present study is having variation in the dimensions and the total submergence volume of all the shapes are kept constant without changing the core dimensions. The parabolic-type FBW is having depth and focus of parabolic FBW same as in Zhang and Ning (2019) and the other parameters are modified to keep submergence volume constant whereas semi-circular-type FBW is considered on modifying the mouth and depth of parabolic FBW. The parameters for the trapezoidal-type FBW is selected based on Patil and Karmakar (2023).

5.4 NUMERICAL RESULTS AND DISCUSSION

The numerical investigation is performed using Ansys AQWA for the variation of different

parameters of ED-WEC and FBW. The ED-WEC is studied for non-dimensional width within $0.25 \leq W_{ed} / h \leq 0.75$, non-dimensional draft of ED-WEC within $0.045 \leq Z_c / h \leq 0.065$, distance between the center of rotation Z_c of ED-WEC and floating breakwater within $0.1 \leq B_k / h \leq 0.3$ and incident angle within $0^\circ \leq \theta \leq 45^\circ$. In addition, the numerical validation of the present model is performed with Ning et al. (2005) and Dimitrios et al. (2021) using appropriate correlation.

5.4.1 Validation of Numerical Model

The validation of the theoretical formulation is performed with the data available in the literatures. The validation for the vertical bottom seated cylinder placed in front of vertical, bottom standing, surface penetrating orthogonal rigid and impermeable breakwater is performed. The global right hand cartesian coordinate system $O-XYZ$ is considered at the origin at the connection of the arms of the orthogonal wall at the seabed with OZ pointing upwards. The radius of the cylindrical body is taken as R and draught is considered to be d_v .

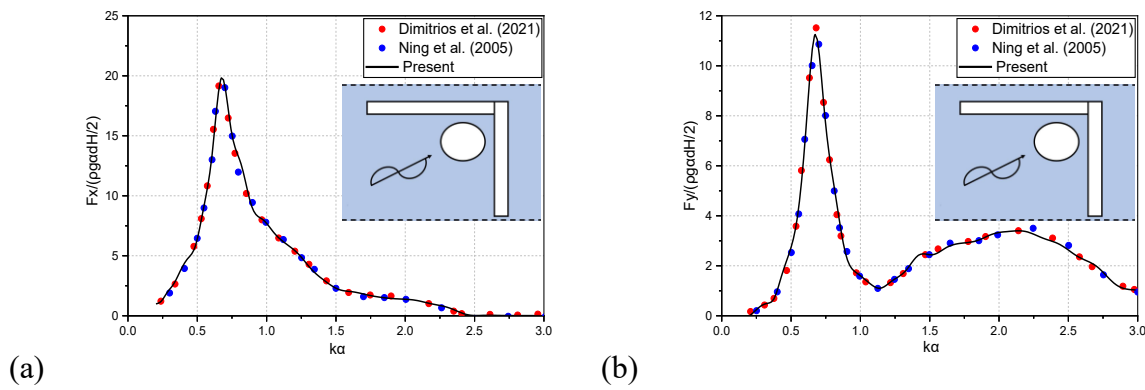


Fig. 3: Excitation wave forces on (a) horizontal and (b) vertical direction of a bottom seated cylinder in front of an orthogonal breakwater.

The spacing between the centre of the cylinder and the two arms of the orthogonal walls is d_1 and d_2 . The local cylindrical coordinate system (x^1, y^1, z^1) is defined from the origin (X, Y) at the sea bottom of the vertical axis of the cylinder, and the distance d_1 and $d_2 = 1.2R$. The length of the arms of the orthogonal walls is taken as $50R$, the water depth equals to $h/R = 2$ and the wave heading angle α is taken as $\pi/6$. In Fig. 3(a,b), the horizontal excitation wave forces on the cylinder in horizontal and vertical direction are compared with the results of Dimitrios et al. (2021) and Ning et al. (2005). The numerical results obtained in the present study shows a very good agreement with the results obtained by Dimitrios et al. (2021) and Ning et al. (2005).

5.4.2 Effect on variation of ED-WEC parameters

The interaction of ED-WEC as a single floater body device is examined to analyse the performance of solo ED-WEC for the variations of its parameters. The variation of change in width and draft of solo ED-WEC in heave direction for (i) motion response and (ii) force response is shown in Fig. 4(a,b) and Fig. 5(a,b) respectively.

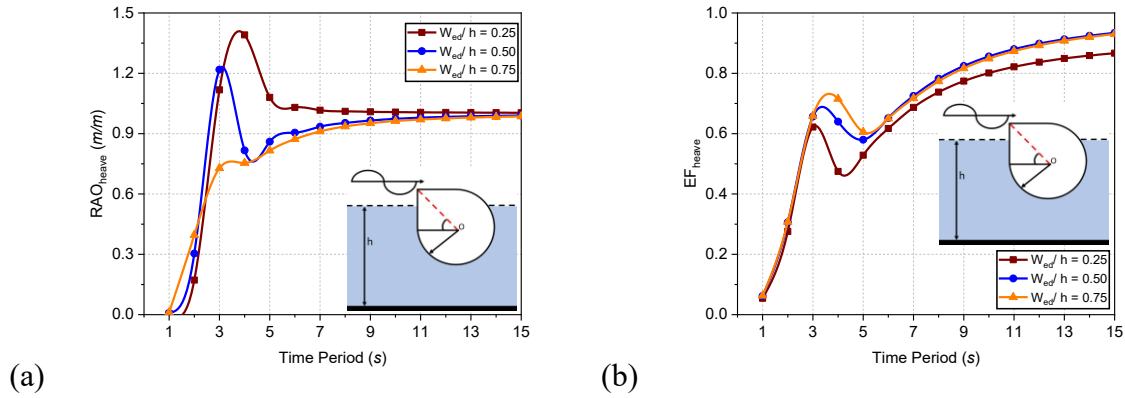


Fig. 4: Variation in (a) motion response and (b) force response in heave direction for $Z_c/h = 0.055$ and $B_k/h = 0.1$ for different width of single ED-WEC.

In Fig. 4(a,b), the motion and force response of the ED-WEC is obtained for varying width of ED-WEC considering $Z_c/h = 0.055$ and $B_k/h = 0.1$. The study noted that, the amplitude of RAO-heave (Fig. 4a) is decreasing with the increase in the width of ED-WEC while the amplitude of wave excitation force for heave on the structure is increasing. In Fig. 4(a), for deep water condition ($1.0s \leq T \leq 5.0s$) the change in behaviour and amplitude for the variation of width is observed with respect to $W_{ed}/h = 0.50$. The amplitude of RAO-heave for $W_{ed}/h = 0.25$ is 12% more while for $W_{ed}/h = 0.75$ is 40% less as compared to $W_{ed}/h = 0.50$ in deep water region. Further, the change in phase is observed for width $W_{ed}/h = 0.50$. In the case of intermediate water condition ($T \geq 6.0s$), the values for RAO-heave tends to converge for different widths. In Fig. 4(b), it is observed that the wave excitation force in heave for $W_{ed}/h = 0.25$ is nearly 10% less and for $W_{ed}/h = 0.75$ is 10% more compared to $W_{ed}/h = 0.50$ for deep water condition. The variation is observed only for the time period within $3.0s \leq T \leq 5.0s$. In the case of intermediate water condition $T \geq 6.0s$, the wave excitation forces tend to converge with a minor variation in the amplitude, while for initial time period $T \leq 3.0s$, the behaviour is almost identical. The study noted that the variation in amplitude or the behaviour for the variation in width is large for $W_{ed}/h = 0.50$. Hence variation in the width $W_{ed}/h = 0.50$ is considered as a threshold value and further study is carried out considering the value for other variations. The decrease in the variation of the amplitude in RAO-heave for increase in width is due to the distribution of energy of incident wave over a large area while increase in the variation in the amplitude of wave excitation force in heave for increase in width is due to the large area for same value of pressure.

In Fig. 5(a,b), on varying the draft of ED-WEC, the motion and force response of ED-WEC is obtained considering $W_{ed}/h = 0.50$ and $B_k/h = 0.1$. It is observed that the amplitude of RAO-heave (Fig. 5a) and the amplitude of wave excitation force is increasing with the increase in draft of ED-WEC. Further, in the case of $Z_c/h = 0.045$ and $Z_c/h = 0.055$ the amplitude in RAO-heave is nearly equal but for $Z_c/h = 0.065$ the amplitude in RAO-heave is 3.4 times higher than the RAO-heave as compared to $Z_c/h = 0.055$ for deep water condition

($1.0s \leq T \leq 5.0s$) at $T = 3.0s$ and for intermediate water condition ($T \geq 6.0s$), the RAO-heave converges to other drafts amplitudes and behaves identically. Hence, the RAO-heave is at resonance at $T = 3.0s$ for draft of $Z_c / h = 0.065$. On the other hand, in Fig. 5(b), it is observed that the variation in amplitude for wave excitation force is less than 10% for $Z_c / h = 0.045$ with no phase difference and for $Z_c / h = 0.065$ it is nearly 42% more as compared with $Z_c / h = 0.055$. Thus, for draft variation, $Z_c / h = 0.055$ it is considered as a threshold value and further studies is carried out considering $Z_c / h = 0.055$ for other variations.

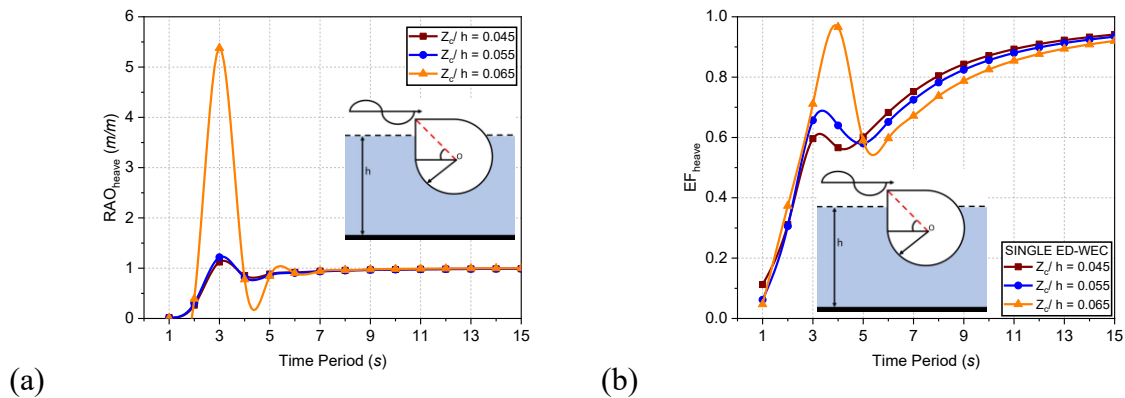
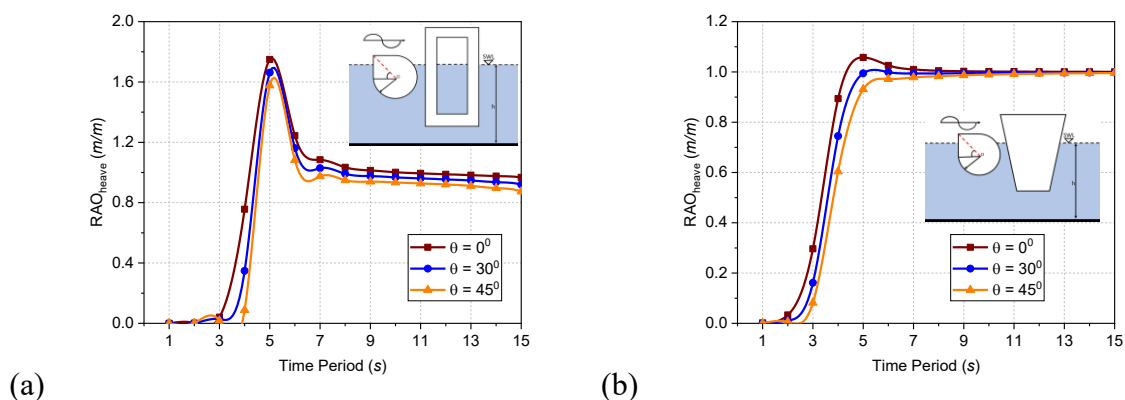


Fig. 5: Variation in (a) motion response and (b) force response in heave direction for $W_{ed} / h = 0.50$ and $B_k / h = 0.1$ for different draft of single ED-WEC.

5.4.3 Effect of incident angle on floating breakwaters

The hydrodynamic analysis of the floating breakwater for change in angle of incident waves are examined in the present sub-section. The variation of incident angles in RAO-heave and wave excitation forces is obtained for different shapes of floating breakwater (box-type FBW, trapezoidal-type FBW, π -type FBW, parabolic-type FBW and semi-circular-type FBW) in hybrid system consisting of ED-WEC and FBW in Fig. 6(a-e) and Fig. 7(a-e) followed by comparison of all different shapes in Fig. 6(f) and Fig. 7(f) for $W_{ed} / h = 0.50$, $Z_c / h = 0.055$, $B_k / h = 0.1$ at wave heading angle of $\theta = 0^\circ$ respectively.



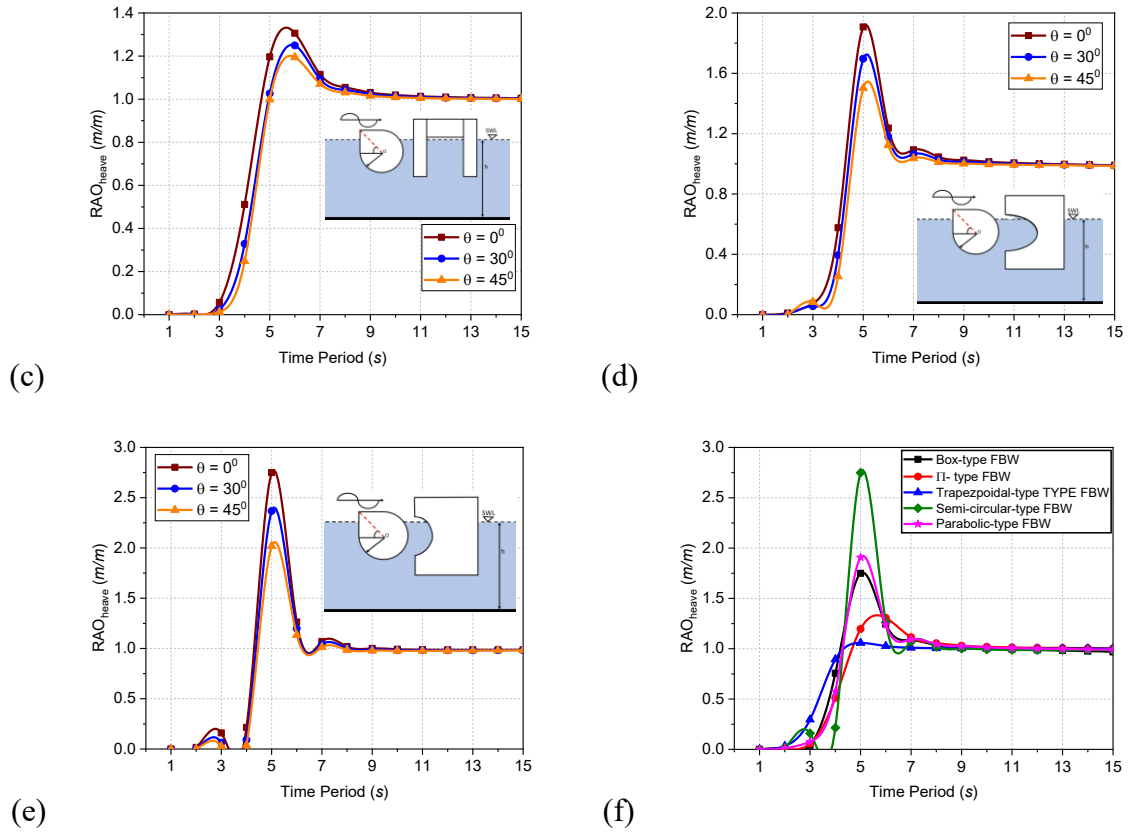
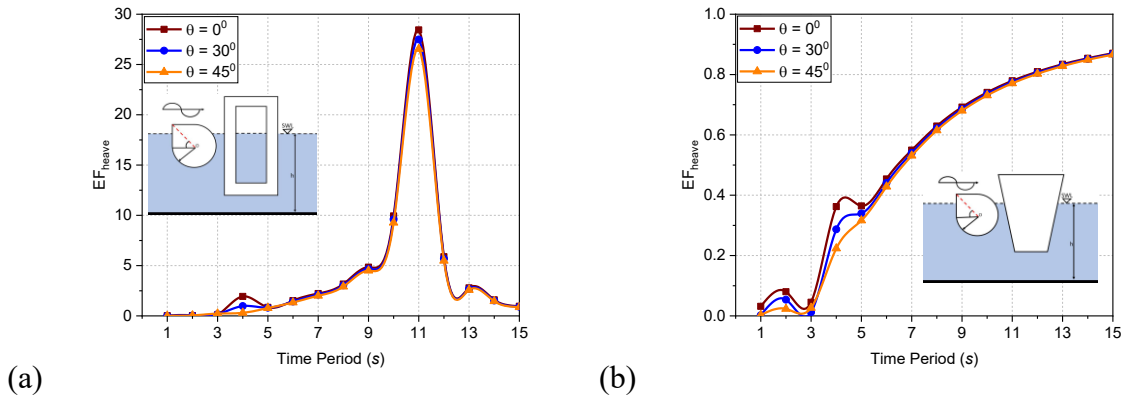


Fig. 6: Variation of motion response in heave direction for (a) box-type FBW (b) trapezoidal-type FBW (c) π -type FBW (d) parabolic-type FBW (e) semi-circular-type FBW for different angle of incident and (f) comparison of different shapes of FBW for $W_{ed} / h = 0.50$, $Z_c / h = 0.055$ and $B_k / h = 0.1$.



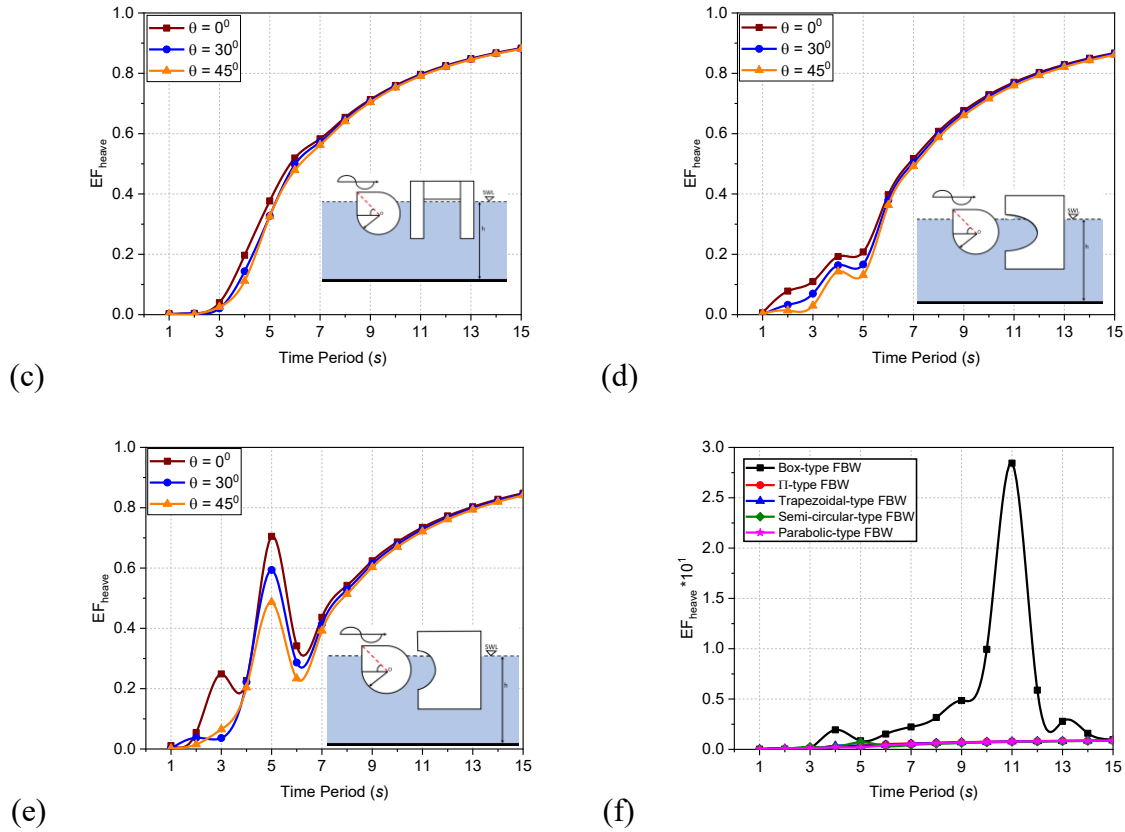


Fig. 7: Variation of excitation force response in heave direction for (a) box-type FBW (b) trapezoidal-type FBW (c) π -type FBW (d) parabolic-type FBW (e) semi-circular-type FBW for different angle of incident and (f) comparison of different shapes of FBW for $W_{ed} / h = 0.50$, $Z_c / h = 0.055$ and $B_k / h = 0.1$.

In Fig. 6(a-e) and Fig. 7(a-e), it is observed that the RAO-heave and wave excitation force in heave is decreasing with the increase in angle of incidence for all shapes of breakwaters in deep water conditions ($1.0s \leq T \leq 5.0s$). This is due to the fact that, with the change in incident wave angle, the translation and rotational motion will increase for same wave energy incident at different angles. Hence RAO-heave and wave excitation force in heave shows reduction in their values. Although the change in amplitude of RAO-heave is very small (Table 2). Further, for RAO-heave all the hybrid system of different shapes of FBW achieves its peak values near $T = 5.0s$ except π -shaped hybrid system. The peak value of π -shaped hybrid system is observed at deep and intermediate water depth. Also, the behaviour in intermediate water depth condition ($T \geq 6.0s$), all values of RAO-heave for all the shapes tends to converge and shows identical behaviour including its amplitude values (Fig. 6f). The maximum and minimum values of RAO-heave for different shapes of hybrid system is presented in Table 2.

Table 2: RAO-heave for different shapes of FBW

Shapes of Floating Breakwater (FBW)	Minimum RAO-Heave (m/m) (i.e., $\theta = 45^\circ$)	Maximum RAO-Heave (m/m) (i.e., $\theta = 0^\circ$)
-------------------------------------	--	---

Box-type FBW	1.58	1.75
Trapezoidal-type FBW	0.93	1.05
π -type FBW	1.20	1.30
Parabolic-type FBW	1.50	1.90
Semi-circular-type FBW	2.00	2.75

In Table 2, it is observed that semi-circular-type of FBW achieved the maximum RAO-heave values with highest difference between maximum and minimum RAO-heave while trapezoidal-type FBW achieved lowest maximum peak values (Fig. 6f). On the other hand, wave excitation force for trapezoidal-type FBW, π -type FBW and parabolic-type FBW shows identical behaviour for all values of incident wave angle in both deep and intermediate water condition. In deep water condition minor variations in amplitude are observed but for intermediate depth the result is nearly identical with continuous increment in the amplitude. Semi-circular-type FBW shows a large variation as compared to other shapes of FBW for deep water condition ($1.0s \leq T \leq 5.0s$) but in intermediate water condition ($T \geq 6.0s$), it behaves similar as other shape of breakwater except box-type FBW. In the case of semi-circular-type FBW, after attaining peak value in deep water condition, the decrement in the value is noted and thereafter attains the similar behaviour as of other FBW except box-type FBW while tending towards intermediate water condition. The box-type FBW is having different behaviour from rest of the shape with highest difference in the magnitude of nearly 97% with respect to rest of the shapes. This can be clearly seen in Fig. 7(f). In the case of deep-water condition, the behaviour is nearly same for all incident wave angle but in intermediate water condition, the resonance condition is achieved at $T = 11.0s$. The maximum and minimum values of wave excitation force in heave for different shapes of hybrid system is mentioned in Table 3.

Table 3. Value of heave excitation force (EF-heave) for different shapes of FBW at $T = 5.0s$.

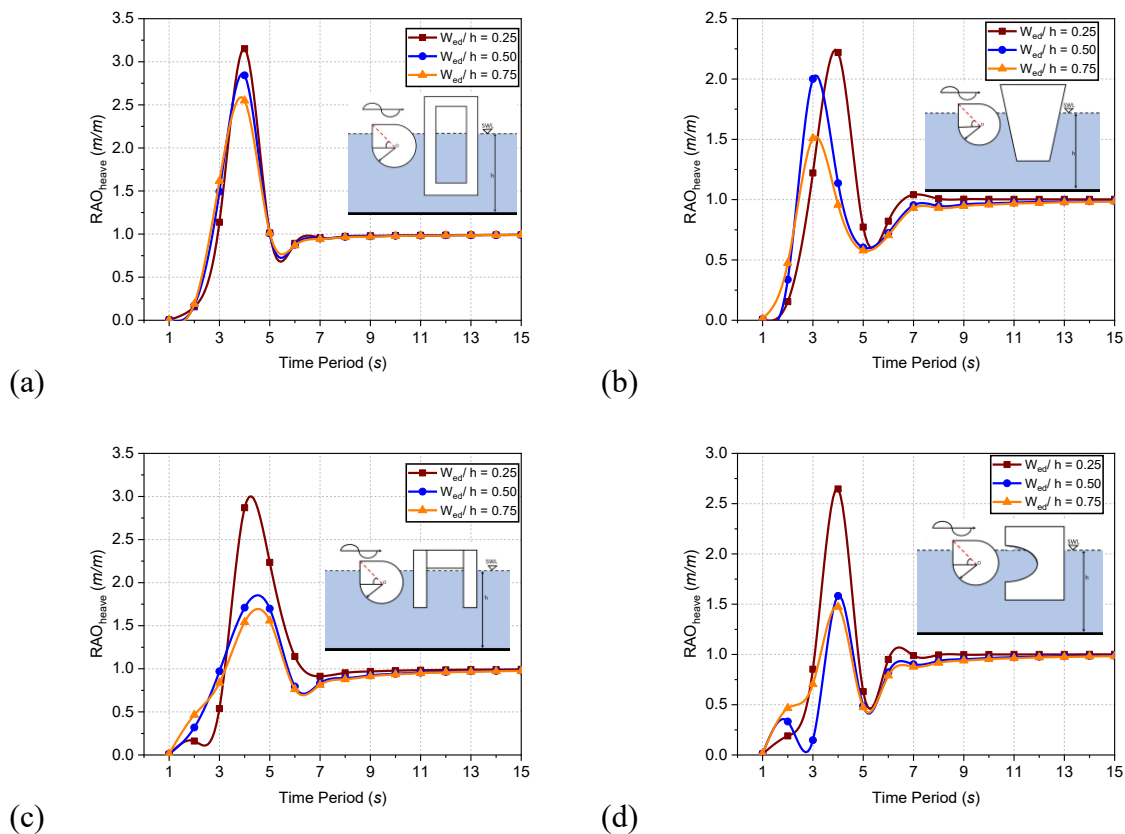
Shape of Breakwater	Minimum EF-heave	Maximum EF-heave
Box-type FBW	0.78	0.78
Trapezoidal-type FBW	0.36	0.32
π -type FBW	0.36	0.31
Parabolic-type FBW	0.21	0.13
Semi-circular-type FBW	0.70	0.49

In Table 3, it is observed that, the resonance value is achieved for box-type FBW and rest of the shapes behaves almost identical. The study suggests that, the effect of incident wave angle for breakwater in the hybrid system is almost independent from the shape of FBWs for intermediate water depth conditions.

5.4.4 Effect of width of WEC

The width of the ED-WEC is one of the important parameters affecting the hydrodynamic behaviour and characteristics of the hybrid floating breakwater system consisting of ED-WEC integrated to floating breakwaters (Zhou et al., 2021, 2022). Different dimensionless widths of ED-WEC are taken into consideration for the analysis with different shapes of breakwaters as

mentioned in section 3. The variation of motion and excitation force response for varied dimensionless widths in heave direction for different shape of breakwaters are presented in Fig. 8(a-e) and Fig. 9(a-e) and comparative study between different shapes of FBW for $W_{ed}/h = 0.50$ are shown in Fig. 8(f) and Fig. 9(f) for $Z_c/h = 0.055$, $B_k/h = 0.1$, at $\theta = 0^\circ$. In Fig. 8(a-e), it is observed that the amplitude for RAO-heave is decreasing with increase in width of ED-WEC in the hybrid system consisting of ED-WEC with FBW similar to Fig. 4(a). In the case of deep water condition ($1.0s \leq T \leq 5.0s$), the variation in RAO-heave for box-type FBW, trapezoidal-type FBW, π -type FBW and parabolic-type FBW have 10%, 10%, 62% and 65% more for $W_{ed}/h = 0.25$ and 10%, 25%, 8% and 6% less for $W_{ed}/h = 0.75$ compared to $W_{ed}/h = 0.50$ respectively, with no phase difference except trapezoidal-type FBW. In trapezoidal-type FBW phase difference by $1.0s$ within $3.0 < T < 4.0$ is observed for $W_{ed}/h \geq 0.50$. On the other hand, for semi-circular-type FBW different behaviour in RAO-heave is observed in deep water conditions. Multi-peaks are achieved in semi-circular-type FBW with decrease in amplitude of RAO-heave. In the case of $W_{ed}/h = 0.25$, the first peak is 12% more while 60% less for $W_{ed}/h = 0.75$ compared to $W_{ed}/h = 0.50$ with phase difference. The second peak is obtained nearly after $2.0s$, for all the variations of draft with 32% more for $W_{ed}/h = 0.25$ and around 4% less for $W_{ed}/h = 0.75$ compared to $W_{ed}/h = 0.50$ with nearly no phase difference. In the case of intermediate water depth condition ($T \geq 6.0s$), all the shapes of breakwater converge to RAO-heave value of nearly 1.0 (Fig. 8f). The variations for draft are significant in deep water conditions but the convergence and the behaviour are identical for intermediate water conditions.



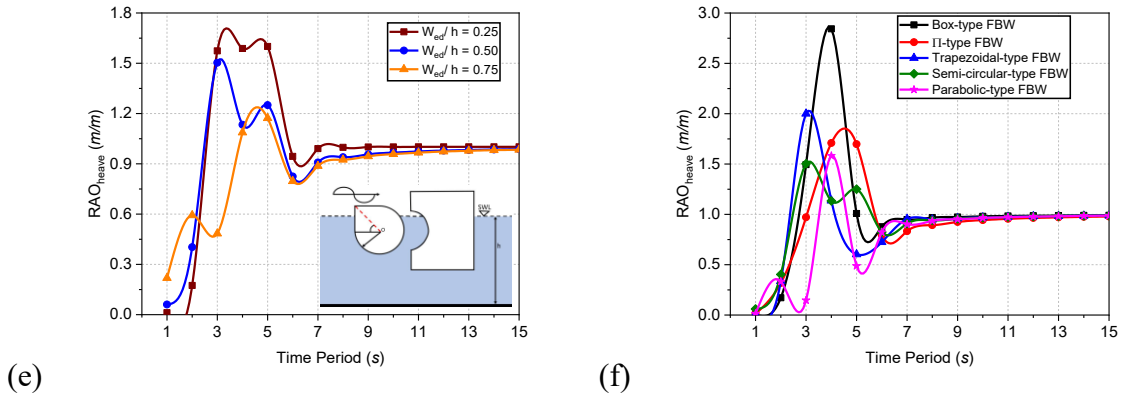


Fig. 8: Variation of motion response in heave direction for (a) box-type FBW (b) trapezoidal-type FBW (c) π -type FBW (d) parabolic-type FBW (e) semi-circular-type FBW for different width of ED and (f) comparison of different shapes of FBW for $W_{ed}/h = 0.50$, $Z_c/h = 0.055$ and $B_k/h = 0.1$.

In Fig. 9(a), for deep water condition ($1.0s \leq T \leq 5.0s$), different behaviour in the pattern of excitation force is observed for box-type FBW. In the case of change in structural width W_{ed}/h , initially the force response decreases but suddenly shows increment for variation in the width. Considering $W_{ed}/h = 0.25$ the force response is noted to be 24% more as compared to $W_{ed}/h = 0.50$ and for $W_{ed}/h = 0.75$ the force response increases to attain its peak value at $T = 4.0s$ which resembles the resonance condition for $W_{ed}/h = 0.75$ at $T = 4.0s$. In intermediate water condition ($T \geq 6.0s$), less variation in force response is observed but at $T = 11.0s$, a sudden fall is noted which shows an instability as the interaction of the structure and the wave is reduced at that period of time resulting in the waves to pass under the structure. As the waves passes under the structure it causes disturbance on the lee ward side of the breakwater and the major purpose of breakwater to create calm condition on lee ward side fails. Similar behaviour is observed for π -type FBW (Fig. 9c) in deep water condition while for intermediate water condition the force response converges for all drafts. In the case of trapezoidal-type FBW (Fig. 9b), the force response decreases with the increase in width. At deep water condition for $T = 3.0s$, $W_{ed}/h = 0.25$, the force response is 62% more while for $W_{ed}/h = 0.75$ the force response is around 13% less compared to $W_{ed}/h = 0.50$ with no phase difference. In the case of parabolic-type FBW (Fig. 9d), initially the force response behaviour is similar to that of box-type FBW in deep water condition, but for $W_{ed}/h = 0.25$ the force response is 9.5% more with no phase difference ($T = 4.0s$) while for $W_{ed}/h = 0.75$ it is 11.5% more with delayed phase difference ($T = 5.0s$) compared to $W_{ed}/h = 0.50$. Meanwhile the structural width $W_{ed}/h = 0.25$ and $W_{ed}/h = 0.50$ attains its lowest values at $T = 5.0s$, where width $W_{ed}/h = 0.75$ is achieves its maximum peak value. In intermediate water condition ($T \geq 6.0s$) the force response behaviour is similar to other configurations of FBW. The force response of semi-circular-type FBW (Fig. 9e) is noted to be different from rest of the shapes

of breakwater. In deep water condition, the force response for width $W_{ed}/h = 0.50$ and $W_{ed}/h = 0.75$ behaves identically except for initial time period within $1.0 < T < 2.0$. In the initial time period within $1.0 < T < 2.0$, the force response for $W_{ed}/h = 0.25$ is 78% less and for $W_{ed}/h = 0.75$ is 91% more compared to $W_{ed}/h = 0.50$. The comparison of different shapes shown in Fig. 9(f) suggest that the highest force response is achieved in the case of parabolic-type FBW in single peak followed by semi-circular-type FBW with multiple peaks.

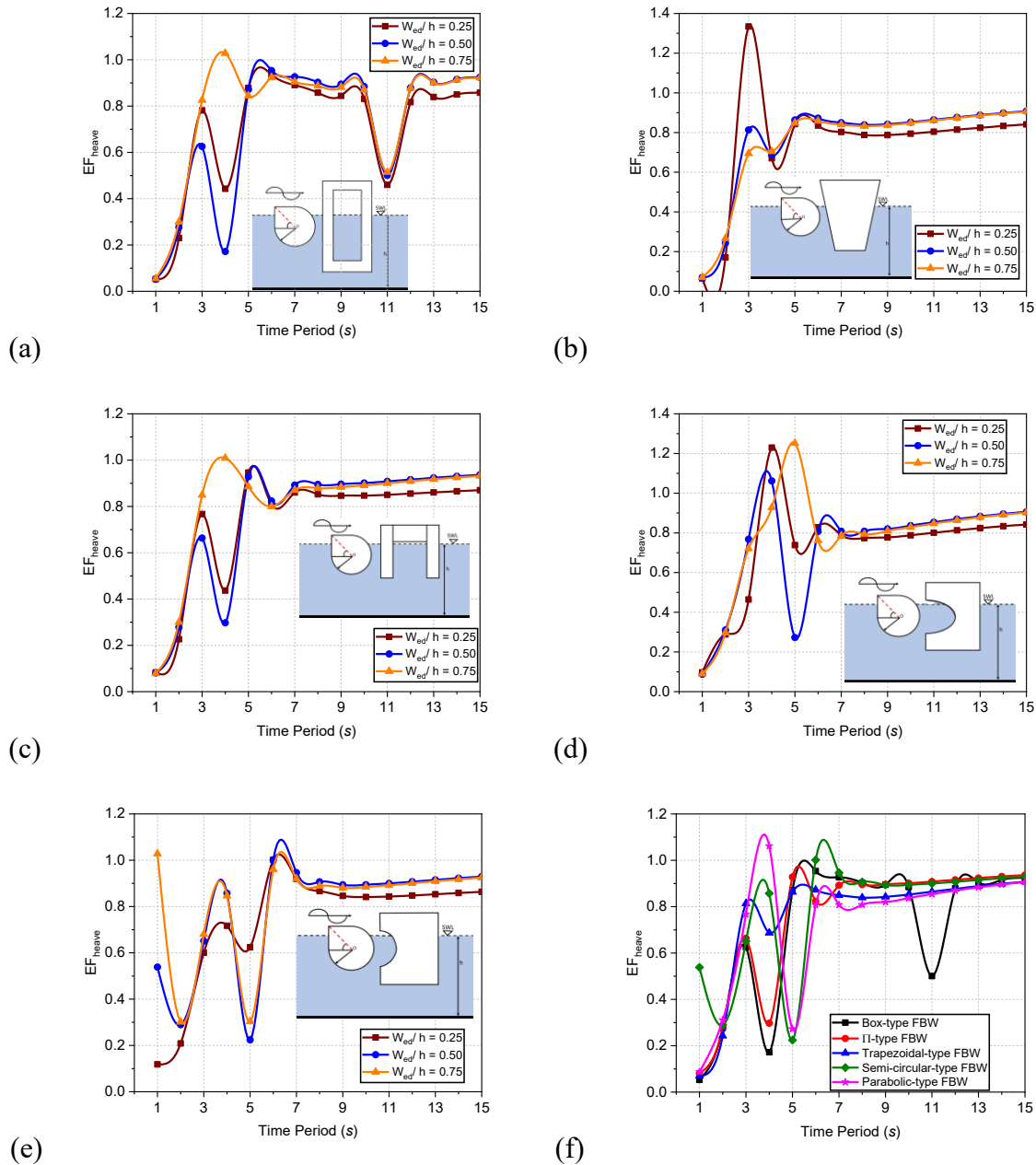
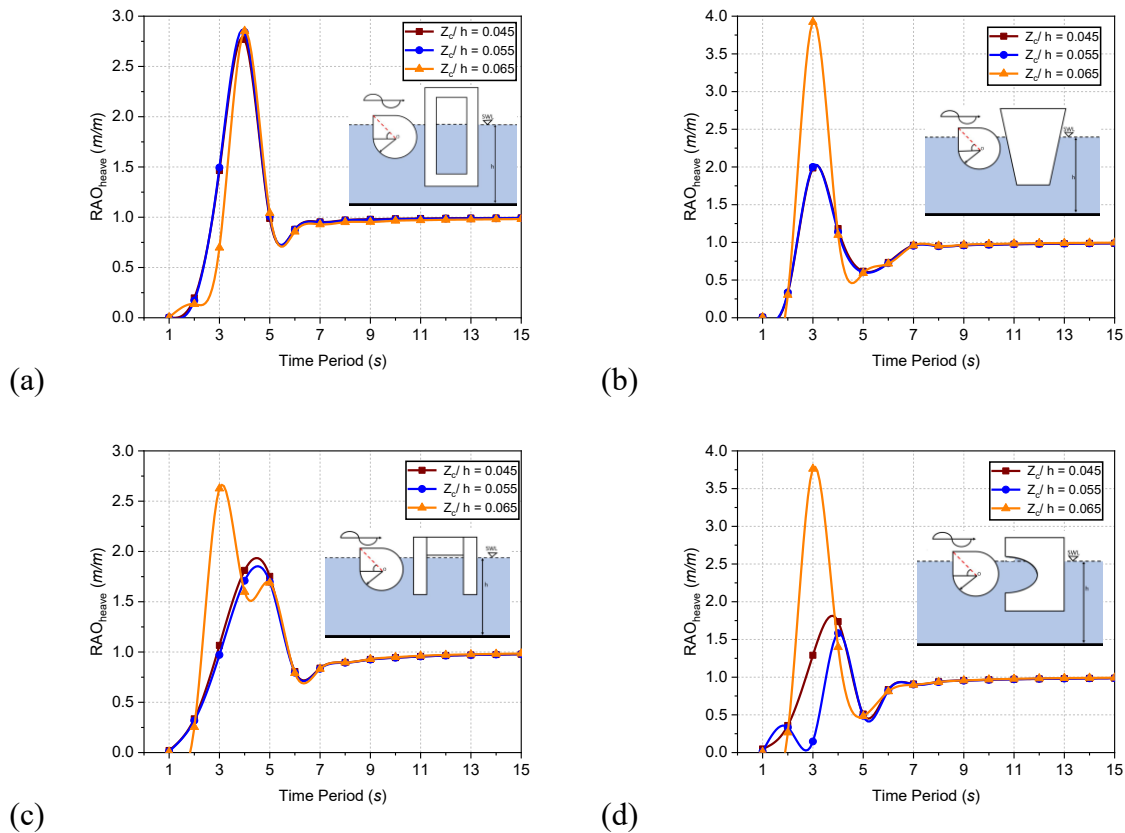


Fig. 9: Variation of excitation force response in heave direction for (a) box-type FBW (b) trapezoidal-type FBW (c) π -type FBW (d) parabolic-type FBW (e) semi-circular-type FBW for different width of ED and (f) comparison of different shapes of FBW for $W_{ed}/h = 0.50$, $Z_c/h = 0.055$ and $B_k/h = 0.1$.

5.4.5 Effect of draft of WEC

The draft of the ED-WEC plays an important role in analysing the hydrodynamics behaviour and the characteristics of the hybrid floating breakwater system consisting of ED-WEC integrated to floating breakwaters (Zhou et al., 2021, 2022). Increasing the draft of ED-WEC increases the buoyancy force as the submerged area is increased. Different dimensionless drafts of the ED-WEC are taken into consideration for the analysis with different shapes of floating breakwaters. The variation of motion response (Fig. 10a-e) and force response (Fig. 11a-e) for varied dimensionless drafts in heave direction for different shaped of floating breakwaters such as box-type FBW, trapezoidal-type FBW, π -type FBW, parabolic-type FBW and semi-circular-type FBW is analysed and the comparison between different shapes of FBW for $Z_c/h = 0.055$ are shown in Fig. 10(f) and Fig. 11(f) for $W_{ed}/h = 0.50$, $B_k/h = 0.1$, at $\theta = 0^\circ$. In Fig. 10(a-f), the variation of the motion response is analysed for different draft in heave direction in the case of ED-WEC integrated with FBW of different configuration. In Fig. 10(a-e), it is observed that, for $Z_c/h = 0.065$, the resonance occurs within $1.0s \leq T \leq 5.0s$ for all the shapes of breakwater in the hybrid system consisting of ED-WEC integrated to floating breakwaters. The resonance is due to the increase in buoyancy force of the ED-WEC for the draft $Z_c/h = 0.065$. In deep water conditions ($1.0s \leq T \leq 5.0s$), for every shape, the motion response pattern is different but for intermediate water condition ($T \geq 6.0s$) the motion response pattern of all the shapes converges.



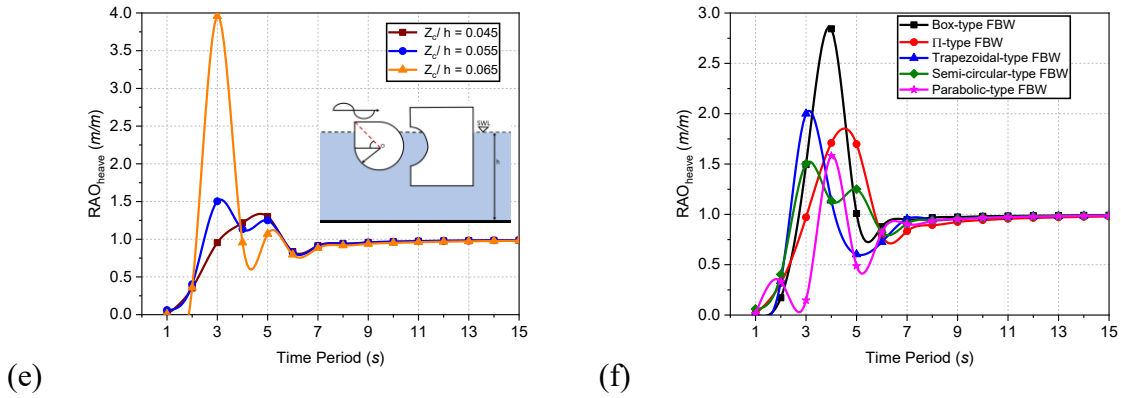
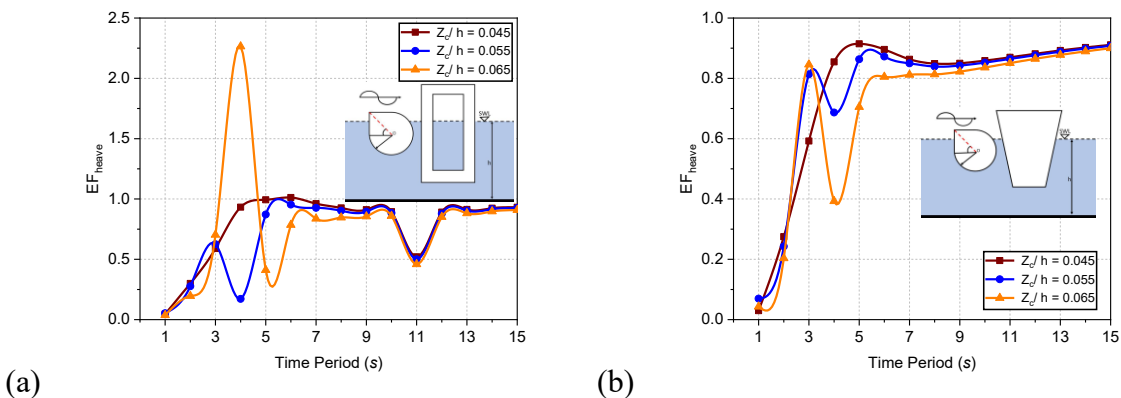


Fig. 10: Variation of motion response in heave direction for (a) box-type FBW (b) trapezoidal-type FBW (c) π -type FBW (d) parabolic-type FBW (e) semi-circular-type FBW for different draft of ED and (f) comparison of different shapes of FBW for $Z_c/h = 0.055$, $W_{ed}/h = 0.50$ and $B_k/h = 0.1$.

In the case of box-type FBW (Fig. 10a), trapezoidal-type FBW (Fig. 10b) and π -type FBW (Fig. 10c), the motion response is identical for the structural draft of $Z_c/h = 0.045$ and $Z_c/h = 0.055$. As compared with structural draft of $Z_c/h = 0.055$, for box-type FBW, the structural draft $Z_c/h = 0.065$ have slight variation of around 3-7% only with no phase difference. In the case of trapezoidal-type FBW at structural draft $Z_c/h = 0.065$, the resonance is observed at $T = 3.0$ s and a variation of 95% is observed with no change in phase. For π -type FBW approximately 44% more variation is observed at resonance condition ($T = 3.0$ s) with phase difference of 1.0 s. For parabolic-type FBW (Fig. 10d), the slight variation of 12.5% is observed for initial structural draft of $Z_c/h = 0.045$ and $Z_c/h = 0.055$, with no change in phase while for the draft $Z_c/h = 0.065$, the resonance is noted with a large variation of nearly 1.4 folds with phase difference of 1.0 s. In the case of semi-circular-type FBW, with the increase in structural draft, the multi-peaks are noted. Though the motion response for $Z_c/h = 0.045$ and $Z_c/h = 0.055$ is having variation of 14% with phase difference of 1.0 s but for $Z_c/h = 0.065$ the variation is about 1.67 times compared to $Z_c/h = 0.055$ with no phase difference.



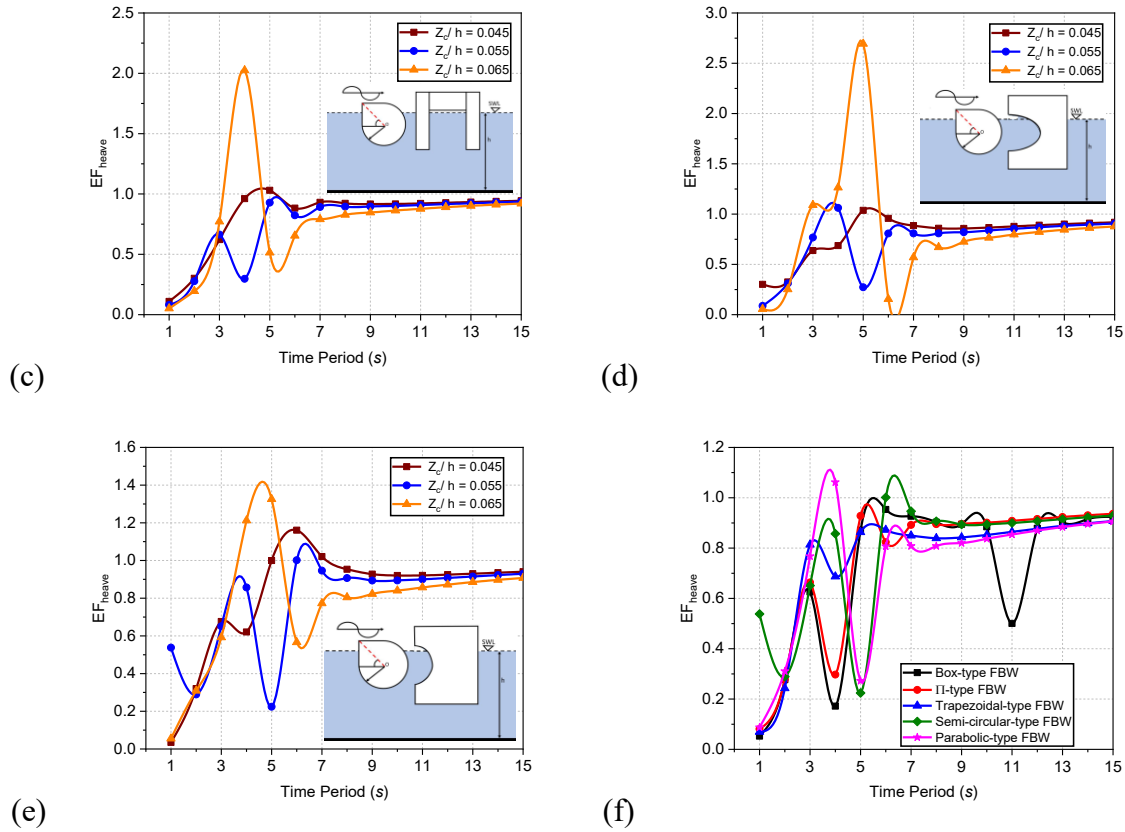


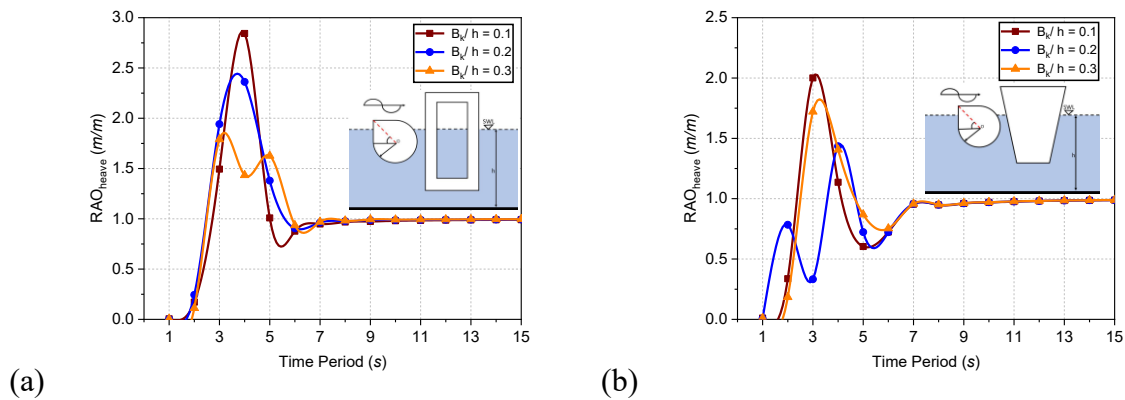
Fig. 11: Variation of excitation force response in heave direction for (a) box-type FBW (b) trapezoidal-type FBW (c) π -type FBW (d) parabolic-type FBW (e) semi-circular-type FBW for different draft of ED and (f) comparison of different shapes of FBW for $Z_c/h = 0.055$, $W_{ed}/h = 0.50$ and $B_k/h = 0.1$.

In Fig. 11(a-e), the variation of the force response in heave is analysed for different draft in the case of ED-WEC integrated with FBW of different configuration. In the deep water conditions ($1.0s \leq T \leq 5.0s$) the box-type FBW (Fig. 11a) at initial structural draft of $Z_c/h = 0.045$ and $Z_c/h = 0.055$ is observed to have decreasing force response for no change in maximum peak value but for change in the structural draft from $Z_c/h = 0.055$ to $Z_c/h = 0.065$ the increasing pattern in force response is observed with resonance value of 9.45 times when compared at $T = 4.0s$ and variation of 1.3 times when compared with peak values. In Fig. 11(b), for trapezoidal-type FBW the decreasing trend in force response is observed with the increment in structural drafts. The variation in peak values for $Z_c/h = 0.045$ is nearly 5% more and for $Z_c/h = 0.065$ is 7% less when compared with $Z_c/h = 0.055$. At $T = 4.0s$, a large decrease in force response of about 43% is observed for structural draft of $Z_c/h = 0.055$ and $Z_c/h = 0.065$. In the case of π -type FBW (Fig. 11c), similar trend of box-type FBW is observed including resonance time period. In the case of parabolic-type FBW (Fig. 11d) and semi-circular-type FBW (Fig. 11e), the single peak is obtained for structural draft of $Z_c/h = 0.045$ and $Z_c/h = 0.065$ while for $Z_c/h = 0.055$ two peaks are obtained. At single

peak amplitude of wave excitation force for structural draft $Z_c/h = 0.065$ is 1.7 times more than that of $Z_c/h = 0.045$ for parabolic-type FBW while for semi-circular-type FBW the force response is 22.5% more at $T = 4.0s$. The second peak at $T = 5.0s$ in the multi-peak of structural draft $Z_c/h = 0.055$ is 22.22% less than the first peak at $T = 3.0s$ and is 66.67% less than that of draft $Z_c/h = 0.065$ for parabolic-type FBW and for semi-circular-type FBW, second peak at $T = 6.5s$ in the multi-peak of structural draft $Z_c/h = 0.055$ is 20% more than the first peak at $T = 3.5s$ and is 29% less than that of draft $Z_c/h = 0.065$. In the Intermediate water condition ($T \geq 6.0s$), slight variation of 10 - 20% is observed within $6.0s \leq T \leq 8.0s$ for all shapes of breakwater. For $T \geq 9.0s$ all shapes of FBW except box-type FBW tends to converge and shows same pattern of force response. For box-type FBW at $T = 11.0s$, a sudden decreasing trend is observed which shows an instability of the ED-WEC with FBW as the interaction of the structure and the wave is reduced at that period, the resulting waves pass under the structure. As the waves passes under the structure it causes disturbance on the leeward side of the breakwater and the major purpose of breakwater to create calm condition on leeward side fails.

5.4.6 Effect of distance between WEC and FBW

The effect of the distance between the ED-WEC and the floating breakwater is examined for the motion response and force response of the FBW in heave. The distance B_k/h between centre of rotation Z_c/h of the ED-WEC and the upstream face of the FBW is an important parameter in deciding the installation position of the ED-WEC with respect to the ocean structures (Zhou et al., 2021, 2022). The variation in motion response (Fig. 12a-e) and force response (Fig. 13a-e) for varied dimensionless distance between ED-WEC and the FBW in heave direction for different shaped of breakwaters is analysed and comparison between different shapes of FBW for $B_k/h = 0.1$ are shown in Fig. 12(f) and Fig. 13(f) for $W_{ed}/h = 0.50$ and $Z_c/h = 0.055$.



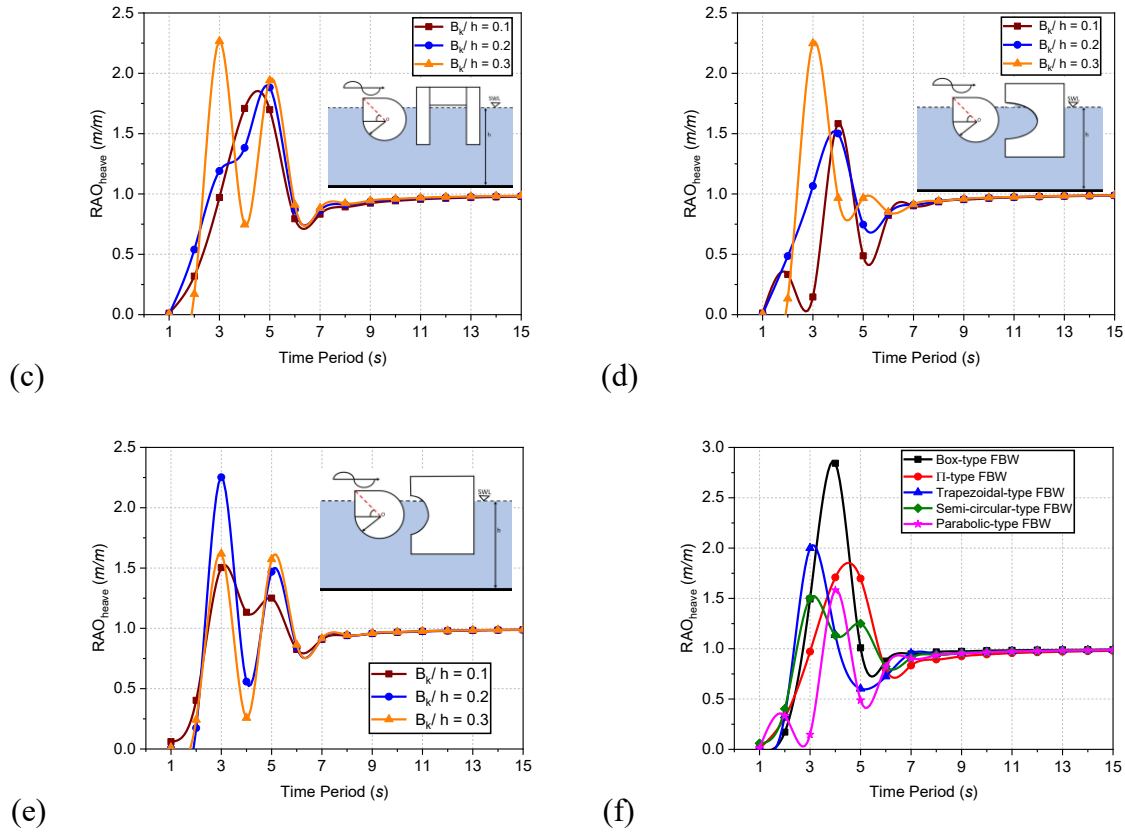


Fig. 12: Variation of motion response in heave direction for (a) box-type FBW (b) trapezoidal-type FBW (c) π -type FBW (d) parabolic-type FBW (e) semi-circular-type FBW for different distance between ED-WEC and FBW, and (f) comparison of different shapes of FBW for $B_k/h = 0.1$, $W_{ed}/h = 0.50$ and $Z_c/h = 0.055$.

In Fig. 12(a-f), the motion response in heave direction for different configurations of FBW integrated with ED-WEC is analysed for distance between ED-WEC and FBW. In deep water condition ($1.0s \leq T \leq 5.0s$), it is observed that for box-type FBW (Fig. 12a), the magnitude of RAO-heave decreases with the increase in B_k/h ratio. The single peak in motion response is noted for $B_k/h = 0.1$ and $B_k/h = 0.2$ while multi-peak is noted for $B_k/h = 0.3$. In the case of other shapes of breakwater, the characteristic change in behavioural pattern is observed after $B_k/h = 0.1$. In the case of trapezoidal-type FBW (Fig. 12b), the behaviour pattern is similar for $B_k/h = 0.1$ and $B_k/h = 0.3$ with single peak and a difference of 10% is noted, while for $B_k/h = 0.2$, two peaks is noted with a variation of 60% and 30% in the magnitude with respect to $B_k/h = 0.1$. For π -type FBW (Fig. 12c), in the case of $B_k/h = 0.1$ and $B_k/h = 0.2$, one peak is observed while for $B_k/h = 0.3$ two peaks are noted. Although the second peak is having slight variation of about 1-2% at same time period but first peak is observed to be 21% more than that of the single peak. In Fig. 12(d), the motion response for parabolic-type FBW, in the case of $B_k/h = 0.1$ and $B_k/h = 0.2$ is approximately equal but for $B_k/h = 0.3$, it is 44% greater than other values with different patterns. In Fig. 12(e), for semi-circular-type FBW two peaks are observed for variation of distance between ED-WEC and FBW with nearly similar

pattern. In the case of first peak there is a sudden increase for $B_k / h = 0.2$ by 53.33% compared to $B_k / h = 0.1$, and for $B_k / h = 0.3$ the motion response is found to be decreasing by 31% compared to $B_k / h = 0.2$. Meanwhile the second peak values increases for variation of distance between ED-WEC and FBW. For $B_k / h = 0.2$ an increment in motion response of 25% is observed and for $B_k / h = 0.3$ an increment in motion response of 33.35 % is observed compared to $B_k / h = 0.1$.

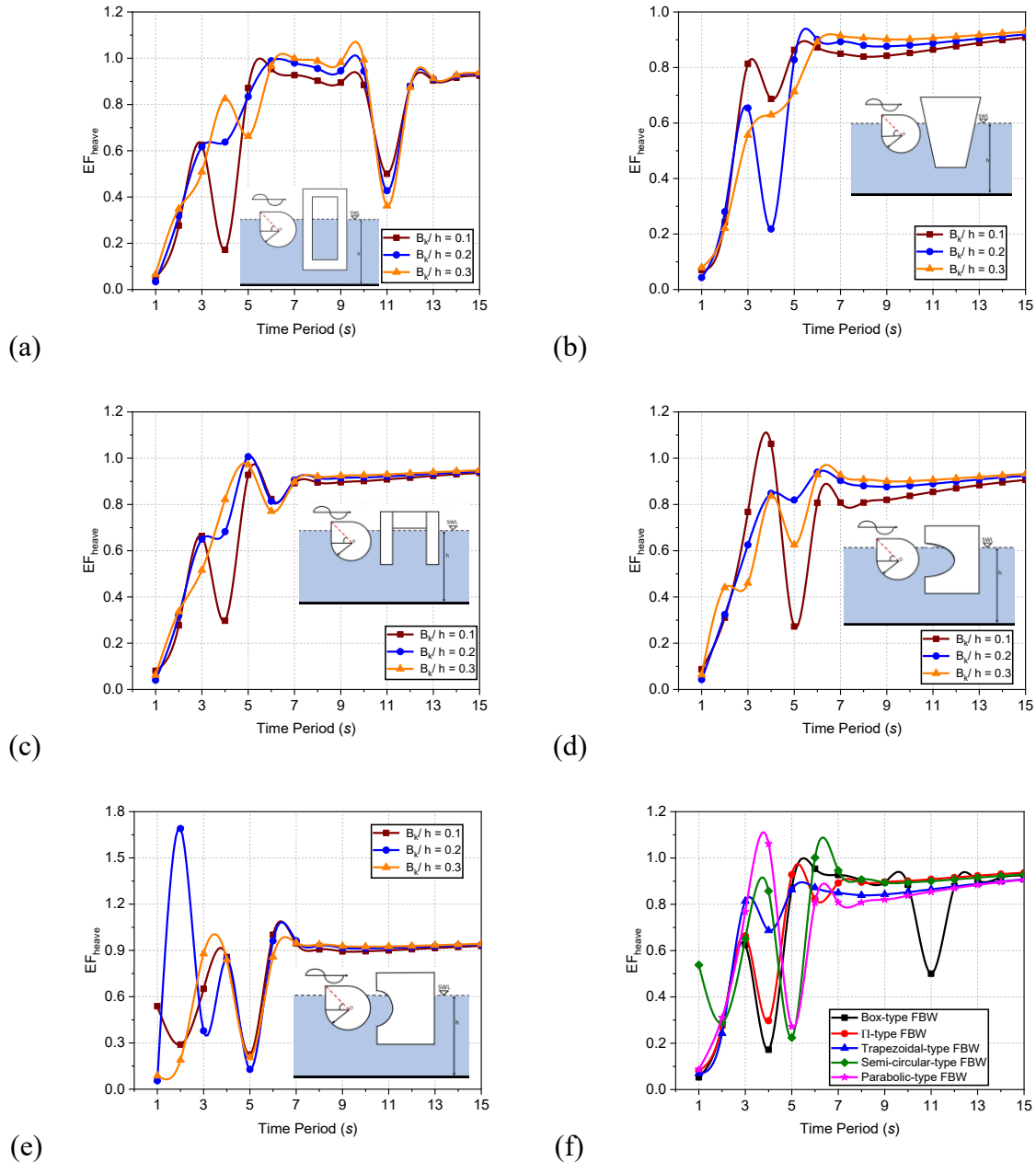
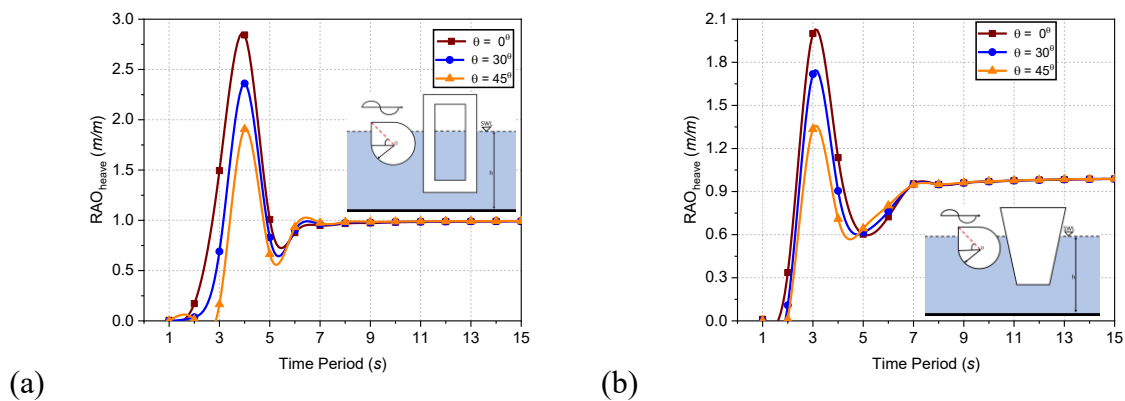


Fig. 13: Variation of excitation force response in heave direction for (a) box-type FBW (b) trapezoidal-type FBW (c) π -type FBW (d) parabolic-type FBW (e) semi-circular-type FBW for different distance between ED-WEC and FBW, and (f) comparison of different shapes of FBW for $B_k / h = 0.1$, $W_{ed} / h = 0.50$ and $Z_c / h = 0.055$.

In Fig. 13(a-f), the force response in heave direction is analysed for different FBW integrated with ED-WEC for varying distance between ED-WEC and FBW. In deep water conditions ($1.0s \leq T \leq 5.0s$) for box-type FBW (Fig. 13a) considering $B_k / h = 0.1$ at $T = 4.0s$, a sudden decrement in force response is observed which shows an instability as the interaction of the structure and the wave is reduced at that period of time resulting waves to pass under the structure. Similar failure is observed for trapezoidal-type FBW (Fig. 13b) for $B_k / h = 0.2$ at $T = 4.0s$, π -type FBW (Fig. 13c) for $B_k / h = 0.1$ at $T = 4.0s$, parabolic Type FBW (Fig. 13d) for $B_k / h = 0.1$ at $T = 5.0s$ and for semi-circular-type FBW (Fig. 13e) at $T = 5.0s$ for all values of B_k / h . At time period $T = 4.0s$ for box-type FBW (Fig. 13a) as compared to $B_k / h = 0.1$, the value of $B_k / h = 0.2$ is 3.33 times more and is 4.67 times more for $B_k / h = 0.3$ and is stable. In the case of trapezoidal-type FBW (Fig. 13b), the force response for $B_k / h = 0.1$ is 2.5 times more while for $B_k / h = 0.3$ force response is 2.25 times more and stable as compared to $B_k / h = 0.2$. Further, for π -type FBW (Fig. 13c), the force response for $B_k / h = 0.2$ is 1.33 times more and for $B_k / h = 0.3$ is 1.83 times more when compared with failure parameter $B_k / h = 0.1$. Similarly, at failure time period of $T = 5.0s$ the force response for $B_k / h = 0.2$ is 1.67 times more and for $B_k / h = 0.3$ is 1.167 times when compared to $B_k / h = 0.1$ for parabolic-type FBW (Fig. 13e). On the other hand, in intermediate water condition ($T \geq 6.0s$), the force response for varying distance between ED-WEC and FBW in heave direction tends to converge and shows similar pattern except box-type FBW.

5.4.7 Effect of wave incident angle on ED-WEC

The hydrodynamic performance of the ED-WEC integrated with FBW for varying angle of incident waves are examined for different configuration of FBW. The variation of incident angles in RAO-heave and wave excitation forces for ED-WEC integrated to different shapes of floating breakwater such as box-type FBW, trapezoidal-type FBW, π -type FBW, parabolic-type FBW and semi-circular-type FBW in hybrid system consisting of ED-WEC and FBW are analysed in Fig. 14(a-e) and Fig. 15(a-e) followed by comparison of ED-WEC for all shapes of FBW together in Fig. 14(f) and Fig. 15(f) for $W_{ed} / h = 0.50$, $Z_c / h = 0.055$ and $B_k / h = 0.1$.



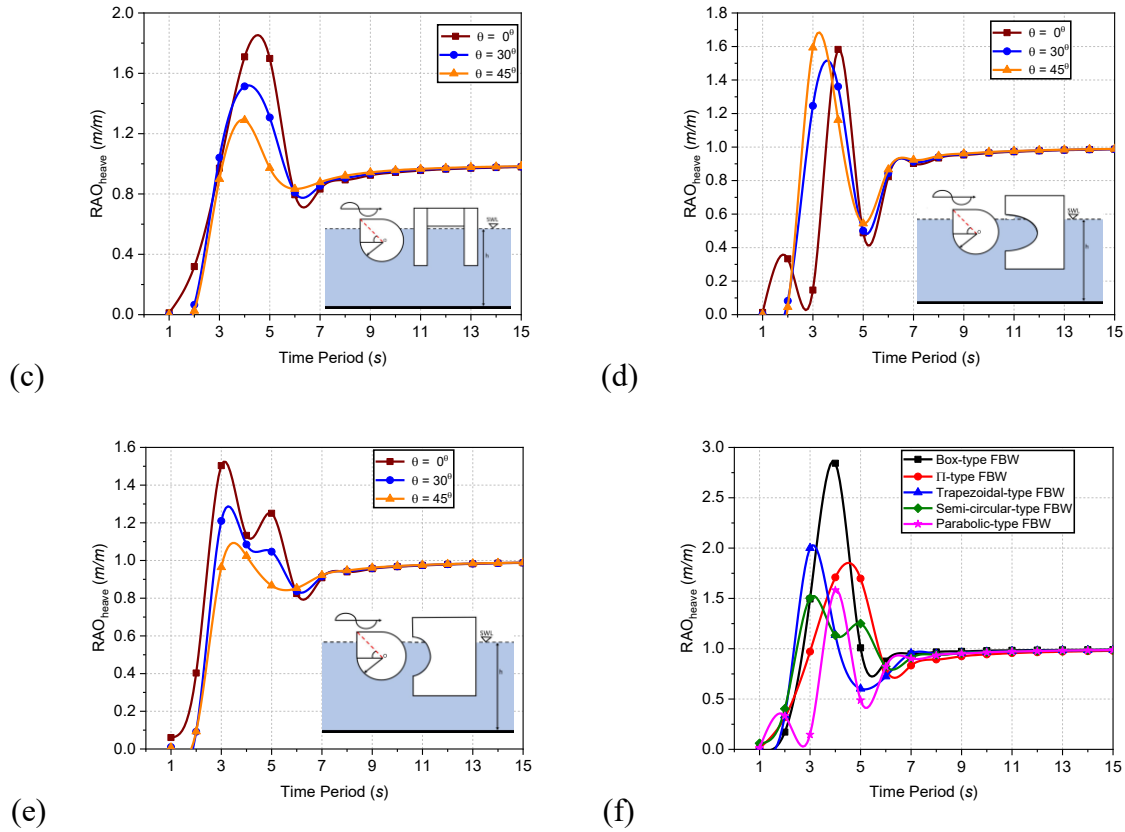


Fig. 14: Variation of motion response in heave direction on ED-WEC for (a) box-type FBW (b) trapezoidal-type FBW (c) π -type FBW (d) parabolic-type FBW (e) semi-circular-type FBW for different angle of incidence, and (f) comparison of different shapes of FBW for particular configuration for $W_{ed} / h = 0.50$, $Z_c / h = 0.055$ and $B_k / h = 0.1$.

Fig. 14(a-e) shows the decrement in values of heave motion response as the wave incident angle increases in deep water conditions except for parabolic-type FBW. The reason for the decrement in values is due to the increment in roll and pitch response of the ED-WEC for the same incident angles. In the case of box-type FBW (Fig. 14a), the heave response decreases in proportion with increment in incident wave angle with nearly no shift in phase of attaining peak magnitudes. The magnitude of RAO-heave is 17% less for $\theta = 30^\circ$ and is approximately 34% less for $\theta = 45^\circ$ as compared to $\theta = 0^\circ$. The heave response for trapezoidal-type FBW is found to be similar with box-type FBW. The magnitude of RAO-heave for trapezoidal-type FBW (Fig. 14b) is 15% less for $\theta = 30^\circ$ and is approximately 32.5% less for $\theta = 45^\circ$ as compared to RAO-heave magnitude for $\theta = 0^\circ$. The heave response for π -type FBW is observed similar to that of box-type FBW and for trapezoidal-type FBW only slight variation in phase is observed for initial wave periods. The magnitude in RAO-heave for π -type FBW is found to be 19% less for $\theta = 30^\circ$ and is 30% less for $\theta = 45^\circ$ compared to magnitude for $\theta = 0^\circ$ and is in Fig. 14(c). The parabolic-type FBW (Fig. 14d) shows different trends in heave response as compared to other shapes. At initial variation of angle, the heave response shows decreasing trends while further variation in angle of incidence, the increasing trend is noted. The variation in motion response for $\theta = 30^\circ$ is 6.2% less than that of magnitude at $\theta = 0^\circ$ and for $\theta = 45^\circ$ the motion

response is 6.25% more than that of $\theta = 0^\circ$. Also, a significant variation in phase is observed while having increment in wave angle incidence. The heave response patterns of semi-circular-type FBW (Fig. 14e) is similar to that of box-type FBW, trapezoidal-type FBW and π -type FBW. The overall comparison of motion response for all the shapes is performed in Fig. 14(f) where the magnitude in RAO-heave is noted maximum for box-type FBW while least for semi-circular-type FBW. In Intermediate water condition, the magnitude of RAO-heave for all shapes tends to converges and behaves similar.

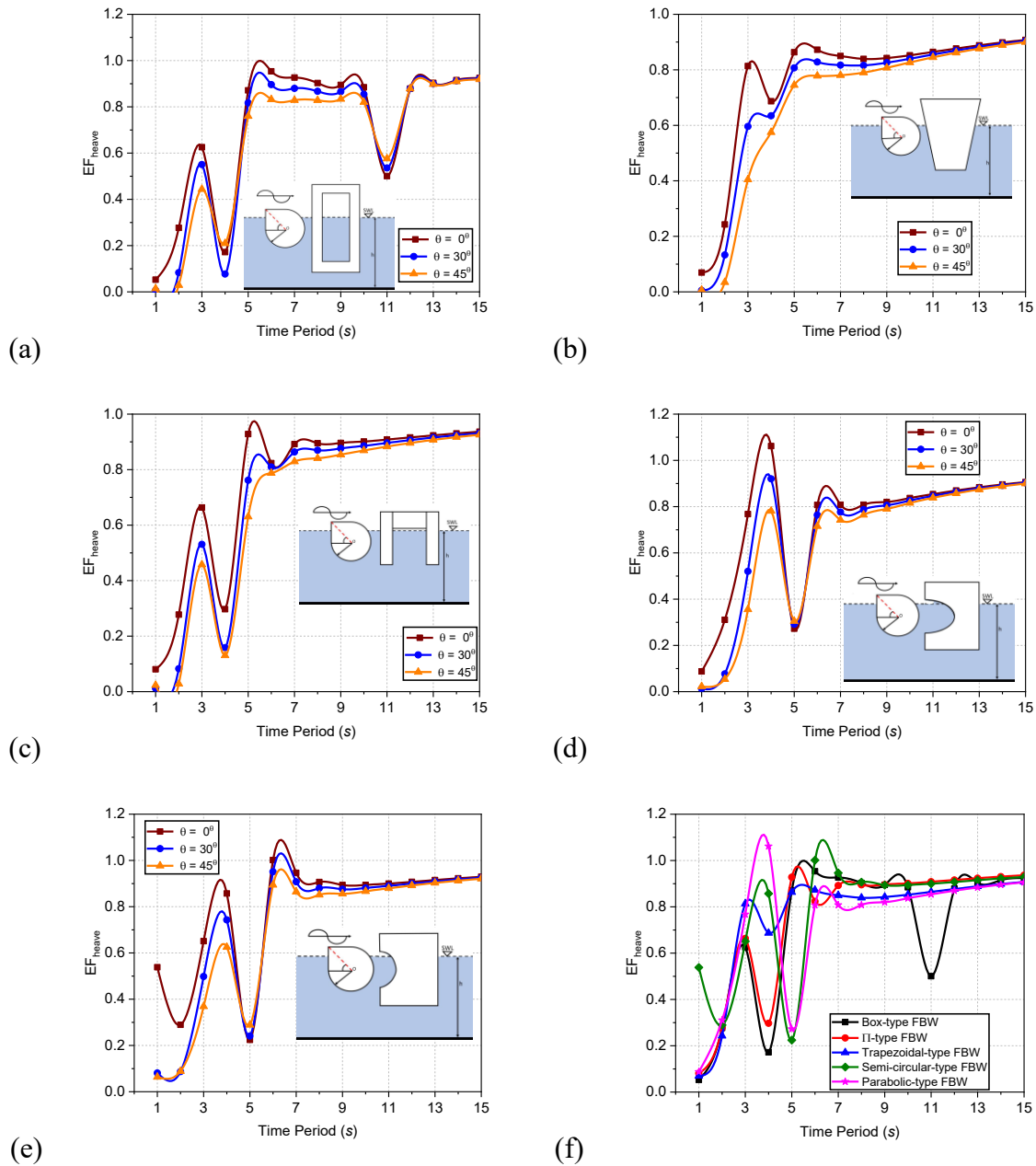


Fig. 15: Variation of excitation force response in heave direction on ED-WEC for (a) box-type FBW (b) trapezoidal-type FBW (c) π -type FBW (d) parabolic-type FBW (e) semi-circular-type FBW for different angle of incidence, and (f) comparison of different shapes of FBW for $W_{ed}/h = 0.50$, $Z_c/h = 0.055$ and $B_k/h = 0.1$.

The wave excitation force for different wave incident angle in Fig 15(a-f) shows decreasing pattern as the wave incident angle varied within $0^\circ < \theta < 45^\circ$. In deep water condition ($1.0s \leq T \leq 5.0s$) for box-type FBW (Fig.15a) at $T = 4.0s$ a sudden decrement in force response is observed which shows an instability as the interaction of the structure and the wave is reduced at that period of time resulting waves to pass under the structure. Similar failure pattern is observed for all other shapes except trapezoidal-type FBW. The π -type FBW (Fig. 15c) shows a similar failure at $T = 4.0s$ for all incident wave angle while parabolic-type FBW (Fig. 15d) and semi-circular-type FBW (Fig. 15e) shows failure at $T = 5.0s$. However, the variation in magnitude of failure is not significant with respect to variation in angle of incidence. In trapezoidal-type FBW (Fig. 15b), the structure shows stable and not does not fail like other structure. A decrease in force response is observed with increase in angle of incidence due to the increase in the magnitude of other motion response like roll and pitch. Further, with the increase in angle of incidence, the multipeak is obtained. The difference in magnitude of wave excitation force for peak values at $T = 5.0s$ is 8% less for $\theta = 30^\circ$ and is 15% less for $\theta = 45^\circ$ as compared to the magnitude of $\theta = 0^\circ$. In intermediate water condition, ($T \geq 6.0s$) all shapes are noted to be stable except box-type FBW. The box-type FBW shows failure at $T = 11.0s$. The failure is similar to the case observed in deep water condition and the effect remains the same as the purpose of using breakwaters to create calm condition is not achieved in the leeside of the breakwater.

2.8 CONCLUSIONS

The present study investigates the hydrodynamic performance of hybrid floating breakwater system consisting of ED-WEC integrated to different shapes of FBWs namely (i) box-type FBW, (ii) trapezoidal-type FBW, (iii) π -type FBW, (iv) parabolic-type FBW and (v) semi-circular-type FBW based on small amplitude wave theory. A theoretical study is performed to analyse the effect of different shape of FBW integrated with ED-WEC. The hybrid system is analyzed for the variations of different parameters of ED-WEC and FBW. The conclusions drawn from the present study are as follows:

- On increasing the width of ED-WEC, the decrement in RAO-heave for different configurations of the FBW integrated with ED-WEC is noted which may be due to the distribution of incident wave energy over a large surface area while the increment in the amplitude in wave excitation force in heave may be due to the availability of large area for same value of pressure.
- Increasing the draft of ED-WEC results in the increment of RAO-heave and wave excitation force. In deep waters, RAO-heave decreases initially and beyond threshold values the heave motion response tends to increase (except box-type FBW and trapezoidal-type FBW). The wave excitation force in deep waters for hybrid FBW system decreases initially and beyond threshold values they tend to increase at a higher pace except trapezoidal-type FBW.
- The effect of distance between ED-WEC and FBW shows negligible variation in RAO-heave and wave excitation force in intermediate water depth whereas in deep waters, the decrement is observed in RAO-heave for box-type FBW with increase in B_k .

On increasing the wave incident angle, the decrement in the magnitude of RAO-heave and wave excitation force is observed for isolated FBW and hybrid FBW system. In intermediate water depth, the variation in magnitude of force response is very minimal and can be concluded that incident angle is not having any significant impact for isolated FBW and hybrid FBW system.

CHAPTER 6

HYDRODYNAMIC PERFORMANCE OF EDINBURGH DUCK INTEGRATED WITH WITH ARRAY OF FLOATING BREAKWATER

6.1 THEORETICAL FORMULATION

In the present study, ED as a point and roll absorbing energy conversion device arranged in array is integrated to different shapes of FBWs. The theoretical formulation formulated for the configuration is represented in Figure 1. The global right hand cartesian co-ordinates of the system $o-xyz$ is introduced at the origin with its line of action passing through $(0,0,Z_c)$. Plane yz is exposed to the incident waves and $o-xy$ lies on the still water level. Plane yz is exposed to the incident waves and $o-xy$ lies on the still water level.

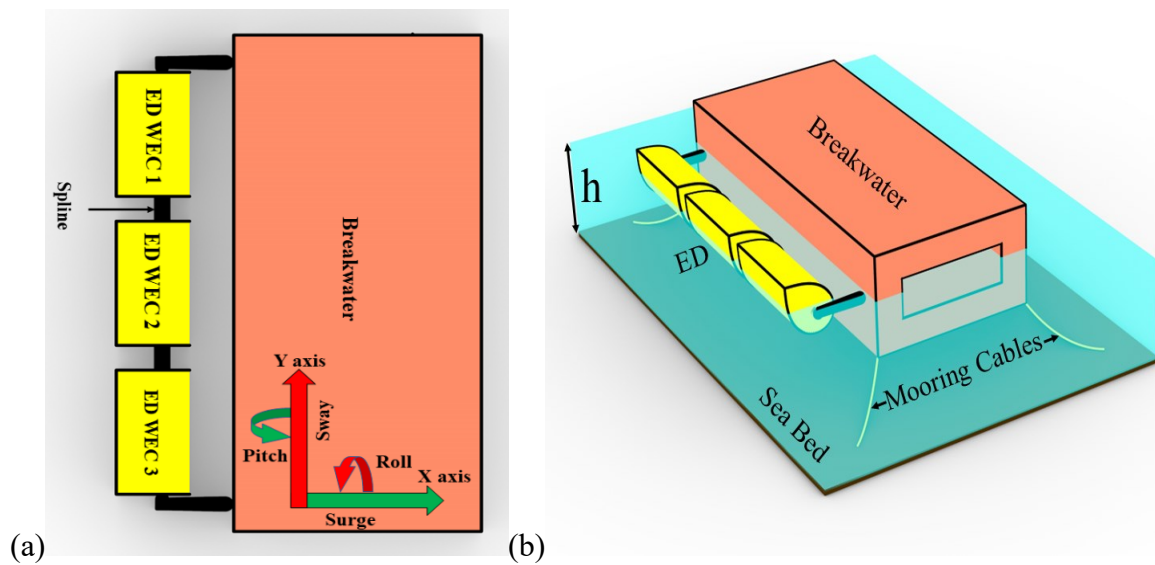


Figure 1. Schematic representation of ED WEC array with box type FBW

The ED WEC is symmetrical about dash line l_d and the stern radius is R and is arranged in array. β is the angle of inclination and non-porous FBW of box type width B , height H_b , length L_b , thickness t_b and draft d_b is integrated to ED. Distance from Z_c to face of FBW is B_k and the distance between two ED is D_k . The array system of three EDs are analysed for ξ_{33} , ξ_{44} and ξ_{55} type DOF for finite water depth h under assumption of regular waves and small amplitude wave theory.

6.1.1 Governing Equations

Theory used is to calculate the wave excitation force on fixed body or wave excitation force and radiation force on fixed or floating body. For analysis of diffraction and radiation waves, first order potential theory is used. Fluid flow field surrounding the floating body, velocity potential is defined as

$$\phi(\vec{X}, t) = \eta \phi(\vec{X}) e^{-i\omega t} \quad (1)$$

where η is the wave amplitude, t is the time period, ω is the wave frequency and $\vec{X} = (x, y, z)$ is the space co-ordinates with respect to origin. The rotational (ξ_{44} , ξ_{55} and ξ_{66}) and translational (ξ_{11} , ξ_{22} and ξ_{33}) motions of the floating body excited by the incident wave of unit amplitude is given by

$$x_j = u_j, \text{ for } j=1,2,3 \quad \text{and} \quad x_j = \xi_j, \text{ for } j=4,5,6 \quad (2)$$

The total potential $\varphi(\vec{X})$ is summation of three component, incident φ_I , diffracted φ_D and radiated wave potential φ_R . All these three velocity potentials must satisfy the Laplace equation's and can be mathematically written as,

$$\varphi(\vec{X})e^{-i\omega t} = \left[\varphi_I + \varphi_D + \sum_{j=1}^6 \varphi_{Rj} x_j \right] e^{-i\omega t} \quad (3)$$

where φ_I is the first order incident wave potential with unit wave amplitude, φ_D is the diffraction wave potential and φ_{Rj} is the radiation wave potential due to the j^{th} motion with unit wave motion amplitude. In the fluid domain, ideal fluid exists a velocity potential which satisfies the Laplace equation for fluid structure interaction behaviour by the following sets of equations and is expressed as

$$\nabla^2 \varphi(x, y, \zeta) = \frac{\partial^2 \varphi}{\partial x^2} + \frac{\partial^2 \varphi}{\partial y^2} + \frac{\partial^2 \varphi}{\partial z^2} = 0 \quad (4)$$

Linear SWL boundary condition at free surface of zero forward speed case can be written as

$$-\omega^2 \varphi + g \frac{\partial \varphi}{\partial z} = 0 \text{ at } z = 0 \quad (5)$$

The body surface condition for the boundary value problem for wave interaction with the ocean structure for velocity potential of incoming wave (φ) on wetted body surface x_0 is given by

$$\frac{\partial \varphi}{\partial n} = -i\omega n_j, \text{ for radiation potential,} \quad (6)$$

$$\frac{\partial \varphi}{\partial n} = -\frac{\partial \varphi}{\partial n}, \text{ for diffraction potential,} \quad (7)$$

The seabed boundary condition s_z for water depth h is expressed as

$$\frac{\partial \varphi}{\partial z} = 0 \text{ at } z = -h \quad (8)$$

6.1.2 Equations of Motion and RAOs

The governing equation for the heaving type point absorber WEC can be expressed as

$$m\ddot{z} = f_e + f_r + f_h + f_{PTO} + f_v \quad (9)$$

where m is mass of the point absorber, f_e is excitation force due to incident wave, f_r is radiation force, f_h is hydrostatic force derived from buoyancy and gravity, f_{PTO} is forced applied by the PTO, f_v is damping force occurring due to viscosity of the fluid interacting the body. f_e represents force introduced due to dynamic pressure of undisturbed waves, while f_r is caused by disturbed waves due to existence and oscillation of point absorber. The value of f_e can be obtained by integrating dynamic pressure p of incident waves over mean wet surface of oscillating buoy, and can be represented as

$$p = -\rho \frac{\partial \phi_1}{\partial t} \quad (10)$$

$$\phi_1 = \frac{g\eta}{\omega} \frac{\cosh k(z+h)}{\cosh kh} \cos(\omega t - kx) \quad (11)$$

where g is gravitational acceleration constant, ρ is fluid density and K is wave number.

6.1.3 Mooring System

In order to analyze the dynamics of cable motion, different factors should be considered such as cable mass, drag and tension. The forces applied to the cable vary with time and it behaves as nonlinearly. The simulation of cable dynamics is required to discretized along its length and assembled mass and applied forces. The general equation for the force and moment acting on the cable can be expressed as

$$\frac{\partial \vec{T}}{\partial l_e} + \frac{\partial \vec{Q}}{\partial l_e} + \vec{W} + \vec{F}_{Eh} = m \frac{\partial^2 \vec{R}}{\partial t^2} \quad (12)$$

$$\frac{\partial \vec{M}}{\partial l_e} + \frac{\partial \vec{R}}{\partial l_e} * \vec{V} = -q \quad (13)$$

Where \vec{R} , \vec{T} , \vec{V} and \vec{M} is position vector, tension force vector, shear force vector and bending moment vector respectively at the first node of cable. \vec{W} , \vec{F}_{Eh} , m and q is element weight, hydrodynamics loading vector, mass and distribution moment loading per unit length. ∂l_e is length of the element and D is diameter of the element.

6.1.3.1 Length and strain

The length of the mooring line can be stretched in response to tensile force arising from the motion of the WEC. The length of the mooring line can be expressed as

$$L = \int_{anchor}^{WEC} dx \quad (14)$$

Strain of mooring force of length L and for change in length due to stretch ΔL is given by

$$\varepsilon = \frac{\Delta L}{L} \quad (15)$$

6.1.3.2 Tension in cable

The tension defines the force that the mooring line impose on the WEC. Moreover, the tension indicates the maximum and cyclic loads that the mooring lines are subjected to and are more vital in mooring design for extreme loads and fatigue analysis. The tension is related to the mooring line strain and strain stress relation can be given by

$$T = f(\varepsilon, \dot{\varepsilon}, s) \quad (16)$$

In the case of linear stress strain relationship can be stated as

$$T = EA\varepsilon \quad (17)$$

where, A is the cross-section area, E is the modulus of elasticity (Young's modulus).

6.1.3.3 Position

The position of the mooring line is generally determined by the two positions in the global reference frame. First the anchor point and second the connection point with the breakwater. The position of the top of the mooring line $x(L)$ can be determined by the position of breakwater x_{BW} center of mass and the mooring line connection point on the breakwater x_ω .

$$x(L) = x_{BW} + x_\omega \cos \varphi \quad (18)$$

6.1.4 Power Take-off System

The equation which governs the direct mechanical driven PTO system in heave is given as

$$m_{PTO}\ddot{z} + C_{PTO}\dot{z} + K_{PTO}z = F_{PTO} + F_f \quad (19)$$

where m_{PTO} is the equivalent mass ($m_{PTO} = A_{jk} + M$), C_{PTO} is the equivalent damping coefficient ($E_{PTO} + C$), K_{PTO} is the spring coefficient (not considered), F_{PTO} is the PTO force and F_f is the friction force which is not considered here of the PTO system.

C_{PTO} optimal for can be calculated as (Bellew et al., 2009)

$$C_{PTO} = \sqrt{\omega^2(A_{jk} + M - \frac{C}{\omega^2})^2 + B_{jk}^2} \quad (20)$$

where A_{jk} is the added mass, M is the mass of the body, C is the restoring force coefficient due to difference in hydrostatic force and weight of the body.

The governing equation of motion for roll and pitch for ED WEC can be determined as

$$I\ddot{\theta} + M_{PTO}\dot{\theta} + E_{PTO} = M_F + M_G \quad (21)$$

where $\dot{\theta}$ is angular displacement and $\ddot{\theta}$ is angular velocity of rotating body, I is rotational moment of inertia, M_{PTO} is mechanical PTO damping torque, E_{PTO} is elastic characteristics of the generator (not considered), M_F is the torque produced by combining pressure torque and viscous torque and M_G is the torque due to gravity. The clockwise direction is taken as positive direction for the formulation. Optimal M_{PTO} can be expressed as (Sun et al., 2018)

$$M_{PTO} = \sqrt{\frac{(I + I_{PTO} + A_{jk})\omega^2 - (E_{PTO} + C_z)^2}{\omega^2} + B_{jk}^2} \quad (22)$$

where B_{jk} is the radiation damping coefficient and C_z is the restoring torque coefficient due to difference in hydrostatic force and weight of the body.

6.1.5 Power Absorption

The average output power for heaving WEC (E_p) can be calculated as

$$E_p = \frac{1}{mT} \int_t^{t+mT} (EF) \dot{z} \partial t \quad (23)$$

$$E_p = \frac{C_{PTO}}{mT} \int_t^{t+mT} (\dot{z})^2 \partial t \quad (24)$$

where EF is wave excitation force in ξ_{33} . Average output power (E_p) for ξ_{44} and ξ_{55} is as

$$E_p = \frac{1}{mT} \int_t^{t+mT} (M\dot{\theta}) \partial t \quad (25)$$

$$E_p = \frac{M_{PTO}}{mT} \int_t^{t+mT} (\dot{\theta})^2 \partial t \quad (26)$$

where M is moment due to fluid and gravity ($M = M_F + M_G$), m is number of WEC motion period.

6.1.6 Capture Width Ratio

Capture width ratio (CWR) is defined as the ratio of the extracted to the input wave power.

$$CWR = \frac{E_p}{E_i B} \quad (27)$$

where E_p is average output power and E_i is input power of the waves. CWR is interpreted as wave front width of WEC which completely absorbed from the incoming waves.

$$E_i = \frac{1}{16} \frac{\rho g H_i^2 \omega}{k} \left(1 + \frac{2kh}{\sinh 2kh} \right) \quad (28)$$

where H_i is the incident wave height.

For deep water condition, the term $\frac{2kh}{\sinh 2kh}$ is negligible. Hence the second term is unity.

6.1.7 Mean Interaction Factor

The hydrodynamic response of the hybrid structure interacting in fluid domain is dependent on wave excitation force due to diffracted and radiated waves by the oscillations of the WEC devices. Due to these interactions both power and response output of a body in hybrid system differ from the output of the same body in isolation. A measure of these differences of the hydrodynamic coupling between devices in array system and same device in isolation is given by an interaction factor (q) and is defined as

$$q = \frac{\text{Net Power from the hybrid system}}{N \times \text{Power from the same device in isolation}} \quad (29)$$

An interaction factor of $q = 1$ indicates that the array system is producing the same power as of the same device producing power in isolation, whereas $q > 1$ and $q < 1$ indicates the constructive and destructive interaction of the system.

To obtain forces acting on the structure, pressure is to be integrated over wetted surface area. To obtain general forms of forces and moments, equations of motion are used for translation and rotational motion corresponding to the rigid body. The generalized form of first order hydrodynamic force and moment component can be expressed as

$$F_j e^{-i\omega t} = \left[-i\omega\rho \int_{x_0} \varphi(\vec{X}) n_j dS \right] e^{-i\omega t} \quad (30)$$

where x_0 is the mean wetted surface. The forces due to fluid are categorized into active and reactive components. The active component consists of Froude-Krylov and diffraction force. The reactive force consists of radiation force due to radiation waves induced on body. The total first order hydrodynamic force is obtained from the solution of Equation 23 and then is divided into its active and reactive component. The active component for Froude-Krylov due to incident wave and after solving for total first order hydrodynamic force it can be written as

$$F_{Ij} = -i\omega\rho \int_{x_0} \varphi_I(\vec{X}) n_j dS \quad (31)$$

while for diffracting force due to diffraction wave, can be written as

$$F_{Dj} = -i\omega\rho \int_{x_0} \varphi_D(\vec{X}) n_j dS \quad (32)$$

and radiation force due to radiation wave induced to rigid body motion for unit amplitude for reactive force is given as

$$F_{Rjk} = -i\omega\rho \int_{x_0} \varphi_{Rk}(\vec{X}) n_j dS \quad (33)$$

This reactive force can also be expressed for real and imaginary parts and given as

$$F_{Rjk} = -i\omega\rho \int_{x_0} \left\{ \text{Re} \left[\varphi_{Rk}(\vec{X}) \right] + i \text{Im} \left[\varphi_{Rk}(\vec{X}) \right] \right\} n_j dS \quad (34)$$

and is substituted into Equation 26 to produce the linear added mass and wave radiation damping coefficients and is written as

$$F_{Rjk} = \omega\rho \int_{x_0} \text{Im} \left[\varphi_{Rk}(\vec{X}) \right] n_j dS - i\omega\rho \int_{x_0} \text{Re} \left[\varphi_{Rk}(\vec{X}) \right] n_j dS \quad (35)$$

$$F_{Rjk} = \omega^2 A_{jk} + i\omega B_{jk} \quad (36)$$

where A_{jk} is linear added mass and B_{jk} is wave radiation damping and is expressed as

$$A_{jk} = \frac{\rho}{\omega} \int_{x_0} \text{Im} \left[\varphi_{Rk}(\vec{X}) \right] n_j dS \quad (37)$$

$$B_{jk} = -\rho \int_{x_0} \text{Re} \left[\varphi_{Rk}(\vec{X}) \right] n_j dS \quad (38)$$

The solution of Laplace equation for the diffraction and radiation problems can be combined with the equation of motion of the FBW to analyze the dynamic response of the structural system in time domain and equation of motion is expressed as

$$m_a \ddot{z}(t) + C_i \dot{z}(t) + Kz(t) = F(t) \quad (39)$$

m_a is added mass in mass matrix, C_i is hydrodynamic damping in damping matrix, K is total stiffness matrix (including spring stiffness), $F(t)$ is total external force acting on system which has constant amplitude. On implementing the convolution integral form in equation 32, then the equation of motion can be expressed as

$$(M + m_a) \ddot{z}(t) + c \dot{z}(t) + Kz(t) + \int_0^t V(t-\tau) \dot{z}(\tau) d\tau = F(t) \quad (40)$$

where c is damping matrix including radiation damping, V is velocity impulse function and K is total stiffness matrix (including spring stiffness). The RAO is the motion of a floating structure in six DOF (Surge, Sway, Heave, Roll, Pitch and Yaw) due to hydrodynamic wave force. RAOs are utilized as an input data for the calculation of displacement, acceleration and velocities at a given location. Generally, RAO is calculated by the ratio of response amplitude of breakwater to the wave amplitude for linear motion and for rotational motion, it is defined as the ratio of response amplitude of breakwater to the wave slope.

$$RAO = \frac{x_j}{\eta_i}, \text{ where } x_j = \xi_j, j = 1, 2, 3 \quad (41)$$

$$RAO = \frac{x_j}{\alpha_i}, \text{ where } x_j = \xi_j, j = 4, 5, 6 \quad (42)$$

All wave forces interacting with the structure in array system are a function of x_0 only and is independent of the structural mass of the body. The velocity in equation 16, is expressed by

$$\dot{z} = \left(\frac{(EF)}{\left((B_{jk} + R_m) + i\omega \left(A_{jk} + M - \frac{S}{\omega^2} \right) \right)} \right) \quad (43)$$

R_m is mechanical damping, S is hydrostatic stiffness and is given by $S = \rho g A_{wp}$. A_{wp} is water plane area.

The amplitude ($|X_{ij}|$) of an oscillating WEC due to incident wave of frequency can be obtained by integrating the velocity expressed in equation 36 in heave is given by

$$|X_{33}| = \left(\frac{(EF)}{i\omega(B_{jk} + R_m) + \omega^2 \left(A_{jk} + M - \frac{S}{\omega^2} \right)} \right) \quad (44)$$

Solving equation 17 and 19 to obtain Power output, periodic motion of waves system is assumed as $X_{33} = |X_{33}| \cos(\omega t)$. Solving this periodic motion of the waves system and substituting it in equation 17 and 19 for the velocity replacing with $|X_{33}|$ the equation will be expressed as

$$E_p = \frac{1}{2} \left(\frac{(EF)}{(B_{jk} + R_m) + i\omega \left(A_{jk} + M - \frac{S}{\omega^2} \right)} \right)^2 C_{PTO} \quad (45)$$

Similar results will be obtained for roll and pitch. Equation 38 can be rewritten as for heave as in equation 39 and for Roll and Pitch as in equation 40.

$$E_p = \frac{1}{2} \omega^2 |X_{33}|^2 C_{PTO} \text{ for } \xi_{33} \quad (46)$$

$$E_p = \frac{1}{2} \omega^2 |X_{33}|^2 M_{PTO} \text{ for } \xi_{44} \text{ and } \xi_{55} \quad (47)$$

Also, the maximum power absorbed after solving the equations for power is obtained as

$$E_{p_{\max}} = \frac{\rho}{2} \left(\frac{gT}{4\pi} \right)^3 H_i^2 \quad (48)$$

The term E_p is the energy absorbed per unit surface and $E_{p_{\max}}$ is maximum power.

6.2 NUMERICAL RESULTS AND DISCUSSION

The numerical model used for simulation is applied to hybrid system consists of ED in array integrated with floating breakwaters on the weather side of the hybrid system. A similar study was undertaken by Alfred and Forehand (2020) for isolated ED array system for power extraction and an open sea trial near WanShan Island, South China sea by Zhang et al. (2019) for maximum energy harnessing under without damaging the prototype. The present study is mainly focused on the behaviour of ED in hybrid system with different shapes of FBWs such as trapezoidal FBW, π FBW, parabolic FBW and semi-circular FBW. The curvature of the ED is governed by an equation and is expressed as

$$X^2 + (5 - Z^2) = R^2 \quad (49)$$

R is distance from center of rotation (Z_c) to curvature of the shape of ED and is expressed as

$$\begin{cases} R = 5e^{\frac{2\pi}{100}Z}, & X < 0, 11.8 \geq R \geq 5 \\ R = 5, & X \geq 0 \end{cases} \quad (50)$$

The stern portion of ED is of circular arc of radius $R = 5.0m$ and is symmetrical about the

dotted red dashed line l_d having length of $11.8m$. The ED is inclined an angle $\beta=45^\circ$ with still sea level. The model for simulation is scaled down to $1/5$. The scaled weight of ED is 20730 kg and scaled down dimensions are $R=1.0m$ and $l_d = 2.36m$. Width of ED is $5.0m$ and draft of ED is $1.1m$ and is investigated for the wave incident angle of 30° .

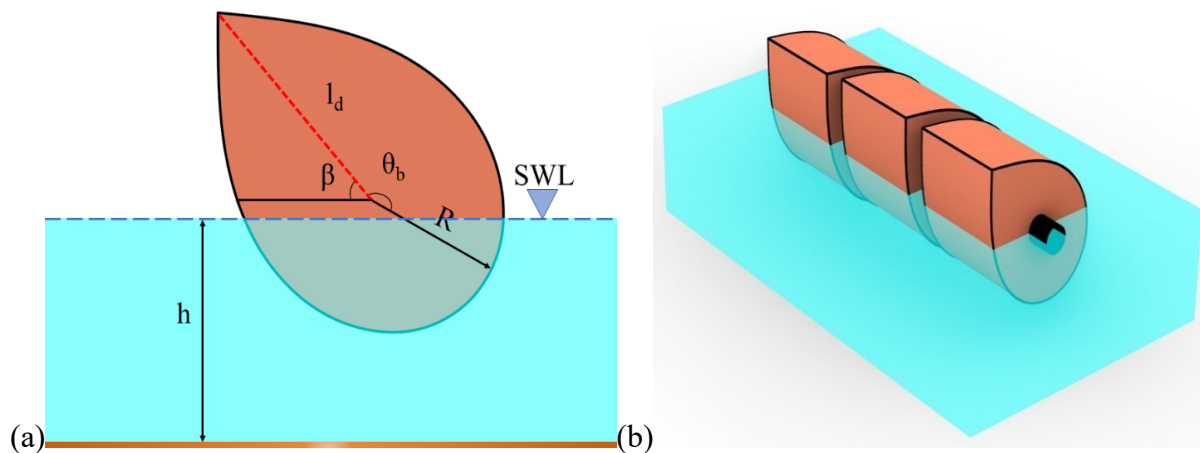


Figure 2. Schematic representation of (a) ED WEC (b) Perspective view in ED array

The EDs configuration mentioned in figure 2 is integrated with different shapes of FBWs with PTO mentioned in figure 3 and these FBWs are used for analysis and comparison study.

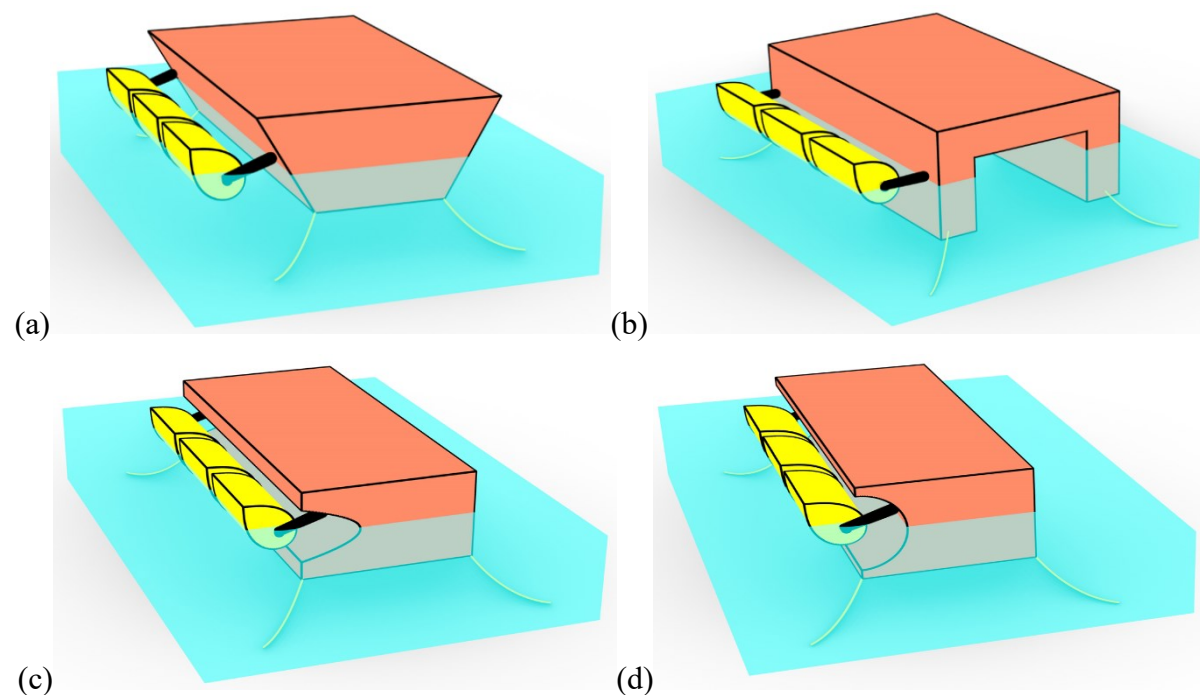


Figure 3. FBWs integrated with ED arranged in array (a) trapezoidal FBW (b) π FBW (c) Parabolic FBW (d) Semi-circular FBW

The parametric details of breakwaters are highlighted in Table 1. Weight of FBWs, width of FBWs and B/d_b ratio is kept similar for all the FBWs as 369000 kg , 20.0 m and 3.0 respectively. The shapes are considered from different literatures and adjusted to the box type

without changing their core dimensions from literatures. Submergence volume is kept similar by varying drafts of FBWs.

Table 1. Parametric model details of FBWs

Shape of floating breakwater	Parameters	Dimensions
Box FBW	Draft (d_b)	3.0m
	Box thickness	1.5m
	Height of center open of box	2.0m
	Submerged open area height	1.5m
Trapezoidal FBW	Draft (d_b)	2.24m
	Base at water surface level	9.31m
	Base at bottom of FBW	6.72m
	Slope of FBW	$\sqrt{3} : 1$
π FBW	Draft (d_b)	4.0m
	Top width of FBW	12.0m
	Depth of top deck	2.0m
	Height of leg of FBW	4.5m
Parabolic FBW	Thickness of leg of FBW	2.25m
	Draft (d_b)	2.5m
	Mouth of parabolic FBW (b)	3.0m
	Depth of parabolic FBW (a)	0.75m
Semi-Circular FBW	Focus of parabolic FBW ($((b/2)^2 / 4a)$)	0.75m
	Thickness of FBW at top & bottom	1.0m
	Draft (d_b)	2.7m
	Radius of Semi-Circle	2.2m
	Thickness of FBW at top & bottom	0.5m

The Edinburgh Duck arranged in array with FBWs is analysed for variation in parameters mentioned in table 2. Also, mooring analysis for FBWs is investigated for the mooring characteristics mentioned in table 3 and are used for investigation of mooring tension in slack/catenary type open mooring and cross mooring configuration shown in figure 4 and the results obtained from investigation are discussed for the same.

Table 2. Parametric variations of ED WEC-FBW

Parameters variations	Dimensionless values
Distance of ED and FBWs (B_k)	$B_k / h = 0.1, 0.2 \text{ and } 0.3$
Distance within ED WECs (D_k)	$D_k / h = 0.025, 0.050 \text{ and } 0.075$

Table 3. Mooring system parameters

Mooring Parameters	Magnitude
--------------------	-----------

Type of mooring	Non-Linear Catenary/slack
Number of mooring lines	4.0
Mass per unit length (m)	20 kg/m
Equivalent cross-section area (A)	0.0008553 m ²
Stiffness (EA)	342119440 N
Maximum expected tension	400,000 N
Equivalent diameter	0.033 m
Longitudinal drag coefficients	0.5
Tolerance	5% of cable length

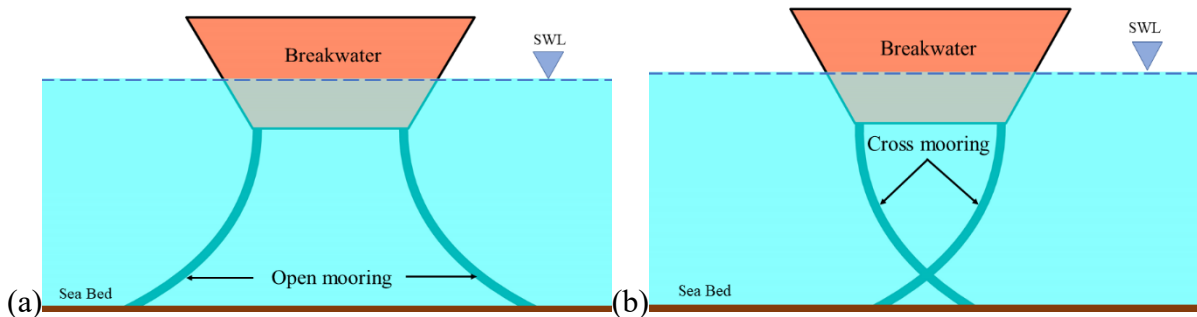


Figure 4. Catenary/slack type mooring configuration in (a) open and (b) cross type mooring.

For FBWs mooring system is required to keep the device stationed. A catenary mooring line heavily relies on chain weightage to provide horizontal restoring force to FBWs. In order to minimize the influence of mooring system on vertical motion of FBWs then top part of mooring should remain horizontal as possible (Davidson and Ringwood, 2017). Number of parameters mooring system and those values must be selected for mooring designing depending on site conditions.

6.3 Numerical Results and Discussion

Results obtained from the numerical model simulation in Ansys AQWA software is discussed in the present section. The numerical validation of the model is verified with the results of Sarah Bellew (2011), Ning et al. (2018), Hu et al. (2020) and Dimitrios et al. (2021), Ning et al. (2005) using appropriate correlation. The results obtained from the validations shows very good agreement with the results obtained from literatures.

6.3.1 Validation of literature study

The validation of the theoretical formulation is performed with the available data from the literatures. The validation for 5×1 array of Hemispherical WEC of radius a with centre to centre spacing of $4a$ subjected to beam sea ($\theta = 90^\circ$) and head sea waves ($\theta = 0^\circ$) and water depth of $5a$ is carried out. Radius of WEC in 5×1 array of hemispherical WEC is taken as $a = 5$ m with centre to centre spacing of $4a = 20$ m subjected to beam sea waves ($\theta = 90^\circ$) and water depth of $5a = 25$ m.

The validation for vertical bottom seated cylinder placed in front of vertical, bottom standing, surface penetrating orthogonal rigid and impermeable breakwater is validated. The radius of the cylindrical body is ϕ and draught d_v . The spacing between the centre of the cylinder and

two arms of the orthogonal walls d_1 and $d_2 = 1.2\phi$. Length of the arms of orthogonal walls is 50ϕ and depth of water equals to $h/\phi = 2$ and wave heading angle (α) is taken as $\pi/6$.

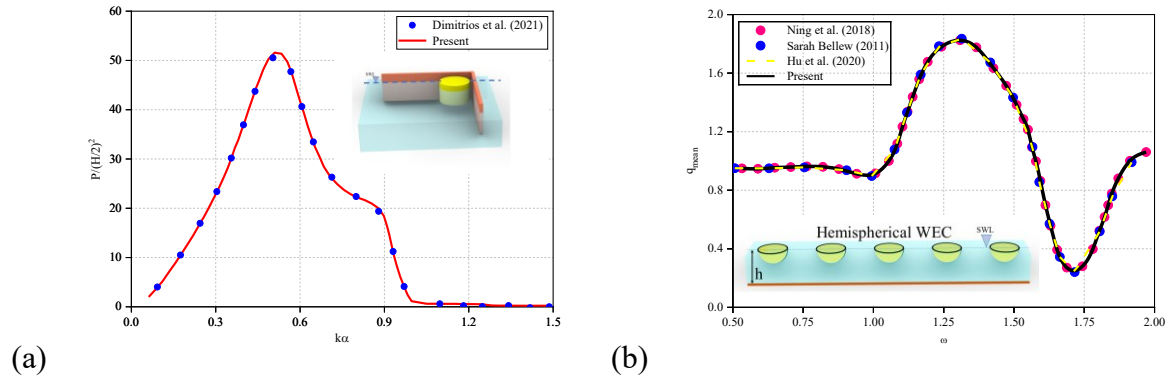


Figure 4. (a) Power absorption of a bottom seated cylinder in front of orthogonal breakwater (b) Mean interaction factor for 5×1 array of Hemispherical WEC.

6.3.2 Hydrodynamics Coefficients

In the present subsection, hydrodynamic coefficients of ED WEC arranged in 3×1 array hybrid system is investigated. Investigated results for hydrodynamic coefficients are discussed in figure 5. Added mass and figure 6. Radiation damping of the array system in ξ_{33} , ξ_{44} and ξ_{55} for the variation in B_k and D_k respectively. Variation of results in percentage (%) are discussed with respect to $B_k = 0.2$ and $D_k = 0.05$.

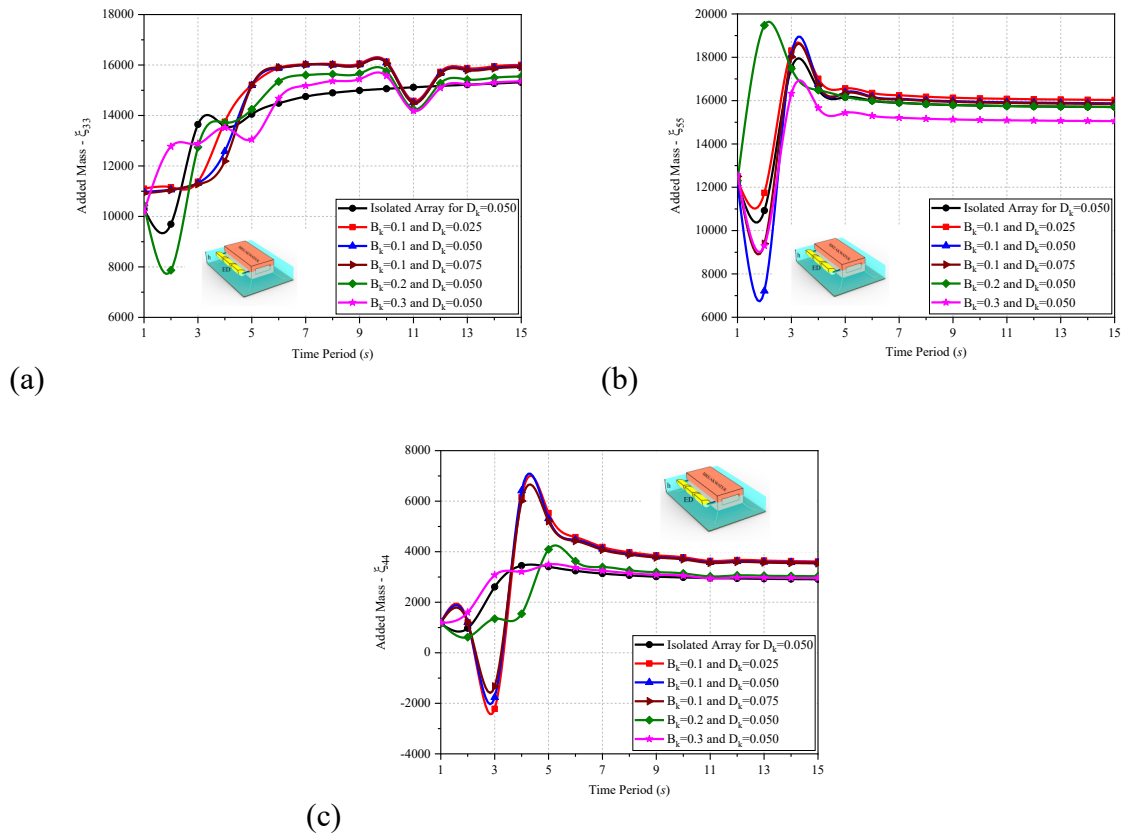


Figure 5. Added mass of array system in (a) Heave (b) Pitch and (c) Roll

Hydrodynamic coefficients (Added mass and Radiation damping) play an important role in evaluating hydrodynamic performance (Capture width ratio, Power absorption and Mean interaction factor) shown in equation 38. During the wave interaction ED will bob up and down with the waves and radiation of waves is generated producing reactions force on the EDs. This force is divided into two parts as added mass and the radiation damping as shown in equation 29. In deep waters ($T \leq 5.0s$) in figure 4(a) minor decreasing variation is observed with the increase in D_k between $3.0s \leq T \leq 5.0s$ in the range of 3-10%. Increment in B_k results in the decrement followed by increment in range of 40-50% for $1.0s \leq T < 3.0s$ and for $3.0s \leq T \leq 5.0s$ increment is followed by the decrement in range of 8.1-3.5%. In intermediate waters ($T \geq 6.0s$), behaviour is identical with D_k increment whereas decrement of 3.5-6.2% is observed for the change in B_k . In figure 4(b), added mass is decreasing followed by increase within 30-60% range of the variation in $1.0s \leq T < 3.0s$ for increasing value of D_k whereas for variation in B_k results in highly added mass for $B_k = 0.2$. For $T \geq 6.0s$, decrement of less than 1.0% is seen for D_k , while for B_k similar trend is observed in the variation range of 2-4.4%. In figure 4(c), increasing trend is observed for D_k while minor variation for B_k is observed with negative added mass at $T = 3.0s$ in deep waters. Negative added mass shows that there is more potential energy than kinetic energy in the near field of wave-structure interaction.

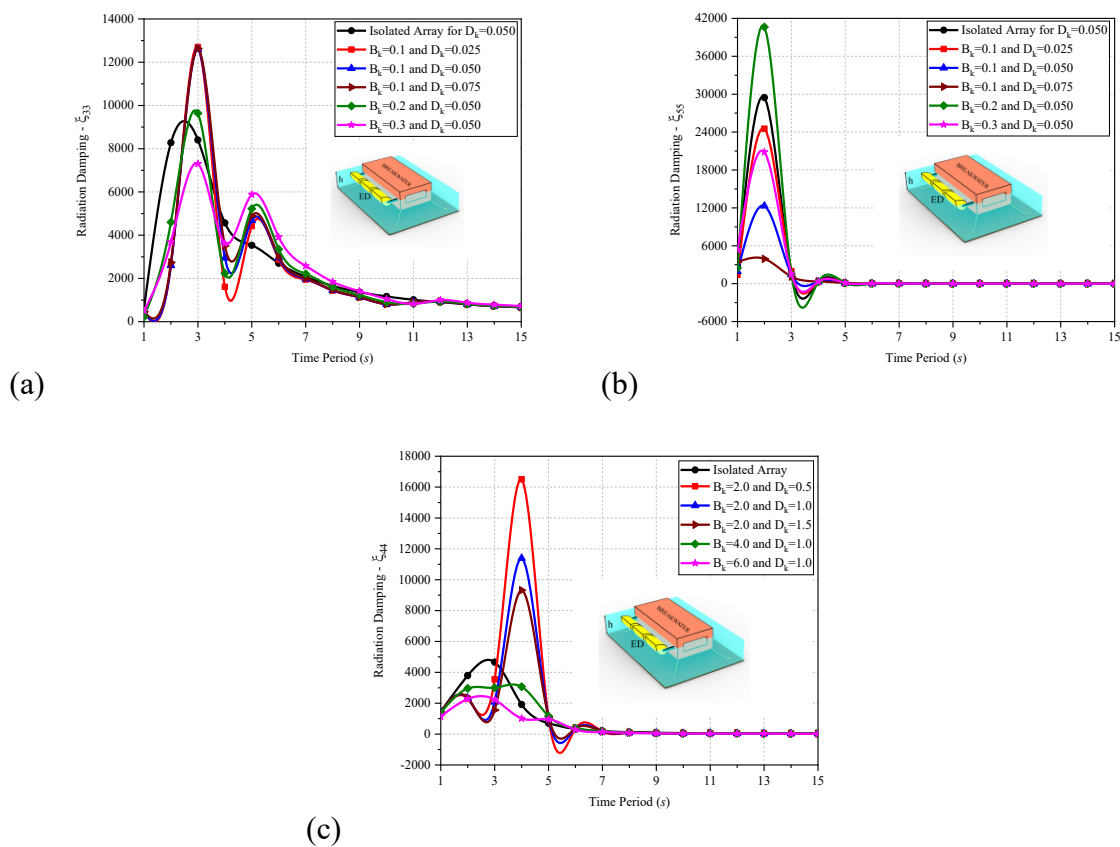


Figure 6. Radiation damping of array system in (a) Heave (b) Pitch and (c) Roll

For deep waters ($T \leq 5.0s$) in figure 6(a), minor variation is observed in D_k with peak value occurring at $T = 3.0s$ with multi-peaks and variation in the range of 45.2-19% increment at $T = 4.0s$. Increase in B_k result in increase in range of 27.87-62% and peak value at $T = 3.0s$. In intermediate waters ($T \geq 6.0s$), variation in D_k results in the identical behaviour while B_k results in increment range of 9.1-15.15%. In figure 6(b) increase in D_k results in increment by 1.0 fold for $D_k = 0.025$ and 68.06% decrement for $D_k = 0.075$ with respect to $D_k = 0.050$ at $T = 2.0s$ whereas variation in pitch shows increment followed by the decrement in range of 70-48.7%. Decreasing trend is observed with increase in D_k and is attaining peak value at $T = 4.0s$ in variation range of range of 44.8-18.3% for $D_k = 0.025$ and $D_k = 0.075$ respectively in figure 6(c). Increasing B_k will results in decreasing of radiation damping in range of 2.7 folds and 69%. For $T \geq 6.0s$, no variation is observed for variation in B_k and D_k . High value in radiation damping results in decrease of amplitude of the waves as it propagates and generates low response.

6.3.3 Hydrodynamic Response

In the present subsection, hydrodynamic response of ED WEC arranged in 3×1 array hybrid system is investigated. The investigated results are discussed for Response Amplitude Operators (RAOs) and wave excitation force in ξ_{33}, ξ_{44} and ξ_{55} for variation in B_k and D_k respectively after comparing the behaviour of isolated and hybrid array system in figure 7. B_k is one of the most important parameters in deciding the installation position of WEC from oceanic structures in order to make system perform effectively (Zhou et al., 2022). Also, spacing between WEC (D_k) in array plays an important role as they influence the behaviour of the nearby WEC structure in array.

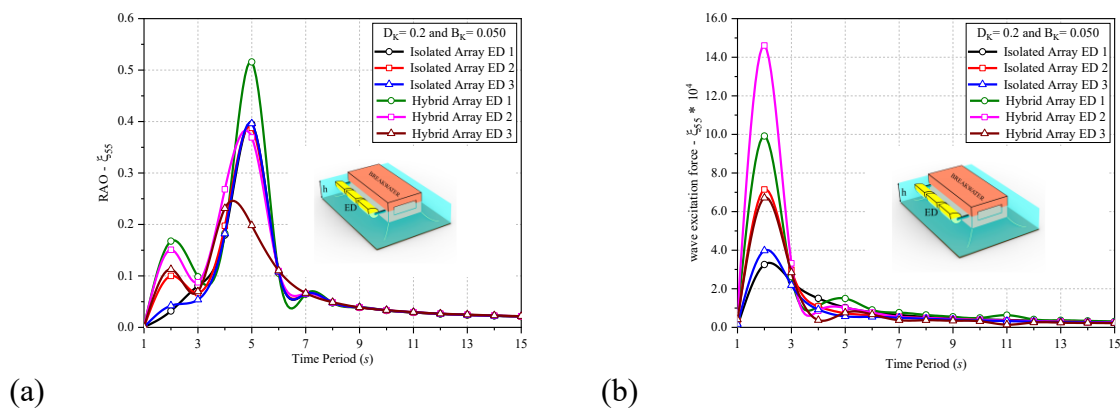


Figure 7. (a) RAO (b) wave excitation force in Pitch for $B_k = 0.2$ and $D_k = 0.05$.

In figure 7, the comparison of isolated and hybrid array is performed for RAO and wave excitation force. In figure 7(a), it is clearly observed that for isolated array minor variation is observed for $T \geq 3.0s$. For $T \leq 2.0s$, variation is in the range of 69-57% for ED-1 and ED-3 compared to ED-2 respectively. The maximum variation at $T = 5.0s$ is in the range of 40-

46.3% with ED-2. However, for $T \geq 7.0s$ negligible variation is observed in hybrid array also. In figure 7(b), an increment is observed followed by decrement in deep waters for isolated and hybrid array in range of 55-44% and 32-54% respectively with resonance condition for ED-2 while minor variations are observed in intermediate waters. For long waves in heave, structure follows wave profile hence showing constant variations for all paraments varied as the transmission of waves are generally more rather than reflecting or scattering. In hybrid array, decrease in RAO and wave excitation force is seen for farther WEC from incident waves due to the utilization of incident wave energy by other WEC to generate response. As less wave energy is incident on farthest WEC, study in the present paper will be more focused on ED-2 in the hybrid array system.

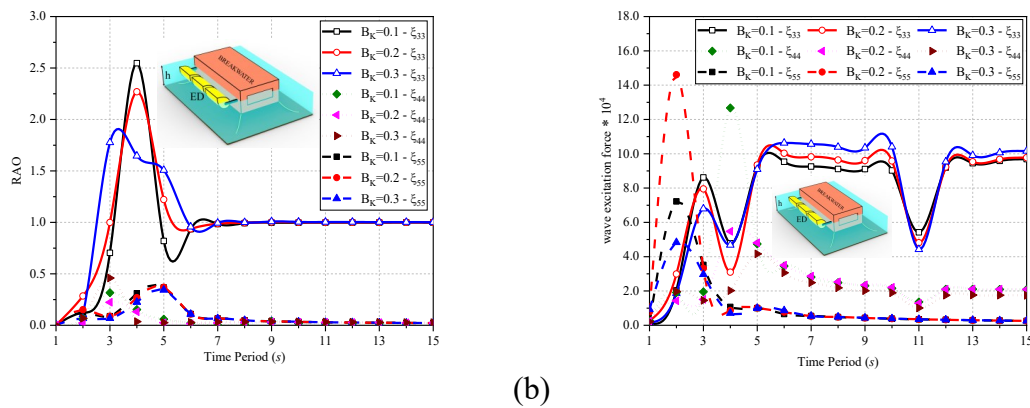


Figure 8. (a) RAO and (b) wave excitation force in heave, roll and pitch DOF for B_k .

Here in figure 8, hydrodynamic response for ED-2 is discussed for variation in B_k with respect to $B_k = 0.2$. RAO in figure 8(a) shows highest amplitude in heave and is decreasing with increase in B_k the range of 12-27.5% in deep waters. Magnitudes of roll and pitch are in approximation with negligible variation in pitch of 0.7-7% while in roll decrement is followed by increment and is in the range of 41.5% to 1-fold for $B_k = 0.1$ and $B_k = 0.3$. In intermediate waters, constant variation is observed for reason discussed earlier. In figure 8(b), wave excitation force is observed to be decreasing with increasing in B_k in the range of 8.4-14.5% in heave with slight failure at $T = 4.0s$ and 1.3-fold to 63% in roll with resonance for $B_k = 0.1$ at $T = 4.0s$. In pitch increment followed by decrement is observed in range of 50% for $B_k = 0.1$ and 67% for $B_k = 0.3$ with respect to $B_k = 0.2$. For $T \geq 6.0s$, constant variation in heave with failure condition at $T = 11.0s$ as a sudden fall is observed showing instability due to reduction in wave-structure interaction. As a result, waves will pass under the structure causing disturbance on the lee ward side of the BW and the major purpose of BW to create calm condition fails. Approximate identical behaviour is observed in roll and pitch.

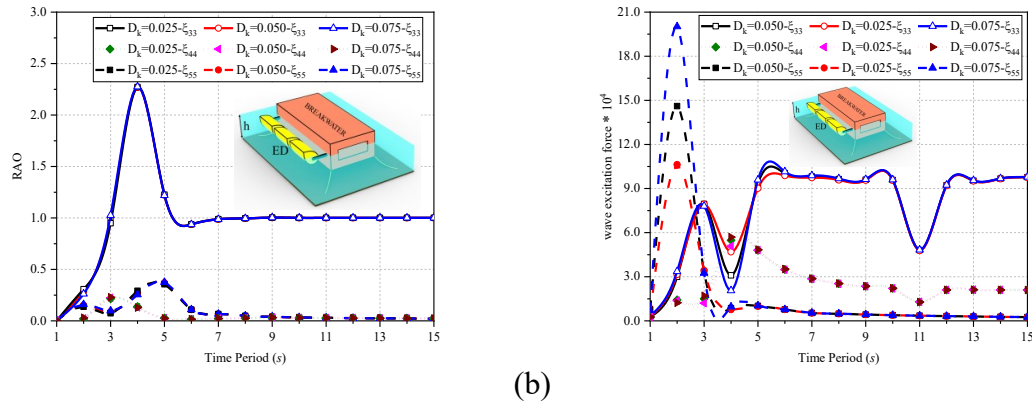


Figure 9. (a) RAO and (b) wave excitation force in heave, roll and pitch DOF for D_k .

Variation discussed in figure 9 for change in D_k shows negligible or identical behaviour in RAO for all considered DOF (Figure 9(a)). However, the magnitude in heave is much greater than pitch and roll. Whereas for wave excitation force in figure 9(b) no significant variation is observed except at $T = 4.0s$ in heave and is approximately identical in pitch DOF. In roll decrement is observed with increase in D_k followed by an increment and is in the range of 37.5-88.5%. For $T \geq 6.0s$, all variations tend to converge with failure at $T = 11.0s$ for the reasons discussed earlier in heave.

6.3.4 Hydrodynamic performance

In the present subsection, hydrodynamic performance of ED WEC arranged in 3×1 array hybrid system is investigated. The investigated results are discussed for power absorption and capture width ratio in ξ_{33} , ξ_{44} and ξ_{55} for variation in B_k and D_k respectively for box shape floating breakwaters.

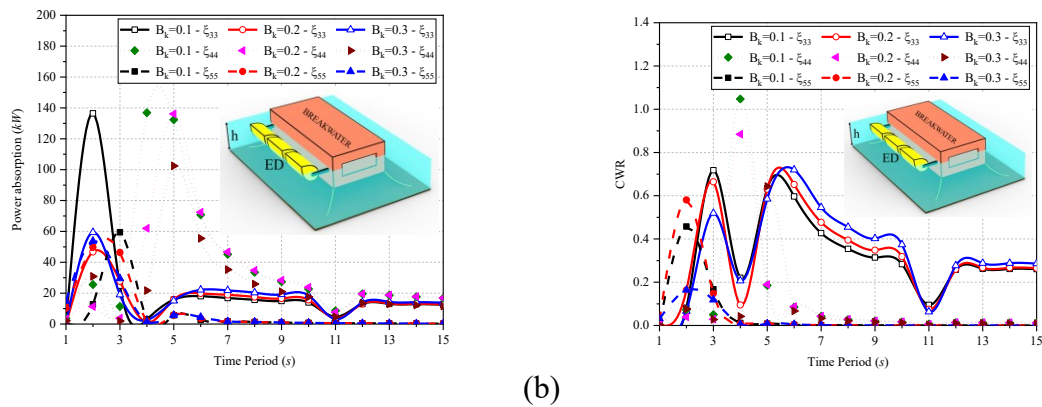


Figure 10. (a) Power absorption and (b) CWR in heave, roll and pitch DOF for B_k .

Power absorption and capture width ratio is discussed in figure 10 and the comparison of results for $B_k = 0.1$ and $B_k = 0.3$ is with $B_k = 0.2$ respectively. Power absorption in figure 10(a) in deep waters is decreasing with increase in B_k followed by increasing in the range of 1.92-fold and 27 % in heave and 19.47-8% in pitch. Whereas in roll DOF only decreasing trend is observed

with increase in in the range of 2.7-24.7%. In intermediate waters, negligible variation is observed for heave and pitch while minor variation in range of 0.7-31% is observed for roll. For capture width ratio in figure 10(b), decreasing pattern is observed for heave and roll with increasing B_k in the variation range of 8-21.8% and 18.46-27.29% respectively for deep waters. At $T = 4.0s$ and $T = 11.0s$, a dip is observed for heave resembling the failure condition due to reduced wave-structure interaction as discussed. In pitch DOF, variation is observed only at $T = 2.0s$ in range of 21.2-17.72% while for rest of the time period negligible variation is observed.

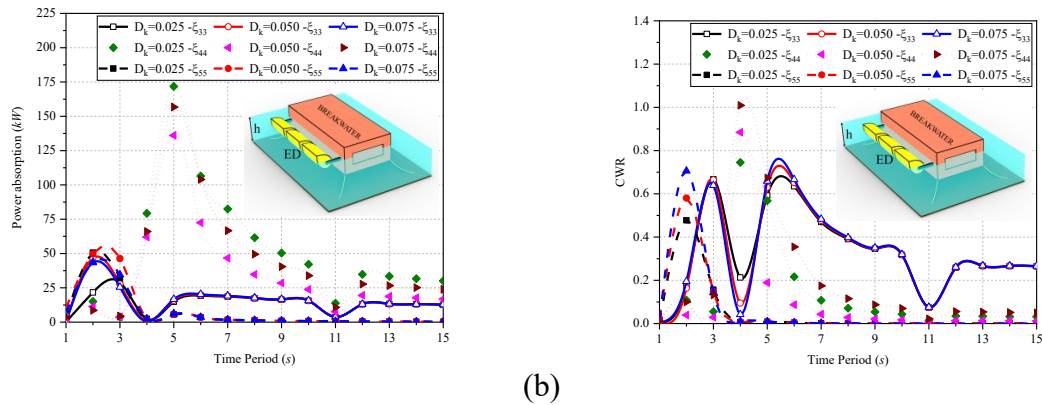


Figure 11. (a) Power absorption and (b) CWR in heave, roll and pitch DOF for D_k .

Power absorption and capture width ratio is discussed in figure 11 and the comparison of results for $D_k = 0.025$ and $D_k = 0.075$ is with $D_k = 0.050$ respectively. Power absorption in figure 11(a) in deep waters seems to be increasing in magnitude and then showing minor variation in heave in range of 53.7-7.2% with increase in D_k . Variation in D_k for roll DOF results in decrement of power absorption followed by increment in range of 43.6-47% with peak value at $T = 5.0s$. A dip is observed for heave and roll at $T = 11.0s$ for $T \geq 6.0s$ showing reduction in wave structure interaction results in less power absorption. In pitch DOF increase in power absorption magnitude at $T = 2.0s$ is observed and is in the variation range of 1.7-12.36%. In intermediate waters, considered DOFs are showing almost negligible variation except roll as it shows approximately constant variation as ED is roll type WEC and is dependent on axial wave thrust not on wave profile. In figure 11(b) CWR for variation in D_k is discussed. With increase in D_k negligible variation is observed for heave except at $T = 4.0s$. A sudden dip is observed and variation is in the range of 1.25-fold to 55.2%. In roll and pitch DOF variation is observed only at specific time period of $T = 4.0s$ and $T = 2.0s$ in deep waters with variation in range of 15.74-14.11% and 17.72-21.62% respectively. In heave and pitch identical behaviour and for roll constant variation is observed.

6.3.5 Comparison of Array system

In the present subsection, comparison in performance of ED WEC arranged in 3×1 array hybrid system is investigated with isolated array system and with different shapes of FBWs. The investigated results are discussed for mean interaction factor, power absorption and capture

width ratio in ξ_{33} , ξ_{44} and ξ_{55} for variation in B_k and D_k respectively.

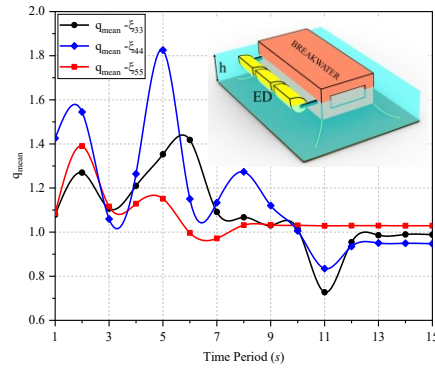
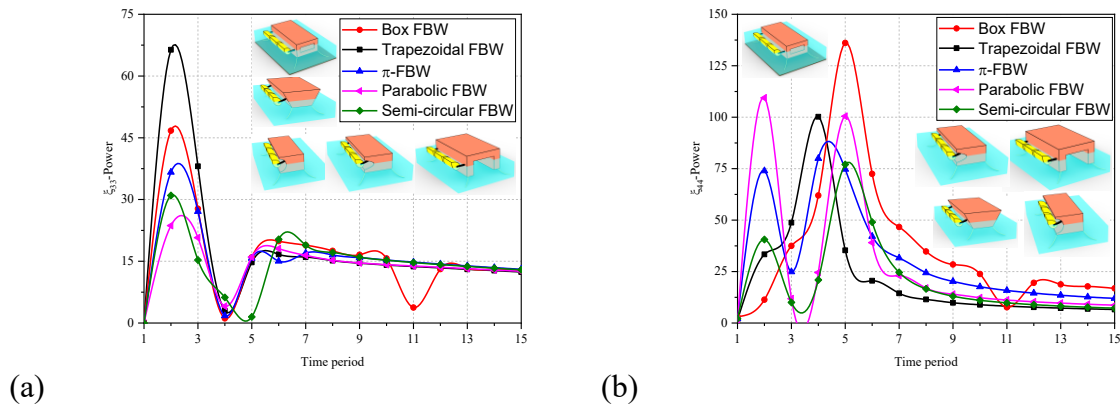
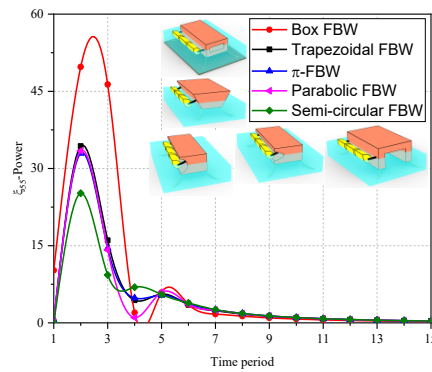


Figure 12. Mean interaction factor of array system for $B_k = 0.2$ and $D_k = 0.05$.

Mean interaction factor is an important parameters to measure the performance of WEC in hybrid to that of isolated system and is useful for the developers to understand the limiting applications to real system. An interaction factor of $q=1$ indicates that the array system is producing the same power as of the same device producing power in isolation, whereas $q > 1$ and $q < 1$ indicates the constructive and destructive interaction of the system. In figure 12, q_{mean} for considered DOF is discussed for ED-2. In deep waters, $q > 1$ which indicated that integration of ED WEC with FBWs is providing a solution of harnessing more wave power with elimination of isolation WEC restrictions of high mooring and cost. The highly constructive effect is observed in roll DOF at $T=5.0s$ followed by heave followed by pitch whereas in intermediate waters, for $6.0s \leq T \leq 10.0s$ heave and roll constructive effect is observed while for $T > 10.0s$ destructive effect is seen specially at $T = 11.0s$. For heave mostly constructive effect is observed in heave.





(c)

Figure 13. Power absorption in (a) heave, (b) roll and (c) pitch for $B_k = 0.2$, $D_k = 0.05$.

From figure 13(a) variation in power absorption is observed in deep waters while in intermediate waters minor variations are observed as all shapes tend to converge except box FBW. Although similar behavioural pattern is observed for all the shapes of FBWs with maximum peak at $T = 2.0$ s for trapezoidal FBW followed by box FBW, π FBW, semi-circular FBW, and parabolic FBW. FBWs belongs to line family shows resonance condition at $T = 2.0$ s while FBWs belongs to curve family gives much little peak variations with respect to line family FBWs. Also, a sudden dip is observed just next to resonance condition showing instability due to reduction in wave-structure interaction. As compared to box FBW, power output of trapezoidal FBW is 42% more while, π , semi-circular, and parabolic FBW are 21.63%, 33.7%, and 49.38% less. In intermediate waters failure is observed for box FBW at $T = 11.0$ s. In figure 13 (b) for deep waters, multipeak are observed for π , semi-circular, and parabolic FBW while single peak for box and trapezoidal FBW. A sudden fall in power absorption is observed between two multipeak indication that waves are interacting with the structure results in the decrease in the productivity of the system. The first peak is obtained at $T = 2.0$ s while second peak at $T = 5.0$ s. For multipeak at $T = 5.0$ s, as compared to box FBW, power output of trapezoidal FBW is 26.36% less while, π is 41.25% less, semi-circular is 43.38% less and parabolic FBW is 26.17% less. Though the behaviour pattern of for π , semi-circular, and parabolic FBW and for box and trapezoidal FBW are similar but parabolic and box are subjected to resonance. In intermediate waters, all shapes power absorption in roll DOF tends to converge except box FBW which is showing a little failure at $T = 11.0$ s. In figure 13(c) it is observed that trapezoidal and π FBW are behaving identical in deep as well as in intermediate waters. While parabolic FBW is showing some variations between $T > 4.0$ s and $T < 6.0$ s. For rest of the time periods, it is behaving similar to that of trapezoidal and π FBW. As compared to box FBW, trapezoidal, parabolic and π FBW is approximately 30% less while semi-circular FBW is 49.37% less. In Intermediate waters all shapes are behaving similar and almost identical.

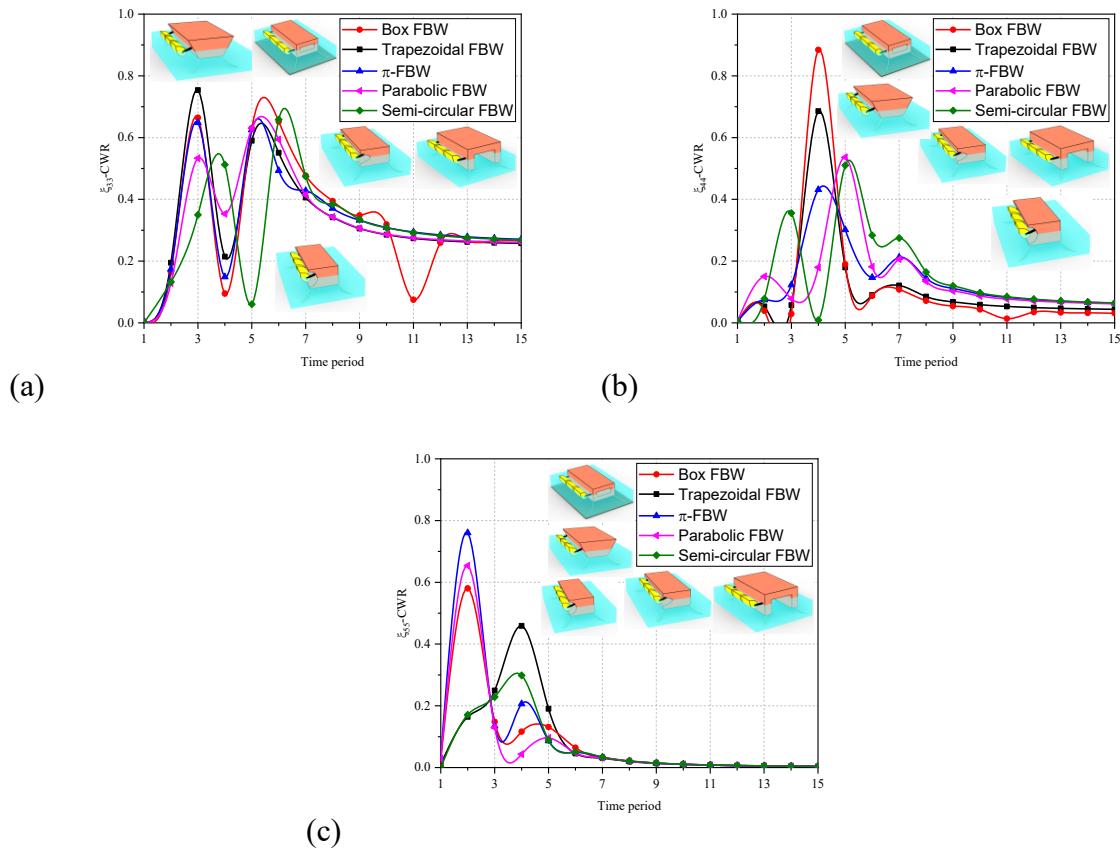


Figure 14. Capture width ratio in (a) heave, (b) roll and (c) pitch for $B_k = 0.2$, $D_k = 0.05$.

From figure 14(a) variation in capture width ratio for deep waters and intermediate waters can be observed clearly in heave DOF. However, the variation and behavioural pattern is similar for all shapes of FBWs considered with phase difference of $1.0s$ for curve family FBWS as compare to that of line family FBWs. Here also multipeak are observed indicating that integrated breakwaters are helping in absorbing more wave power by reflecting and diffracting the waves towards WECs. Peaks are obtained at $T = 3.0s$ and $T = 5.0s$ with a sudden dip indicating destructive nature by reducing wave power absorption. As compared to box FBW, power output of trapezoidal FBW is 13.47% more while, π , semi-circular, and parabolic FBW are 2.4%, 22.87%, and 19.72% less. In intermediate waters failure is observed for box FBW at $T = 11.0s$ while other FBWs shows constant variation as in heave in intermediate water WEC follows wave profile resulting in constant variation. In figure 14(b) it is observed that only single peak is obtained by all shapes of FBWs with minimum CWR of approximately reaching $\geq 50\%$. The time period at which ($T = 4.0s$) peaks is obtained by Line family FBWs, at same time curve family FBWs are showing minimum CWR magnitude and vica-versa at $T = 5.0s$. As compared to box FBW maximum CWR attained by, trapezoidal and π FBW is approximately 22.455% and 51.20% less while semi-circular and parabolic FBW is 42.31% and 39.34% less respectively. From figure 14(c), single peak performance is obtained by all shapes of FBWs with box, π and parabolic FBWs attaining at $T = 2.0s$ while trapezoidal and semi-circular FBW at $T = 4.0s$. Trapezoidal and semi-circular FBW is showing CWR in larger region of time period while others are shoeing resonance generating conditions. As compared

to box FBW maximum CWR attained by, π and parabolic FBWs is 31.024% and 12.68% more while for trapezoidal and semi-circular FBW it is 20.93% and 48.57% less. In intermediate waters behaviour is similar and with negligible variations.

6.3.6 Mooring Analysis

For FBWs mooring system is required to keep FBWs stationed. Mooring system influences the dynamic behaviour of FBWs, contributing nonlinear resistance and reactance to the FBWs dynamics. Mooring system must ensure and maintain the FBWs position under extreme loading conditions ensuring its serviceability in operational conditions. The mooring system used for the present study is catenary or slacked typed mooring. Slack mooring lines may also present dynamic restoring forces in the case of high frequency. Parametric details of mooring are mentioned in Table 3 previously. In this subsection mooring tension analysis for open and cross mooring configuration for front and rear end mooring respectively in figure 15(a,b) and figure 16(a,b).

In figure 15(a) mooring tension in open configuration for front end mooring line is discussed. It can be observed that the tension generating for π -FBW, parabolic FBW and semi-circular FBW is much more than the expected tension of 400 kN while for box and trapezoidal FBW tension generated is almost negligible when compared with rest of the shapes. Expected tension for π -FBW, parabolic FBW and semi-circular FBW is crossed after 25.0s, 34.0s and 11.0s respectively while box and trapezoidal FBW is much more lesser than the expected tension. The mooring exceeding its expected tension generates for the resonance condition results in the FBWs to move in heave suddenly results in enormous tension generation and sometimes leads to breakage or failure of mooring system. In figure 15(b) mooring tension in open configuration for Rear end mooring line is discussed and it is observed that mooring tension for semi-circular FBWs exceeds at the early stage of the response while Parabolic mooring is exceeding at some time periods but not in enhanced magnitude and π -FBW is exceeding its expected tension for 40.0s.

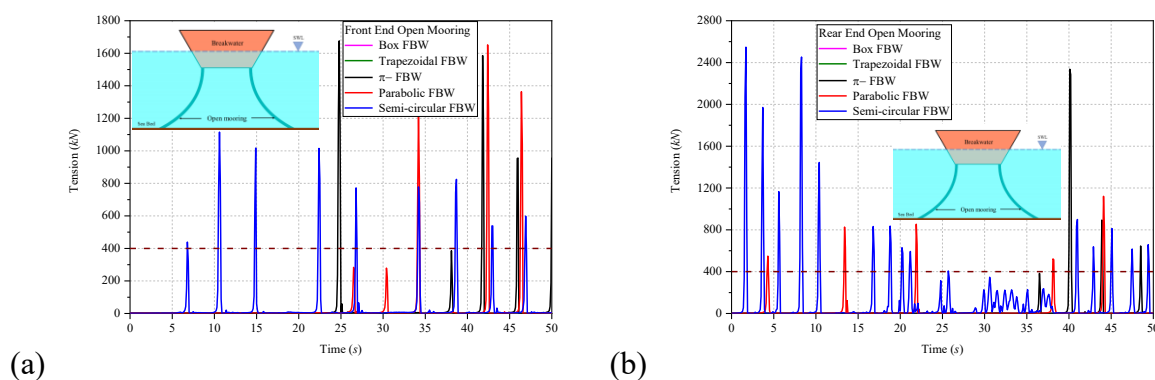


Figure 15. Time response mooring tension for open configuration (a) Front end (b) Rear end for different shapes of FBWs at 4.0s.

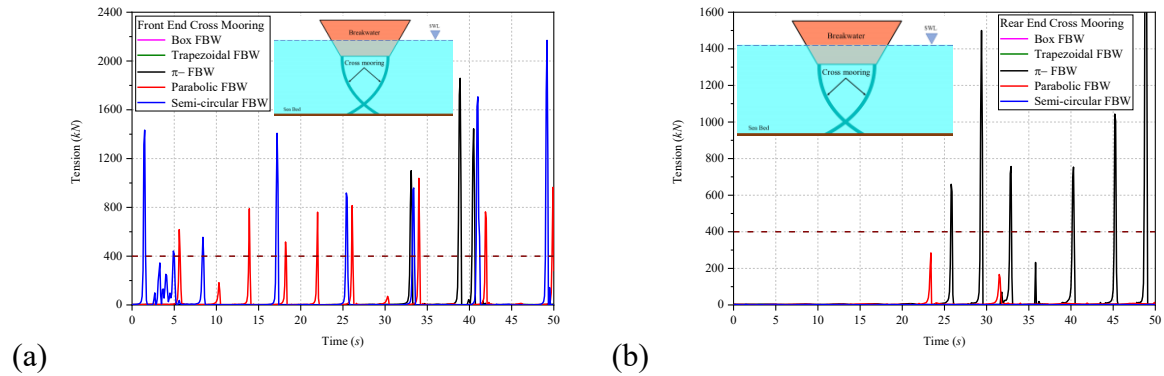
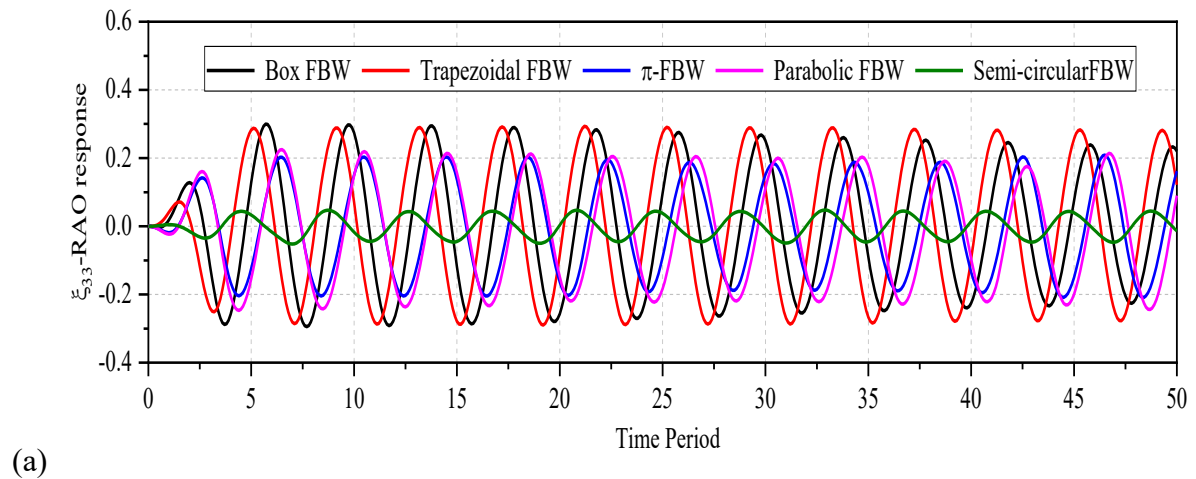
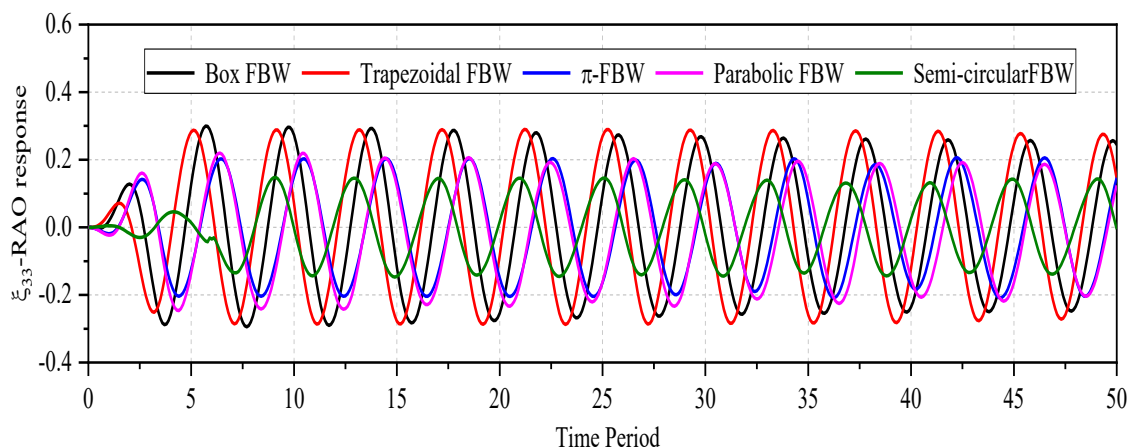


Figure 16. Time response mooring tension for cross configuration (a) Front end (b) Rear end for different shapes of FBWs at 4.0s .

In figure 16(a) mooring tension in cross configuration for front end mooring line is discussed. It is observed that for semi circular FBW expected tension of 400kN is exceeded at a very early time period and further exceeded many times. Similarly Parabolic FBWs is also exceeding its limit but is less than that of semi-circular FBW while π -FBW exceed its limit at 39.0s . For box and trapezoidal FBW mooring tension is much lesser than that of the other FBWs. In figure 16(b) mooring tension in cross configuration for Rear end mooring line is discussed and it is observed that only π -FBW is exceeding its expected tension limit. In figure 15 and figure 16 all FBWs exceeding its tension limit except box FBW and Trapezoidal FBW.

To investigate the wave pattern around the FBW, a wave is applied to the FBWs for 1.0m amplitude and a period of 4.0s in regular waves to show the wave amplitude variation after interacting FBWs in lower time period in open mooring and cross mooring configuration.





(b)

Figure 17. RAO based response for (a) Open and (b) cross mooring configuration in heave

Figure 17 (a,b) shows the time response of the RAOs in heave for different FBWS in open and closed mooring configuration at 4.0s. Response simulation performed for time of 50.0s with the step size of 0.1s for incident wave height of 1.0m. The effect of shape and the configuration of FBWs response is discussed in the time domain. In figure 17 for open mooring and cross mooring RAO response in heave shows that Box FBW has biggest magnitude followed by trapezoidal, π -FBW and parabolic while semi-circular FBW has the least. The motions observed are of regular. Anyhow the behaviour of π FBW and parabolic FBWS is approximately similar in pattern as well as in magnitude. Based on this result in stability criteria semi-circular FBW is more stable.

6.4 CONCLUSIONS

Present study investigates the hydrodynamic performance and mooring tension analysis of Edinburgh Duck Wave Energy Converter (ED WEC) arranged in array integrated to Box Floating Breakwater (FBW) under the light of small amplitude wave theory and then the results are compared with different shapes of FBWs namely: trapezoidal FBW, π -FBW, parabolic FBW and semi-circular FBW. The results are investigated for heave, roll and pitch for parameters varied like Distance of ED WEC in array from FBW (B_k) and Distance between ED WEC within (D_k) for $W_{ed} = 5.0m$, $Z_c = 1.1m$ at $\theta = 30^\circ$. Analysing the results of these variations, following conclusion can be drawn.

- Renewable energies are the energy for future generation and when coupled with energy storage device can support sustainable energy with zero carbon footprints. WEC when integrated with marine structures enhance performance of the WECs reducing cost of mooring and construction.
- Hydrodynamics coefficients plays an important role in behavior of hydrodynamics characteristics and performance of WEC arranged in array in hybrid system. Negative added mass shows more potential energy available than kinetic energy in fluid domain and high radiation damping decreases amplitude of waves.
- Integration of WEC array with hybrid system enhance the performance of WEC by reflecting and scattering the incident waves back towards WEC and increasing its capture with ratio by constructive interaction within hybrid system.

- Increasing distance between WEC and FBWs reduces RAOs and wave excitation force of the system in heave as wave energy starts dissipating before reaching WEC in deep waters. RAO and wave excitation force in roll keeps decreasing because of counter action of incident and reflected waves for some time periods. In pitch variation is almost negligible for RAO but increases decreases in for excitation force with resonance condition for $B_k = 0.2$. Increasing distance within WEC array shows negligible variation for RAO while increases only pitch.
- Increasing distance between WEC and FBWs shows decreasing variation in roll for power absorption and capture width ratio. In heave resonance is observed for $B_k = 0.1$ and is decreasing for power absorption and capture width ratio. In pitch variation is decreasing for power absorption and is increasing for capture width ratio but is negligible. Increasing distance between EDs results decreasing variation in roll while negligible variation for heave and pitch for power absorption. For capture width increasing trends for roll and pitch while no major variation is observed for heave.
- For deep waters in heave power absorption for trapezoidal FBW is more followed by box FBW, π -FBW, semi-circular FBW while Parabolic FBW has least power absorption. In roll DOF, multi peak is obtained for π -FBW, parabolic FBW and semi-circular FBW with highest power absorption by box FBW followed by parabolic FBW, trapezoidal FBW, π -FBW and semi-circular FBW with least magnitude. Whereas in pitch box FBW having highest while semi-circular FBW having least power absorption magnitude while others lie between these two with approximately same magnitude. For intermediate waters, all shapes tend to converge with a failure for box FBW at $T = 11.0s$ in heave and roll while in pitch all FBWs behaves nearly identical.
- For CWR in deep waters for heave multipeak is obtained for all FBWs with highest magnitude for box FBW while least id for π -FBW along with a dip at $T = 4.0s$. In roll single peak pattern is observed with highest magnitude for box FBW followed by trapezoidal FBW, parabolic FBW and semi-circular FBW while π -FBW is having least magnitude. Also, failure at $T = 4.0s$ for semi-circular is observed. In pitch highest magnitude of CWR is for π -FBW while parabolic and box FBWs follows it and it is followed by trapezoidal and semi-circular FBWs with lag difference of $2.0s$. In intermediate waters, all shapes either tends to converge or behave identical for all shapes in considered DOF except box FBW for heave.
- Mooring system is required to keep FBWs stationed. Mooring system must ensure and maintain the FBWs position under extreme loading conditions ensuring its serviceability in operational conditions. For open mooring configurations, π -FBW, parabolic FBW and semi-circular FBW are exceeding expected tension while box and trapezoidal FBW have negligible mooring tension compared with other FBWs for both front and rear mooring cables while for cross mooring, parabolic FBW and semi-circular FBW is exceeding tension limit while π -FBW is exceeding tension limit only at $39.0s$ for front end mooring while for rear end mooring only π -FBW is exceeding it limit. Rest all are behaving within limits and are much smaller in magnitude.
- Open and cross mooring RAO response in heave shows that Box FBW has largest

tension magnitude followed by the trapezoidal, π -FBW and parabolic while semi-circular FBW has least. Anyhow the behaviour of π FBW and parabolic FBWS is approximately similar in pattern as well as in magnitude. Stability criteria semi-circular FBW is more stable.

CHAPTER 7

HYDRODYNAMIC PERFORMANCE OF HYBRID FLOATING BREAKWATER INTEGRATED WITH OSCILLATING WATER COLUMN WEC

7.1 THEORETICAL FORMULATION

The present theoretical formulation is based on the small amplitude wave theory, which assumes fluid as homogeneous, inviscid and incompressible, flow as irrotational, wave amplitude is small compared to the wavelength and water depth and applicability of follows potential flow theory. The governing equation is the Laplace equation which is given by

$$\nabla^2 \Phi = 0 \quad (1)$$

The kinematic bottom boundary condition stating that the vertical velocity at sea bed is expressed as

$$w = \frac{\partial \phi}{\partial z} = 0 \text{ at } z = -h \quad (2)$$

Further, the dynamic free surface boundary condition is expressed as

$$\eta = \frac{1}{g} \left(\frac{\partial \phi}{\partial t} \right) \text{ at } z = 0 \quad (3)$$

The velocity potential at any location, $\vec{O} = (x, y, z)$ for a propagating wave in finite water depth is expressed as

$$\Phi(\vec{O}) = \left[(\phi_I + \phi_D) + \sum_{j=1}^6 \phi_{Rj} x_j \right] \quad (4)$$

where ϕ_I is the first-order incident wave potential with unit wave amplitude, ϕ_D is the corresponding diffraction wave potential, ϕ_{Rj} is the radiation wave potential due to the j^{th} motion with unit motion amplitude.

The relation between wavelength, wave period and water depth known as a dispersion relation consisting of wave number can be expressed as

$$\omega^2 = gk \tanh kh \quad (5)$$

The incident wave-induced Froude-Krylov force, the diffraction wave-induced diffracting force, and the radiation wave-induced radiation force caused by unit rigid body motion make up the total first order hydrodynamic force. The radiation force can be given by

$$F_{rjm} = \omega^2 A_{jm} + i\omega B_{jm} \quad (6)$$

where F_{rjm} is the j^{th} radiation force due to the radiation wave induced by the m^{th} unit amplitude motion of the body, the real part consists of added mass A_{jm} and imaginary part consists of radiation damping B_{jm} where n_j is j^{th} motion amplitude.

$$A_{jm} = \int_{\Omega_0} \frac{\text{imag}[\phi_{rm}(\vec{O})]\rho n_j}{\omega} d\Omega \quad (7a)$$

$$B_{jm} = \int_{\Omega_0} -\text{real}[\phi_{rm}(\vec{O})]\rho n_j d\Omega \quad (7b)$$

When wave interacts with a floating structure it causes motion and put force on the structure of the structure, which can be determined by solving the problem in terms of wave diffraction and radiation. The Ansys AQWA solver is employed in the present study to solve the diffraction and radiation problem of wave structure interaction which follows a boundary integral approach and satisfies the condition

$$-\omega^2 \phi + g \frac{\partial \phi}{\partial z} = 0 \text{ at } z = 0 \quad (8)$$

$$\frac{\partial \phi}{\partial n} = \begin{cases} -i\omega n & \text{for } \phi_R \\ -\frac{\partial \phi}{\partial n} & \text{for } \phi_D \end{cases} \quad (9)$$

Considering the above-mentioned conditions and using Green's Theorem, the velocity potential for radiated and diffracted waves can be given by

$$\phi(\vec{O}) = \frac{1}{c_0} \int_{\Omega_0} \left\{ \phi(\vec{\xi}) \frac{\partial G(\vec{O}, \vec{\xi}, \omega)}{\partial n(\vec{\xi})} - \partial G(\vec{O}, \vec{\xi}, \omega) \frac{\partial \phi(\vec{\xi})}{\partial n(\vec{\xi})} \right\} d\Omega \quad (10)$$

$$\text{where, the position of a source is } \vec{\xi} = (\xi, \zeta, \eta) \text{ and } c_0 = \begin{cases} 0 & \text{for } \vec{O} \notin \Gamma \cup \Omega_0 \\ 2\pi & \text{for } \vec{O} \in \Omega_0 \\ 4\pi & \text{for } \vec{O} \in \Gamma \end{cases}$$

Further with introduction of source distribution for the fluid potential over the mean wetted surface and employing the Hess-Smith constant panel method, AQWA solves the fluid potential. It assumes each panel's potential and source strength are constant and taken as the matching average values throughout the panel's surface and discretize the potential equation which is further solved for the potential determination. The discretized equation is given as

$$\phi(\vec{O}) = \frac{1}{4\pi} \sum_N^{n=1} \sigma_n G(\vec{O}, \vec{\xi}_n, \omega) \Omega_n \quad \text{for } \vec{O} \in \Gamma \cup \Omega_0 \quad (12)$$

$$\frac{\partial \phi(\vec{O}_m)}{\partial n(\vec{O}_m)} = -\frac{2}{\sigma_m} + \frac{1}{4\pi} \sum_N^{n=1} \sigma_n \frac{\partial G(\vec{O}_m, \vec{\xi}_n, \omega)}{\partial n(\vec{O}_m)} \Omega_n \quad \text{for } \vec{O} \in \Omega_0, m=1, N \quad (13)$$

where, N is the total number of diffracting panels, σ_n and σ_m are intensity of sources of the n^{th} and m^{th} panel respectively, Ω_n is area of n^{th} panel, and $\vec{\xi}_n$, \vec{O}_m are the coordinates of panel geometric centre of the n^{th} and m^{th} panel respectively. AQWA resolves a number of linear algebraic equations to evaluate the body's harmonic responses to periodic waves. The term response amplitude operators (RAOs) refer to these response properties that are proportional to wave amplitude. The equation of motion is given by

$$[-\omega^2 (M_{str} + M_{am} + M_{udam}) - i\omega (C + C_{ud}) + K_{hss} + K_{udhss} + K_{astr}] [x_{jn}] = [F_{jn}] \quad (14)$$

where ω is incident wave frequency, M_{str} is the total structural mass matrix, M_{am} is the total added mass matrix due to diffracting panels and Morison elements, M_{udam} is the user-defined additional added mass matrix, C is the hydrodynamic damping matrix by the diffracting panel elements, C_{ud} is the user-defined additional linear hydrodynamic damping, K_{hss} is the assembled hydrostatic stiffness matrix, K_{udhss} is the user-defined additional hydrostatic stiffness matrix, K_{astr} is the additional structural stiffness matrix, and F_{jn} are the total Froude-Krylov and diffracting force and moments.

The hydrodynamic performance assessment parameter for the OWC which is integrated with floating breakwater is considered to be its power capture efficiency. The efficiency calculations are performed using Ansys Fluent simulations. As the wave strikes on the OWC structure it causes free water surface inside OWC chamber to move in an oscillating manner which results in chamber air's pressure changes causing air to force its way out and comes in when pressure decreases. This movement of air could be then converted to electrical energy using Wells turbine. Ansys Fluent is used to get the pressure fluctuation in oscillating water chamber and air flow through outlet orifice on top due to the said pressure change. A multiphase Volume of Fluid (VOF) flow model is used to simulate sea waves which consider two fluid phases, namely, air and water, which interacts near the free surface region. By resolving a continuity equation for the volume fraction of one of the phases, it is possible to trace the interface between the phases. The volume fraction equation for the i^{th} phase is given by

$$\frac{\partial(\alpha_i \rho_i)}{\partial t} + \nabla \cdot (\alpha_i \rho_i \vec{v}_i) - \sum_{i'=1}^{t_s} (\dot{m}_{i'i} - \dot{m}_{ii'}) = S_{\alpha_i} \quad (15)$$

where, α_i is i^{th} fluid volume fraction which can take value of 0 for no fluid existence in the cell, 1 for full fluid existence in the cell and between 0 to 1 at the interface of two fluid phases, $\dot{m}_{i'i}$ is the mass transfer function from phase i' to i and $\dot{m}_{ii'}$ is the mass transfer function from phase i to i' , S_{α_i} is the source term by default it is zero but it can be defined otherwise, ρ_i and \vec{v}_i are the density and velocity of fluid phase i . The volume fraction equation can be solved and discretized using implicit formulation, which is useful for both time-dependent and steady-state calculations given by

$$\left[\frac{\alpha_i^{t_s+1} \rho_i^{t_s+1} - \alpha_i^{t_s} \rho_i^{t_s}}{\Delta t} \right] V + \sum_f (\alpha_{i,f}^{t_s+1} \rho_i^{t_s+1} U_{i,f}^{t_s+1}) - V \left[\sum_{i'=1}^{t_s} (\dot{m}_{i'i} - \dot{m}_{ii'}) \right] = S_{\alpha_i} V \quad (16)$$

where, $\alpha_i^{t_s+1}$ and $\alpha_i^{t_s}$ is the cell volume fraction at current time step ($t_s + 1$) and previous time step (t_s), $\alpha_{i,f}^{t_s+1}$ is the face value of volume fraction at $t_s + 1$, $U_{i,f}^{t_s+1}$ is flux of volume via the face at $t_s + 1$ and V is cell volume. The momentum equation shown below is a common equation shared by all phases to determine the velocity field is given by

$$\nabla p + \nabla \cdot (\rho \vec{v} \vec{v}) - \nabla \cdot [\mu (\nabla \vec{v} + \nabla \vec{v}^T)] = \rho \vec{g} + \vec{F} - \frac{\partial(\rho \vec{v})}{\partial t} \quad (17)$$

Open channel wave boundary condition is set according to the wave theory which used in the study. To suppress the numerical reflection of waves caused by outlet boundary a momentum damping sink term S_k is added in the momentum equation for the cell zones near pressure outlet boundary which is given by

$$S_k = - \left[D_1 \rho \hat{v} + 0.5 D_2 \rho \hat{v} |\hat{v}| \right] f(x) f(z) \quad (18)$$

where, D_1 and D_2 are the linear and quadratic damping resistance respectively, \hat{v} velocity along vertical direction along gravity, $f(x)$ and $f(z)$ are damping function in flow direction and vertical direction respectively. The above provision also called numerical beach treatment. The solution in this study follows SIMPLE algorithm of fluent solver with the default values of the under-relaxation factors. The power capture efficiency ε of the OWC can be determined by

$$\varepsilon = \frac{P_{cap}}{P_{inc}} \quad (19)$$

where, P_{cap} is power captured by the OWC chamber and P_{inc} is the power in incoming wave striking the structure. The incident wave power can be given by (CERC, 1984)

$$P_{inc} = \frac{\rho g H_i^2}{8} C_g \quad (20)$$

where, C_g is wave group velocity and it is given by,

$$C_g = \begin{cases} (\lambda / T) & \text{for shallow water region} \\ \frac{\lambda}{2T} \left[1 + \frac{2kh}{\sinh(2kh)} \right] & \text{for intermediate water region} \\ 0.5(\lambda / T) & \text{for deep water region} \end{cases} \quad (21)$$

The captured power (Ning et al., 2016) is expressed as

$$P_{cap} = \frac{1}{T} \int_t^{t+T} \Delta p(t) \cdot \Delta q_0(t) dt \quad (22)$$

where, over the total simulation time of t , $\Delta p(t)$ is change in air pressure inside OWC chamber under the action of incident wave and $\Delta q_0(t)$ is change in air flow rate through OWC chamber outlet.

7.2 Numerical Model Validation

The validation of the numerical model is performed for the hydrodynamic diffraction analysis of a floating breakwater (Cebada-Relea et al., 2022) using Ansys AQWA and computational fluid dynamics simulation of offshore stationary floating oscillating water column (Deng et al., 2019) using Ansys Fluent. The floating breakwater model (Cebada-Relea et al., 2022) is considered to be having $b/h = 0.593$, $d/h = 0.207$, and $L/h = 2.948$, is validated for its motion responses (RAOs) in six-degrees of freedom without viscous damping for three wave heading angles (0° , 45° and 90°). The results obtained (Fig. 1) are compared with Cebada-Relea et al. (2022) and it is worth noting that the numerical results are in good agreement with Cebada-Relea et al. (2022). Further, it can be noted that out of all the motion responses, only the surge, heave, and pitch motions are significant when wave incidence is normal to the floating breakwater structure.

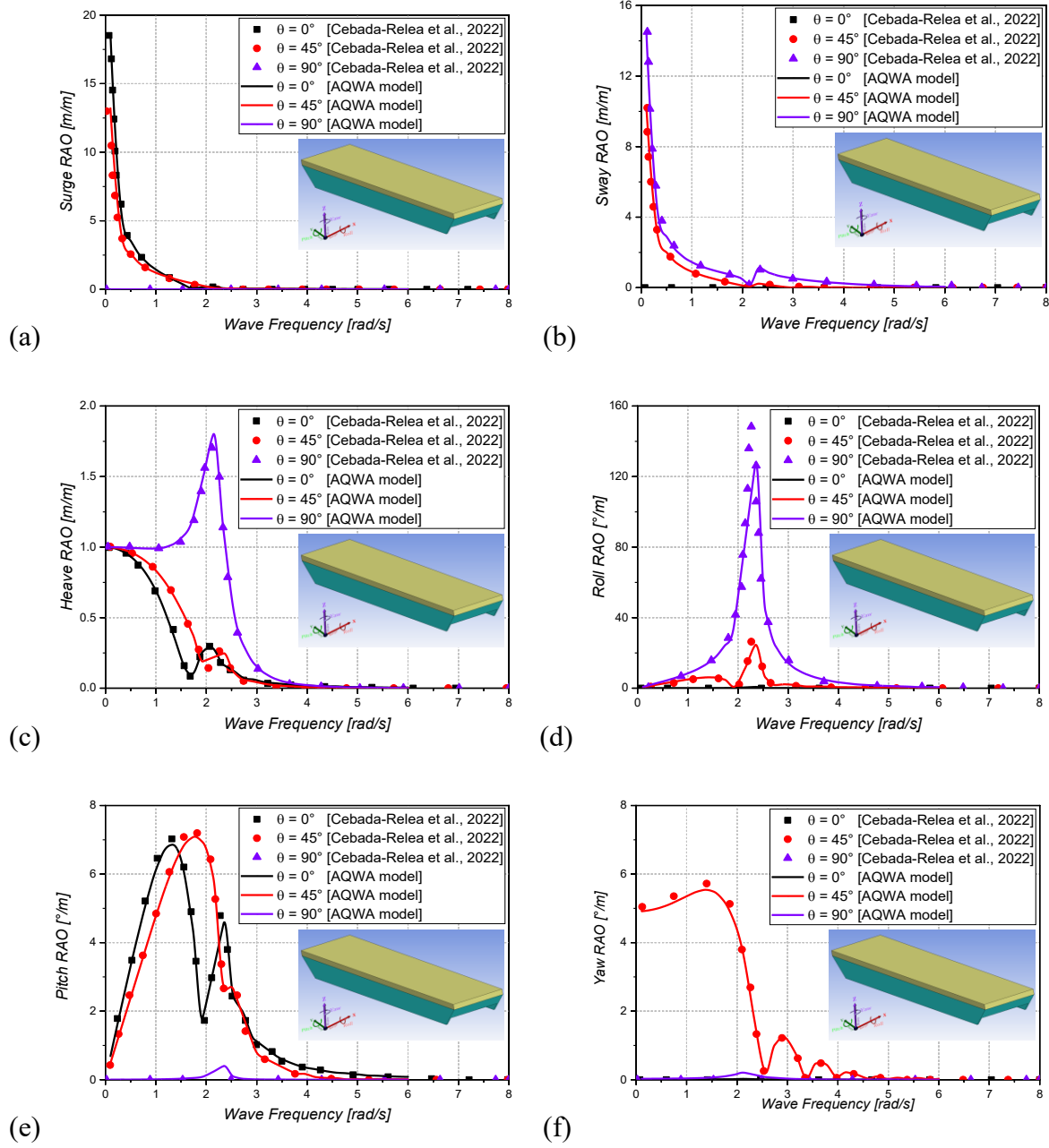


Fig. 1: RAOs of floating breakwater model (Cebada-Relea et al., 2022) in (a) surge, (b) sway, (c) heave, (d) roll, (e) pitch, and (f) yaw motion for different θ considering $b/h = 0.593$ and $d/h = 0.207$.

Further, in Fig. 2, the experimental study of an offshore stationary OWC device as in Deng et al. (2019) is compared and validated with Ansys Fluent to study the efficiency of OWC. The OWC with $c_x/h = 0.45$, $d_1/h = 0.25$, $d_2/h = 0.50$, and $c_0/c_x = 0.22$ (representing outlet area opening ratio of 1.2%) is modelled and based on the experimental setup as in Deng et al. (2019), the numerical domain is prepared in fluent and regular wave incidence is simulated and OWC chamber's air pressure variation and velocity of air flow through outlet is obtained and

efficiency is calculated. The result obtained from present fluent modelling seems to converge with the experimental results from the literature.

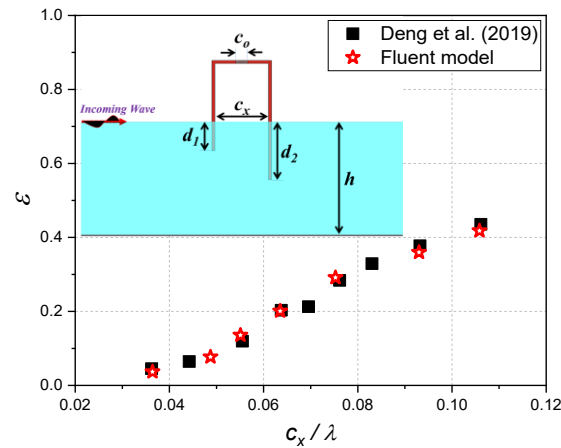


Fig. 2: Power capture efficiency verses c_x / λ for OWC with $c_x / h = 0.45$, $d_1 / h = 0.25$, $d_2 / h = 0.50$, and $c_0 / c_x = 0.22$.

7.2.1 Model Description of Floating Breakwater

The width of floating breakwater (FB) to water depth ratio (i.e., relative width, b / h) and draft of floating breakwater to water depth ratio (i.e., relative draft, d / h) are two important parameters to decide the breakwater dimensions. The floating breakwater model of different cross sections, considered in the study are having same relative draft ($d / h \approx 0.2$) and relative width ($b / h \approx 0.6$) as the floating breakwater prototype installed at Baiona Port (Peña et al., 2011). On considering b / h and d / h same, different cross-sectional shapes of the floating breakwaters (Table 1) are decided for same volume of displaced water by all shapes of FBs (i.e., mass of each floating breakwater unit is same). To attain approximately equal mass for all FB models, the L / h is considered different for each model. The trapezoidal-shape cross-section of HFB is having side slope of 1H:2V and it is kept constant in the present study. The different shapes of floating breakwater are then integrated with a J-shape OWC. The OWC integrated floating breakwater structure is named as hybrid floating breakwater (HFB). The three-dimensional schematic representation of different study models is presented in Fig. 3 along with the OWC which is integrated inside FB. The OWC dimensions are same in all HFB models and its chamber width c_x and the depth of its inlet below water level x to water depth ratio, are $c_x / h = 0.1$, and $x / h = 0.083$ respectively. Further, other OWC dimensions such as, inlet height c_i , diameter of outlet for air flow c_o , chamber height c_h , length c_l , and radius of

the curved section of the geometry (R_1 and R_2) are fixed with respect to c_x . In the present study the dimensions for the OWC are considered as $c_i/c_x = 1.0$, $c_h/c_x = 1.17$, $c_0/c_x = 0.5$, $c_l/c_x = 2.0$, $R_1/c_x = 1.0$, and $R_2/c_x = 2.0$.

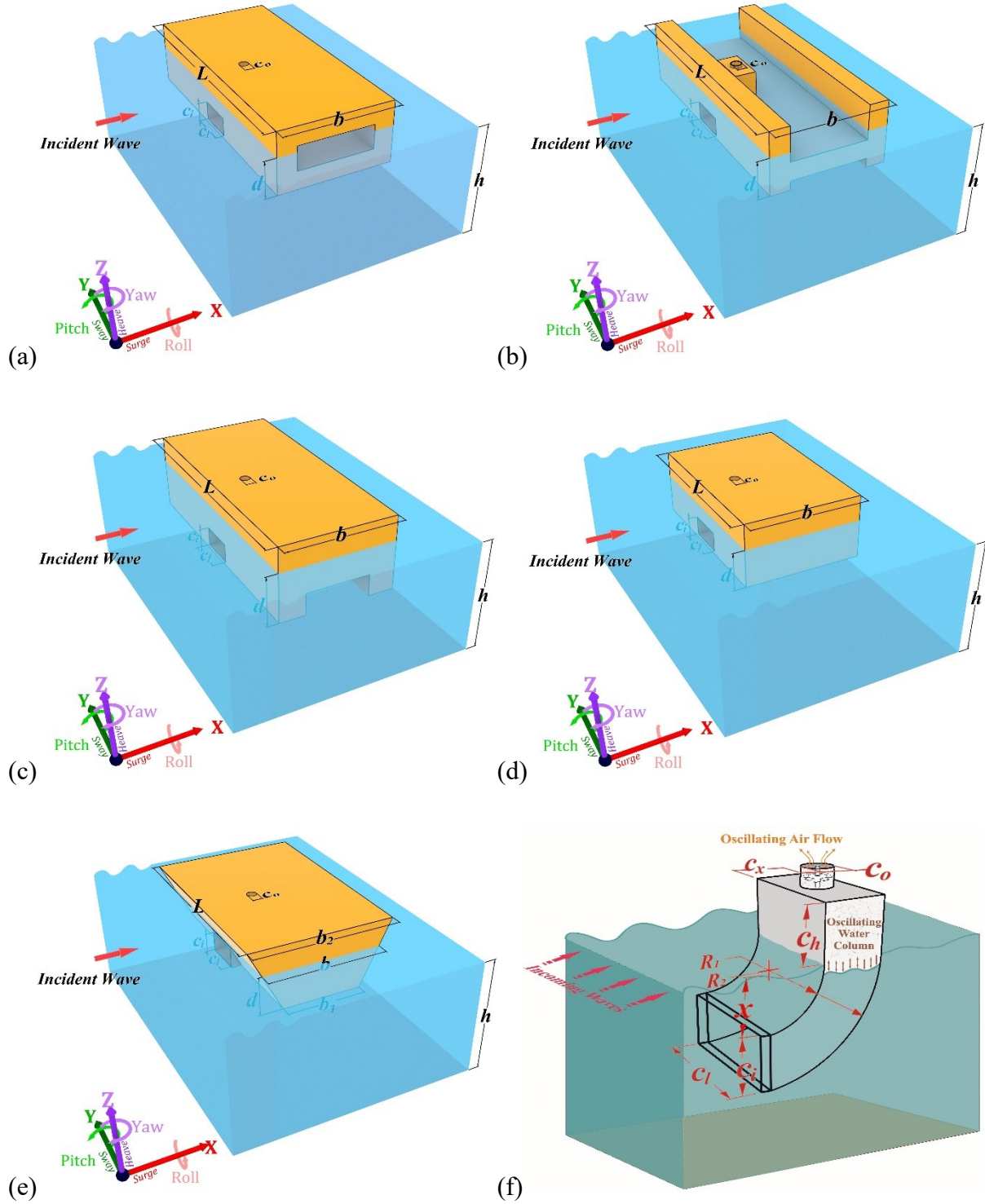


Fig. 3: Schematic representation of (a) box-type HFB, (b) H-type HFB, (c) Π -type HFB, (d) rectangular-type HFB, (e) trapezoidal-type HFB, and (f) J-shape OWC.

Table 1: Dimensions of different HFB models

HFB type	FB dimension						OWC dimension			
	b/h	d/h	L/h	t/h	b_1/h	b_2/h	x/h	c_x/h	c_0/h	c_l/h
Box-type HFB	0.60	0.20	1.33	0.10	-	-	0.083	0.10	0.05	0.20
H-type HFB	0.60	0.20	1.33	0.10	-	-	0.083	0.10	0.05	0.20
Π-type HFB	0.60	0.20	1.33	-	0.13	0.33	0.083	0.10	0.05	0.20
Rectangular-type HFB	0.60	0.20	0.89	-	-	-	0.083	0.10	0.05	0.20
Trapezoidal-type HFB	0.60	0.20	1.07	-	0.40	0.73	0.083	0.10	0.05	0.20

7.3 Numerical Results and Discussion

The numerical investigation of different HFB models is performed for the hydrodynamic performance in terms of response amplitude operators RAO_j , transmission coefficient C_T and wave energy conversion efficiency ε to compare the performance of different cross-sectional shapes of HFBs. The numerical results presented in this section are based on small amplitude wave theory within $0.1 \leq kh \leq 8.0$. The importance to study the interaction of structure with gravity waves is that, most significant forces that the ocean environment exerts on structures are due to surface gravity waves (Sarpkaya, 2010). The motion responses in surge RAO_1 , heave RAO_3 , and pitch RAO_5 motions for $\theta = 0^\circ$ and C_T are determined using hydrodynamic diffraction analysis.

7.4 Effect of Change in Shape of HFB

The numerical models for different cross-sectional shapes of floating breakwater integrated with OWC are examined for its hydrodynamics performance and for comparison of results certain parameters are kept constant for all HFB models (such as, $b/h = 0.6$, $d/h = 0.2$ and $\theta = 0^\circ$). For better comparison between HFBs, the variations of results in all other shapes are indicated with respect to rectangular-type HFB as it is simplest shape of floating breakwater and extensive investigation has been performed on this type of floating breakwater (Dai et al., 2018). The power capture efficiency of the HFB models is compared for an ideal case of floating body in which the HFB models are considered to be stationary (i.e., having no motions). The efficiency of HFB is evaluated to understand the effect of motions on the hybrid

structure to improve the wave energy conversion of integrated OWC device (Howe et al., 2020).

7.4.1 Motion Responses

The motion response for different types of HFB is performed for the freely floating body considering six-degrees of freedom in terms of RAOs. In Fig. 4(a-c), the motion responses for HFBs are presented in surge, heave and pitch motions for $0.1 \leq kh \leq 8.0$. The frequency domain analysis of each motion response shows a downward trend towards deep waters ($kh > 3.14$) reaching minimum values of $RAO_1 = 0.06\text{m/m}$ (Fig. 4a), $RAO_3 = 0.02\text{m/m}$ (Fig. 4b), and $RAO_5 = 0.13^\circ/\text{m}$ (Fig. 4c), in surge, heave, and pitch motion respectively.

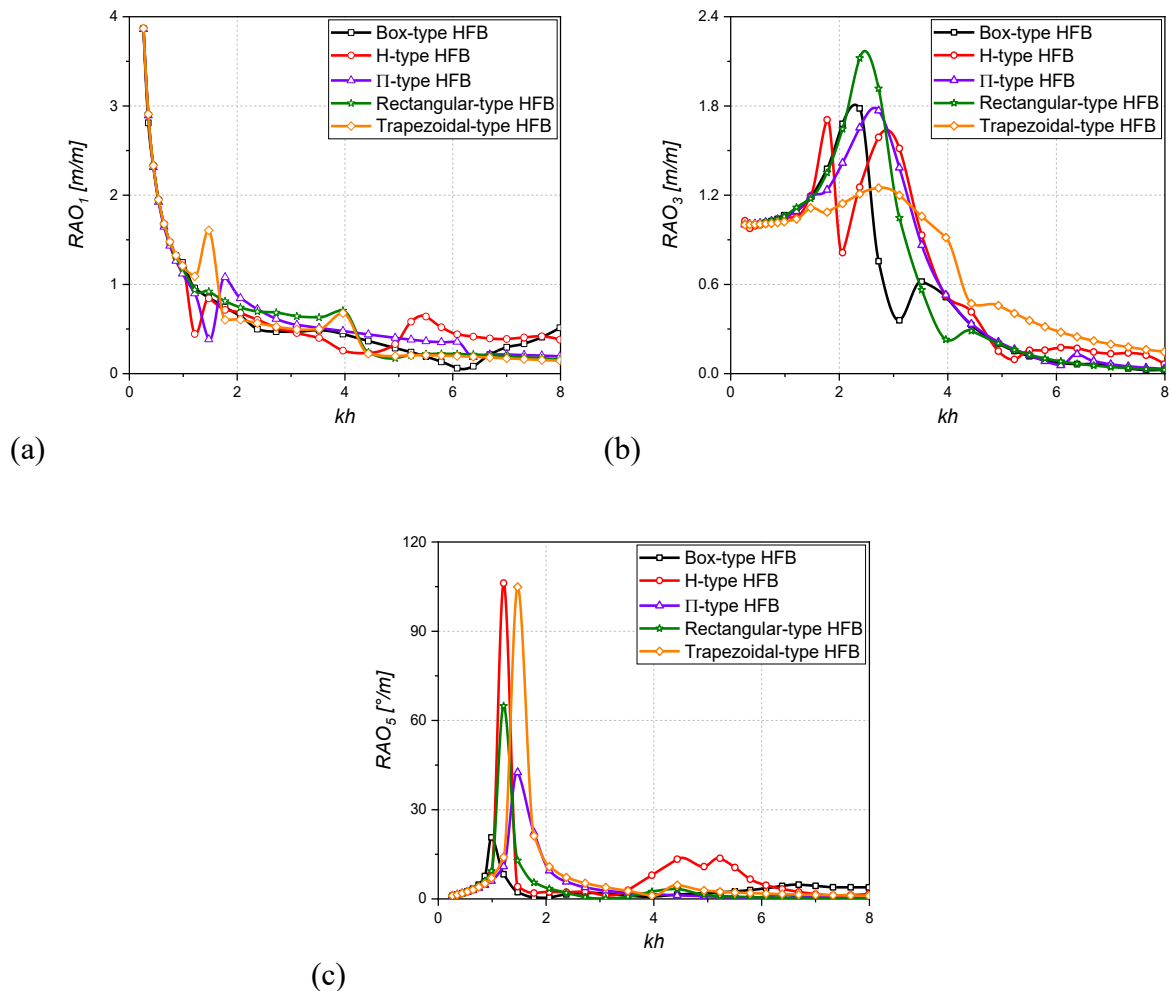


Fig. 4: Motion response of HFB configurations in (a) surge, (b) heave, and (c) pitch verses kh considering $b/h = 0.6$, $d/h = 0.2$ and $\theta = 0^\circ$.

The variation in surge motion (Fig.4a) is observed to decrease in the range of about 1% to 38% for box-type HFB and 8% to 63% for H-type HFB with respect to rectangular-type HFB for

$0.314 \leq kh \leq 3.96$. For $kh > 3.96$, the surge motion increases for H-type HFB by about 90% to 190% in comparison with surge of rectangular-type HFB which may be due to high wave induced forces on the structure in short waves as high energy concentration will be near free surface for these waves. Similar, trend in case of Π -type and box-type FB is noticed in Fig. 4(a). The trapezoidal-type FB shows different behaviour in surge in deep waters than other FB having the surge motion decreased by about 6% to 21% for $1.78 \leq kh \leq 3.14$ and 18% to 25% decrease with respect to surge motion of rectangle-type HFB which could be due to higher wave transmission than rectangular-type HFB in that region. From Fig. 4(b), it can be contemplated that the heave RAO values for each study model are approximately close to 1 m/m for $kh \leq 1.5$, which implies that the motion of the floating structure in heave direction is just about equal to the incoming wave amplitude. This can occur due to long wavelength of incident waves passing the structure. In case of $kh > 1.5$, noticeable variation in heave motion is there for all types of HFBs. When $kh > 3.14$, the heave RAO in H-type and trapezoidal-type HFB observed to be 1.2 to 5 times more than that of rectangular-type HFB. This could be due to change in diffracting surface area with change in shape causing changes in the wave interaction characteristics of floating body. For the considered wave frequencies highest value of heave RAO is observed for the rectangular-type HFB for $kh = 2.38$ and for other shapes the peak lies in the range of $1.77 < kh < 2.73$ which falls in range of intermediate water region. In deep waters, the rectangular-type HFB shows least heaving motion response and box-type HFB also shows approximately same response. This could be due to short wave getting reflected or attenuated more by these HFBs. Fig. 4(c) represents pitching motion RAOs for different type of HFBs, among them sudden rise in pitching motion has extremely high value of RAO_θ as equal to about $21^\circ/\text{m}$, $107^\circ/\text{m}$, $43^\circ/\text{m}$, $65^\circ/\text{m}$, and $105^\circ/\text{m}$ for box, H, Π , rectangle, and trapezoidal type HFB, respectively, in the range of $0.95 < kh < 1.50$. This value can be attributed as a result of the incident wave frequency being close to the structure's pitching natural frequency. Apart from the earlier said range of frequency the rectangular-type HFB experiences less pitching motion response among all HFBs. With respect to rectangular-type HFB, all other HFBs shows significantly high value of pitching motion in deep waters and among them H-type and box-type observed to be more unstable in pitching motion. If we avoid the natural frequency region of the HFBs, then rectangular, Π , and trapezoidal seems to be stable. As breakwaters are supposedly installed in shallow and intermediate water region therefore, the geometry of the HFBs can be further optimised to eliminate the occurrence of

natural frequency in the desired region so that structural integrity will be maintained while it is operating in such water regions.

7.4.2 Wave Transmission

The second comparison of HFBs is based on its hydrodynamic performance as a wave attenuating structure, which is evaluated by determining wave transmission coefficient (C_T) towards the lee-side of the floating structure (Fig.5) at a fixed distance of $1.5b$. By comparing all other types of HFBs with the rectangular-type HFB, it is worth noting that all of them shows less wave transmission than rectangular-HFB, which can be due to better wave attenuation or reflection. This indicates that changing the shape of the HFB will help in reducing the transmission of waves toward lee-side. The major reduction in C_T in comparison to rectangular-type HFB is found to be in range of about 12% to 59% in case of box-type, about 20% to 72% in case of H-type, about 11% to 43% in case of Π -type, and about 5% to 28% in case of trapezoidal-type for part of intermediate and full deep water region ($kh > 1.78$). The C_T value seems to be of irregular nature (random increase and decrease) for H-type HFB after a sudden drop at $kh=2.38$ and a similar observation for box-type also can be made in which C_T decreases and then increases and then suddenly drops. This random behaviour of increase and decrease in wave transmission can be due to trap and release of wave into hollow portion of box-shape and into middle portion of the H-shape models, which might be causing this behaviour at different wave frequencies. Fig. 5 further shows that the Π -type HFB performs better than all other HFBs in terms of wave transmission over considered range of wave frequencies. Further it can be noted that wave transmission in short waves i.e., in deep water region is less for all HFB models and considering the threshold value of 0.6 all models except rectangular-type show better performance in the earlier said water region.

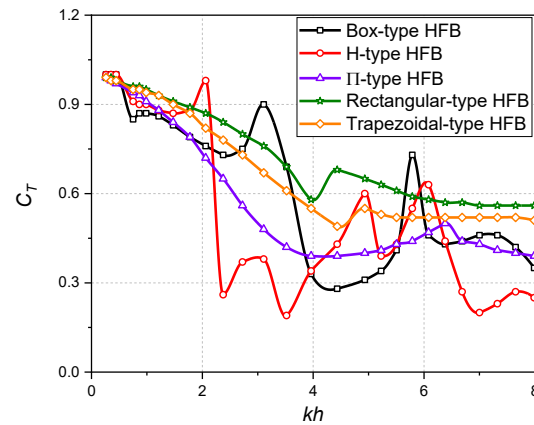


Fig. 5: Wave transmission coefficient of HFB models verses kh for $b/h = 0.6$, $d/h = 0.2$ and $\theta = 0^\circ$.

7.4.3 Power Capture Performance

The third important comparison of different HFB models can be made on the basis of its power capture performance. The power capture efficiency (ε) of the integrated OWC device is determined by simulating the models in Fluent and the power capture efficiency is plotted with respect to kh for considered points of wave frequency representing the full range of $0.1 < kh < 8.0$ (Fig. 6). For the considered parameters of HFB models the power capture performance is significant in the range of $1.77 < kh < 3.61$, considering a threshold value of $\varepsilon = 0.25$. The highest value of ε is observed for the box-type HFB for $kh = 2.51$, which could be due large amplitude oscillations of the water surface inside OWC attached with box-HFB and it leads to large airflow velocities resulting in high efficiency. For box, Π , and H-type HFBs the power capture ratio is increasing beyond 1.0 which indicate better power conversion and the results of this kind is also obtained by the researcher (Howe and Nader, 2017; Howe et al., 2020) for OWC integrated hybrid floating breakwater studied by them through numerical and experimental investigations. Further, it is worth noting that the trapezoidal and rectangular-type HFB models demonstrated broader bandwidth of the power capture ratio and it is almost in the region of 75% to 80%, which is the good power conversion bandwidth. The maximum efficiency of power capture for H-type HFB $\varepsilon = 1.56$ is for $kh = 2.06$, for Π -type HFB $\varepsilon = 1.17$ is for $kh = 2.51$, for rectangular-type HFB $\varepsilon = 0.90$ is for $kh = 3.03$, for trapezoidal-type HFB $\varepsilon = 0.90$ is for $kh = 3.03$. This indicates that for the floating breakwater integrated OWC wave energy converter device the performance is better in intermediate water region.

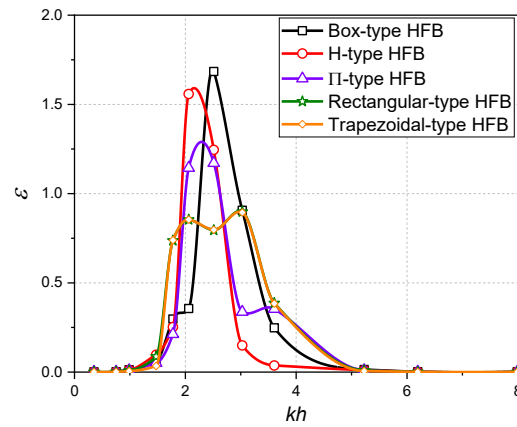


Fig. 6: Power capture efficiency of HFB models verses kh for $b/h=0.6$, $d/h=0.2$, $c_x/h=0.1$, $x/h=0.083$, and $\theta=0^\circ$.

The streamline for the air flow velocity through the OWC chamber for HFB models is presented for box, H, Π , rectangle, and trapezoidal type in the Fig. 7, Fig. 8, Fig. 9, Fig. 10, and Fig. 11 respectively for regular incident wave of $kh=2.51$ at different flow time instances of simulation for better visualization of flow pattern inside OWC chamber. The time instances are chosen for representation of a complete oscillation indicating upward and downward flow of air through the outlet of the OWC. In Fig. 7(a, b, and c) downstream flow can be observed which is followed by an upstream flow as visible in Fig. 7(d, e, and f) for the box-type HFB.

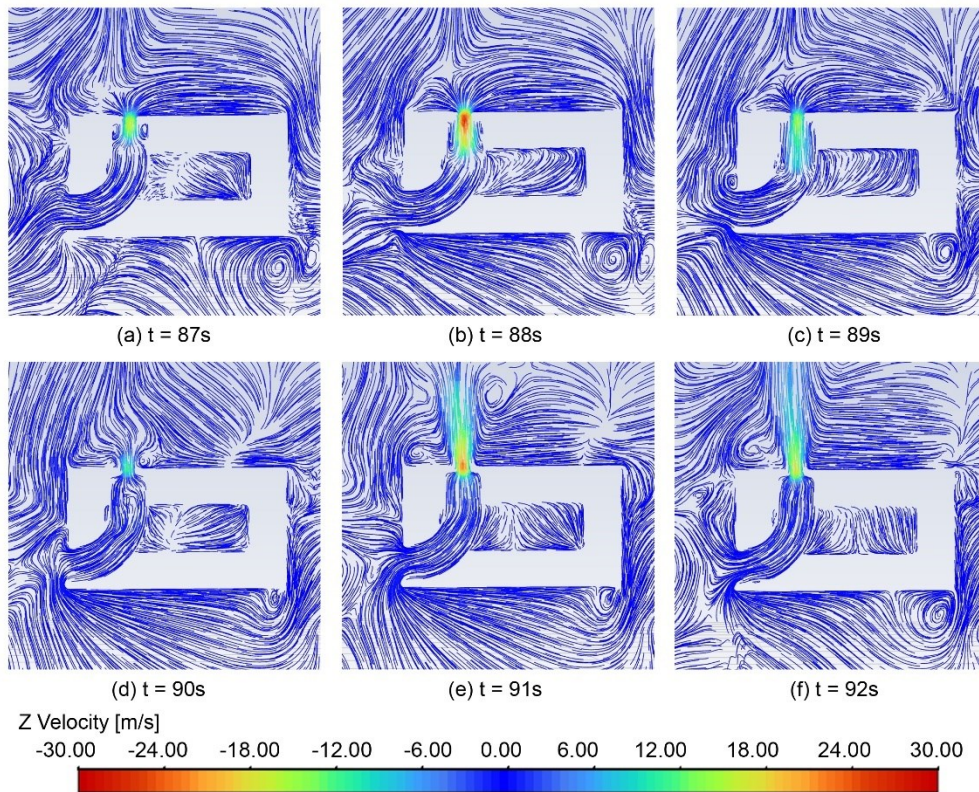


Fig. 7: Vertical velocity pathlines of the box-type HFB for $kh = 2.51$ and $\theta = 0^\circ$ at different time instances (a) $t = 87s$, (b) $t = 88s$, (c) $t = 89s$, (d) $t = 90s$, (e) $t = 91s$, and (f) $t = 92s$.

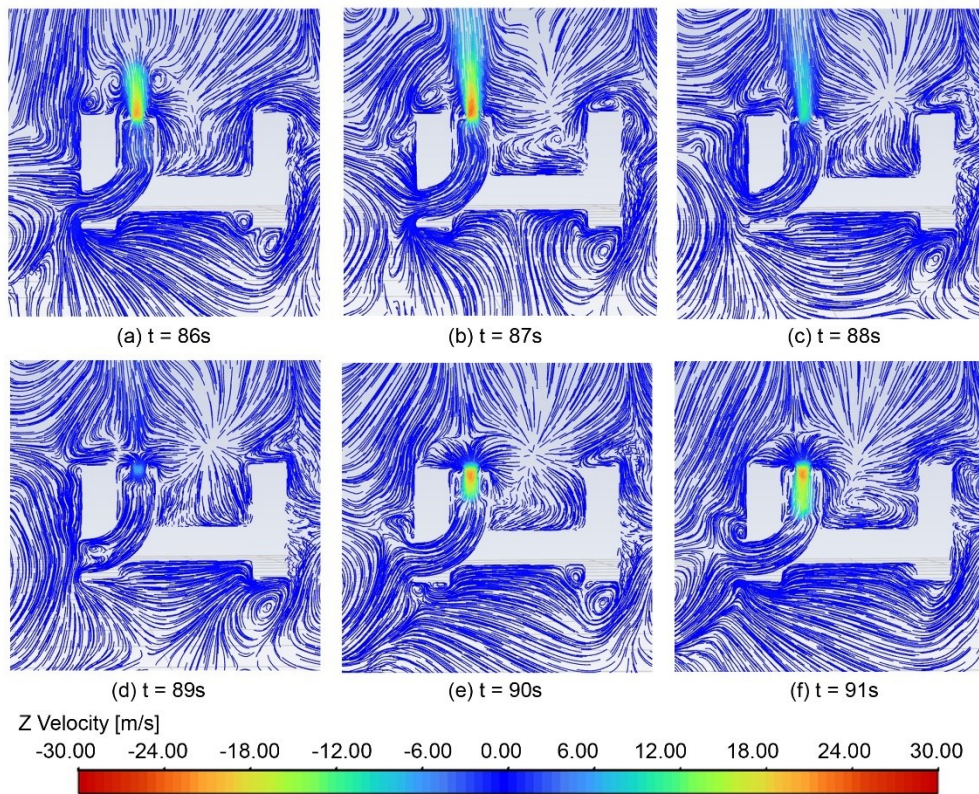


Fig. 8: Vertical velocity pathlines of the H-type HFB for $kh = 2.51$ and $\theta = 0^\circ$ at different time instances (a) $t = 86s$, (b) $t = 87s$, (c) $t = 88s$, (d) $t = 89s$, (e) $t = 90s$, and (f) $t = 91s$.

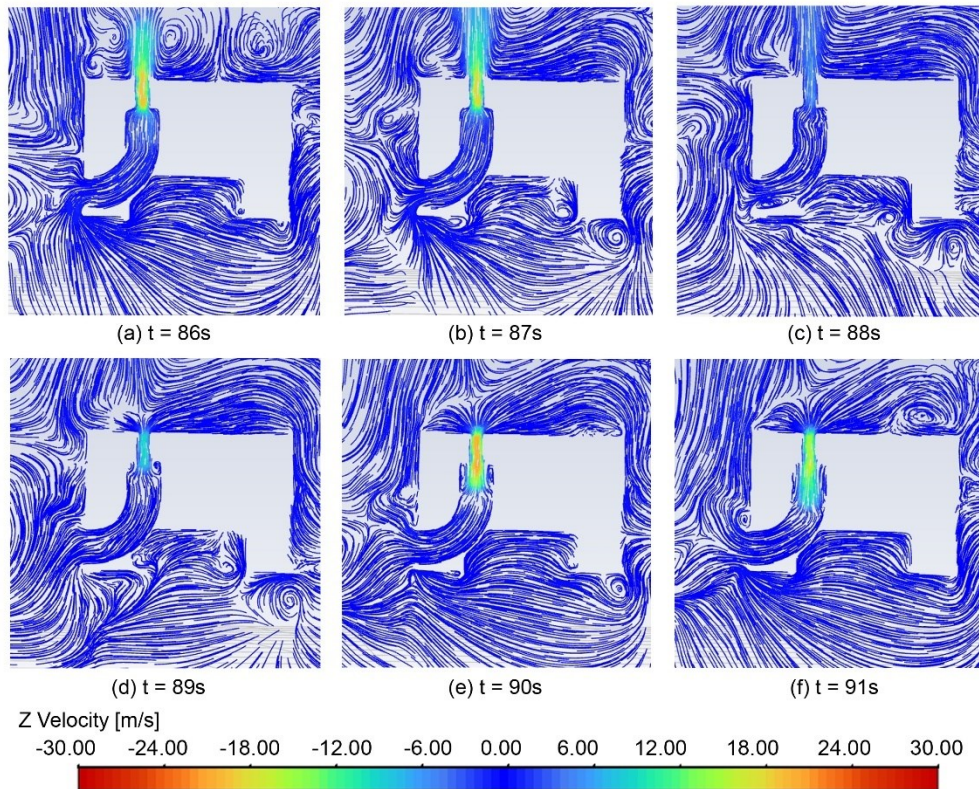


Fig. 9: Vertical velocity pathlines of the Π -type HFB for $kh = 2.51$ and $\theta = 0^\circ$ at different time instances (a) $t = 86s$, (b) $t = 87s$, (c) $t = 88s$, (d) $t = 89s$, (e) $t = 90s$, and (f) $t = 91s$.

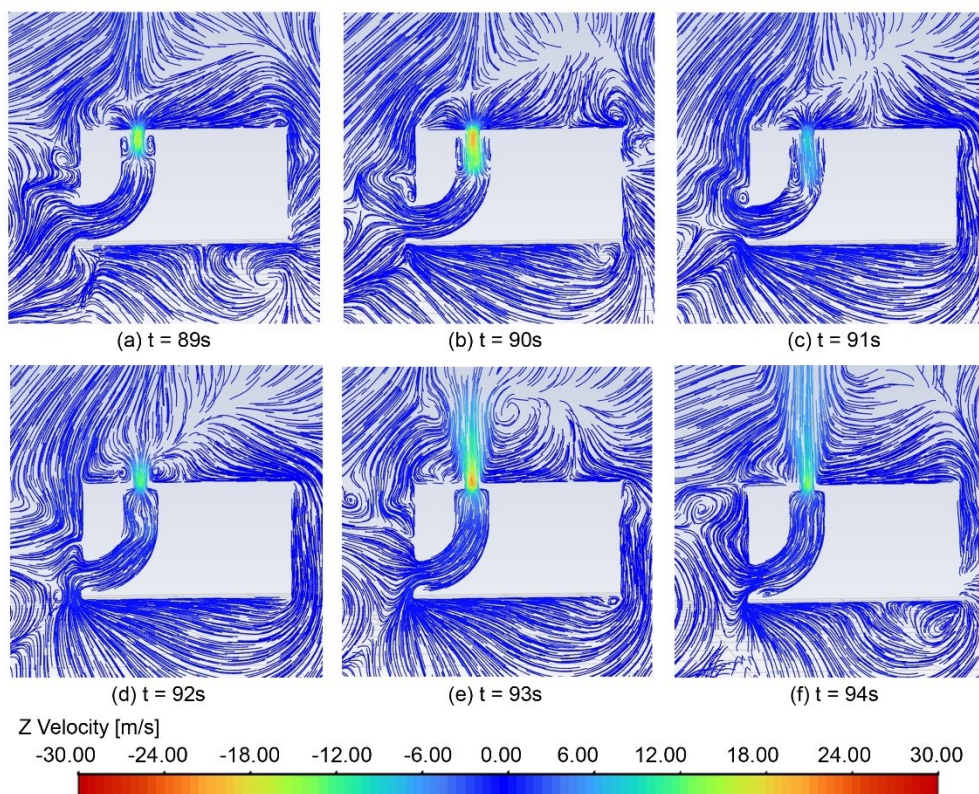


Fig. 10: Vertical velocity pathlines of the rectangle-type HFB for $kh = 2.51$ and $\theta = 0^\circ$ at different time instances (a) $t = 89s$, (b) $t = 90s$, (c) $t = 91s$, (d) $t = 92s$, (e) $t = 93s$, and (f) $t = 94s$.

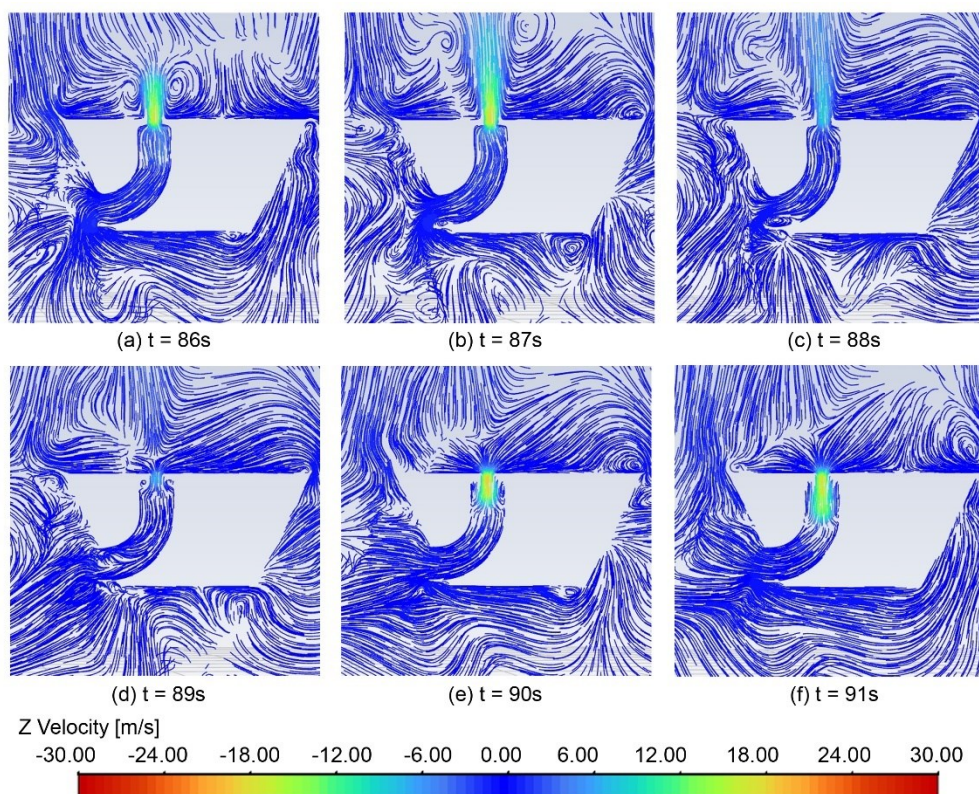


Fig. 11: Vertical velocity pathlines of the trapezoidal-type HFB for $kh = 2.51$ and $\theta = 0^\circ$ at different time instances (a) $t = 86s$, (b) $t = 87s$, (c) $t = 88s$, (d) $t = 89s$, (e) $t = 90s$, and (f) $t = 91s$.

Similarly for other HFBs maximum upstream and downstream flow velocity can be observed and it can be noted that the flow velocity in box type is highest among all HFBs for the same incoming wave and it can be identified by the red colour in pathlines (Fig.7b and 7e). This variation is the primary reason for the high power capture efficiency in box-HFB at $kh = 2.51$. The water inside chamber provides the momentum to air during the up stroke as the water level rises and it builds pressure inside the chamber leading to migration of air toward vertical direction with a larger magnitude of velocity and it exits through the outlet orifice. The high velocity of flow in downstream is due to fall in pressure inside chamber causing air to rush into the chamber. This strong oscillations in air flow can be further utilized by a Wells turbine (which rotates in a single direction regardless of the direction air is flowing through it) to generate electricity. Another worth noting point is the flow pattern around different shape of HFBs, which can be seen to vary for each shape of HFB (Fig.7, 8, 9, 10, 11) and could be the reason for the significant differences in the power capture performance of different HFB models with same OWC dimensions.

In view of the results discussed in this section for different shapes of HFBs for their hydrodynamic characteristics and preferring the wider bandwidth of power conversion along

with less wave transmission, the trapezoidal shape HFB can be considered to be performing better. Due to non-random nature of the transmission coefficient plot and efficiency plot for the trapezoidal-type HFB, it can be said that it is better suited for the optimisation. The RAO responses and transmission coefficient of this HFB can be improved by parametric variation which is discussed in next section.

7.5 Parametric Study

The aim of the parametric study is to assess the motion response and wave transmission characteristics of the selected HFB model from the study of different shape. The hydrodynamic characteristics of the selected HFB (i.e., trapezoidal-type HFB) is analysed for different drafts, widths, lengths relative to water depth (d/h , b/h , L/h respectively), and angle of wave incidence (θ) and the effect of variation of one parameter is obtained by keeping all other parameters constant. The hydrodynamic performance characteristics such as RAOs (RAO_j) and transmission coefficient (C_T) is investigated in this section for freely floating body with six-degrees of freedom. The cross-sectional dimensional representation of the trapezoidal-type HFB is given in Fig. 12.

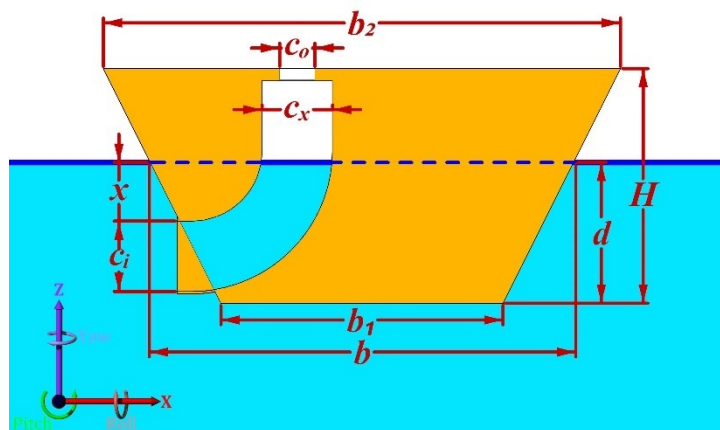


Fig. 12: Cross-sectional representation of trapezoidal HFB model dimensions with side slope of 1H:2V.

7.5.1 Length Variation

The first parametric study is performed for the variation of L/h and RAOs and wave transmission coefficients are determined for each L/h value and it is compared. The wave condition is taken as regular wave incoming at $\theta = 0^\circ$ and other parameters are kept same for each L/h variation. For $b/h = 0.6$, $d/h = 0.2$, $c_x/h = 0.1$, $x/h = 0.083$ motion responses

in surge (RAO_1), heave (RAO_3), and pitch (RAO_5) are determined and presented in Fig. 13 and wave transmission coefficient (C_T) in Fig. 14. A Clear observation form Fig. 13(a) may be drawn as, no significant changes in surge RAO over the considered range of $0.1 \leq kh \leq 8.0$ except at $kh = 1.47$.

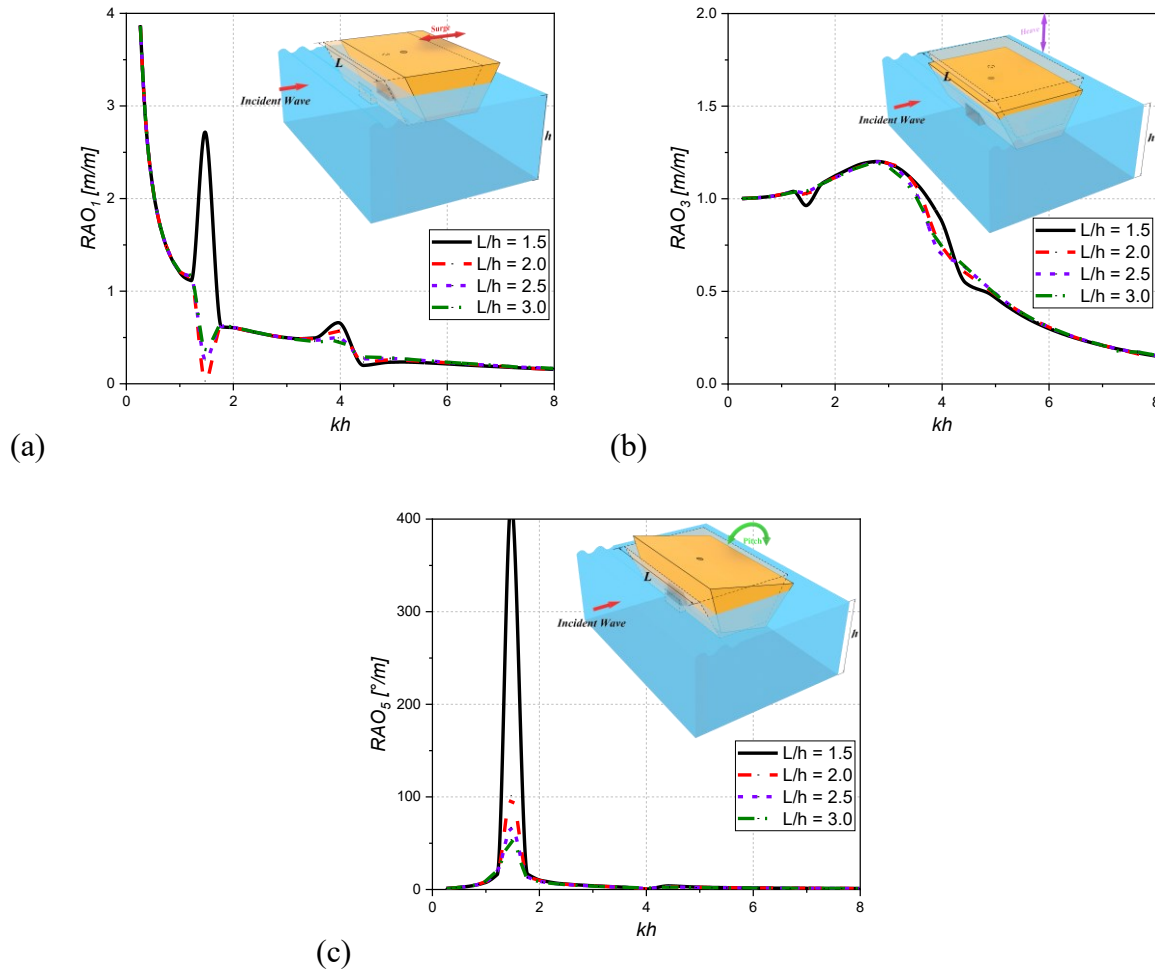


Fig. 13: Variation of RAOs (a) RAO_1 , (b) RAO_3 , and (c) RAO_5 , of trapezoidal-type HFB for different L/h versus kh , having $b/h = 0.6$, $d/h = 0.2$, $c_x/h = 0.1$, $x/h = 0.083$, and $\theta = 0^\circ$.

For $kh = 1.47$, when L/h increases within $1.5 < L/h < 2.0$, RAO_1 drops by about 98% and when $L/h > 2.0$ each increase shows rise in RAO_1 firstly by a large value of about 7 times and then a small rise of about 44% from its previous value respectively for $L/h = 2.5$ and $L/h > 3.0$. The main reason for this variation on a particular $kh = 1.47$ is occurrence of pitching resonant motion, which is clearly visible Fig. 13(c). The peak amplitude of RAO_5 can be observed to be dropping as L/h increases within $1.5 < L/h < 3.0$ by about 76%, 34%, and 19% sequentially (Fig.13c). Which can be due to the large length helping in reducing the

pitching motion of the floating body which is advantageous in stabilizing the motions of the structure. Apart from the earlier said changes the change in L/h results almost no change in heave RAOs (Fig.13b).

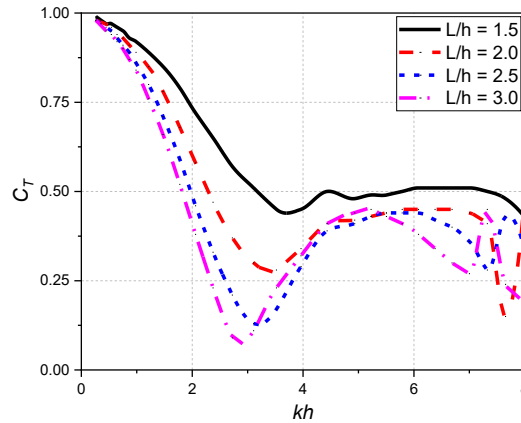


Fig. 14: Variation of C_T of trapezoidal-type HFB for different L/h verses kh , having $b/h = 0.6$, $d/h = 0.2$, $c_x/h = 0.1$, $x/h = 0.083$, and $\theta = 0^\circ$.

The variation in C_T with increase in L/h shows that there is decrease in value of C_T especially within $2.0 \leq kh \leq 4.0$ and this indicates improvement in transmission characteristics of trapezoidal-type HFB (Fig.14). In intermediate water region ($kh < 3.14$), the drop in C_T with rise in L/h is about 2% to 41% within $1.5 < L/h < 2.0$, about 2% to 57% within $2.0 < L/h < 2.5$, and about 2% to 58% within $2.5 < L/h < 3.0$. In deep water region ($kh > 3.14$), C_T decreases by about 10 to 70% for changes within $1.5 < L/h < 2.0$, about 10 to 70% for changes within $2.0 < L/h < 2.5$ and after that rise in L/h results in variation C_T by about $\pm 5\%$ to $\pm 40\%$. The reason for the variation in C_T with increment in length of HFB can be the changes in diffracting surface area, as more wetted surface area will be present for interaction with the waves it will create more reflection and attenuation of wave resulting in increased water-shaded area behind the HFB. For an upper threshold value of 0.45, trapezoidal HFB with $L/h = 2.5$ and $L/h = 3.0$ both shows good performance. Therefore, considering the above results (Fig.13 and 14) and to save computation time the $L/h = 2.5$ is considered for subsequent parametric study of having b/h , and d/h variations.

7.5.2 Width Variation

The variation in width of trapezoidal-type HFB is investigated by changing b/h and determining RAO_j and C_T for regular waves incoming at $\theta = 0^\circ$. For this study, the constant

values of different parameters are taken as $L/h = 2.5$, $d/h = 0.2$, $c_x/h = 0.1$. The results for different b/h are presented for motion response in Fig. 15 and for wave transmission in Fig. 16.

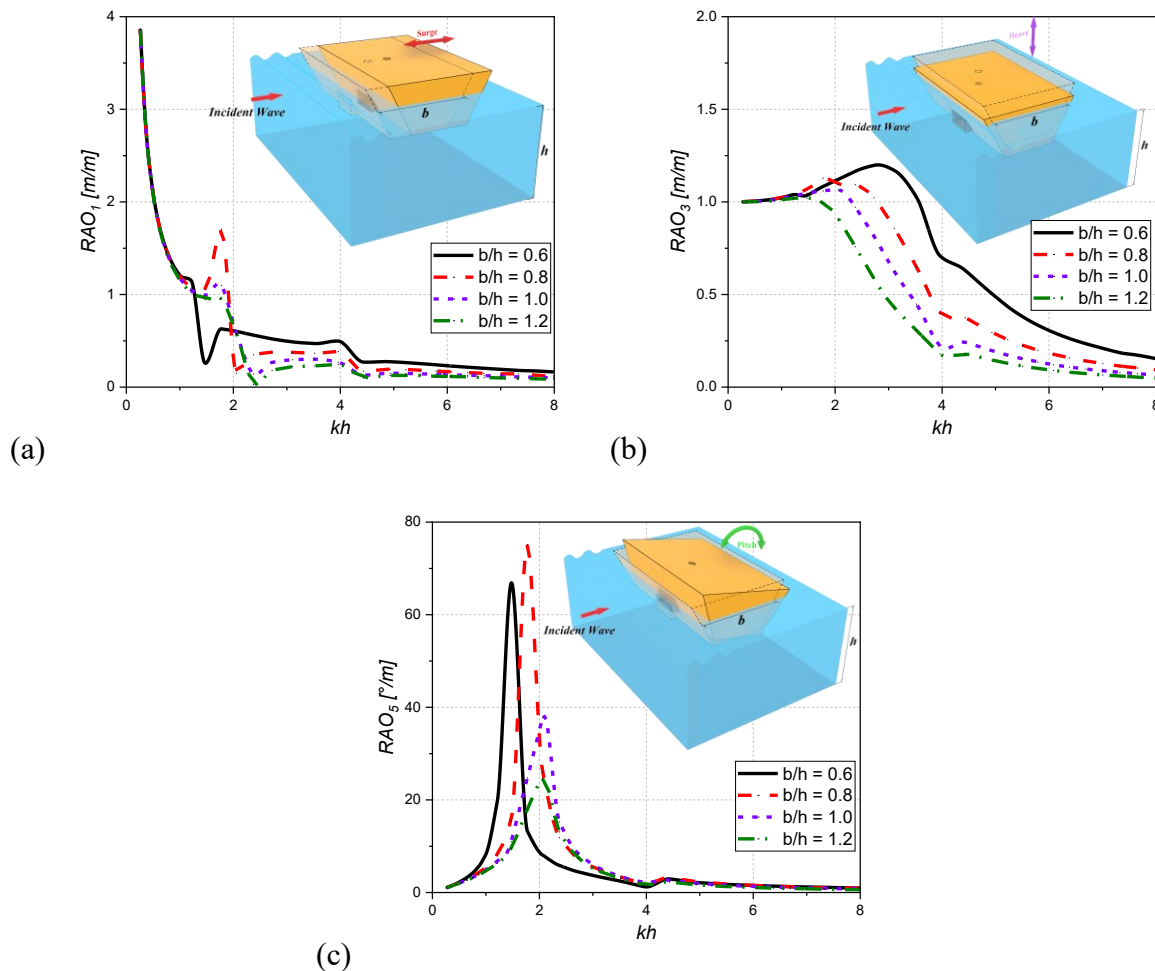


Fig. 15: Variation of RAOs (a) RAO_1 , (b) RAO_3 , and (c) RAO_5 , of trapezoidal-type HFB for different b/h verses kh , having $L/h = 2.5$, $d/h = 0.2$, $c_x/h = 0.1$, $x/h = 0.083$, and $\theta = 0^\circ$.

For $kh \leq 1.21$, there is no significant changes in RAO_1 is observable due to incidence of waves having long wavelength ($\lambda > 4b$ for the largest width of HFB considered in the study). With increase in b/h , for the part of intermediate water region and full deep water region ($2.73 \leq kh \leq 8.0$), the RAO_1 decreases by about 20% to 38% for increment within $0.6 < b/h < 0.8$, about 16% to 30% for increment within $0.8 < b/h < 1.0$, and about 9% to 25% for increment within $1.0 < b/h < 1.2$ (Fig.15a). Maximum decrement of about 38%, 60%, and 79% is observed in RAO_1 for each increment of b/h respectively at $kh = 2.38$. The above observations indicates that for $kh > 2.0$, the HFB with largest width ($b/h = 1.2$) experiences least surge motion among all considered width of HFB. The reason for this observation can be

the increase weight of the HFB due to increase in width resulting in rise in metacentric height leading to stability of the floating body and it may resist the forces causing translational motions in surge and heave directions. Fig. 15(b) shows that the rise in b/h results in less heaving motion and the reason for which is discussed earlier. The value of RAO_3 is noticed to decrease by about 36% to 45% for each increment in b/h within $0.6 \leq b/h \leq 1.0$ and about 25% to 30% for increment in width within $1.0 \leq b/h \leq 1.2$ for $kh > 2.0$. This indicates that the HFB model with $b/h = 1.2$ is very slight heaving motion for the waves in deep waters and for some part of intermediate waters. The motion response in pitching motion (Fig.15c) shows that with expansion of width of HFB the peak amplitude of pitch RAO reduces and reach to about $RAO_5 = 25^\circ/m$ for $b/h = 1.2$ at $kh = 2.06$ and this accounts to about 30% to 50% reduction for increase in b/h within $0.8 \leq b/h \leq 1.2$. Apart from variations in peak amplitude region of RAO_5 , each increment of width of HFB with in $0.8 \leq b/h \leq 1.2$ shows reduction of about 5% to 25% in deep waters and parts of intermediate waters. The reduction in pitch motion as the width of the trapezoidal HFB increases may be the result of higher attenuation of the waves at the structure as a result of a large wetted surface.

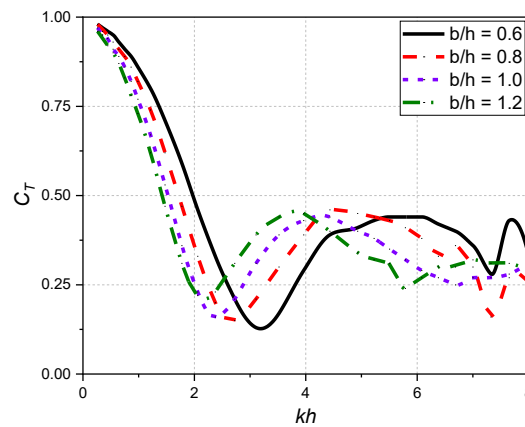


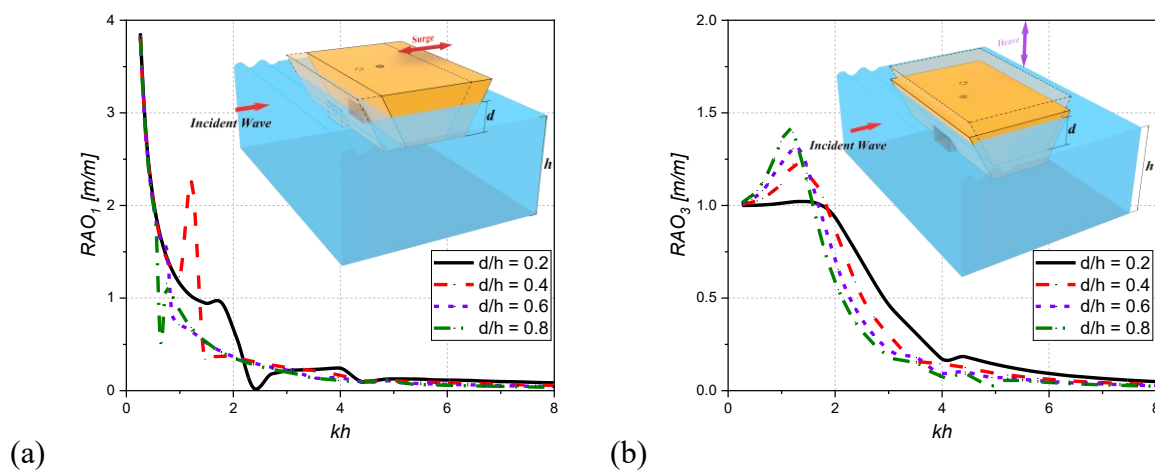
Fig. 16: Variation of C_T of trapezoidal-type HFB for different b/h verses kh , having $L/h = 2.5$, $d/h = 0.2$, $c_x/h = 0.1$, $x/h = 0.083$, and $\theta = 0^\circ$.

The change in width of trapezoidal HFB is perceived to be affecting wave transmission in a particular manner, resulting in shifting of lowest wave transmission value towards lower kh value for each increment in b/h . For each variation of b/h , the trend of C_T variation is almost same, only the values of C_T with respect to kh changes in the range of about $\pm 47\%$ (Fig.16). The shift in the drop point in the C_T value, in range of $2.06 \leq kh \leq 3.11$, is due to the shifting of peak value of heave motion for the corresponding kh and similar phenomenon was observed

for Π -shape floating breakwater studied by Gesraha (2006). Apart from shift in the response, the C_T is observed to be in range of $0.13 \leq C_T < 0.46$ for $kh > 2.0$ within variation of $0.6 \leq b/h \leq 1.2$. For $2.38 \leq kh \leq 5.23$, the every single rise in b/h (within $0.6 \leq b/h \leq 1.2$) results in variation in C_T of about -40% to +65%. Further, it can be deduced that, with the b/h alterations, effects on waves transmission varies with respect to wave frequency and considering the upper threshold of $C_T = 0.46$, the wave transmission performance for all b/h variations is good.

7.5.3 Draft Variation

To assess the effects due to change in draft of the floating structure (in terms of relative draft, d/h), the b/h and L/h is taken based on the results of the earlier sections corresponding to the best performance in terms of its stability and wave attenuation (i.e., $b/h = 1.2$ and $L/h = 2.5$). The rest of the dimensional parameters are kept same ($c_x/h = 0.1$, $x/h = 0.083$, and $\theta = 0^\circ$) and there is no change in position and dimension of integrated OWC. The variation in surge RAO (RAO_1) is shown in Fig. 17(a) and it indicates that there is decrease of about 12% to 32% with each increase in relative draft within $0.2 \leq d/h \leq 0.8$ for deep water region ($kh > 3.14$). There are some irregularities in the value of RAO_1 for $0.64 < kh < 2.06$, that may be caused by the occurrence of resonance in pitching motion at the same frequencies. Overall, for $kh > 2.73$, the value of RAO_1 lies below 0.23 for all d/h , which is shows that body is almost stable in surge motion for short waves.



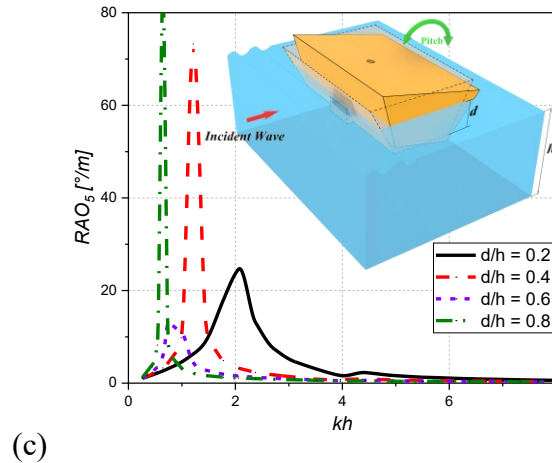


Fig. 17: Variation of RAOs (a) RAO_1 , (b) RAO_3 , and (c) RAO_5 , of trapezoidal-type HFB for different d/h verses kh , having $L/h = 2.5$, $b/h = 1.2$, $c_x/h = 0.1$, $x/h = 0.083$, and $\theta = 0^\circ$.

From Fig. 17(b), it is worth noting that as d/h increases, it results in increase in heave RAO (RAO_3) value for $kh < 1.47$ and this rise is not that much large as it lies in range of about 1% to 15% for each increment of d/h within $0.2 \leq d/h \leq 0.8$. This characteristic is caused by a floating body's undamped natural frequency shifting due to increase in relative draft towards the long wave zone, which may cause the HFB in this region to heave and pitch more. For $kh > 1.78$, RAO_3 decreases by about 35%, 20% and 15% for increase of d/h within $0.2 \leq d/h \leq 0.4$, $0.4 < d/h \leq 0.6$, and $0.6 < d/h \leq 0.8$ respectively. This clearly indicates that rise in draft helps in reduction of heave motion for part of intermediate waters and deep water regions. The reason for this change is increase in mass and inertia of the floating body by increment of its draft leading to more dissipation of wave energy in short wave region. A distinct observation from Fig. 17(c) is shifting of the pitch resonance frequency as d/h increases. This can be due to the increase in weight of the floating structure, which causes its natural frequency to decrease, leading to shift of resonance frequency toward high period waves. Aside from the region of maximum pitching motion, each increment in d/h within $0.2 \leq d/h \leq 0.8$ causes decrease in RAO_5 by about 55%, 35% and 19% respectively. Therefore, based on the above observations it can be stated that increasing the draft of the HFB helps the structure to get more stability in terms of motion and the stability for $kh > 1.47$ is attained when $d/h \geq 0.4$. Which is beneficial because the power capture performance is good for $1.77 < kh < 3.61$ as found earlier for stationary trapezoidal-type HFB and in that region for $d/h \geq 0.4$ the motion responses are very less and structure seems to be stable.

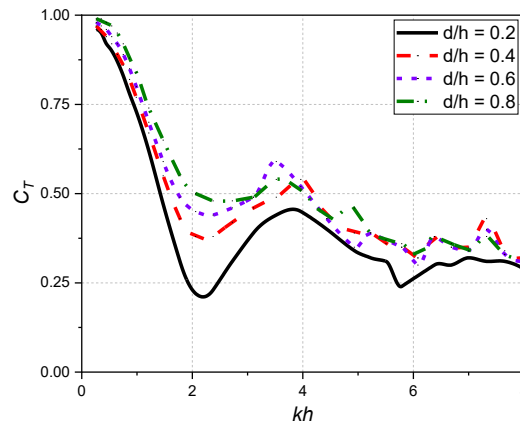


Fig. 18: Variation of C_T , of trapezoidal-type HFB for different d/h verses kh , having $L/h = 2.5$, $b/h = 1.2$, $c_x/h = 0.1$, $x/h = 0.083$, and $\theta = 0^\circ$.

The results for wave transmission shows that the increment of d/h leads to increase in value of C_T for considered range of kh (Fig.18). The increment in C_T is up to about 8% for each increment of d/h within $0.2 \leq d/h \leq 0.8$ for $kh \leq 1.21$, and for $1.21 < kh \leq 3.14$ maximum increase in C_T is noted to be about 73%, 19% and 13% for relative draft rise within $0.2 \leq d/h \leq 0.4$, $0.4 < d/h \leq 0.6$, and $0.6 < d/h \leq 0.8$ respectively. The reason for this behaviour can be the change in bottom width of the trapezoidal cross-section of the structure as draft increases. Due to fixity of the side slope of trapezoidal geometry, it results in decrease in bottom width of the structure causing waves to easily pass through and leading to more wave transmission in intermediate water range as wavelength is relatively long. In deep water region ($kh > 3.14$) when d/h increases within $0.2 \leq d/h \leq 0.4$, fluctuating increase in the range of about 10% to 45% is observed and for $d/h > 0.4$, the increment of relative draft causes very small change and C_T seems to be lying in approximately same range for all ($0.3 \leq C_T \leq 0.5$). The reason for this can be the less interaction of short waves with the bottom portion of the structure in larger draft, as the short waves are more concentrated within free water surface region, therefore, the performance of the wave transmission is not significantly impacted by the change in draft for $kh > 3.96$.

7.5.4 Wave Incidence Angle Variation

The performance of trapezoidal-type HFB, considering its motion response, wave transmission with upper threshold value of 0.5, and good power capture bandwidth for $kh > 1.47$ is found to be good for model with $L/h = 2.5$, $b/h = 1.2$, and $d/h = 0.4$ as discussed in previous

sections. Hence the motion response and wave transmission are analysed for this model for change in θ within $0^\circ \leq \theta \leq 45^\circ$ and presented in this section (Fig.19 and 20).

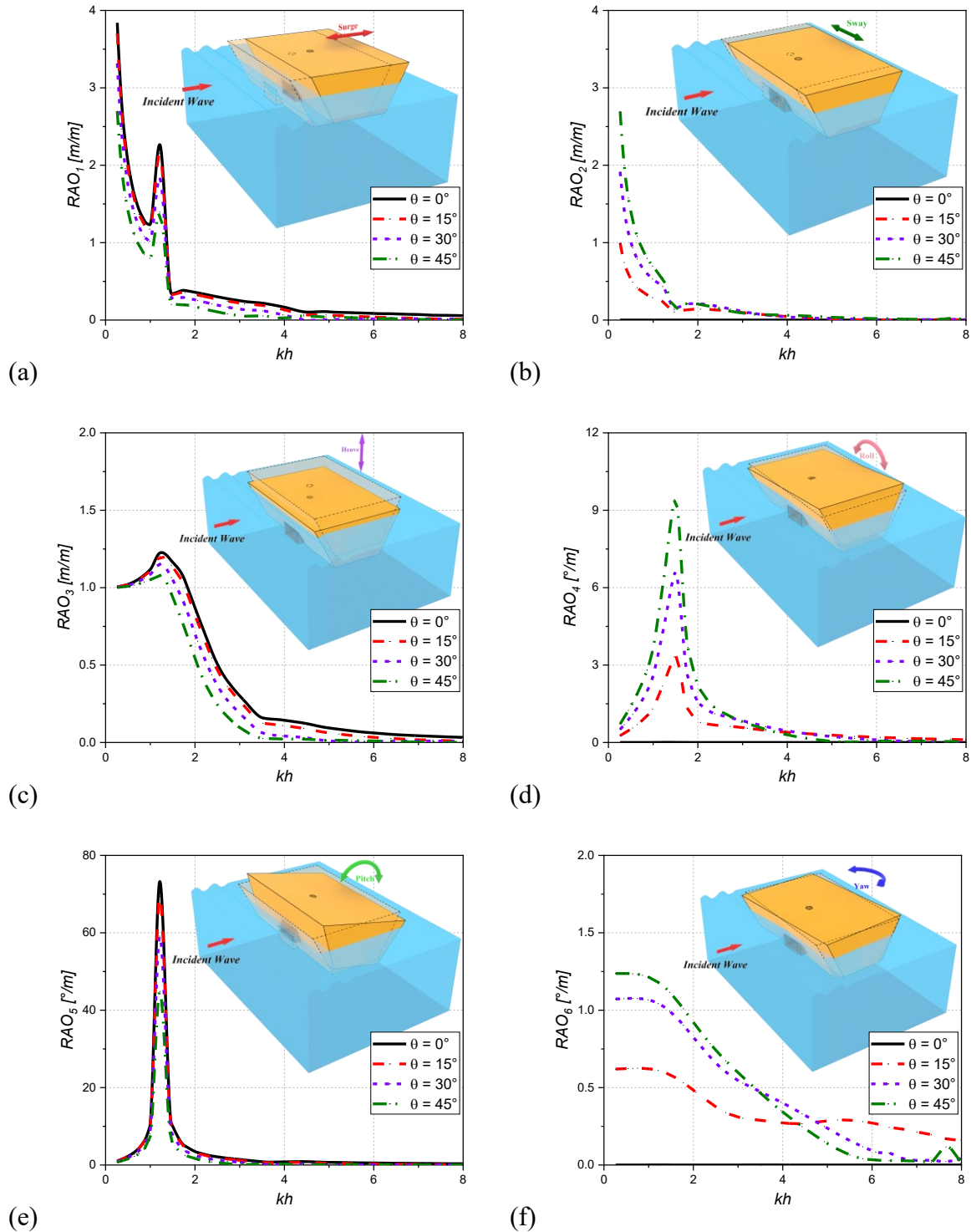


Fig. 19: Variation of RAOs (a) RAO_1 , (b) RAO_2 , (c) RAO_3 , (d) RAO_4 , (e) RAO_5 , and (f) RAO_6 , of trapezoidal-type HFB for different θ versus kh , with $L/h=2.5$, $b/h=1.2$, $d/h=0.4$, $c_x/h=0.1$, and $x/h=0.083$.

Fig. 19 shows that the sway (RAO_2), roll (RAO_4), and yaw (RAO_6) motions are none for $\theta = 0^\circ$ and with the increase in θ , these motions are observed to be rising. In shallow and intermediate water region ($kh \leq 3.14$), the RAO_1 is observed to be dropping by about 3% to 13%, 10% to 36%, and 18% to 62% respectively for each 15° increment in θ within $0^\circ \leq \theta \leq 45^\circ$ and in deep waters ($kh > 3.14$), the drop in RAO_1 is about 13% to 95% for the same change in θ (Fig.19a). Similar, trend is observed for the variation of RAO_3 , and RAO_5 with change in θ . The RAO_5 value at resonance frequency is observed to be dropping by about 5%, 15%, and 24% for increase of θ within $0^\circ \leq \theta \leq 15^\circ$, $15^\circ < \theta \leq 30^\circ$, and $30^\circ < \theta \leq 45^\circ$ respectively (Fig.19c). The reason for the observed drop can be because the change in θ results in a decrease in wave excitation in surge, heave and pitch directions which are dominant for $\theta = 0^\circ$, and it leads to reduction in the impacting forces that are responsible for the motions mentioned earlier. The reduction in impacting forces is because of the cosine component of fluid particle velocity which decreases with increase in θ , resulting in decrease in velocity. The motions which were insignificant for normal wave incidence ($\theta = 0^\circ$) starts showing significance when θ increases (Fig.19b, 19d, 19f). The variation in RAO_2 is observed to be in the form of increase of about 30% to 90% for $kh \leq 3.14$ with each rise in θ within $15^\circ < \theta \leq 45^\circ$ and for rise between $0^\circ < \theta \leq 15^\circ$ huge difference can be observed over each value of considered kh . When θ increases within $15^\circ < \theta \leq 30^\circ$, the RAO_4 increases by about 20% to 98% for some part deep waters and complete intermediate and shallow water region ($kh \leq 3.96$) and for the incidence angle rise in the said range for $kh > 3.96$, the RAO_4 value decreases in the range of about 17% to 98% (Fig.19d). The RAO_4 , for $kh \leq 2.06$, rises by about 42% when θ rises within $30^\circ < \theta \leq 45^\circ$. Similar behaviour can be observed for RAO_6 with the changes in θ (Fig.19f). The reason for the rise in these motions is due to increase of velocity component with increase in θ , because the relation of θ with velocity component in sway, roll, and pitch directions is sine instead of cosine as mentioned earlier.

With the variation of θ , the transmission of wave through trapezoidal-HFB of selected parameter can be perceived to be positively influenced by first increment of θ by 15° . A point is considered at a fixed distance to assess the impact of change in θ on wave transmission. It is worth noting that for increase in θ within $0^\circ < \theta \leq 15^\circ$ results in reduction in C_T at the considered point in the water-shade area on lee-side of the structure. The said reduction is in the range of 20% to 63% for $kh \geq 1.78$ (Fig.20). This reduction may occur due to change in

wave diffraction angle as θ changes resulting in more wave attenuation due to increased wave interaction with structure and due to this the considered point can get more shaded from influence of waves.

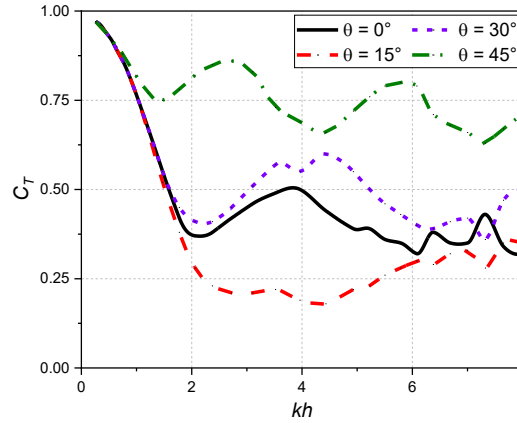


Fig. 20: Variation of C_T , of trapezoidal-type HFB for different θ verses kh , having $L/h = 2.5$, $b/h = 1.2$, $d/h = 0.4$, $c_x/h = 0.1$, and $x/h = 0.083$.

From Fig. 20 it can be observed that for $kh \geq 1.21$ there is rise in C_T when $\theta > 15^\circ$ and this rise is approximately equal to 5% to 230%, and 7% to 110% for increment of θ within $15^\circ < \theta \leq 30^\circ$, and $30^\circ < \theta \leq 45^\circ$ respectively. Beyond a certain point, an increase in wave incidence angle may expose the lee-side to waves, and it may lead to a reduction in the number of diffracting panels on the structure's wetted surface area that is directly influenced by waves, resulting in an increase in wave transmission. Additionally, it is worth noting that for $kh > 1.21$ the wave transmission is found to be least for $\theta = 15^\circ$ among analysed variation in θ .

7.6 Conclusions

The present study analyses different cross-sectional shapes of hybrid floating breakwaters integrated with a single J-type OWC device and the OWC dimensions in all HFBs are kept same so that good comparison can be obtained. The hydrodynamic performance of HFB models is performed for the regular waves following linear wave theory for the wave frequency range of surface gravity waves. The characteristics for assessment of hydrodynamics of HFBs are considered to be its motion responses, wave transmission and power conversion capability through its wave energy conversion device. Further, parametric study is performed to optimise the motion response and water shading properties by changing different geometric dimensions. Considering the findings of this study, the following conclusions can be drawn:

- The motion response analysis of different type of HFB reveals among all HFB models the H-type is observed to be more unstable with respect to surge, heave, and pitch response. The instability of HFBs, considering pitching motion, is in the range $1.77 < kh < 2.73$ which is in intermediate water region and as floating breakwaters are apparently installed in intermediate region therefore, the HFB's natural frequency should not fall in this region and this can be achieved by optimising the geometry of HFB, which will help in eliminating the occurrence of natural frequency in the desired region of operation and maintain the structural integrity.
- By comparing all other types of HFBs with the rectangular-type HFB, it is worth noting that all of them shows less wave transmission than rectangular-HFB and over the range of frequencies the pi-type HFB performs better followed by trapezoidal-type HFB. Henceforth, it is discernible that changing the shape of the HFB significantly affects its wave transmission behaviour.
- The maximum power capture is noticed to be within range of $1.77 < kh < 3.61$ considering a threshold value of $\varepsilon = 0.25$ and stationary floating HFBs. The values are: $\varepsilon = 1.56$ for H-type HFB, $\varepsilon = 1.17$ for Π -type HFB, $\varepsilon = 0.90$ for rectangular-type HFB, $\varepsilon = 0.90$ for trapezoidal-type HFB and this indicates performance of HFBs in intermediate water region to be good for the considered parameters.
- Giving precedence to broad bandwidth of power capture with good performance related to wave transmission, the comparison of the different HFB models exhibits that trapezoidal-type HFB is best among considered HFB models as it shows 75% to 90% wave power capture within $1.77 < kh < 3.61$ and it is considered for parametric study to improve its stability and wave transmission by geometric modifications.
- The parametric study reveals that increasing the length and width of the trapezoidal-type HFB improve the hydrodynamic performance by reducing motion responses and wave transmission. Increasing the draft of HFB turned out to be better in shifting the natural frequency of HFB but due to trapezoidal geometry, the wave transmission seems to be increase with increase in draft due to reduction of bottom width of trapezoidal-HFB as side face slope of trapezoidal geometry in this study is assumed to be fixed.
- It is worth noting that for $kh > 1.21$ the trapezoidal-HFB with having $L/h = 2.5$, $b/h = 1.2$, $d/h = 0.4$, $c_x/h = 0.1$, and $x/h = 0.083$ is found to be most stable and with least wave transmission of the regular wave incoming with $\theta = 15^\circ$.

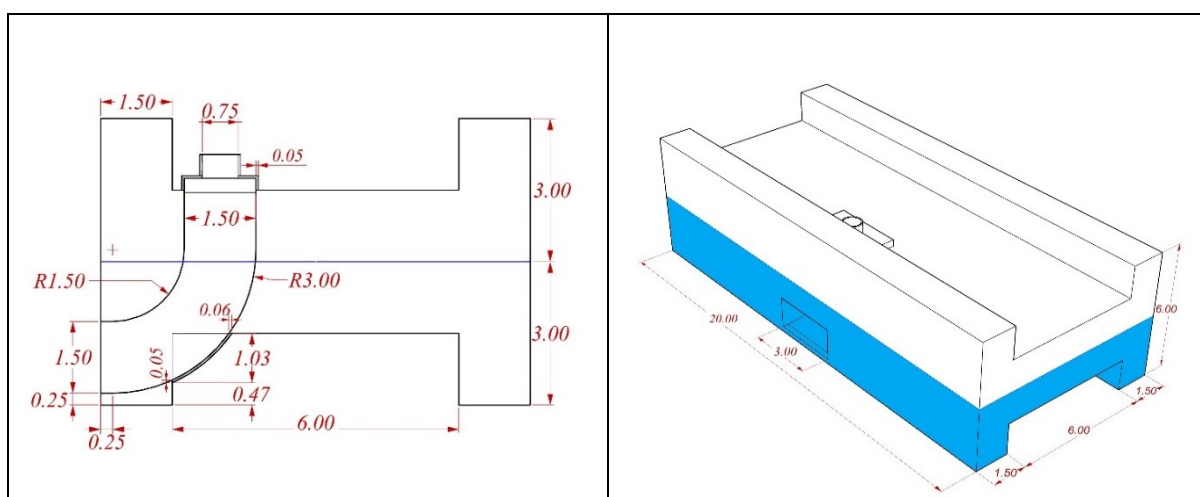
The present study follows linear wave theory and examines interaction of floating structure in case of regular waves; therefore, it is necessary to analyse the hybrid model for various wave theories as well as the case of irregular waves in order to further scrutinize its applicability. The power capture in this study is determined for a hypothetical hybrid floating breakwater, where it is expected that the structure would remain in place when waves interacted with it. This condition is used to get the maximum possible power capture from the hybrid models. Therefore, in future more study can be performed on the power capture from HFB for restricted three-degrees of freedom and full six-degrees of freedom. Further, the trapezoidal-HFBs can be examined to assess its performance of power capture in the case of multiple OWCs with different spacing between them.

CHAPTER 8

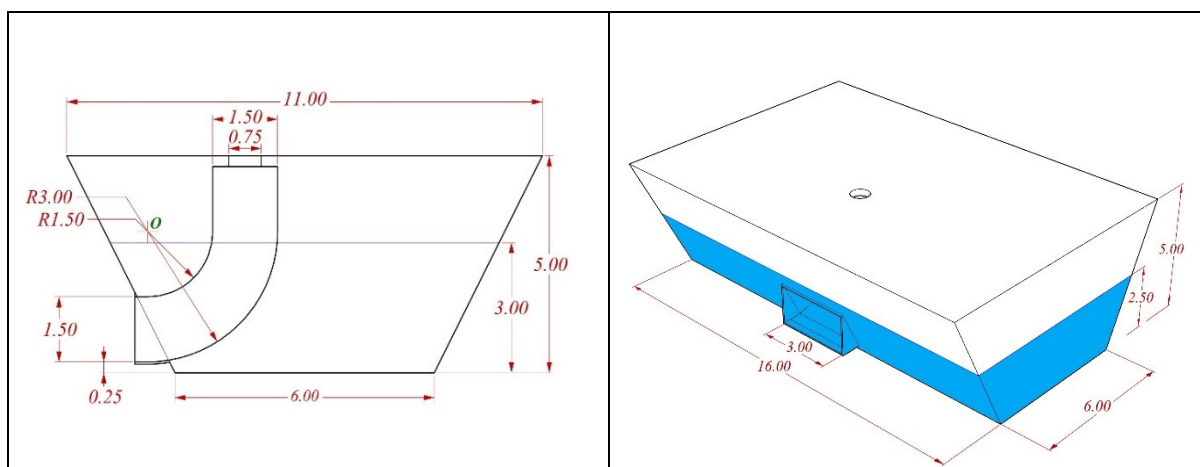
MOORING ANALYSIS OF HYBRID FLOATING BREAKWATER

8.1 HYBRID FLOATING BREAKWATER MODEL

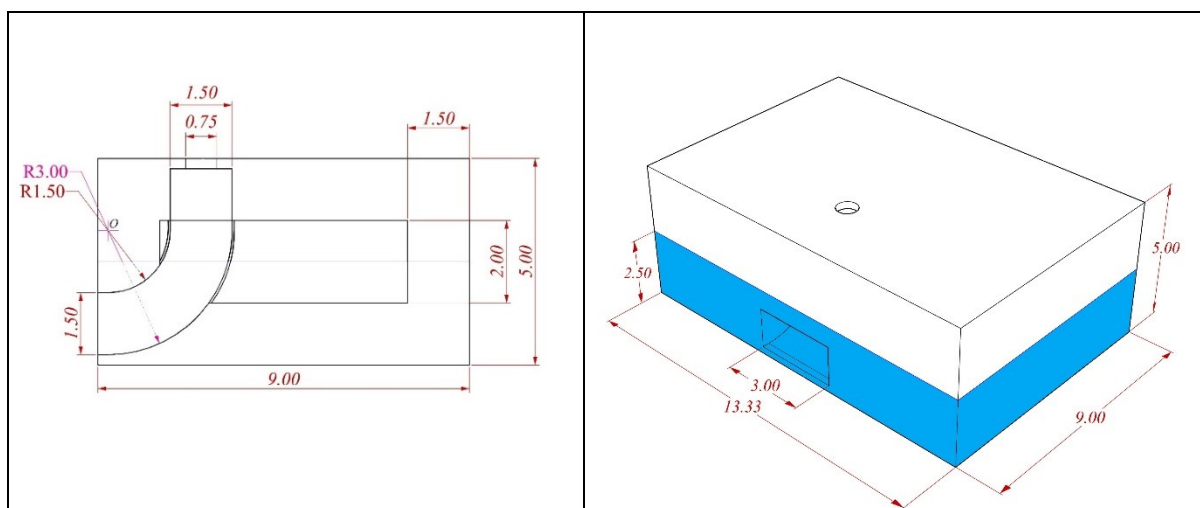
5 different shapes of Floating Breakwater (FLBW) integrated with oscillating water column (OWC) is studied, which are represented in figures below with dimensions. The study is done by keeping water depth same ($h = 30\text{m}$) for analysis of all models. For comparison of different shapes of FLBW model, their dimensions are decided by keeping draft to width ratio ($d/B = 3$) and weight (369000kg) both same for all models. Then OWC is integrated in each model which is shown in Fig. 16. The OWC dimensions are given in Fig. 17 separately.



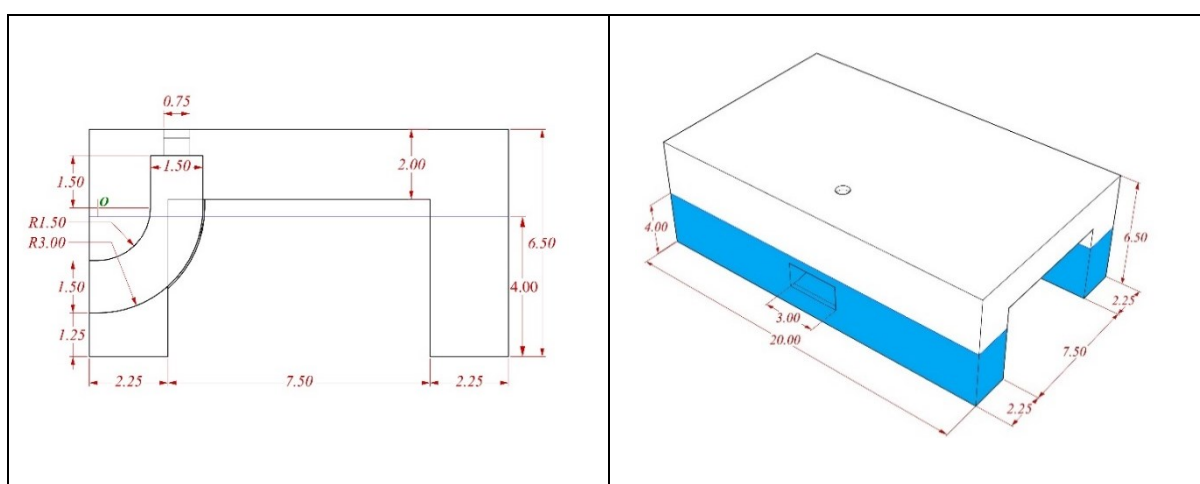
(a) H-shape FLBW integrated with OWC



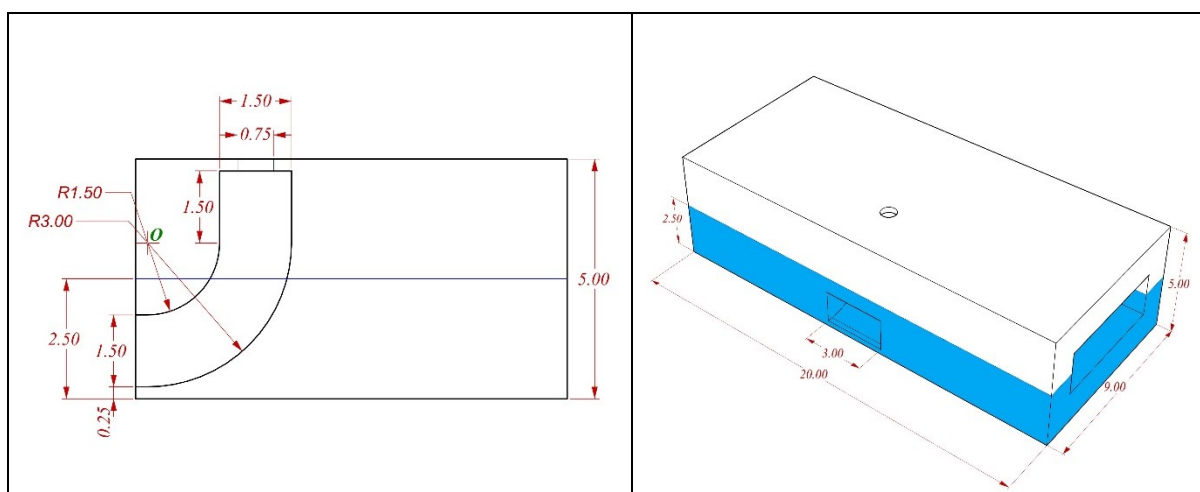
(b) Trapezoidal FLBW integrated with OWC



(c) Box -shape FLBW integrated with OWC



(d) π -shape FLBW integrated with OWC



(e) Rectangular FLBW integrated with OWC

Fig. 16: Cross section and 3D view of hybrid floating breakwater models.

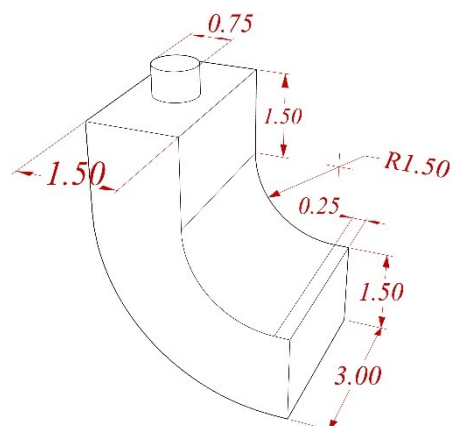


Fig. 17: Dimension of OWC considered

OWC model is simple J shape which is having opening of 1.5m x 3.0m at inlet section and the air chamber is having same cross section. The outlet where turbine will be installed is modelled as opening of 0.75m in diameter. The top position of inlet of OWC is kept 1.25m below sea water level (SWL). The blue colour in figure 1 represents portion of body below SWL.

8.2 MOORING ANALYSIS

The hybrid floating breakwater with oscillating water column is moored to the sea bed for its stability. Different mooring configurations such as Open Mooring (OM) and Cross Mooring (CM) are analysed and their comparison is done by comparing the tensile force on the mooring cables. Mooring line details are given in Table 4 and their connection points coordinates for structure and anchor are given in Table 5. The mooring line opt for the study is slacked catenary mooring line connected at two different levels of structure as per mooring configuration. For open mooring, the mooring line is connected at sea water level and for cross mooring it is connected at the base of the floating structure. Mooring configuration is depicted in figures below for each configuration and for each shape of hybrid breakwater.

Table 4: Non-linear catenary section mooring line parameters

Mooring Line Details			
Parameters	Units	For Mooring at Water Level	For Cross Mooring
Line Diameter	m	0.0809	0.0809

Unstretched Length	m	45	49
Cross-Sectional Area	m ²	0.0051	0.0051
Line Stiffness	N/m	1.25E+06	1.25E+06

Table 5: Coordinates for mooring line connections [considering mooring at 45° angle in both x-y and x-z plane]

For Open Mooring	Units	Box + OWC	H + OWC	Rectangle + OWC
Fairlead 1 @WL	m	(-4.5, 9.5, 0)	(-4.5, 9.5, 0)	(-4.5, 12.83333, 0)
Fairlead 2 @WL	m	(-4.5, -9.5, 0)	(-4.5, -9.5, 0)	(-4.5, -12.83333, 0)
Fairlead 3 @WL	m	(4.5, -9.5, 0)	(4.5, -9.5, 0)	(4.5, -12.83333, 0)
Fairlead 4 @WL	m	(4.5,9.5,0)	(4.5,9.5,0)	(4.5,12.83333,0)
Anchor Point 1	m	(-25.7132, 30.7132, -30)	(-25.7132, 30.7132, -30)	(-25.7132, 34.04653, -30)
Anchor Point 2	m.0	(-25.7132, -30.7132, -30)	(-25.7132, -30.7132, -30)	(-25.7132, -34.04653, -30)
Anchor Point 3	m	(25.7132, -30.7132, -30)	(25.7132, -30.7132, -30)	(25.7132, -34.04653, -30)
Anchor Point 4	m	(25.7132, 30.7132, -30)	(25.7132, 30.7132, -30)	(25.7132, 34.04653, -30)
For Open Mooring	Units	Trapezoidal + OWC	Pi + OWC	
Fairlead 1 @WL	m	(-4.5,7.5,0)	(-6,9.5,0)	
Fairlead 2 @WL	m	(-4.5, -7.5,0)	(-6, -9.5,0)	
Fairlead 3 @WL	m	(4.5, -7.5,0)	(6, -9.5,0)	
Fairlead 4 @WL	m	(4.5,7.5,0)	(6,9.5,0)	
Anchor Point 1	m	(-25.7132,28.7132, -30)	(-27.2132,30.7132, -30)	
Anchor Point 2	m	(-25.7132, -28.7132, -30)	(-27.2132, -30.7132, -30)	
Anchor Point 3	m	(25.7132, -28.7132, -30)	(27.2132, -30.7132, -30)	
Anchor Point 4	m	(25.7132,28.7132, -30)	(27.2132,30.7132, -30)	

For Cross Mooring	Units	Box + OWC	H + OWC	Rectangle + OWC
--------------------------	--------------	------------------	----------------	------------------------

Fairlead 1 @BL	m	(-4, 9.5, -3)	(-4, 9.5, -3)	(-4, 12.83333, -3)
Fairlead 2 @BL	m	(-4, -9.5, -3)	(-4, -9.5, -3)	(-4, -12.83333, -3)
Fairlead 3 @BL	m	(4, -9.5, -3)	(4, -9.5, -3)	(4, -12.83333, -3)
Fairlead 4 @BL	m	(4, 9.5, -3)	(4, 9.5, -3)	(4, 12.83333, -3)
Anchor Point 1	m	(-25.7132, 30.7132, -30)	(-25.7132, 30.7132, -30)	(-25.7132, 34.04653, -30)
Anchor Point 2	m	(-25.7132, -30.7132, -30)	(-25.7132, -30.7132, -30)	(-25.7132, -34.04653, -30)
Anchor Point 3	m	(25.7132, -30.7132, -30)	(25.7132, -30.7132, -30)	(25.7132, -34.04653, -30)
Anchor Point 4	m	(25.7132, 30.7132, -30)	(25.7132, 30.7132, -30)	(25.7132, 34.04653, -30)
For Cross Mooring	Units	Trapezoidal + OWC		Pi + OWC
Fairlead 1 @BL	m	(-2.5, 7.5, -3)		(-5.5, 9.5, -4)
Fairlead 2 @BL	m	(-2.5, -7.5, -3)		(-5.5, -9.5, -4)
Fairlead 3 @BL	m	(2.5, -7.5, -3)		(5.5, -9.5, -4)
Fairlead 4 @BL	m	(2.5, 7.5, -3)		(5.5, 9.5, -4)
Anchor Point 1	m	(-25.7132, 28.7132, -30)		(-27.2132, 30.7132, -30)
Anchor Point 2	m	(-25.7132, -28.7132, -30)		(-27.2132, -30.7132, -30)
Anchor Point 3	m	(25.7132, -28.7132, -30)		(27.2132, -30.7132, -30)
Anchor Point 4	m	(25.7132, 28.7132, -30)		(27.2132, 30.7132, -30)

The time response analysis of the model with mooring lines is performed for monochromatic linear waves with wave heading angle of 0° and amplitude of 0.5m for wave period varying from 3s to 26s. The time step used for this analysis is kept at .001s for a total time response analysis time of 100s. By considering the dynamics of cable, time responses of different hybrid floating breakwater models are obtained and maximum mooring cable tension force (F_{ML-MAX}) is plotted for each mooring configuration with respect to dimensionless wavenumber, kh.

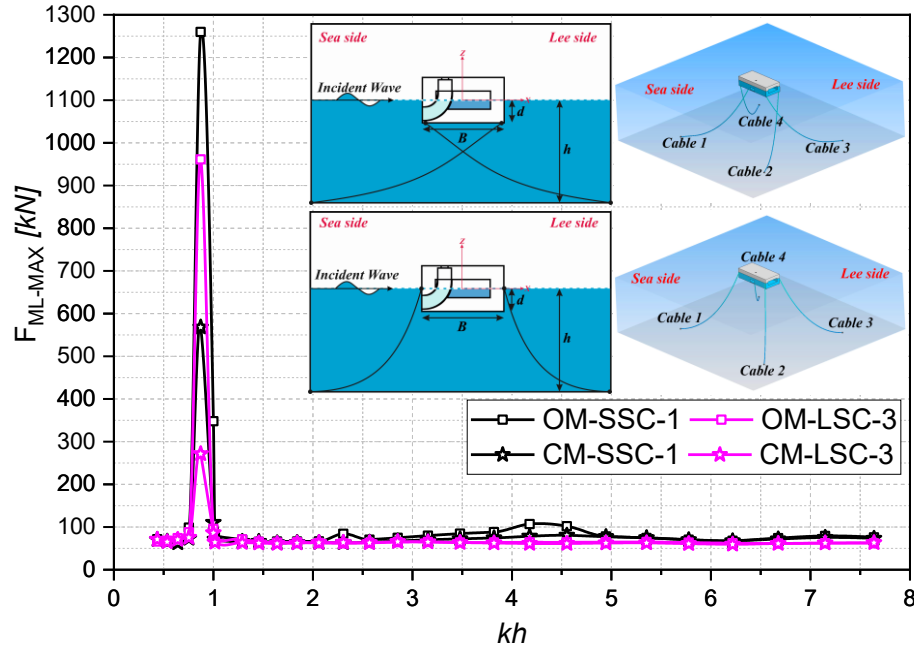


Figure 18: Mooring line force for Box-shape floating breakwater integrated with OWC

As it is visible from the graph shown in Figure 18 for box-shape hybrid floating BW that for kh value of 0.872 highest mooring tension force ($\sim 1260\text{kN}$) is found in sea side cable-1(SSC-1). Further it can be seen that for other wave numbers (from 1 to 7.6) the cable tension is almost in same range of 50-100kN on both side in both configurations.

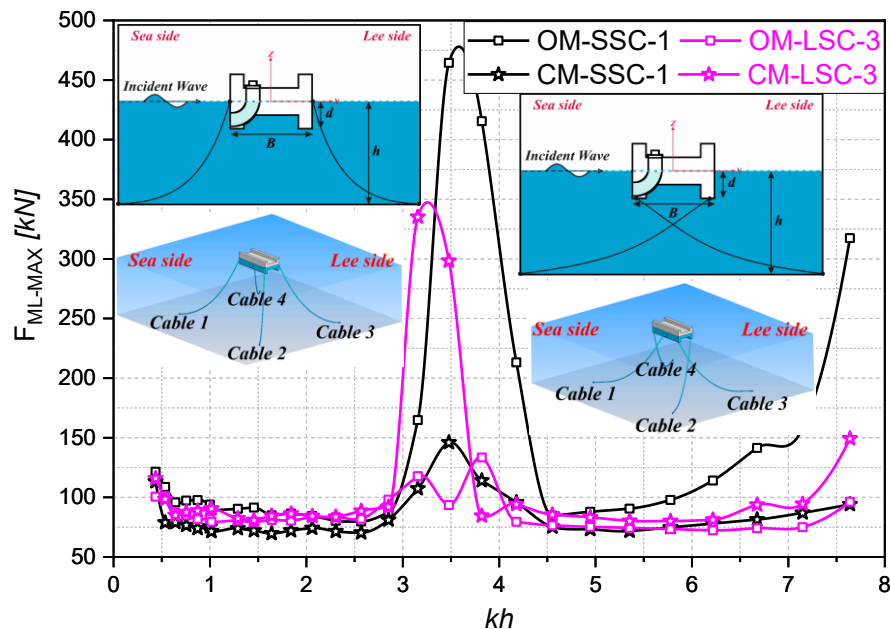


Figure 19: Mooring line force for H-shape floating breakwater integrated with OWC

The value of cable tension for H-shape hybrid FLBW is highest ($\sim 465\text{kN}$), in sea side cable 1, corresponding to kh value of 3.479 for open mooring configuration. In Figure 19, for kh value up to 3 cable tension remains in range of 50-100kN for and after that variation can be seen.

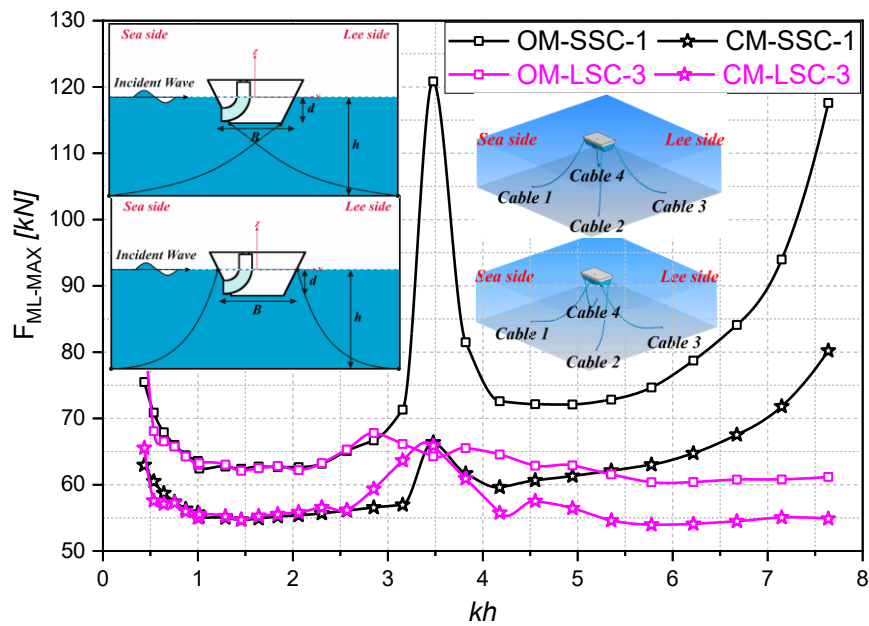


Figure 20: Mooring line force for Trapezoidal-shape floating breakwater integrated with OWC

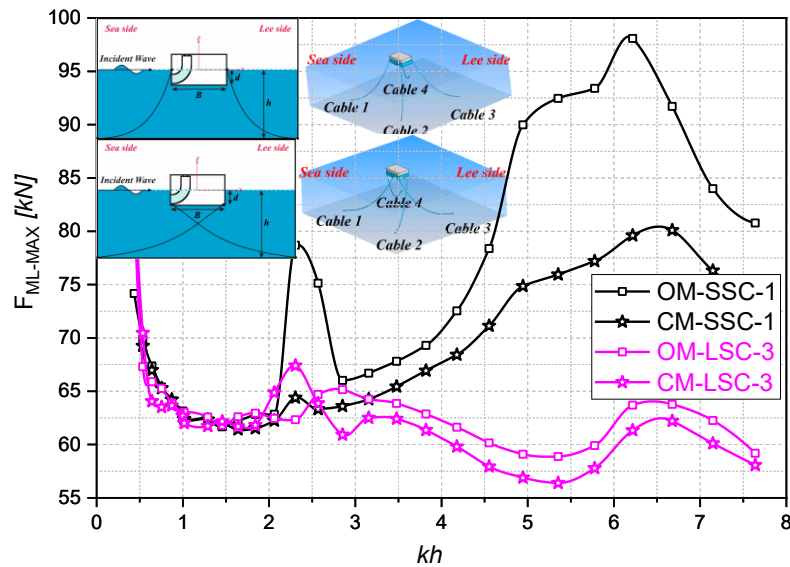


Figure 21: Mooring line force for Rectangular solid-type floating breakwater integrated with OWC

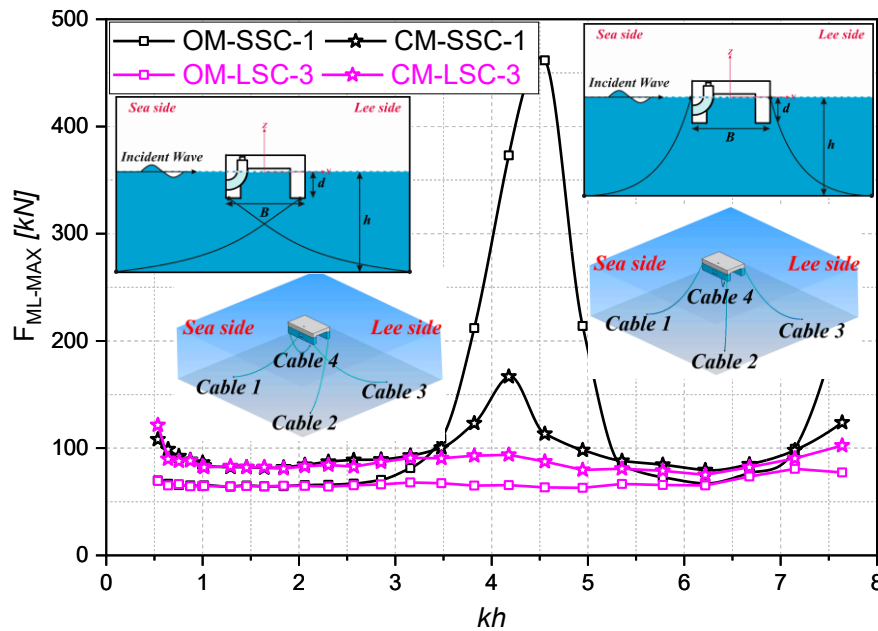


Figure 22: Mooring line force for π -type floating breakwater integrated with OWC

For hybrid FLBW having trapezoidal cross section, the mooring tension force is highest ($\sim 120.83\text{kN}$) for kh of 3.479 as we can see in Figure 20. Similarly, we can observe the highest cable tension force for rectangular FLBW $\sim 98\text{kN}$ for $kh = 6.218$ and for π -shape FLBW $\sim 462\text{kN}$ for $kh = 4.553$ in Figure 21 and Figure 22 respectively. From depth consideration for analysis, $kh > 3.14$ represents deep water condition and $kh \leq 0.314$ represents shallow water conditions and kh between 3.14 and 0.314 represents intermediate water condition. Higher mooring cable tension can be seen in case of deep-water region in comparison with shallow and intermediate water region, because the wave energy will be concentrated near sea surface in deep water region. This can be seen in all graphs except figure 3, in case of Box shape hybrid FLBW we are getting highest cable tension in intermediate water region because of resonance phenomenon for structure at $kh = 0.872$.

By comparing the mooring results corresponding to different hybrid models, it is clear that mooring tensile force in sea side cable 1 is lesser in cross mooring compared to open mooring in all models. In cross mooring configuration cable 3 is experiencing more cable tension than cable 1 only for H-shape breakwater. The highest mooring tension is observed in box type FLBW and in that case cross mooring is better option for mooring compared to open mooring because it reduces the tension coming on sea side cable by a significant amount of about 690kN . In rest of the models also this phenomenon of reduction in mooring tension can be seen in case of cross mooring.

CHAPTER 9

MODEL FABRICATION & EXPERIMENTAL INVESTIGATION

10.1 DIMENSIONAL ANALYSIS

Dimensional analysis is the study of physical quantities' relationships by determining their basic quantities and units of measurement. The basis quantities are a collection of measurements chosen in such a way that none of them can be stated as a combination of other quantities, but all other quantities may be expressed as their combination. Dimensional analysis decreases the number of variables that must be taken into account in any particular mathematical representation of physical phenomena.

Following the dimensional analysis adopting the Buckingham theorem, the dimensionless factors influencing the stability studies of the Floating breakwater were determined.

H_i / L - Wave steepness parameter

H_i / gT^2 - Relative incident wave height parameter

$K_R = |H_r / H_i|$ - Wave reflection coefficient

$K_T = |H_T / H_i|$ - Wave transmission coefficient

10.2 MODEL SCALE

The wave environment off the coast of Mangalore, as well as the ranges of wave heights and wave periods that may be created in the wave flume to fit a sea depth of 0.5 m, are taken into account while determining the model scale. For the current experimental studies, a geometrically comparable model scale of 1:30 was used to recreate the field circumstances of wave height, wave period, and water depth using Froude's law (Hughes, 1993). The Mangalore coast's wave height and period range from 1 m to 5.4 m and 8 s to 12 s, respectively. One regular wave in the range of 0.02m to 0.24m with periods 0.8 sec to 4 seconds may be created in the laboratory using the wave flume at NITK, Surathkal Mangalore. For the present study, a Froude's model scale of 1:30 is adopted.

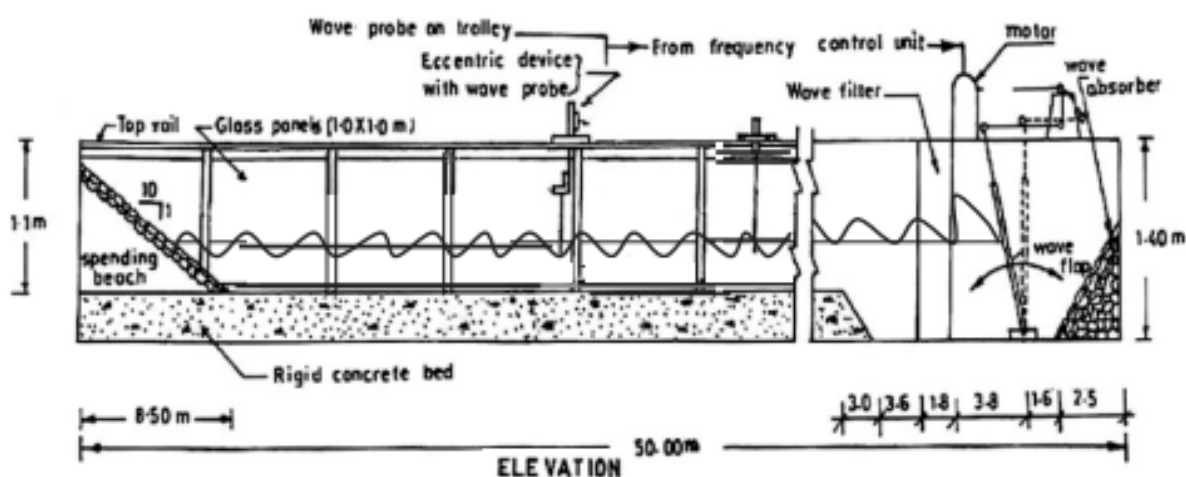
10.3 METHODOLOGY OF THE PRESENT EXPERIMENTAL WORK

A series of experiments are conducted to estimate the hydrodynamic characteristics of a hybrid floating breakwater built to be partially filled liquid rectangular-box type floating breakwater with a depth of fill varying between 10% to 30%. The tank was agitated at its natural frequency, causing the partly filled liquid to slosh at its resonance. Without considerable dampening, sloshing energy is turned into a long-term linear motion of built-in buoys within the liquid tank. The sloshing wave energy is converted into power by driving the buoys using the PTO system placed in the tank to create electricity.

10.4 Test Facilities

10.4.1 Wave flume Details

Wave flume at NITK, Surathkal Department of Water Resources and Ocean Engineering is 50 m long, 0.71 m wide, and 1.1 m deep and has a smooth concrete bed for a length of 42 m with a 6 m long wave-generating chamber at one end and a beach of 1V:10H slope consisting of rubble stones at another end. The flume is provided with a bottom-hinged flap-type wave generator. The wave generator is operated by a 7.5 HP, 11 kW, 1450 rpm induction motor. This motor is regulated by an inverter drive (0–50 Hz) rotating at 0–155 rpm. The system can generate regular waves of 0.02–0.24 m heights of periods ranging from 0.8 to 4 s at a maximum water depth of 0.5 m. The longitudinal section and plan view of wave flume is shown in Fig 3.



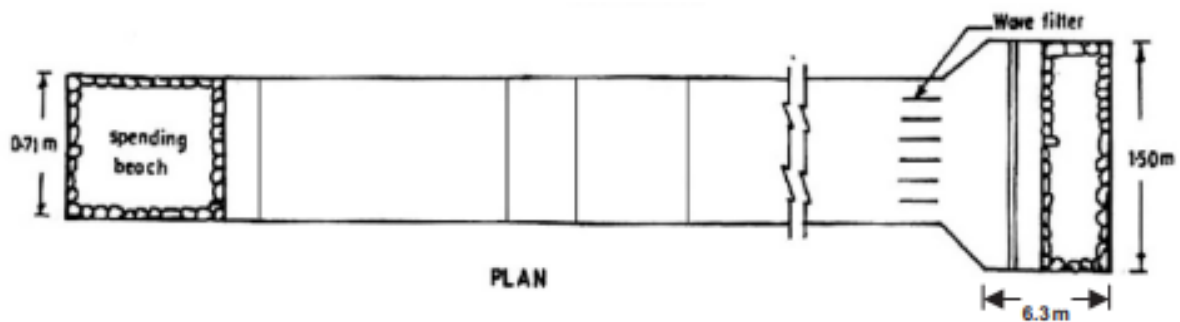


Fig. 3: The longitudinal section and plan view of wave flume.

10.4.2 Data acquisition system

Incident H_i and reflected wave heights H_r were measured using capacitance wave sensors and computer data collecting systems. The probe will be used to measure incident wave height and transfer the information to a computer via the data-gathering system. The major parameter, wave surface height on the model's seaward side, is translated into an electrical signal using appropriate equipment. This electrical signal is digitally saved using a software-controlled 12-bit A/D converter with 16 digital input/output channels. Before each setup, the probes were calibrated. The first probe was put a wavelength (L) away from the model, and the distance between probes was one-third of the wavelength ($L/3$). The superposed waves were measured using three probes, and the incident and reflected waves were decomposed from the superposed waves using the three probes approach by Michael Isaacson's (1991).

10.4.3 Wave Probes

Wave probes are devices that record incoming wave heights, time periods, and other relevant parameters. They are positioned at pre-set distances in the flume on the seaward side of the hybrid floating breakwater model, depending on wavelengths. The study used Michael Isaacson's (1991) three-probe approach, therefore the probes were set at L , $L+L/3$, and $L+2L/3$ distances from the front wall of a hybrid floating breakwater. Before the experiment begins, the wave probes were calibrated by setting the voltage value corresponding to the still water level to read zero.

10.5 CALIBRATION OF THE WAVE FLUME

In order to obtain the desired wave height at the structure position, it is required to establish a relationship between the frequency of the motor, the eccentricity of the board, the wave height, and the wavelength for different wave periods at varying water depths. The input to the motor is varied by changing the frequency input through the inverter and by changing the eccentricity

of the flywheel, it is possible to change the stroke of the wave flap, thus generating waves of different heights. Therefore, the wave height is a function of the frequency of the motor and the eccentricity of the board. The wave height created in the wave flume is proportional to the wave board's eccentricity and the frequency of the inverter is inversely proportional to the wave period. Using L as the distance between the wave paddle and the model, and λ as the wavelength, the burst of waves necessary for the formation of appropriate wave heights and wave periods can be calculated as, number of waves in a burst = L / λ .

In the present experimental study burst of 6 waves were generated and the digital voltage signals collected from the three wave sensors (Probes) by the EMCON (Environmental Measurements and Controls) Software were translated into wave height and wave period. This procedure is repeated for different water depth to obtain the wave height and wave period.

The range of wave excitation frequency for which the slosh natural frequency ω_n is achieved was first determined for the calibration of the floating breakwater integrated with S-WEC model.

For a partially filled rectangular tank, the slosh natural frequencies of the fluid are given by Jung (2015) as

$$\omega_n = \sqrt{\frac{n\pi g}{L_T} \tanh\left(\frac{n\pi d}{L_T}\right)}.$$

Table 1: Natural frequency of partially filled Hybrid floating breakwater.

Tank length (m)	Tank width (m)	Tank height (m)	n	% Fill	depth of fill, d (m)	ω_n	T_n (sec)	f_n
1	0.6	0.6	1	10	0.06	2.40	2.62	0.38
1	0.6	0.6	1	15	0.09	2.91	2.16	0.46
1	0.6	0.6	1	20	0.12	3.33	1.89	0.53
1	0.6	0.6	1	25	0.15	3.68	1.71	0.59
1	0.6	0.6	1	30	0.18	3.97	1.58	0.63

Repeated 3 trials are conducted to reduce the effect of errors and thus increase the reliability of the results of an experiment. Table. 1 shows the calibration of wave flume-1 for a water depth of 0.5m. From the data obtained, a general relation is drawn between these parameters by multi-regression analysis as shown in Fig. 4

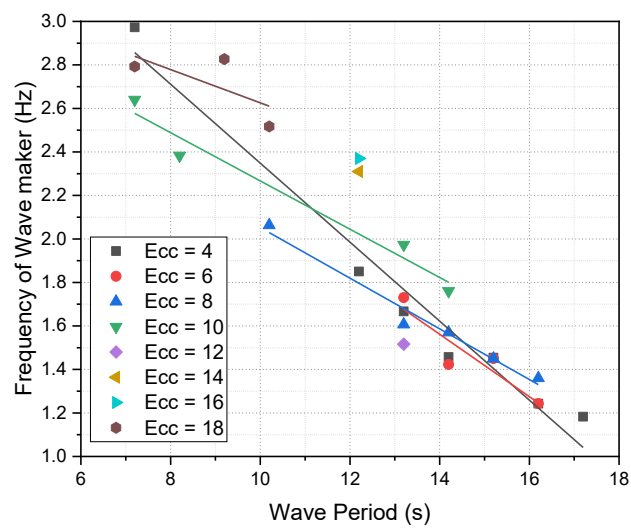


Fig. 4: Calibration of wave flume for $d = 0.5\text{m}$.

Equation	$y = a + b \cdot x$							
Plot	Ecc = 4	Ecc = 6	Ecc = 8	Ecc = 10	Ecc = 12	Ecc = 14	Ecc = 16	Ecc = 18
Weight	No Weighting							
Intercept	4.1639 ± 0.20819	3.56948 ± 0.63634	3.21718 ± 0.15023	3.37612 ± 0.1651	-- \pm --	-- \pm --	-- \pm --	3.39 ± 0.72448
Slope	-0.18155 ± 0.0149	-0.1434 ± 0.04316	-0.11646 ± 0.01077	-0.11095 ± 0.01484	-- \pm --	-- \pm --	-- \pm --	-0.07643 ± 0.08091
Residual Sum of Squares	0.07299	0.01863	0.00737	0.0163	--	--	--	0.03055
Pearson's r	-0.98357	-0.9201	-0.98742	-0.98257	--	--	--	-0.68668
R-Square (COD)	0.9674	0.84659	0.975	0.96544	--	--	--	0.47153
Adj. R-Square	0.96088	0.76989	0.96667	0.94817	--	--	--	-0.05694

Table 2: Time Period T_e , wavelength, and corresponding wave height H_i for the Flume-1, with water depth $h = 0.5\text{m}$

Eccentricity (cm)	4		6		8		10		12		14		16		18	
frequency (Hz)	T_e	Wave Height (mm)	T	Wave Height (mm)	T_e	Wave Height (mm)	T_e	Wave Height (mm)	T_e	Wave Height (mm)	T_e	Wave Height (mm)	T_e	Wave Height (mm)	T_e	Wave Height (mm)
17.2	1.18	84.69	-		-		-		-		-		-		-	
16.2	1.24	75.75	1.24	111.62	1.36	150.72	-		-		-		-		-	
15.2	1.45	80.67	1.45	112.92	1.45	157.46	-		-		-		-		-	
14.2	1.46	77.70	1.42	104.88	1.57	147.49	1.76	176.50							-	
13.2	1.67	77.05	1.73	95.05	1.61	130.14	1.97	149.17	1.52	174.30					-	
12.2	1.85	65.78	-		-		-		-		2.31	172.61	2.37	180.25	-	
11.2	-		-		-		-		-		-		-		-	
10.2					2.06	88.51									2.52	167.69
9.2	-		-		-		-		-		-		-		2.83	150.21
8.2	-		-		-		2.38	71.61	-		-		-		-	
7.2	2.97	25.12	-		-		2.64	60.34	-		-		-		2.79	94.01

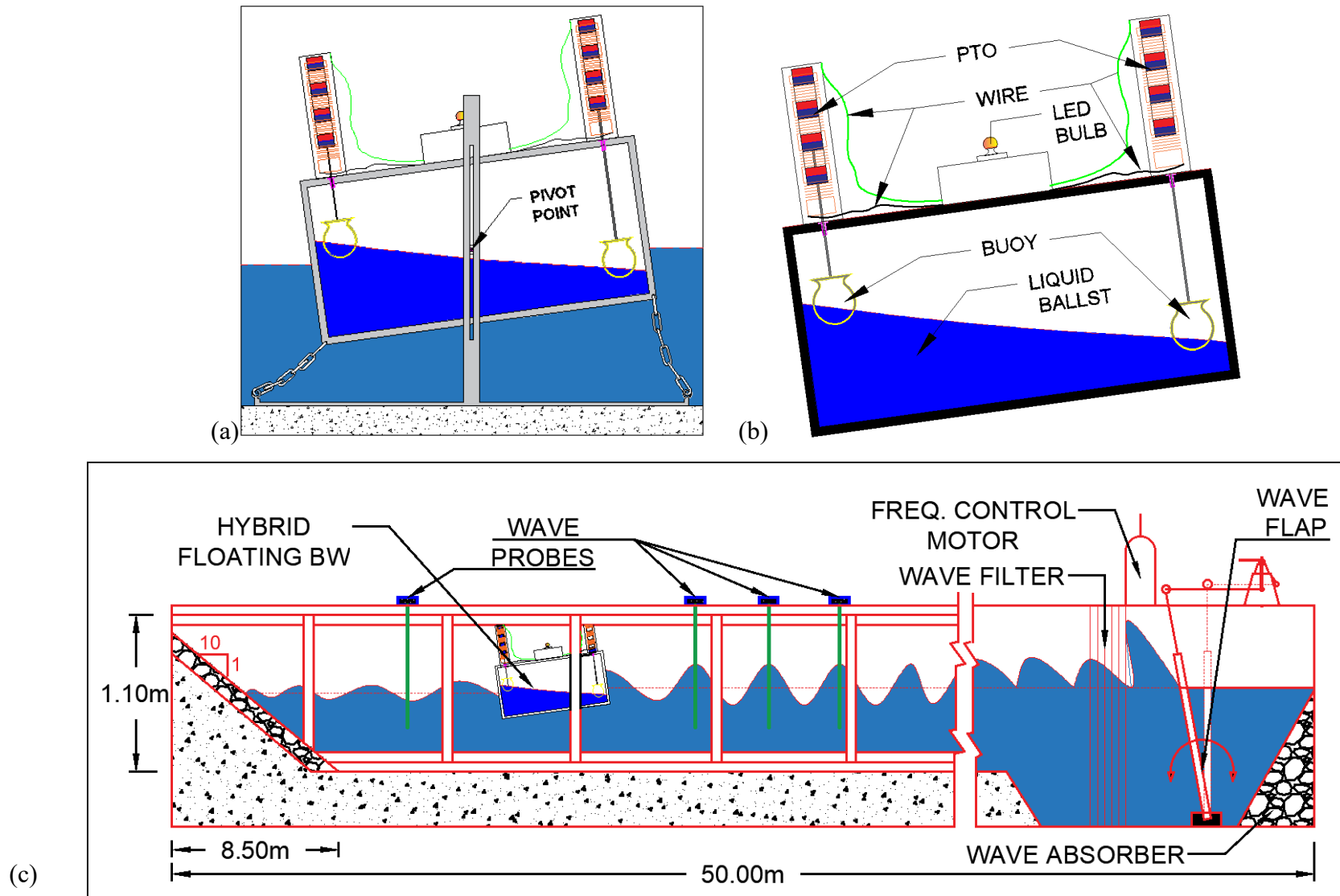


Fig. 5: Schematic diagram of Hybrid floating breakwater in a wave flume

10.6 PHYSICAL MODEL OF HYBRID FLOATING BREAKWATER WITH S-WEC

The hybrid floating breakwater was fabricated into a rectangular shape of length 1m x width of 0.6m and a depth of 0.6m using an 8mm thick acrylic sheet and was supported by a steel frame with Mild Steel as shown in Fig. 6(a and b). Two floating buoys of negligible mass (weight less than 20 grams) were installed at the two extreme ends of the tank so as to capture the sloshing energy that can be converted into electricity through the linear inductance generator as shown in Fig. 7(a and b) respectively. In operation, the hybrid floating breakwater is oscillated external with a bottom-hinged flap-type wave generator in the wave flume, which subsequently activates the internal sloshing motion. After that, the sloshing waves further excite the floating buoys to drive the PTO system. Thus, the mechanical energy first transfers from ocean waves to the floating structure, and then to sloshing waves and oscillating buoys, before reaching the PTO system. Here the PTO system is constructed as a linear inductance generator that can produce an electrical current in the wire loop through relative motions between the wire loop and magnet. This is achieved by letting a permanent magnet move through a coil or vice versa. The linear generator (PTO) was built using a cylindrical shaped permanent magnet 25mm in diameter and 12mm in thickness of N52 Grade Neodymium arranged at 25mm intervals in 4 numbers. The copper wire was coiled around a 40mm diameter cylindrical PVC pipe creating a coil of 5 numbers each 500 windings separated at 25mm interconnected in series.

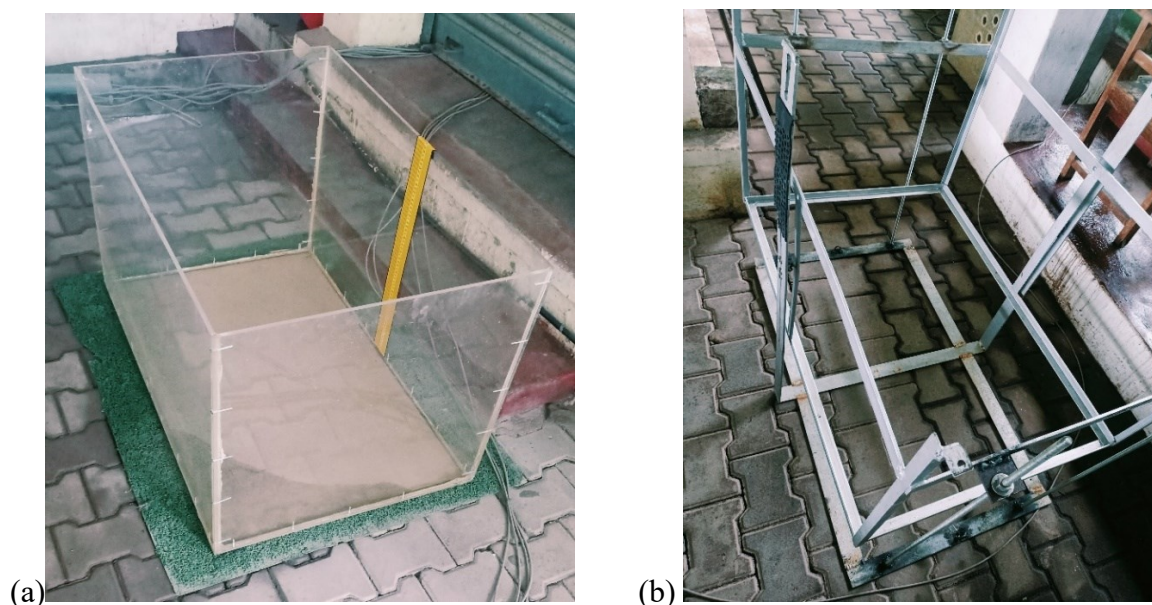


Fig 6: (a) Floating breakwater fabricated into a rectangular shape of size 1m x 0.6m x 0.6m (b) Supporting steel frame for the rectangular-shaped floating breakwater.



Fig 7: (a) Floating breakwater with built-in buoys (b) Floating breakwater with built-in buoys connected to linear inductance generator.

10.7 EXPERIMENTAL CONDITIONS

The following set of assumptions and test conditions is considered for the present experimental investigation.

- The flume bed is horizontal and rigid.
- Secondary waves during wave generation are to be neglected.
- The density difference between freshwater and seawater is not considered.
- Generated waves are of a simple regular type.
- Reflection from the sides of the wave flume is not considered.
- Only the hydraulic performance of the test model is considered.
- Bottom frictional effects have not been accounted

10.8 RANGE OF EXPERIMENTAL VARIABLES

Table 3: Wave and Floating breakwater integrated with S-WEC parameters

Parameters	Experimental range of values
Wave parameters	
Water depth (m)	0.50
Incident wave height (m)	0.06, 0.065, 0.07, 0.075, 0.080, 0.085, 0.095, 0.10, 0.12, 0.13, 0.14, 0.15, 0.16, 0.17, and 0.18
Wave Period (sec)	2.0, 2.1, 2.2, 2.3, 2.4, 2.5, 2.6, 2.7, 2.8, 3.0, 3.1, 3.2, and 3.6

Structure parameters	
Height of the tank (m)	0.6
Width of the tank (m)	0.67
Length of the tank (m)	1.0
Thickness of the tank (m)	transparent plexiglass plates of thickness 0.08 m, Density = $1.18 \times 10^3 \text{ kg/m}^3$
Depth of fill (m)	0.06(10%), 0.09(15%), 0.12(20%), 0.15(25%) and 0.18 (30%)
Floating buoy	Hemispherical Coin Container made of plastic of 0.15m diameter.
Linear inductance generator (PTO)	
Permanent Magnet	The cylindrical shape of 25mm diameter 12mm thick Neodymium magnet of N52 Grade.
Winding coil	28-gauge (0.37mm) copper coil

10.9 EXPERIMENTAL RESULTS AND DISCUSSION

Seaports are highly energy-demanding infrastructures and are exposed to wave energy, which is an abundant resource and largely unexploited. As a result, there has been a rising interest in integrating wave energy converters (WEC) into the breakwaters of seaports. The experimental investigation is carried out to analyse the hydrodynamic performance characteristics of a floating rectangular-shaped box-type breakwater with partially filled liquid in terms of wave reflection and transmission coefficient, as well as to convert the slosh dynamics of partially filled liquid into electricity. Zhang et al. (2022) conducted similar experimental and numerical studies on the slosh-WEC device by giving a harmonic excitation on a shaking table along the length side of the tank, with a displacement amplitude of 0.01 m for a constant fill $d = 0.3m$ in a tank of dimension 0.5m x 0.2m x 0.6m. In the current study, the floating rectangular-shaped box-type breakwater is subjected to a roll motion an external wave-induced force generated by a frequency-controlled wave generator in a 2-dimensional wave flume for various wave heights as mentioned in Table 3. Because of the roll excitation, the partially filled liquid in the tank sloshes, causing the liquid to rise and fall along the tank's side walls. Because of the buoyancy of the floating buoy, the rise and fall of the liquid intern induces linear motion in the PTO, and thus wave energy is absorbed through the sloshing of a liquid filled in the floating breakwater as a ballast, which is further transformed into mechanical energy and then to electric energy via the PTO. As a result of this, the ensuing wave transmission on the leeward side is decreased,

proving that this hybrid floating breakwater is both useful to port operations and capable of capturing wave energy.

10.10 WAVE REFLECTION AND TRANSMISSION COEFFICIENT.

The surface floating breakwater aids in the attenuation of surface waves via the wave reflection K_R and transmission coefficient K_T mechanisms. The current work is experimentally studied with the goal of building an efficient Hybrid floating breakwater capable of wave energy conversion and optimizing the wave transformation characteristic. The following Fig (8-12) depicts the resulting wave reflection K_R and transmission coefficient K_T against the non-dimensional wave height H_i / gT^2 for varying fill $d = 10\%$ to 30% respectively. For the comparison let us fix the threshold value of wave reflection K_R and transmission coefficient K_T as 0.5. However, in reality, the operability thresholds are determined by the maximum acceptable ship motions, induced by the metocean conditions, for safe and efficient operations (Molina-Sanchez, 2020).

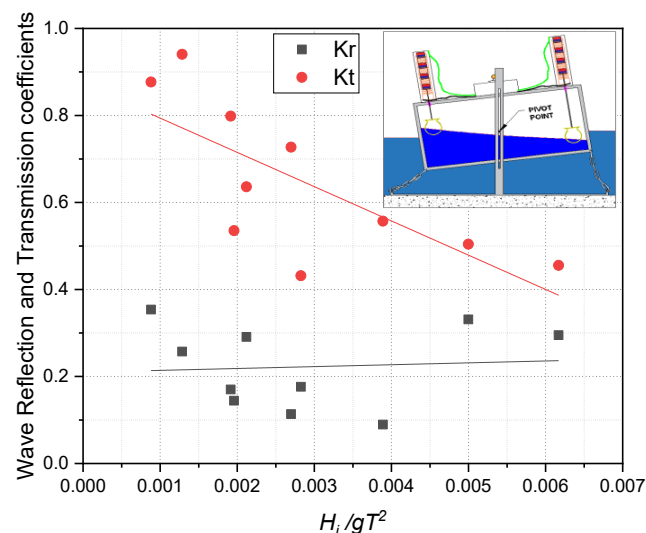


Fig 8: Wave reflection K_R and Transmission coefficient K_T Vs non-dimensional wave height H_i / gT^2 for 10% depth of fill.

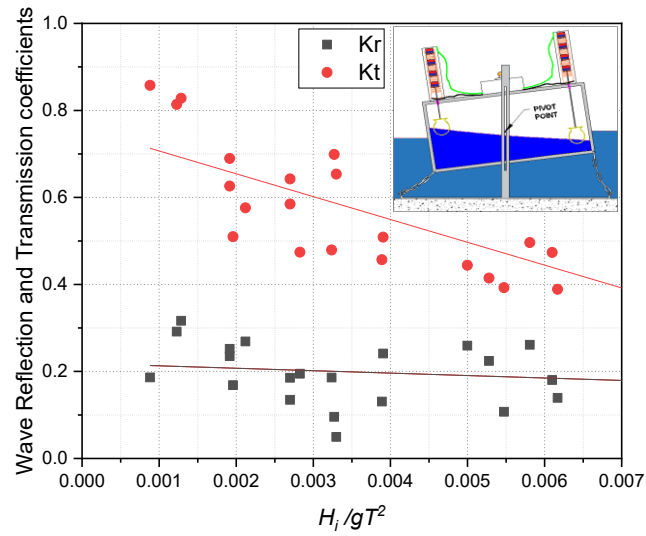


Fig 9: Wave reflection K_R and Transmission coefficient K_T Vs non-dimensional wave height H_i / gT^2 for 15% depth of fill.

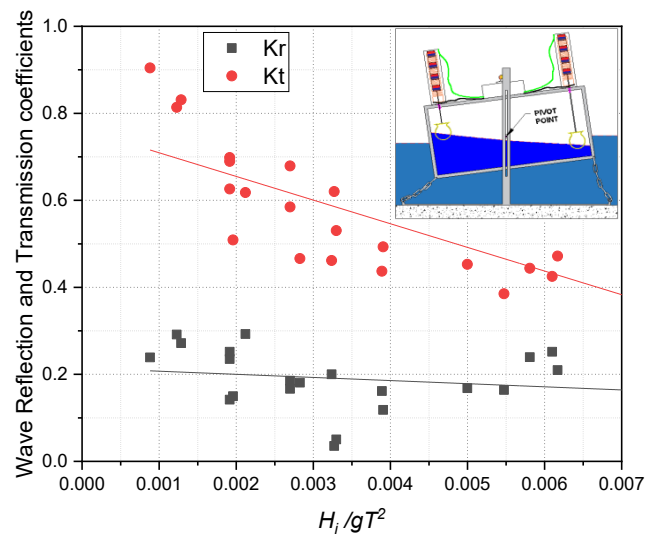


Fig 10: Wave reflection K_R and Transmission coefficient K_T Vs non-dimensional wave height H_i / gT^2 for 20% depth of fill.

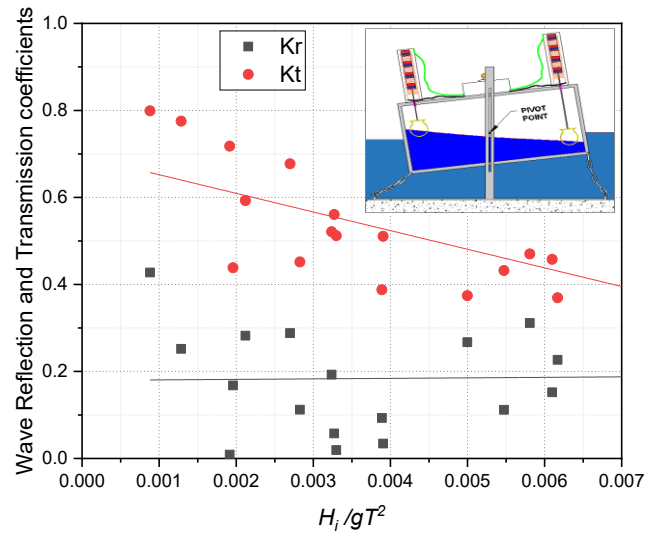


Fig 11: Wave reflection K_R and Transmission coefficient K_T Vs non-dimensional wave height H_i / gT^2 for 25% depth of fill.

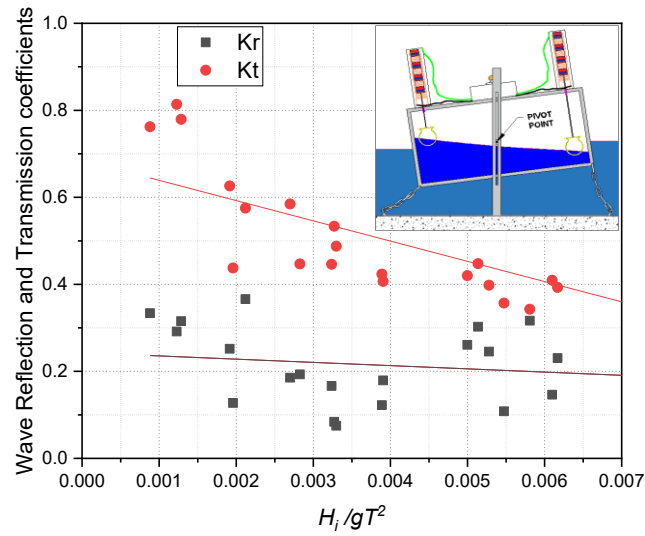


Fig 12: Wave reflection K_R and Transmission coefficient K_T Vs non-dimensional wave height H_i / gT^2 for 30% depth of fill.

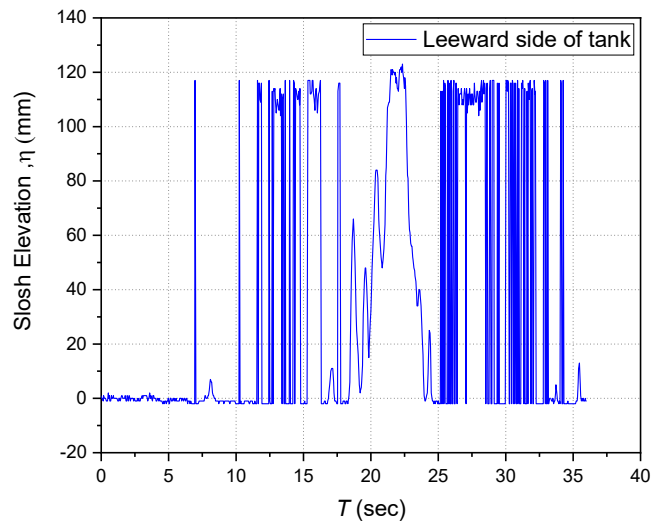
The wave transmission coefficient K_T reduces with increasing incident wave height H_i / gT^2 for all the depth of fills d , as seen in Fig. (6-10), since lower wave heights $H_i / gT^2 \leq 0.02$ simply escape from below without interacting with the hybrid floating breakwater. The water column mass interacting with the hybrid floating breakwater grows as the wave height H_i / gT^2 increases, providing energy to the structure's body, which is further reduced by the

sloshing of a liquid in the tank, resulting in a decreased wave transmission coefficient K_T . On the other hand, the wave reflection coefficient K_R seems to remain much lower than the set threshold wave reflection $K_R = 0.5$ for all the depth of fill d and with increase in incident wave height H_i / gT^2 the reflection coefficient K_R slightly increases.

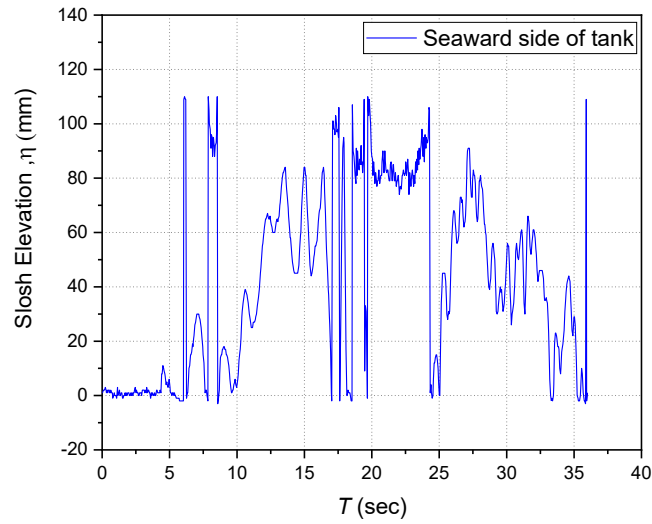
As the depth of fill in the hybrid floating breakwater increases it will not only add to float stability but also contributes in reduction in the wave transmission K_T . This is because the increased draft d_f of the hybrid floating breakwater achieves stable equilibrium as the metacentric height shifts significantly above the centre of gravity; in fact, this decrease is significant below the set threshold wave transmission coefficient K_T , for incident wave height $H_i / gT^2 \geq 0.02$ for higher percentage depth of fill $d \geq 15\%$. The wave reflection coefficient K_R , on the other hand, which originally increased with rising wave height for $d = 10\%$, will remain unaltered for greater depth of fill. For depth of fill $d \geq 20\%$, the wave transmission coefficient K_T stays lower than the set threshold $K_T = 0.5$ for incident wave heights $H_i / gT^2 \geq 0.03$.

10.11 WAVE RUNUP IN THE PARTIALLY FILLED HYBRID FLOATING BREAKWATER

Runup probes affixed to the inner face of the tank's front and rear walls were used to quantify the liquid displacement caused by sloshing in the partially filled hybrid floating breakwater during the roll motion when the incident waves interact with the structure. The rate of movement of the permanent magnet in the linear inductance generator is determined by the quantum of rise and fall of liquid in the tank and its variation with respect to time t . The greater the fluid displacement and impulsive rate of change with respect to time t , the greater the magnet flux through the copper windings of the linear induction generator, and therefore the greater the electricity generated. Fig. 13(a) shows the variation of the relative run-up against the time for a particular case of 25% depth of fill of liquid in the hybrid floating breakwater for which the time period is $T_e = 1.760s$ and the incident wave height H_i is 0.1765m.



(a)



(b)

Fig 13: Slosh elevation, (η) Vs time T for 25% depth of fill (a) for Leeward side of tank (b) Seaward side of tank.

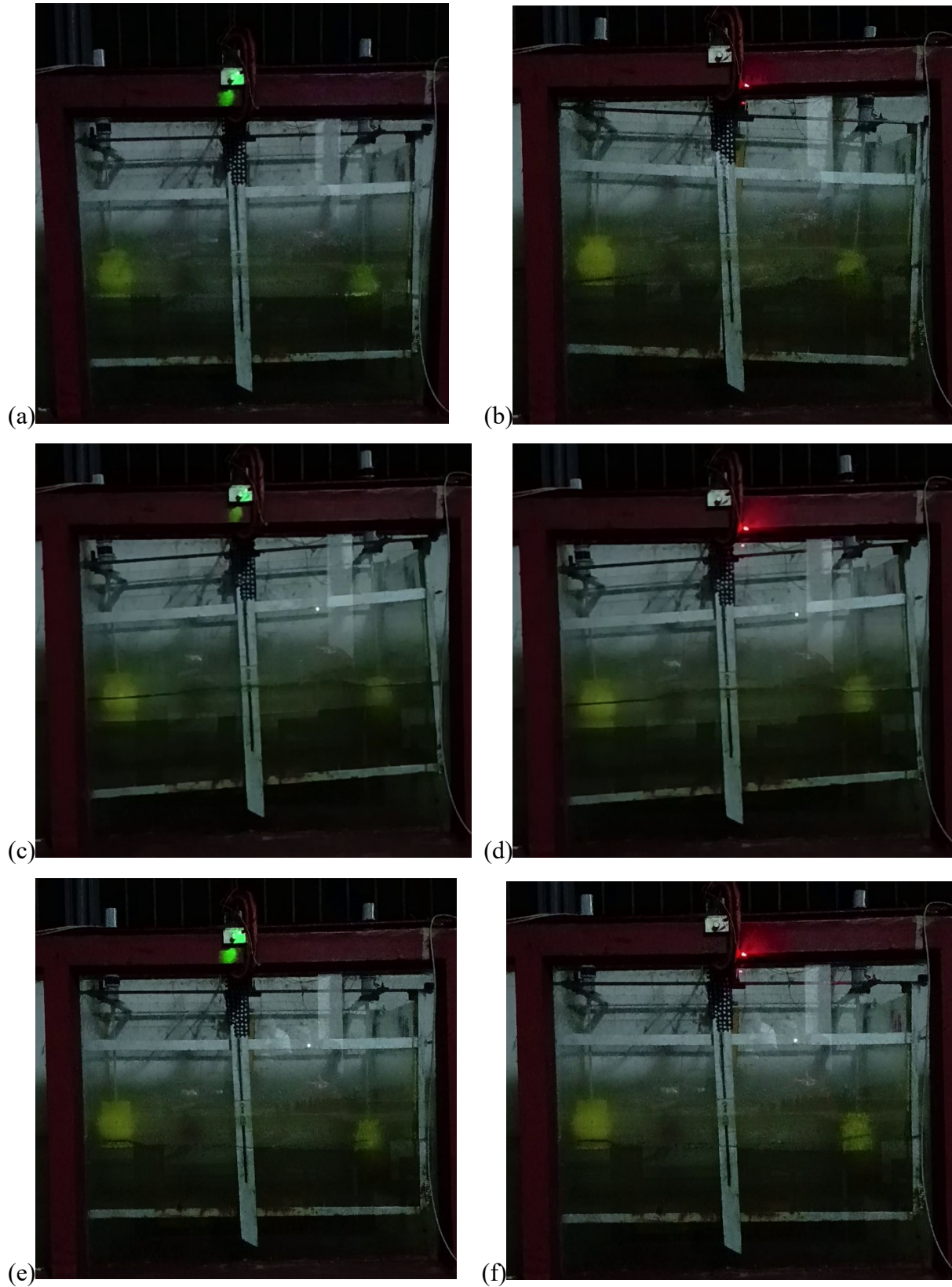


Fig. 14: Still frames of electricity generation from the videos captured during the experiments for (a and b) $T_e = 1.243$ sec, (c and d) $T_e = 1.760$ sec and (e and f) $T_e = 2.82$ sec respectively.

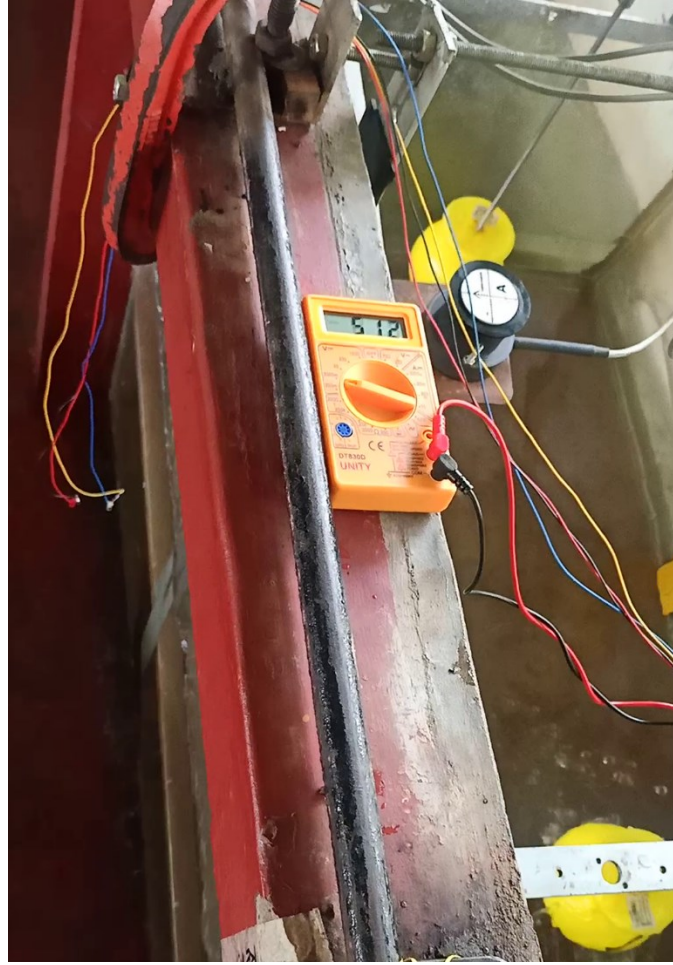


Fig. 15: Still frame of volt meter reading recorded during the experiment for $T_e = 2.82$ sec

It is obvious from Fig. 13 (a and b) that when the incident wave frequency (excitation frequency) corresponds with the fundamental natural frequency ω_n of the hybrid floating breakwater, there is impulsive slosh elevation η that varies with time t . As a result of the permanent magnet varying strongly across the copper coil windings, the magnetic flux rose, and a greater voltage was recorded in the volt multimeter as in Fig. 15 in a range that could light the Light Emitting Diode (LED) bulbs. As a result of the wave-induced excitation, the resonant response of the hybrid floating breakwater was adequate to illuminate two LED lamps alternately in each cycle of sloshing as shown if Fig.14 (a to f). A series of experiments were carried out to encapsulate the effect of liquid fill depth d in hybrid floating breakwater from $d = 10\%$ to 30% of breakwater's height H on the efficiency of hybrid structure as WEC. It was discovered that initially for smaller depth of fill $d \leq 10\%$ the sloshing set the system in roll motion was limited to those excitation frequencies which are 10-15% closer to the tank fundamental natural frequency ω_n , and the number of cycles of slosh was not more than 3, as well as there was a lack of completeness in each cycle. A full sloshing cycle due to roll motion

was seen for a wide range of excitation frequency corresponding to time periods $T_e = 1.243$ to 2.827 sec as the depth of fill d increased from 10% to 15%, 15 to 20%, and 20 to 25%. This was mostly due to the enhanced floating stability provided by the increased ballast weight, which resulted in an increase in the hybrid floating breakwater draft d_f . However, increasing the draft d_f by increasing the percentage of fill $d = 30\%$ resulted in roll motion suppression due to the necessity of a larger magnitude of wave excitation that might roll the hybrid floating breakwater. This implies that the hybrid floating breakwater has a draft d_f bandwidth beyond which the structure serves as a breakwater that is capable of attenuating the incoming progressive waves much lower than the set threshold values of wave reflection K_R and transmission coefficient K_T as defined in section 3.8.1.

Physical experiments are carried out on a 1:30 scaled hybrid floating breakwater model to investigate its usefulness as a port-protecting structure and as a wave energy capture device in a 2-D linear wave flume. With the goal of developing an efficient Hybrid floating breakwater capable of wave energy conversion and optimising the wave transformation characteristic, it is subjected to a series of linear 2-D waves for a variety of wave periods and incident wave heights as shown in Table 3 for varying depth d of partially filled liquid that serves as ballast for the hybrid floating breakwater. When subjected to wave excitation, the model is designed to be a floating rectangular-shaped box-type breakwater with partially filled liquid and restricted to have a roll motion, causing the liquid in the breakwater to slosh during operation. This sloshing not only dampens the incoming wave energy far below the set threshold values of wave reflection and transmission, but it also converts the slosh energy to mechanical energy by moving the buoys in a linear vertical motion of a permanent magnet attached to a linear inductance generator, changing the flux density of the coil and thus inducing a current in the coil. The following are the conclusion drawn from the experimental investigation on hydrodynamics of hybrid floating breakwater with S-WEC.

- Standing waves were generated on the seaward side of the hybrid floating breakwater when the excitation frequency ω_e was near to the fundamental natural frequency ω_n of the floating breakwater. This would easily induce equal-amplitude roll motion in both directions, resulting in evident sloshing events, which was an ideal condition for wave energy conversion.

- The roll displacement of the floating breakwater was relatively less under short wave situations irrespective of the depth of fill d . So, while the wave transformation was within the desired range, the lack of rolling resulted in zero sloshing, which was undesirable for the proposed hybrid floating breakwater with S-WEC.
- For shallower fill depths $d \leq 10\%$, the hydrodynamic restoring force of a partially filled hybrid floating breakwater may appear insufficient to stable the structure back to its equilibrium position, which lacked the ability to set roll motion into the hybrid floating breakwater. Thus, this condition show undesirable for the proposed hybrid floating breakwater with S-WEC.
- The hybrid floating breakwater attains its floating stability for the depth $d = 15 - 25\%$ of partially filled liquid for which the propose of its design as a dual system as floating breakwater as well as WEC system is achieved for a wide range of excitation frequencies corresponding to time periods $T_e = 1.243$ to 2.827 sec. otherwise, this hybrid floating breakwater serves as a barrier that is capable of attenuating the incoming progressive waves much lower than the set threshold values of wave reflection K_R and transmission coefficient K_T .
- When the wave excitation frequency is equal to half power band width for the range of frequencies considered in the study, an impulsive slosh dynamic of partially filled liquid as ballast is observed, with the constraint that the hybrid floating breakwater is in state of dynamic float equilibrium. This optimal condition was met in this investigation when the depth of fill $d = 25\%$.
- It was worth noting that even when the incident wave energy discussed in the range was insufficient to cause the hybrid floating breakwater to roll, the use of liquid as ballast contributed to energy absorption through sloshing of liquid and it could generate electricity at least to light a 1-volt LED during its operation.

REFERENCES

- [1]. Abul-Azm, A. G., (1994). Diffraction through wide submerged breakwaters under oblique waves. *Ocean Engineering*, 21(7), 683–706.
- [2]. Adee, B.H., (1974). Analysis of floating breakwater mooring forces. *Ocean Engineering Mechanics*, 1, 77–92.
- [3]. Adee, B.H., (1975). Analysis of floating breakwater performance. *Proceedings of the Symposium on Modeling Techniques (ASCE)*, Vol-2, pp. 1585–1602.
- [4]. Adee, B.H., (1976). Floating breakwater performance. *Proceedings of the 15th Conference on Coastal Engineering (ASCE)*, Vol-3, pp. 2777–2791.
- [5]. Adee, B.H. and Martin, W. (1974). Theoretical analysis of floating breakwater performance. *Proceedings of the Floating Breakwater Conference*. University of Rhode Island, Kingston, pp. 21–40.
- [6]. Adee, B.H., Richey, E.P. and Christensen, D.R., (1976). Floating Breakwater Field Assessment Program, Friday Harbor, Washington. Technical Report 76–17. U.S. Army, Corps of Engineers, Coastal Engineering Research Center, Fort Belvoir.
- [7]. Au, M.C. and Brebbia, C.A. (1982), Numerical prediction of wave forces using the boundary element method, *Applied Mathematical Modelling*, 6(4), 218-228.
- [8]. Bando K., and Sonu C. J., (1987), Evaluation of numerical models for a floating breakwater. Department of the army US Army Corps of Engineers Washington, DC 20314-1000
- [9]. Bayram, A. (2000). Experimental study of a sloping float breakwater. *Ocean Engineering*, 27, 445–453
- [10]. Ivan Catipovic, Maro Corak, Neven Alujevic and Josko Parunov, (2019). Dynamic Analysis of an Array of Connected Floating Breakwaters, *J. Mar. Sci. Eng.* 2019, 7, 298; doi:10.3390/jmse7090298
- [11]. Carver, R.D. (1979). Floating breakwater wave-attenuation tests for east bay marina, Olympia Harbor, Washington. Technical Report HL-79–13. U.S. Army Engineer Waterways Experiment Station.
- [12]. Carr, J. H. (1951). Mobile Breakwaters. *Coastal Engineering Proceedings*, 1(2), 25. <https://doi.org/10.9753/icce.v2.25>
- [13]. Cho, Y.S., Lee, J.I. and Kim, Y.T. (2004). Experimental study of strong reflection of regular water waves over submerged breakwaters in tandem. *Ocean Engineering*, 31(10), 1325-1335.

- [14]. Chen, K.H., Chen, J.T., Chou, C.R. and Yueh, C.Y. (2002) Dual boundary element analysis of oblique incident wave passing a thin submerged breakwater, *Engineering Analysis and Boundary Elements*, 26, 917-928.
- [15]. Cheng L.H, Fen C.Y, Li Y.H and Jiang W.Y (2013) Experimental study on a new type floating breakwater. *Proceedings of the 7th International Conference on Asian and Pacific Coasts (APAC 2013) Bali, Indonesia, September 24-26.*
- [16]. Cui Jie, Liu Hui, Deng Xiaokang, Tao Shenghui and Li Qian. (2019), An experimental study on hydrodynamic performance of a box-floating breakwater in different terrains, *Journal of Marine Science and Technology*, <https://doi.org/10.1007/s00773-019-00695-4>.
- [17]. Dalrymple, R.A., Losada, M.A. and Martin, P.A. (1991). Reflection and transmission from porous structures under oblique wave attack. *Journal of Fluid Mechanics*, 224, 625–644.
- [18]. Deng, Zhengzhi Wang, Lin; Zhao, Xizeng Huang, and Zhiyong (2019). Hydrodynamic performance of a T-shaped floating breakwater. *Applied Ocean Research*, 82(), 325–336. doi:10.1016/j.apor.2018.11.002
- [19]. Drimer, N, Agon, Y and Stiassnie, M, (1992): A Simplified Analytical Model for a Floating Breakwater in Water of Finite Depth, *Applied Ocean Research*, Vol.14, pp 33-41.
- [20]. Duan, W. Xu, S. Xu, Q. Ertekin, R.C. and Ma, S. Performance of an F-type floating breakwater: A numerical and experimental study. *Proc. Inst. Mech. Eng. Part M-J. Eng. Marit. Environ.* 2017, 231, 583–599
- [21]. Elchahal, G., Younes, R and Lafon, P. (2006). Wave Interaction with fixed and floating vertical breakwater based on analytical modelling. *ASME Joint U.S.-European Fluids Engineering Division Summer Meeting.*
- [22]. Fawzi, S., Nadji, C. and Mohammed El-Amine, D. (2019). Performance evaluation of bottom-standing submerged breakwaters in regular waves using the meshless singular boundary method, *Oceanic and Coastal Sea Research*, 18, 823-833.
- [23]. Gesraha, M.R., (2006). Analysis of the pi-shaped floating breakwater in oblique waves: Impervious rigid wave boards. *Applied Ocean Research* 28(5), 327–338.
- [24]. Hay, D. (1966). Considerations for the design of a floating breakwater. *Department of Public Works of Canada, Vancouver.*
- [25]. Hales, L.Z., (1981). Floating breakwaters-state of the art literature review. *Coastal Engineering Research Centre, Fort Belvoir. Technical Report no. 81–1.*

- [26]. Ijima, T. and Okuzono, H. (1982). Reflection of normal incident waves at porous quaywall, *Memories of the Faculty of Engineering, Kyushu University*, Vol. 42, No. 4, pp. 217-243.
- [27]. Ji, C., Deng, X. and Cheng, Y. (2018). An experimental study of double-row floating breakwaters. *Journal of Marine Science and Technology*, 24, 359-371.
- [28]. Joly, J. (1905), *On Floating Breakwaters*, *Scientific Proceedings of the Royal Dublin Society*, Vol. 10, pp. 378-383.
- [29]. Jones, D.B., (1971). *Transportable Breakwaters--A Survey of Concepts*, Technical Report R-727, U.S. Navy Civil Engineering Laboratory, Port Hueneme, Calif., May 1971.
- [30]. Karmakar D., Bhattacharjee J., and Soares, C. G. (2012). Scattering of gravity waves by multiple surface-piercing floating membrane, *Applied Ocean Research*, 39, 40–52.
- [31]. Karmakar, D., Bhattacharjee, J. and Soares, C. G. (2013) Scattering of gravity waves by multiple surface-piercing floating membrane, *Applied Ocean Research* 39, 40– 52.
- [32]. Koutandos, E., Prinos, P., and Gironelia, X., (2005). Floating Breakwater Under Regular and Irregular Wave Forcing: Reflection and Transmission Characteristics. *Applied Journal of hydraulic Research*, Vol. 43, No. (2), pp 174-188.
- [33]. Koraim, A. S. and Rageh, O. S. (2013). Effect of under connected plates on the hydrodynamic efficiency of the floating breakwater. *China Ocean Engineering*, 28(3), 349–362. doi:10.1007/s13344-014-0028-1
- [34]. Kue-Hong Chen, Jeng-Tzong Chen, Sheng-Yih Lin, and Ying-Te Lee (2004) Dual Boundary Element Analysis of Normal Incident Wave Passing a Thin Submerged Breakwater with Rigid, Absorbing, and Permeable Boundaries, *Journal of Waterway, Port, Coastal and Ocean Engineering* © ASCE /179
- [35]. Lee, J. (1995). A boundary element model for wave interaction with porous structures. *Transactions on Modelling and Simulation*, 9, 145–152.
- [36]. Lee, Jeongwoo Cho, and Woncheol (2003). Hydrodynamic analysis of wave interactions with a moored floating breakwater using the element-free Galerkin method. *Canadian Journal of Civil Engineering*, 30(4), 720–733. doi:10.1139/103-020
- [37]. Li, J., Fu, Z. and Chen, W. (2015). Numerical investigation on the obliquely incident water wave passing through the submerged breakwater by singular boundary method. *Computers and Mathematics with Applications*, 71(1), 381-390.
- [38]. Li, Xueyan Li, Qin Wang, Qing Hou, Chengyi Song, Kezhi Xie, Tian; Zhang, Zhenhu Wan, Xiang Xie, Xiaomi, and Wang, Yukun (2020). Numerical and experimental

- investigation on the hydrodynamic characteristics of an arc-shaped plate-type breakwater under the action of long-period waves. *Ocean Engineering*, 108198–. doi: 10.1016/j.oceaneng.2020.108198
- [39]. Liang Nai-Kuang, Huang Jen-Sheng, and Li Chih-Fei (2004). A study of spar buoy floating breakwater., 31(1), 43–60. doi:10.1016/s0029-8018(03)00107-0
- [40]. Losada, I.J., Silva, R. and Losada, M.A. (1996). 3-D nonbreaking regular wave interaction with submerged breakwaters. *Coastal Engineering*, 28(1), 229-248.
- [41]. Macagno, E. O., (1953). Fluid mechanics: experimental study of the effects of the passage of a wave beneath an obstacle, *Proceedings of the Academic des Sciences*, Paris, France.
- [42]. Masoudi E, and Zeraatgar H. (2017). Hydrodynamic Analysis of Various Cross Sections of Floating Breakwaters. 7th International Offshore Industries Conference.
- [43]. McCartney, B. L. (1985). Floating breakwater design. *Journal of Waterway, Port, Coastal, and Ocean Engineering*, 111(2), 304-318.
- [44]. Manisha, Kaligatla, R.B. and Sahoo, T. (2019). Effect of bottom undulation for mitigating wave-induced forces on a floating bridge. *Wave Motion*, 89, 166–184. doi:10.1016/j.wavemotion. 2019.03.007
- [45]. Nikpour, A.H., Moghim, M.N. and Badri, M.A., (2019). Experimental study of wave attenuation in trapezoidal floating breakwaters. *China Ocean Engineering*, 33(1), 103–113.
- [46]. Ouyang, H.T., Chen, K.H., and Tsai, C.M., (2016). Wave characteristics of Bragg reflections from a train of submerged bottom breakwaters. *Journal of Hydro-Environment Research*, 11, 91-100.
- [47]. Patil, S.B and Karmakar, D. (2021). Performance evaluation of submerged breakwater using Multi-domain Boundary Element Method. *Applied Ocean Research*, 114-10276. <https://doi.org/10.1016/j.apor.2021.102760>
- [48]. Pantonan, C., Rachman, T., Ahury and Putra T.P. (2020). The analytical solution of waves transmission coefficient on semi fixed floating breakwater, *IOP Conf. Series: Materials Science and Engineering*, 875, 012082.
- [49]. Pena E. and Ferreras J. (2011). Experimental study on wave transmission coefficient, mooring lines and module connector forces with different designs of floating breakwaters. *Ocean engineering*, 1150-1160.

- [50]. Peng W., Lee K S., Seung-Ho M. N., (2013). Numerical simulation of interactions between water waves and inclined-moored submerged floating breakwaters. *Coastal Engineering*, 82, 76–87. doi:10.1016/j.coastaleng.2013.07.002
- [51]. Sannasiraj, S., Sundar, V., and Sundaravadivelu, R. (1998). Mooring forces and motion responses of pontoon-type floating breakwaters. *Ocean Engineering*, 25, 17–48.
- [52]. Seelig, W.N. and Ahrens, J.P., (1981). Estimation of wave reflection and energy dissipation coefficients for beaches, revetments, and breakwaters, U.S. Army Corps of Engineers, Coastal Engineering Research Centre, Technical Paper No. 81-1.
- [53]. Senouci F., Chioukh, N., and Dris Mohammed E., (2019). Performance Evaluation of Bottom-Standing Submerged Breakwaters in Regular Waves Using the Meshless Singular Boundary Method. *Journal of Ocean University of China*, 18(4), 823–833. doi:10.1007/s11802-019-3854-1
- [54]. Sollitt, C.K. and Cross, R.H., (1972). Wave reflection and transmission at permeable breakwaters, Massachusetts Institute of Technology, R.M. Parsons Laboratory Technical Report, 147.
- [55]. Tseng I-F, You Chi-S and Tsai Chia-C., (2020). Bragg Reflections of Oblique Water Waves by Periodic Surface-Piercing and Submerged Breakwaters. *J. Mar. Sci. Eng.*, 8, 522; doi:10.3390/jmse8070522
- [56]. Williams A.N., Lee H.S., and Huang Z. (2000). Floating pontoon breakwaters. *Ocean Engineering* 27 221–240.
- [57]. Zhang, Xiao-song Ma, Shan Duan, and Wen-yang (2018). A new L type floating breakwater derived from vortex dissipation simulation. *Ocean Engineering*, 164(), 455–464. doi:10.1016/j.oceaneng.2018.06.059
- [58]. Zhao et al. (2017) Analytical Study On an Oscillating Buoy Wave Energy Converter Integrated into a Fixed Box-Type Breakwater. *Math Probl Eng*.
- [59]. Zhanga et. al. (2021) Sloshing dynamics of liquid tank with built-in buoys for wave energy harvesting.
- [60]. Zhou T and Li Z., (2020). Research and application of floating breakwater. *International Journal of Engineering and Applied Sciences*. ISSN: 2394-3661, Volume-7, Issue-6